UNIVERSITY OF LONDON THESIS

Degree PHD Year 2006 Name of Author SIBTHORPE Anthony John

COPYRIGHT

This is a thesis accepted for a Higher Degree of the University of London. It is an unpublished typescript and the copyright is held by the author. All persons consulting the thesis must read and abide by the Copyright Declaration below.

COPYRIGHT DECLARATION

I recognise that the copyright of the above-described thesis rests with the author and that no quotation from it or information derived from it may be published without the prior written consent of the author.

LOAN

Theses may not be lent to individuals, but the University Library may lend a copy to approved libraries within the United Kingdom, for consultation solely on the premises of those libraries. Application should be made to: The Theses Section, University of London Library, Senate House, Malet Street, London WC1E 7HU.

REPRODUCTION

University of London theses may not be reproduced without explicit written permission from the University of London Library. Enquiries should be addressed to the Theses Section of the Library. Regulations concerning reproduction vary according to the date of acceptance of the thesis and are listed below as guidelines.

A. Before 1962. Permission granted only upon the prior written consent of the author. (The University Library will provide addresses where possible).

B. 1962 - 1974. In many cases the author has agreed to permit copying upon completion of a Copyright Declaration.

C. 1975 - 1988. Most theses may be copied upon completion of a Copyright Declaration.

D. 1989 onwards. Most theses may be copied.

This thesis comes within category D.

☐ This copy has been deposited in the Library of UCL

☐ This copy has been deposited in the University of London Library, Senate House, Malet Street, London WC1E 7HU.

Precision Non-Conservative Force Modelling For Low Earth Orbiting Spacecraft

Anthony John Sibthorpe

Thesis submitted for the degree of Doctor of Philosophy of the University of London

2006

Department of Geomatic Engineering

University College London

ProQuest LLC
789 East Eisenhower Parkway
P.O. Box 1346
Ann Arbor, MI 48106-1346

Abstract

Low Earth Orbiting spacecraft are used in various ways for remote observation and measurement of system Earth; some classes of measurements are only useful when modelled in a spatial reference frame. As the position of a satellite at a particular epoch is used to provide a fixed point of reference, it is vital that we know these positions both accurately and precisely. Non-conservative forces, which change the energy state of a spacecraft system, can have a dramatic effect on the estimated position of a satellite if unmodelled or, as is often the case, are modelled only crudely. Downstream Earth observation data can inherit significant errors as a result. As an example of this, it has been recognised that apparent long wavelength signals can be introduced into interferometric synthetic aperture radar (SAR) images by orbit error. Such images are used to monitor surface deformation, and may provide an indication of strain accumulation as a pre-cursor to Earthquake activity. It makes sense therefore to better model these non-conservative forces, thus improving the quality of the Earth observation data.

This project develops precise methodologies for modelling of solar radiation pressure / thermal re-radiation / eclipse modelling / Earth radiation pressure / spacecraft internal heat distribution / on-board instrument power output, and applies these techniques to the European Space Agency's ENVISAT satellite. This complicated satellite has necessitated the development of a significant number of new algorithms for dealing with a large number of geometric primitives. A graphical display tool, developed during this research, allows rapid model development and improved error checking. Resultant models are incorporated into the GEODYN II orbit determination software, developed at NASA's Goddard Space Flight Centre. Precise orbits computed using tracking data in combination with the newly developed force models are compared against precise orbits generated using nominal force models to ascertain the improvement this modelling effort affords. The new models are shown to systematically decrease both measurement residuals and empirically estimated once-per-revolutions accelerations. As a result, the ENVISAT model has now also been adopted in the GIPSY-OASIS II orbit determination software developed by NASA's Jet Propulsion Laboratory.

Acknowledgements

Dr Marek Ziebart can be held directly responsible for inspiring my passion in this subject; I hold him in the highest regard. Marek, along with Professor Paul Cross is to be thanked for giving me the opportunity to undertake this research, and for providing a wonderful atmosphere and working environment. Among my closest colleagues, [now Dr.] Sima Adhya is to be singled out for the 'heated' discussions on thermal re-radiation, eclipse modelling and whether we should quit and start a private detective agency (which neither of us has!). I could not have asked for a better friend and collaborator. The following people (in no particular order) have helped to make my time in the Department of Geomatic Engineering worth remembering: Stuart Robson, Zhenhong Li, Simon Edwards, Peter Arrowsmith, Nick Forrest and Mike Dunderdale.

While Dr Frank Lemoine from NASA's Goddard Space Flight Centre and Andrew Robson from EADS Astrium should be singled out for the expert assistance they provided, this project would not have been a success without help from around the globe. I offer the following in recognition of all such people, especially for those not explicitly named:

> "*Often, as I flew near the air corridor separating East from West I saw American jet fighters on the other side...Sometimes, as a mark of mutual respect, we tipped our wings in the recognition of a fellow pilot.*" (Scott & Leonov [American & Russian Astronauts / Cosmonauts], 2004).

My friends Jo and Kerry are to be thanked for extracting me from the daily toil of London and PhD life; they took me away on many wonderful and relaxing trips to the British countryside. Similarly, Martin and Gwladys have always inspired me with their love of life, willingness to adventure and the ease with which they always provide excellent food!

I leave you with the following thought: "*If you can't see gravitation acting here, you have no soul.*" (Feynman, 2005, Section 7.5).

Dedicated to HJABS.

I literally could not have

done it without you.

Table of Contents

Table of Figures

Table of Tables

Glossary

1CPR	Once-per-revolution
ACC1B	GRACE Level 1B Accelerometer Measurements
ANGARA	Analysis of Non-Gravitational Accelerations due to Radiation and Aerodynamics
AOCS	Attitude and Orbit Control System
API	Application Program Interface
ASAR	Advanced SAR
AT	Along Track accelerations
BFS	Body-Fixed coordinate System
BOL	Beginning-Of-Life
Cd	Coefficient of drag
CFRP	Carbon-Fibre Reinforced Plastic
CHAMP	CHAllenging Minisatellite Payload
CNES	Centre National d'Etudes Spatiales: French Space Agency
COMET	Centre for the Observation and Modelling of Earthquakes and Tectonics
Cr	SRP scale factor
CSR	Centre for Space Research, University of Texas at Austin
CT	aCross Track accelerations
DEM	Digital Elevation Model
DEOS	Department of Earth Observation and Space Systems
DInSAR	Differential InSAR
DOPRI8	Dornier & Prince 8^{th} order numerical integrator
DORIS	Doppler Orbitography and Radiopositioning Integrated by Satellite
DOY	Day Of Year
DSMC	Direct Simulation Monte Carlo
ECEF	Earth Centred Earth Fixed coordinates
ECI	Earth Centred Inertial coordinates
EM	Electromagnetic
ENVISAT	ESA Environmental Satellite

EOL	End-Of-Life
EPS	Earth-Probe-Sun angle
ERBE	Earth Radiation Budged Experiment
ERP	Earth Radiation Pressure
ESA	European Space Agency
ESARB	UCL ENVISAT SAR Baselines web tool, developed for COMET
ESOC	European Space Operations Centre
ESS	Equatorial Separation of Sun and orbit plane
ESTEC	European Space Research and Technology Centre
EUV	UltraViolet electromagnetic radiation
F10.7	Solar radio noise flux
FFT	Fast Fourier Transform
GA	General Along track accelerations, estimated by GEODYN II
GAST	Greenwich Apparent Sidereal Time
GDR	Geophysical Data Record
GEODYN II	NASA GSFC orbit determination software, version 2.0
GFZ	GeoForschungsZentrum
GIPSY-OASIS II	GPS Inferred Positioning SYstem and Orbit AnalySIS software, version 2.0
GNSS	Global Navigation Satellite System
GOCE	Gravity Field and Steady-State Ocean Circulation Explorer
GPS	Global Positioning System
GRACE	Gravity Recovery And Climate Experiment
GSFC	NASA Goddard Space Flight Centre
HCL	Height, Cross and aLong track coordinates
HWM-93	Horizontal Wind Model 93
IERS	International Earth Rotation Service
IGS	International GNSS Service
InSAR	Interferometric SAR
JPL	NASA Jet Propulsion Laboratory
LEO	Low Earth Orbiting
LOD	Length Of Day

LR BRM	Low Rate Background Regional Mission
MCD	Mission Conventions Document
MEO	Medium Earth Orbit
MET V2	NASA Marshall Engineering Thermosphere model, version 2.0
MLI	Multi-Layer Insulation
MLST	Mean Local Solar Time
MSIS86	Mass Spectrometer and Incoherent Scatter 1986 neutral atmosphere model
MSS	Minimum angle Separating Sun vector and BFS YZ plane
MVBB	Minimum Volume Bounding Box
NASA	National Aeronautics and Space Administration
nBFS	Nominal BFS
NCEP	National Center for Environmental Prediction
NCF	Non-Conservative Forces
NOAA	National Oceanic and Atmospheric Administration
NOM	Nominal
NSZ	Normalised Sun vector Z values
OCM	Orbit Control Manoeuvre
OCS	Object Coordinate System
ODD	Orbit Data Derived minimum angle separating Sun vector and BFS YZ plane
ODR	Delft orbital data record
OpenGL	Open Graphics Language
PRC	ESA precise orbit
Qrate	Net thermal output from a satellite bus
RA2	Radar Altimeter, version 2.0
RAAN	Right Ascension of the Ascending Node
RMS	Root Mean Square
ROI_pac	InSAR processing software
SA	Surface Area
SAR	Synthetic Aperture Radar
SATAN	SATellite ANalysis software for SLR processing

SFCM	Stellar Fine Control Manoeuvre
SINDA	Systems Improved Numerical Differencing Analyser
SLR	Satellite Laser Ranging
SRP	Solar Radiation Pressure
STD	Spherical Trigonometry Derived minimum angle separating Sun vector and BFS YZ plane
STL	Standard Template Library
SYSM	Stellar Yaw Steering Mode
TOA	Top Of the Atmosphere (30km above WGS84)
TOD	True of Date
Topex Poseidon (T/P)	Ocean TOPography EXperiment satellite with Poseidon altimeter
TPMC	Test Particle Monte Carlo
TRASYS	Thermal Radiation Analysis System
TRR	Thermal Re-Radiation
UCL	University College London
UCL_SRP	UCL's SRP modelling software suite
UTC	Universal Time Coordinated
VIF	Version Independent Format
WGS84	World Geodetic System 1984

PART I

1. Introduction

Our Earth is constantly affected by physical processes such as vulcanism, earthquakes, and the melting of ice sheets which pose a threat to human life; few of these, if any, are completely understood. The current era of growth in the remote observation of our planet from space presents an unprecedented opportunity to develop new insights into these matters and to consolidate existing theories.

Data captured from most space-based instrumentation, often a low Earth orbiting (LEO) satellite(s), must be attached to appropriate spatial and temporal reference frames if it is to have any meaning. In most cases the reference frame of choice is known relative to the position of the spacecraft. Therefore, if the position of the spacecraft is poorly known, this will impact directly upon the quality of any measurement modelling. Scientists from many different disciplines including sea level analysts, interferometric synthetic aperture radar (InSAR) specialists and GPS geodesists are starting to place severe demands on systems that were not necessarily built specifically for their purpose. This means that current assumptions used in the production of precise orbit products must be reviewed, and replaced with improved versions where possible in order to allow the highest accuracies to be extracted from any resultant data.

It is understandable that orbit specialists from around the world, working to produce high quality orbit solutions, wish to announce improvements they have made to their processing strategies (e.g. Lichten & Border, 1987, Beutler et al., 1994, Bar-Sever et al., 1996, Doornbos et al., 2002, Hugentobler & Beutler, 2003, and Haines et al., 2004). However, this means it is often left to others, in many cases downstream data users, to point out deficiencies in these orbit products. Indeed, orbital position errors have been specifically targeted by several authors (e.g. Reigber et al., 1996, Klees & Massonnet, 1999, Hanssen, 2001 and Li et al., 2004) as being a major limiting factor in what is achievable with InSAR in the domain of geophysical deformation monitoring.

This thesis seeks to address the important and demanding process of non-conservative force modelling for LEO satellites. Unlike conservative (i.e. gravitational) forces, non-conservative forces change the energy state of a spacecraft. In the past, considerable simplifications to non-conservative force models have been adopted (e.g. Marshall et

al., 1992) purely for reasons of efficiency and a lack of computational resources. Yet, if too simplistic, these non-conservative force models can become significant contributors to orbit error. Major non-conservative forces and their impact on orbit accuracy are examined in detail, specifically in relation to their effect upon deformation monitoring using InSAR.

The ENVISAT satellite is used as a case study throughout, as not only does it have a SAR antenna aboard, but it is also the flagship Earth observation satellite of the European Space Agency (ESA). ENVISAT brings its own problems, as it is an extremely large satellite with a complicated attitude regime, making it appear difficult to model. To help combat these apparent hurdles, a graphical viewer tool is developed which allows computer simulations of the satellite to be visualised, interrogated and checked for gross errors. Several new algorithms are detailed and implemented:

- a 'block-modelling' technique used to speed up the computation of non-conservative force models
- new, improved and corrected attitude algorithms for ENVISAT
- a new algorithm for accurately determining eclipse boundary crossing times for low Earth orbiting satellites.

Finally, rigorous evaluation of model performance is conducted through tests performed both at UCL, and in collaboration with NASA Goddard Space Flight Centre (GSFC).

1.1. Problem Statement

Current non-conservative force modelling methods seek to limit the effects of modelling deficiencies using empirical 'soak-up' parameters but, as is shown, errors from one source can alias unexpectedly into soak-up terms intended for other errors. Perhaps more significantly, if these soak-up parameters fail to correctly absorb all of the orbital error, the error will remain in the published orbit solutions. It is shown that apriori high-precision analytical modelling of these non-conservative forces, the central topic of this thesis:

- reduces the need for soak-up parameters
- reduces aliasing
- improves the overall accuracy of final orbit solutions.

The following outlines the three main questions asked, and answered, by the remaining sections of this thesis:

- How can we efficiently compute high precision non-conservative force models for very large and complex low Earth orbiting satellites?
- What effect do high precision non-conservative force models have on once-per-revolution empirical 'soak-up' parameters?
- Do these high precision models improve overall orbit accuracy?

1.2. Introducing ENVISAT

ENVISAT, a European Space Agency satellite, was launched from Kourou in French Guiana on the 28th of February 2002. It is a very large and complex low Earth orbiting satellite (see Figure 1-1), having an on-orbit configuration of 25m x 10m x 7m and housing 10 scientific instruments for remote observation of Earth processes on a global scale.

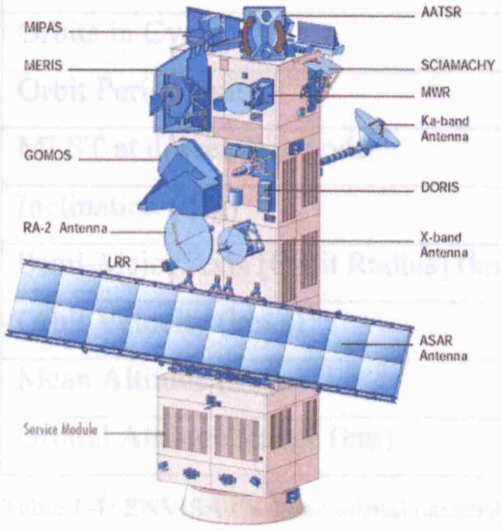

MIPAS – Michelson Interferometer for Passive Atmospheric Sounding.
GOMOS – Global Ozone Monitoring by Occultation of Stars.
SCIAMACHY – Scanning Imaging Absorption Spectrometer for Atmospheric Cartography.
MERIS – Medium Resolution Imaging Spectrometer.
AATSR – Advanced Along Track Scanning Radiometer.
ASAR – Advanced Synthetic Aperture Radar.
RA-2 – Radar Altimeter 2.
MWR – Microwave Radiometer.
DORIS – Doppler Orbitography and Radiopositioning Integrated by satellite.
LRR – Laser Retro-Reflector.

Figure 1-1: ENVISAT Instruments[1].

ENVISAT's orbit is near circular and has an altitude of almost 800km. The orbit is Sun-synchronous which means that the orbit plane maintains a near constant separation (c.30°) with respect to the direction of the Sun from the Earth. ENVISAT crosses the

[1] Image from http://envisat.esa.int/instruments/tour-index/

point where the orbit plane intersects the equator on the Sun facing side of the Earth (the descending node) at the same mean local solar time (MLST) each orbit (c.10am). This Sun-synchronous behaviour is facilitated by the orbit being near-polar with an inclination of c.98.5°. A result of this configuration is that Earth's oblateness introduces a torque (i.e. extra gravitational pull at the equator) that slowly rotates the plane of the orbit about the spin axis of the Earth at a speed which matches the motion of the Sun across the sky. Moving at a speed of almost 7.5km/s, ENVISAT completes one orbit (arc length of c.45,000km) in just under 101 minutes. The repeat period is the length of time taken before a satellite is in [almost] the same place with respect to the surface of the Earth, which for ENVISAT takes 35 days. ENVISAT experiences an eclipse period, when the satellite passes through the Earth's penumbra and umbra, which lasts approximately 30 minutes every orbit. A description of ENVISAT's mean orbital parameters is given in Table 1-1.

Orbits per Day	$14\,^{11}/_{35}$
Repeat Cycle (days)	35
Orbits in Cycle	501
Orbit Period (min)	100.59
MLST at descending node	10:00
Inclination (deg)	98.55
Semi-Major Axis [Orbit Radius] (km)	7159.5
Orbit Velocity (km/s)	7.45
Mean Altitude (km)	799.8
Orbital Altitude Range (km)	780 - 820

Table 1-1: ENVISAT's mean orbital parameters[2].

Figure 1-2 shows a rendered view of the highly detailed model of ENVISAT used throughout this thesis.

[2] http://esa.envisat.int/m-s/mission/operations.html

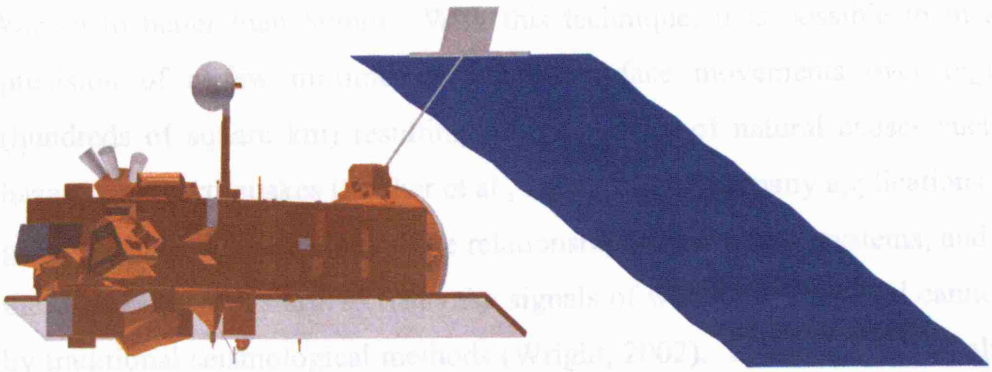

Figure 1-2: Rendered model of ENVISAT used in this study.

ENVISAT forms the central case study of this thesis, but the tools developed are largely generic, and are capable of being applied to spacecraft which orbit at any altitude. These tools have already shown good results when applied to other satellites including JASON-1, a French and US altimetry satellite with an orbital altitude of c.1,300 km, and GPS satellites (Adhya, 2005 and Haines et al., 2004) which have an orbital altitude of c.20,000 km.

1.3. Chapter Overview

What follows is a brief introduction and contextual background to the methodology adopted for this thesis and also the structure of the remaining chapters and related areas which must be understood when undertaking research of this nature.

1.3.1. ENVISAT and SAR

Many geophysicists, including those from the Centre for the Observation and Modelling of Earthquakes and Tectonics (COMET[3]), use space based radar instruments to measure the accumulation of strain across large areas of our planet to assess Earthquake hazards. COMET are particularly interested in data from ENVISAT's Advanced Synthetic Aperture Radar (ASAR) antenna, and use a technique known as Differential Interferometric SAR (DInSAR) which makes use of two or more radar images taken at different times. In agreement with arguments developed in section 2.4, COMET require that the horizontal baseline between the satellite position at these two epochs should be

[3] http://comet.nerc.ac.uk/

known to better than 50mm. With this technique, it is possible to measure, with a precision of a few millimetres, minute surface movements over regional extents (hundreds of square km) resulting from a variety of natural causes such as volcanic hazards and earthquakes (Zebker et al., 1994). This has many applications including the gathering of intelligence about the relationship between fault systems, and the nature of the composition of Earth's crust - the signals of which are slow and cannot be detected by traditional seismological methods (Wright, 2002). It can also tell us about so-called anthropogenic deformation including mining, landslip and that due to groundwater extraction (Bawden et al., 2001).

COMET use DInSAR to measure deformation specifically due to tectonic activity. This technique can not only provide accurate measurements of the well-known often large and catastrophic co-seismic shifts along fault lines, but is also capable of providing information on the build up of energy in the Earth's crust (interseismic strain) between these events. This can help us to better understand the earthquake cycle (the repetition of earthquakes on the same fault), and should eventually lead to more accurate and more rapid predictions of earthquake hazards. However, errors in resulting interferograms can have very similar length-scales to seismic signals, or alternatively can be so large as to just swamp them. SAR errors come from a wide variety of sources, including those that directly affect the radar signal itself (particularly signal path delays due to water vapour variation in the atmosphere), and problems with the many different steps required to process the radar data itself.

Variation in atmospheric water vapour is perhaps the largest error source for DInSAR but this subject has been widely investigated and some success in this area has recently been achieved (Li, 2005). Orbit error, perhaps the second largest error source for DInSAR has, by comparison, received little attention other than review articles or attempts to remove these errors with post-processing (Reigber et al., 1996, Hanssen, 2001 and Li et al., 2004). DInSAR is an area in which significant gains in orbit accuracy can be easily appreciated, leading to improved measurements of earthquakes and other physical processes which can help us to tune existing approaches or develop new models of these hazardous events, and will potentially save lives. A more comprehensive account of how orbit errors impact upon DInSAR is found in chapter 2.

1.3.2. Orbit Dynamics

The true geometry of a spacecraft trajectory is shaped by the force field in which it operates. Conventionally, this force field is broken down into conservative and non-conservative forces (NCF). The conservative, and in this case gravitational, force field is now thought to be well understood and very well determined, especially in the light of recent extremely successful gravity missions such as that of the GRACE satellite. There is still possibly more work to be done here, especially for low Earth orbiting satellites, but this is well outside the scope of the current project. This conservative force field includes principally: the Earth gravity field itself, modelled as spherical harmonic expansions; time variable inhomogeneous constituents due essentially to mass redistribution from precession of the Earth's spin axis, the deforming effects of the Sun and moon on the solid Earth and oceans, global isostatic adjustment, plus contributions from the atmosphere, hydrology, oceans and the cryosphere; and direct gravity terms from third bodies such as the Sun, Moon, Mars, Venus and Jupiter which rely upon accurate knowledge of the bodies' positions, and relativistic corrections. However, the non-conservative force field is far less well understood and has previously been treated through the estimation of empirical scale parameters which tune a basic spacecraft model. As several of these forces are dependent upon the complexity of the spacecraft's geometry, it is the computationally efficient modelling of certain members of this set of forces which forms the basis of the current research. A comprehensive review of literature concerned with non-conservative force modelling is presented in chapter 3.

Non-conservative forces change the energy state of a spacecraft, and those modelled here include the following:

- Solar Radiation Pressure (SRP) - momentum exchange from solar photons impacting upon the spacecraft is the principal driver of the NCF field unless a satellite has a very low altitude (<c.600km), then atmospheric drag may dominate.
- Thermal Re-radiation (TRR) – a satellite may heat up differentially from a radiation source such as the Sun due to attitude constraints. If this heat energy is re-radiated anisotropically, a net force results. On-board computer systems and instrumentation can also generate heat within the spacecraft bus, and may result in what is referred to here as the Qrate force [EADS Astrium, ESA's principal

contractor for ENVISAT, define a Qrate as the heat output of internal spacecraft components, in Watts].

- Earth Radiation Pressure (ERP) - thermal and visible radiation emitted and reflected respectively from the Earth affects satellites in a manner conceptually similar to SRP and TRR.
- Atmospheric drag – Low Earth Orbiting satellites may still operate within the Earth's atmosphere even though the gases are rarefied compared with those found at the surface of the Earth. The drag force is largely dependent upon altitude, mass and frontal (ram) area etc. presented to the particulate flux.
- Antenna thrust – a recoil force due to the emission of high-power signals from on-board instrumentation such as the ASAR array.

Mathematically, the trajectory of a spacecraft is completely determined by a set of initial conditions (position and velocity) and a description of the force field which acts upon it. Theoretically, numerical integration of the second order differential equations of motion from these initial conditions should yield a precise ephemeris. In practice, neither the initial conditions nor the force field are known with sufficient accuracy, and can result in relatively large differences ('observation' residuals) between a pure integrated trajectory, and one which also incorporates many thousands of measurements (a precise orbit). To counteract these deficiencies, once-per-revolution (1CPR) parameters are often estimated which, it is hoped, will effectively absorb all of the unmodelled effects not attended to apriori. However, if large residuals remain after parameter estimation, as is the case with ENVISAT, this implies that the modelling is imperfect and that orbit error may alias into geophysical measurements.

ENVISAT's solar radiation pressure and thermal re-radiation models form the central core of non-conservative force models for this satellite. Although the force due to atmospheric drag is expected to be of a similar order of magnitude to that due to SRP, there are severe limitations on the precision of an apriori drag model. As the accuracy of the algorithms used to compute the SRP and TRR models have already been proven (e.g. Haines et al., 2004), it is hoped that this will reduce any aliasing of errors in these values into parameters estimated for atmospheric drag. This should then result in

improved drag estimates which will in turn allow the ambient spacecraft environment to be reconstructed at a later date.

A more detailed introduction to spacecraft dynamics is to be found in chapter 4, while chapters 5, 6 and 7 cover the major advances and innovations in the modelling of non-conservative forces made during this research project.

1.3.3. Satellite Attitude

Most Earth-observing satellites have a well defined attitude regime which may specify, for example, that their measuring instruments are always Earth facing, and that their solar array(s) must maximise Sun exposure. Consideration of the orientation of a satellite is critical for its correct positioning as assumptions about the location of the satellite's tracking equipment (ENVISAT uses the French DORIS (Doppler Orbitography and Radiopositioning Integrated by Satellite) system and SLR (satellite laser ranging)) and the application of non-conservative forces during orbit computation, depend upon it. A good understanding of a satellite's attitude provides another means to improve the efficiency of analytical NCF models, as they are very closely related. If it is known that the satellite will never present a particular aspect to an incident flux, for NCF forces which involve radiation or particles striking exposed surfaces of a satellite, then the resultant acceleration will never be required and does not need to be computed. ENVISAT's attitude is complex; this research assesses how well the published bus model meets specifications, correcting it as appropriate, and also develops a completely new solar array pointing model which exposes severe flaws in the original methodology. The modelling of ENVISAT's attitude is the subject of chapter 8.

1.3.4. SRP and TRR Model Computation

One way to reduce the compute time for any non-conservative force model is to consider only those regions of a satellite which are affected by any particular force. Chapter 9 investigates ways in which the modelling 'regions of interest' for ENVISAT can be determined, and also outlines the dangers associated with a reliance on techniques which over-simplify the problem.

1.3.5. Eclipse Boundary Determination

Solar radiation is the main source of both SRP and TRR, it is therefore essential that the degree to which the Sun is obscured from the satellite by the Earth's shadow is known accurately. Previously, for simplicity of implementation and execution, the most commonly used approach treated the Earth as a sphere (e.g. Montenbruck & Gill, 2001). For greater accuracy, a new eclipse function is developed to correctly determine eclipse period boundaries when modelling the Earth as an oblate spheroid. The model is detailed in full in chapter 10, as well as a practical experiment which tests its validity for LEO satellites.

1.3.6. Model Validation

For the purpose of initial validation, "orbit prediction" techniques are used as opposed to "orbit determination". Orbit prediction here refers to the process of numerically integrating a trajectory from initial conditions (position and velocity) taken from a precise orbit using only dynamic models, whilst orbit determination refers to the process of computing an orbit solution using a combination of tracking data and dynamic models. It should again be emphasised that during the prediction process NO observational data is used. The integrator used was developed at UCL and is an 8th order embedded Runge-Kutta integrator, which uses the models of the dynamics presented here, plus the oblate Earth eclipse model and gravitational forces. RMS 'errors' have been generated for different cases by differencing against the precise orbit used to seed the integrator, allowing a relative assessment of their accuracy and fidelity. A variational estimator is used to adjust the initial conditions to improve the fit to the precise orbits; the size of the adjustments is another useful metric. Predicted orbits, which are almost fully reliant upon the modelled dynamics, are not only useful for validating non-conservative force models, a pertinent applied example is the forecasting of the intensity of tropical cyclones / hurricanes (Goni & Trinanes, 2003). The authors use near real-time orbits for altimetry satellites and the dynamics are critical. Measured sea-surface heights help to reconstruct the sub-surface ocean thermal structure; these data are used to predict the path and intensity of tropical cyclones which can wreak untold damage on populated areas if forecasts are inaccurate. Better dynamics should lead to better near real-time orbits and hence improved forecasts. A performance assessment between long-term orbits predicted with both the UCL (used from this point

on as the name for the ENVISAT model suite developed by this author during the current study) and the nominal (NOM) non-conservative force models (produced by the Centre National d'Etude Spatiales (CNES)) is given in chapter 11.

The 'final word' in model validation comes from measurement residuals over long arcs determined with observations of ENVISAT by its on-board and ground-based tracking facilities (DORIS, and SLR - Satellite Laser Ranging). During a visit to NASA's Goddard Space Flight Centre (GSFC) over the Easter period of 2005, FORTRAN code written at UCL to model the ENVISAT attitude and non-conservative accelerations due to SRP, TRR, Qrates and ASAR antenna thrust was incorporated into GSFC's GEODYN II orbit determination software. GEODYN II was used to produce two different sets of orbits, the first using the UCL model and the second using the NOM macromodel, both solutions use only DORIS data over the whole of the year of 2004 to compute the orbit allowing SLR measurements to be used as truly independent observations. Results of comparisons between the two orbit solutions and their analysis are also the subject matter of chapter 11.

1.4. Summary

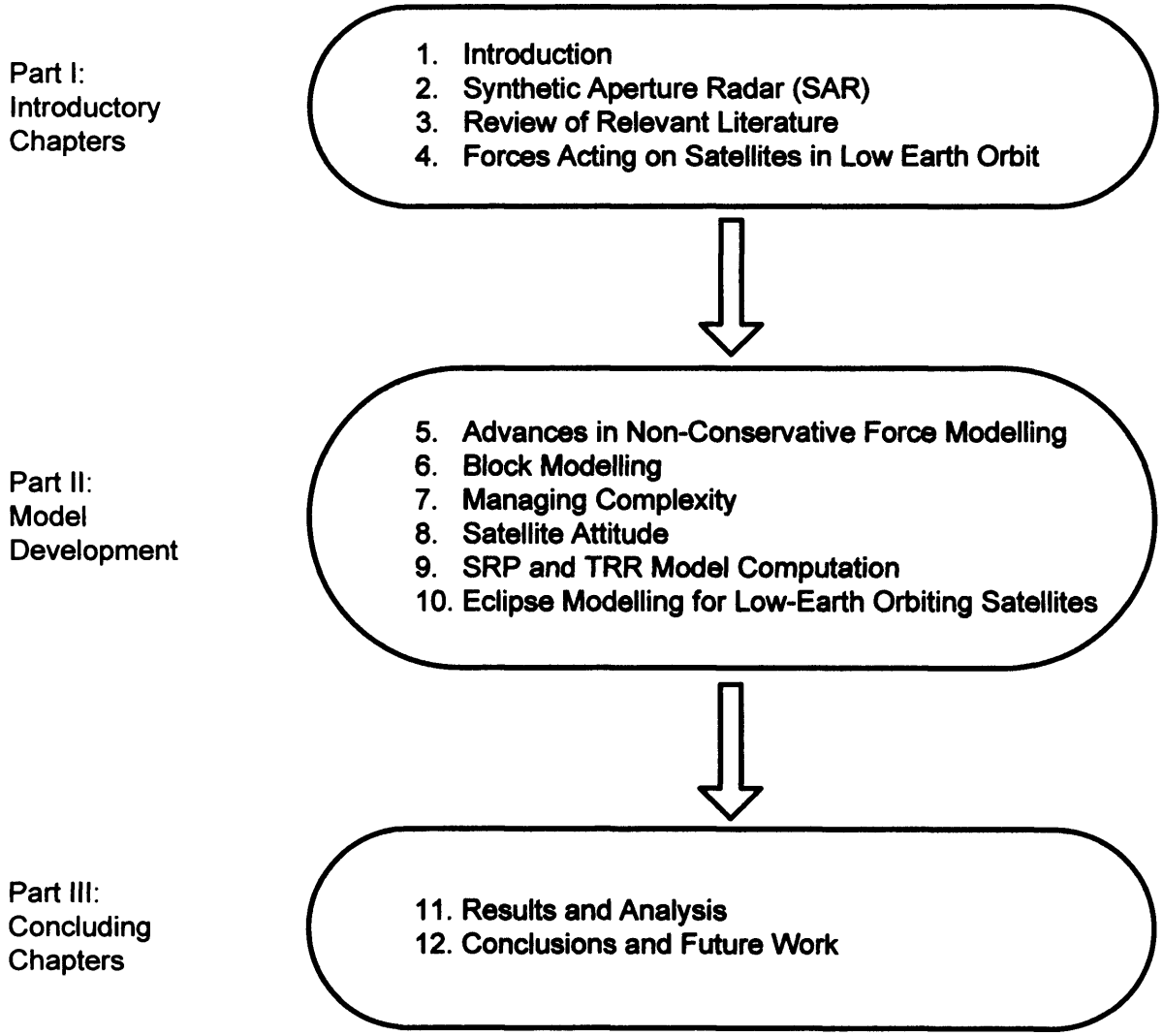

Figure 1-3: Thesis Structure.

2. Synthetic Aperture Radar (SAR)

This chapter introduces precise non-conservative force modelling, and clearly demonstrates a context in which it is absolutely essential for some Low Earth Orbiting satellites. The ENVISAT satellite has been adopted as a case study for this research and the current level of orbit accuracy for ENVISAT is assessed, with particular emphasis given to the impact of orbit error on differential interferometric synthetic aperture radar (DInSAR).

2.1. Introducing InSAR

Data from ENVISAT's Advanced Synthetic Aperture Radar (ASAR) antenna can be used by the technique of Differential Interferometric SAR (DInSAR) to measure, with a theoretically achievable precision of a few millimetres, minute surface movements over large extents (hundreds of square km) resulting from a variety of natural causes such as volcanic hazards and earthquakes (Zebker et al., 1994). Due to its large areal observation extent SAR can also inform us about triggered slip, where faults in the region of an earthquake (though still up to tens of km distant) are caused to slip by small amounts even though not part of the main earthquake. This allows intelligence to be gathered about the relationship between fault systems, and on the nature of the composition of Earth's crust which enables such dependent slip events to occur.

This technique is capable of providing information on the build up of energy in the Earth's crust (interseismic strain) before being released in large earthquakes. The cycle of interseismic strain accumulation and coseismic strain release (an earthquake) can have a period of several hundred years. Early models of earthquake mechanics, such as Reid's elastic-rebound model (Reid, 1910), are too simplistic. Reid, based upon observations of the 1906 San Francisco earthquake, posited that distant forces result in a gradual build up of elastic energy which causes an existing fault to suddenly and catastrophically rupture, releasing the stored energy. However, Reid's theory ignores the way in which rock properties change with depth and cannot explain features such as postseismic deformation (rapid surface change in the immediate aftermath of an earthquake). However, it is difficult to come up with alternatives to Reid's model that do a better job of explaining the earthquake cycle, though DInSAR observations of

surface deformation at various stages in the earthquake cycle contribute significantly by placing bounds on competing models (Wright, 2002), but:

> *"Measuring the build-up of elastic strain between earthquakes (interseismic strain) using InSAR is not straightforward. The strain rates are extremely small – the North Anatolian Fault, for example, moves at around 24 mm per year horizontally ... interseismic deformation associated with faults that are locked at the surface is typically distributed on a length-scale of 30-150km, and therefore much harder to distinguish from atmospheric and orbital errors."* (Wright, 2002).

In order to use DInSAR for such purposes all significant areas of the observation error budget must be attacked. SAR error sources are many and varied in nature, including: processing of the raw radar signals by a technique known as focusing (not discussed here) which can require hundreds of billions of operations (Massonnet & Feigl, 1998); height and co-registration errors in digital elevation models (DEM); radar signal path delays due to difficult to model water vapour variation in the atmosphere across a scene, leading to up to 10cm errors in deformation products with only a 20% change in relative humidity (Klees & Massonnet, 1999 and Zebker et al., 1997); phase unwrapping (Burgmann et al., 2000) - the re-construction of deformation across a scene relative to a fixed point required due to the ambiguity inherent in the phase measurements, and; temporal decorrelation [or incoherence] (Klees & Massonnet, 1999). Coherence is a measure of the similarity of a surface's response to two different radar pulses emitted at different times and/or locations. Coherent radar echoes are correlated with each other "if each represents nearly the same interaction with a scatterer or set of scatterers" (Zebker & Villasenor, 1992). The word "nearly" is used because each surface element has a random backscatter element which can never be determined, and remains unknown. Coherence is affected by the spatial separation and orientation of the antenna(e) and changes to the properties of the surface being imaged over time.

Two SAR datasets collected over the same area from slightly different view points (e.g. subsequent points on a repeat orbit track) can be combined to produce an interferogram, which shows the relative difference between the phase measurements at each epoch. Hence, as the wavelength of the radar signal is known, this phase shift can be converted

to a deformation map after substantial processing (see section 2.3 for more details). Wright continues:

> *"In an ideal world, we would look at interferograms spanning a very long time-interval, but, in areas such as Turkey, interferograms with time-intervals of larger than two years are generally incoherent. We are therefore restricted to shorter period interferograms, but these contain such a small deformation signal that they tend to be swamped by noise"* (Wright, 2002).

DInSAR relies upon knowledge of the position of the satellite in space, as this supplies a fixed location to which SAR measurements can be referred. Furthermore, deformation studies with this technique require the use of two or more passes of the satellite over a site before and after an earthquake event or, for interseismic strain, over a particular period of time between earthquake events. In this case, it is important that the relative separation of the satellite at these two epochs is known accurately. DInSAR is an area in which significant gains in orbit modelling can be easily appreciated, and this chapter deals with it in some detail. The remainder of the current chapter also assesses the current level of accuracy in ENVISAT orbits and how DInSAR is directly affected by orbit errors.

Small non-conservative forces affect the satellite's position, and mean that orbit determination at the required level of accuracy (c.50mm) is a far from trivial matter: ENVISAT is hurtling through space at almost 7.5kms^{-1} and travels approximately 45,000km each time it orbits the Earth (every c.101 minutes). As discussed in subsequent chapters, this research project is aimed at producing accurate non-conservative force models which take full account of the structural complexity and surface properties of the satellite to enable more accurate orbits to be produced. This project is most certainly not restricted to improving orbit solutions for DInSAR work. The modelling techniques have been developed with an eye to increasing overall orbit accuracy and are generic for satellites at all altitudes and configurations and may yield improvements in, for example, an area such as operational oceanography.

2.2. Orbits and DInSAR

To first order a satellite orbit can be described as elliptical - the motion being confined to a plane, and position being described using two axes (U,V) (see Figure 2-1). In three dimensions, the radial direction (height) runs from the geocentre to the satellite (i.e. the in-plane Earth centred position vector) and the along-track vector points approximately in the direction of the satellite's velocity vector, the right-handed set is completed by the direction perpendicular to the ellipse, called the across-track (out-of-plane) direction. When ENVISAT repeats its passage over a particular region of the Earth (after a period of 35 days) it will not travel along exactly the same ellipse as previously, and a 3D baseline will separate the satellite at these two distinct epochs. For the work that COMET are undertaking, it is vitally important that the across-track component of this baseline in particular (relative to the instantaneous 3D coordinate system defined at one epoch) is known very accurately – a target of better than 50mm relative across-track accuracy has been set by COMET.

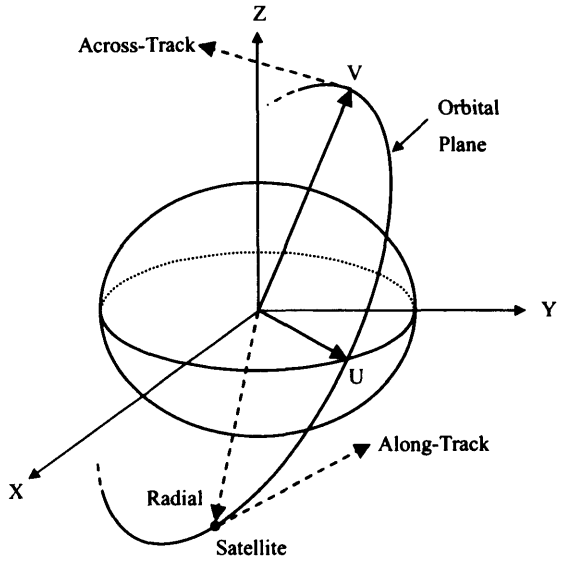

Figure 2-1: A possible orbit coordinate system, showing radial, along and across-track vectors.

Precision orbit products from centres around the world (European Space Agency (ESA), National Aeronautics and Space Administration's Goddard Space Flight Centre (NASA GSFC), Department of Earth Observation and Space Systems (DEOS)) are used to generate baseline information for DInSAR work. Failure to generate high enough quality orbit solutions introduces apparent deformation signals into differential interferograms. The left-hand image in Figure 2-2 shows the difference between two

ASAR interferograms generated using slightly different quality orbit solutions. Each dark fringe [red/blue boundary] implies surface movement of 2.8cm which corresponds to one half wavelength (the measurement is two-way, from the satellite to the surface and back). This is a long wavelength signal that can be interpreted as resulting from the whole scene tilting in one particular direction. The right-hand image in Figure 2-2 results after a SAR processing algorithm known as 'baseline refinement' which removes any planar tilt in the resulting interferogram using an empirical parameter, it can be seen on the right of this image that there is also possibly some contribution due to topography. The problem however, is that because of the 'catch-all' nature of such empirical parameters, geophysical signals may alias into the baseline refinement process for example, such as that used by the well known ROI_pac SAR processing software:

> *"The 'baseline' that is calculated in ROI_pac from the unwrapped phase and DEM is often different by several meters from the baseline determined from the orbits ... it is really an 'effective baseline' that is including other systematic effects on the interferogram phase and not just the baseline. It does not have a physical meaning. For example, a long-wavelength atmospheric water vapor change across the scene can be partially removed by changing the effective baseline. Long-wavelength Earth deformation signals can also have functional forms similar to baseline length errors and be mapped into an effective baseline change. The fitting procedure in ROI_pac attempts to remove any phase variation that can be matched by a baseline length change"* (Eric Fielding, ROI_pac co-developer, pers. comm.).

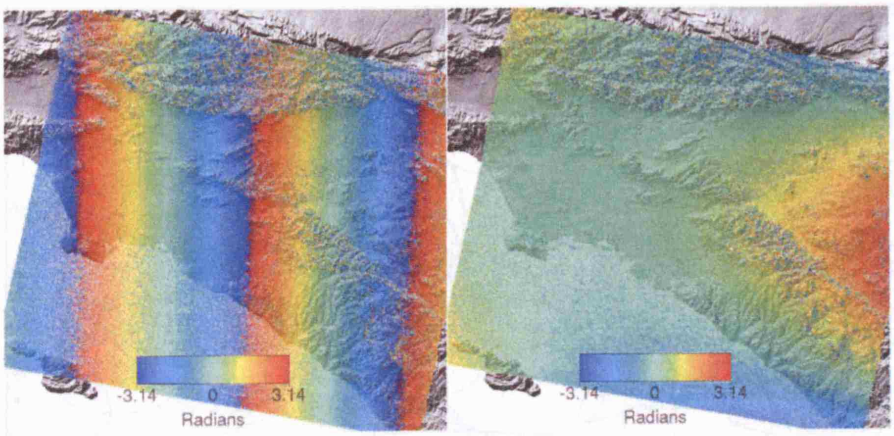

Figure 2-2: Image from Li, 2005. Difference between ESA precise (PRC) and Delft orbital data record (ODR) orbits for ERS-2, track 170, frame 2925. SAR collection dates: 24/06/00 and 18/08/01. Along-track direction runs from top to bottom of the images, tilt runs left to right due to the side looking nature of the SAR imaging geometry.

Moreover, it is extremely unlikely that this approach is able to completely remove all of the non-linear errors that impact upon an interferogram during the time taken to collect its underlying phase information. The best solution is to remove as many errors as possible up front, a priori, by using dedicated techniques such as precise non-conservative force modelling.

2.2.1. ENVISAT Tracking Geometry

In this section it is shown that ENVISAT orbits are routinely produced by combining sophisticated estimation strategies along with many thousands of DORIS (Doppler Orbitography and Radio-positioning In Space) and SLR (Satellite Laser Ranging) observations, plus a priori models of Earth gravity, third body gravity, tidal effects, relativistic effects and non-conservative dynamics. Due to the distribution of DORIS and SLR observing stations across the Earth (See Figure 2-3 & Figure 2-4) and ENVISAT's relatively low orbit, it is not possible to track ENVISAT across its entire orbit. Also, owing to the second generation DORIS antenna mounted on ENVISAT, it is possible to measure from only two DORIS ground stations simultaneously, although even this is not always achievable (see Figure 2-3).

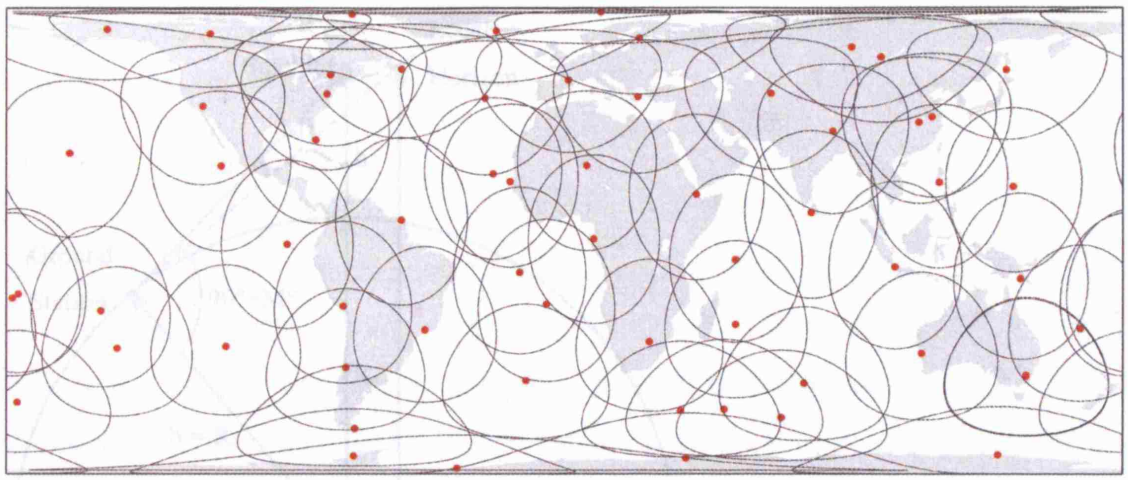

Figure 2-3: Operational DORIS beacon network visibilities on 07/06/2005 for the ENVISAT Satellite: minimum elevation of 10 degrees. Behrmann equal area projection with a 0° central meridian. DORIS site coordinates from http://ids.cls.fr/html/doris/sitelog.html .

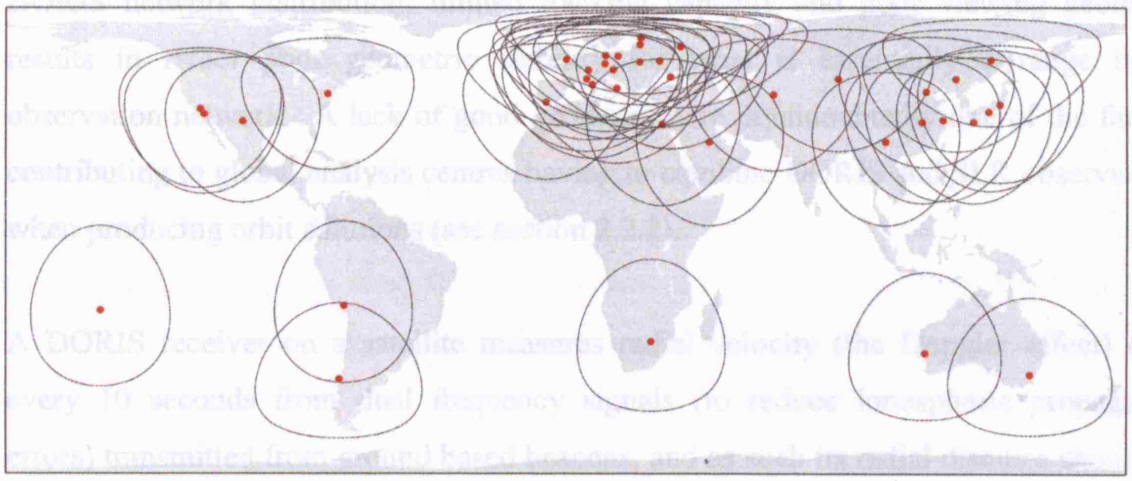

Figure 2-4: Operational SLR station network visibilities on 07/06/2005 for the ENVISAT Satellite: generous minimum elevation of 10 degrees (some are as high as 30°, http://ilrs.gsfc.nasa.gov/stations/). Behrmann equal area projection with a 0° central meridian.

Figure 2-5 shows that a simple calculation provides the radius of the viewing circle, over which it is possible to view a satellite from an arbitrary point on a spherical Earth when observing a satellite at altitude h, and with a mask angle M. Distance c can readily be solved for using the sine rule - a 10° mask angle gives a value of circa 2370km.

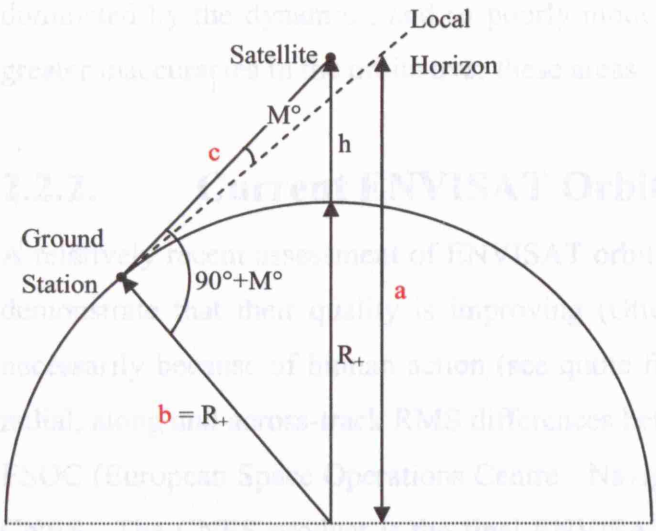

Figure 2-5: Visibility calculation based on a spherical Earth and a mask angle M°.

DORIS network distribution, limited tracking capacity and poor viewing geometry results in rather poor geometric stability for what is essentially a range based observation network. A lack of good geometry here is undoubtedly one of the factors contributing to global analysis centres having to combine DORIS and SLR observations when producing orbit solutions (see section 2.2.2).

A DORIS receiver on a satellite measures radial velocity (the Doppler effect) once every 10 seconds from dual frequency signals (to reduce ionospheric propagation errors) transmitted from ground based beacons, and as such its radial distance should be very well known[4]. However, ENVISAT precise orbit determination now includes a 6.5 microsecond datation bias (adjusted value, no physical explanation) for DORIS data, as this reduces satellite laser ranging residuals from 2.0 - 2.5 cm[5] to 1.5 - 2.0 cm. This is potentially a serious problem, as it is equivalent to c.5cm of along-track error at a speed of c.7.5km/s. For ENVISAT, SLR observations however have obvious geographically limited extents (see Figure 2-4), being dominated by stations in the northern hemisphere, and this should be borne in mind when evaluating the SLR residual analysis discussed in section 2.2.2. Poor tracking geometry does not occur over the entire orbit, but it does mean that there are 'weak spots' where the satellite motion is

[4] http://www.jason.oceanobs.com/html/doris/systeme_uk.html

[5] ENVISAT POD Group: current standards, Gilles Tavernier (pers. Comm.), CNES, 09/09/2005.

dominated by the dynamics, and so poorly modelled dynamics may especially lead to greater inaccuracies in the orbits over these areas.

2.2.2. Current ENVISAT Orbit Accuracy

A relatively recent assessment of ENVISAT orbit products up to April 2005 appears to demonstrate that their quality is improving (Otten & Boomkamp, 2003), though not necessarily because of human action (see quote from Otten below). Figure 2-6 shows radial, along and across-track RMS differences between precise orbits produced by both ESOC (European Space Operations Centre - Navigation Support Office (TOS-GN)) and CNES. The CNES product is the final ENVISAT precise orbit released as part of the Geophysical Data Record (GDR) for Altimetry products. As with the ESOC products, they have a latency of 6-9 weeks and combine both DORIS and SLR data in the solution. CNES radial accuracy based upon SLR residual analysis is quoted at the level of c.3cm RMS, while the ESOC values are closer to 1.5cm RMS (Otten & Boomkamp, 2003) – note however that SLR can no longer be regarded as providing an independent check because of its inclusion in the orbit product! The authors note that ESOC produced their own orbit solutions and conducted the SLR residual analysis for orbits from all analysis centres using their own software, and so the results for ESOC may be biased in their favour. Full details of the SLR analysis are given below in Table 2-1, allowing inter-comparison between solutions from several global analysis centres.

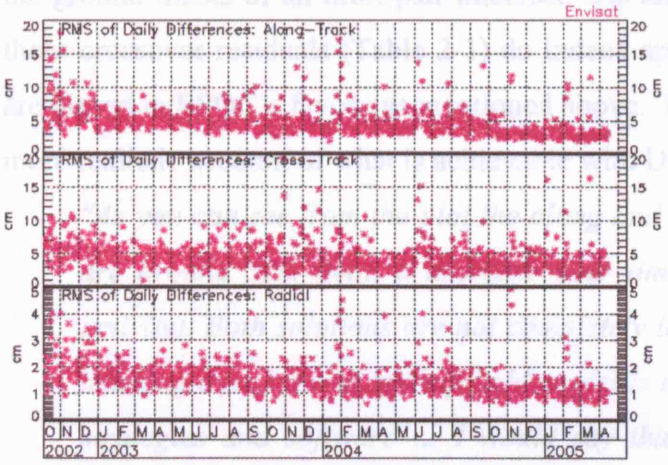

Figure 2-6: Radial, along and across-track RMS differences between precise orbits produced by ESOC (European Space Operations Centre - Navigation Support Office (TOS-GN)) and CNES. Otten & Boomkamp, 2003.

Solution (cm)	No. Obs.	SLR RMS	SLR Mean	Xover RMS	Xover Mean
ESOC	4527	1.43	0.10	6.86	-0.63
NCL	4527	1.88	0.07	6.47	-0.50
DEOS	4527	1.97	0.51	6.46	-0.23
CNES	4527	2.93	0.32	7.03	-0.89
GFZ	4527	3.14	-1.45	6.58	0.07
JPL-DORIS	4527	10.66	0.41	8.05	-0.55

Table 2-1: Overall SLR and altimeter crossover (Xover) residual statistics for each orbit solution in cm.

The campaign covered a period of 35 days (10/12/02 – 13/01/03) over orbit cycle 12. Table 2-1 shows RMS residuals for the different orbit solutions against an SLR 'truth' model; it should be noted that all of the centres (apart from JPL) have folded SLR observations into their orbit solutions, and therefore the SLR 'truth' model is no longer a truly independent check. Whilst the production of orbits from SLR data is not unheard of (e.g. failure of part of ERS-1's tracking system caused these orbits to be computed from SLR data only (Doornbos et al., 2002)), neither is it always routinely undertaken and is clearly not a desirable situation to be in. Altimeter crossover residuals are produced by differencing altimeter height measurements at points where the ground tracks of an orbit pair intersect. As an independent check on orbit quality, these crossover residuals (Table 2-1) do indeed appear to confirm that the SLR results are biased in ESOC's favour as mentioned above. However, the JPL solution provides a more realistic account of what is achievable with DORIS only:

> *"As you can see from the plot the along and cross track daily RMS values are around 5cm (with a decrease over time mainly due to lower solar activity). Both solutions are not completely independent because the same tracking data set and gravity field model is used but both do use different strategies and software ... I would say that 2-3cm is probably a more accurate value for the more recent data. And indeed all solutions (except the JPL solution) in the test campaign included the SLR data in their orbit determination process, so the SLR residuals will give you a too optimistic indication of orbit errors as they are no longer independent of the solution"* (Michiel Otten, 06/06/2005, pers. comm.).

A good rule-of-thumb for across and along-track error is quoted as being almost three times the radial error (Remko Scharroo, DEOS & NOAA, pers. comm), and would mean that ENVISAT's current across-track error alone is closer to 5-10cm RMS. Otten & Boomkamp (2003) believe that a realistic total orbit error of around 10cm is applicable to ENVISAT, with radial accuracy being around 3cm. Whichever of these scenarios is in fact true, some believe that "The required absolute accuracy for...[SAR]...orbit determination would need to be on the order of 1mm to fully correct the residual interferometric fringes, which is far below the current value of around 5-10cm" (Hanssen, 2001). Indeed, for SAR work conducted with ERS satellites, it has been explicitly demonstrated that precise orbits (50mm radial accuracy) introduce fewer spurious fringes than restituted orbits (8-10cm radial accuracy) (Closa, 1998). To properly describe how restituted orbits are computed, it is necessary to introduce the concept of operational predicted orbits which use 3 days of S-band tracking data to predict the satellite's position 1 day into the future for real-time mission control analysis. Restituted orbits also use 3 days of S-band data but are post-processed, and the middle day is taken as being the period over which the solution is valid[6].

Returning to Figure 2-6 once again, and remembering that these are RMS values, we can see that there is still plenty of work to be done if we are to produce the highest quality orbits to support new and exciting possibilities in planetary geodesy.

2.3. InSAR and DInSAR Basics

SAR (Synthetic Aperture RADAR (radio detection and ranging)) satellites such as ENVISAT uses a C-band (Frequency: 5.331 GHz, Wavelength: 5.66cm) active microwave sensor array to illuminate the ground with energy of known and carefully controlled properties, and because of this can operate day and night. ENVISAT's SAR antenna features enhanced coverage capacity and more modes of operation than the ERS tandem mission it succeeds. There are also SAR sensors in operation on aircraft platforms (e.g. AIRSAR/TOPSAR), but these will not be considered further here. The wavelength is often chosen to penetrate cloud cover with signal attenuation being small

[6] http://earth.esa.int/rootcollection/sysutil/ORB_QL.html

enough so as to be insignificant for much mapping work. Both the amplitude and phase of the waves that bounce back are recorded; however it is primarily the phase of the returned waves that are used to make an interferogram.

An integer number of whole wavelengths plus the phase (fractional part of a wavelength) of the return radar signal reflects the distance from the satellite to the ground and back again.

Comparing two radar images of an area on the Earth taken at different times from the same point in space means any ground movement towards or away from the satellite shows up as a phase difference between the images. Although it is not possible to steer the satellite to exactly the same point in space when performing the imaging, in theory, small geometric misalignments can be corrected later provided that the orbit information is capable of precisely telling us the baseline separation of the satellite at these two epochs. However, as shown in section 2.2.2, ENVISAT orbits are currently unable to allow SAR measurements to be made to COMET's requirements.

Figure 2-7 shows how such a measurement might occur, where the recorded phase difference will be twice that indicated in the figure because the phase difference at the ground is also contained in the signal which returns to the satellite from the ground. In addition, a random phase shift is added to a signal as it is backscattered from the ground, and will depend upon vegetation (e.g. leaf growth between scene acquisitions) and surface roughness etc. The growth of this portion of the signal over time can lead to temporal decorrelation / incoherence.

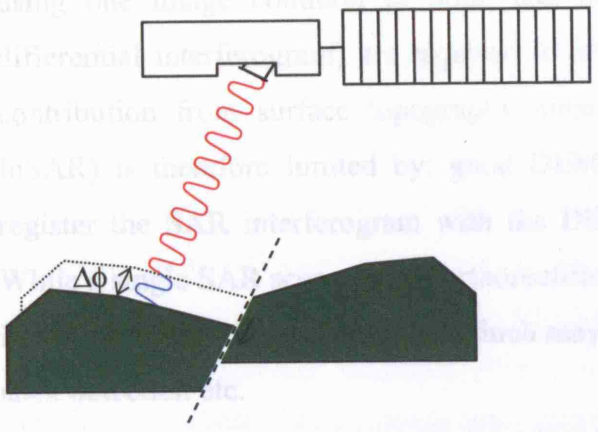

Figure 2-7: InSAR measurement of a ground surface before (red) and after (blue) deformation occurs.

The phase value of the signal returned from a ground surface is measured as an angle between 0 and 2π radians (see Figure 2-8) which describes its position within the wave cycle, and allows measurement to be made at the level of fractions of a wavelength (c.f. GPS).

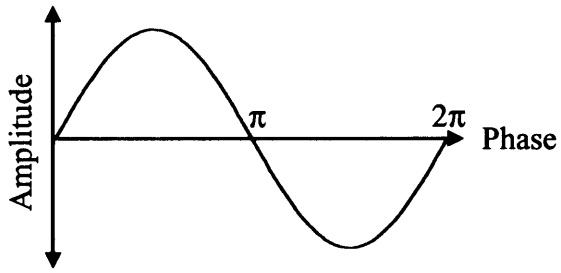

Figure 2-8: Wave phase and amplitude.

Following the necessary geometric corrections, measurements from two or more SAR images can be combined together in a process sometimes called "interfering", hence the name interferogram. Combining the two waves causes them to either reinforce or cancel each other, depending on their relative phases. The final effect can be captured as an image (an interferogram) if the degree to which a particular pixel's wave is either reinforced or cancelled is represented by a colour scale.

A minimum of two passes are required to produce a single SAR interferogram. Due to necessary geometric correction procedures, a minimum of two passes plus a reference DEM (repeat-pass InSAR), or three independent passes (two scenes are constructed using one image common to both, and are then subtracted to produce the final differential interferogram) are required to produce a differential interferogram, as the contribution from surface topography must be removed. DInSAR (or repeat-pass InSAR) is therefore limited by: good DEM availability; a capacity to precisely co-register the SAR interferogram with the DEM (Zebker et al., 1994) and; coherence. While a single SAR scene can be orthorectified using a DEM, it will contain little useful information apart from amplitude, which may be of use in the limited application of oil-slick detection etc.

For deformation studies, SAR images of a particular area can be obtained both before and after an earthquake, and the two sets of phase data can be combined to create an interferogram. Figure 2-9 shows a real differential interferogram produced by COMET for the 1999 Izmit earthquake in Turkey. Adjacent contours of the same colour denote a change of one half wavelength (i.e. c.2.8cm) in the phase recorded before and after the earthquake. The closer the fringes are together, the steeper the deformation gradient on the ground - the thick red lines mark the source of the earthquake (the North Anatolian Fault), where the fringes are closest together. Interferograms such as this one allow scientists to determine the precise location and magnitude of an earthquake, and what type of modelling is appropriate for assessing the future seismic hazard of an area.

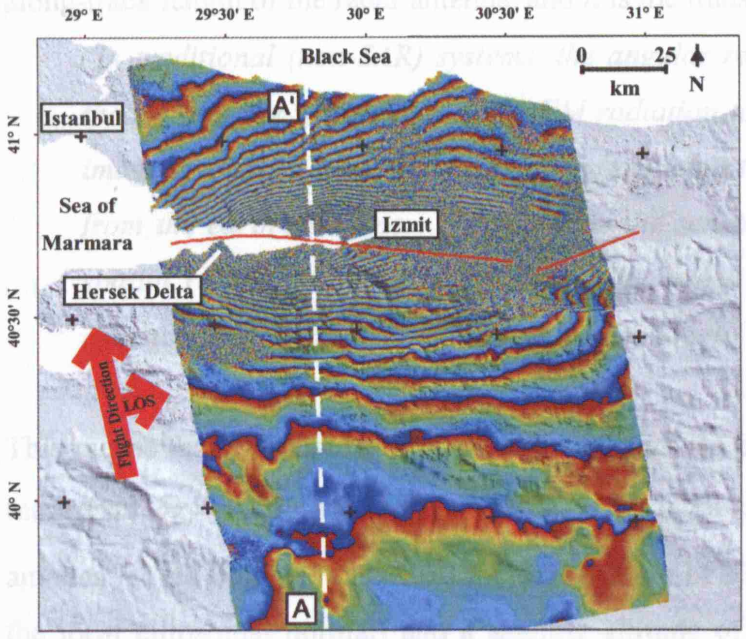

Figure 2-9: Radar interferogram of the deformation field following the 1999 Izmit (Turkey) earthquake, the red line shows the surface rupture. A and A' denote a profile which can be seen in the original document (Fig. 5b), but is not shown here. Image provided by T.J. Wright (Fig. 5a in Wright, 2002).

Validation studies have been carried out for DInSAR against continuous GPS network solutions. DInSAR allows the measurement of relative spatial deformation across a region over a certain time period, whereas GPS is better at measuring absolute deformation at discrete locations; these two techniques are clearly complementary. Zebker et al. (1994) demonstrate sub-centimetre agreement between InSAR and GPS measured displacement fields following a 1992 earthquake at Landers, California, and

Bawden et al. (2001) show similar agreement following groundwater extraction across Los Angeles, recording signals as small as a couple of millimetres per year. Additionally, although it has been claimed that a 31MHz frequency difference means that a 1992 ERS-1 image will not combine with a 2007 ENVISAT image to form a 15 year interferogram (Massonnet & Feigl, 1998), thanks to the development of more sophisticated modelling and processing techniques, data from ENVISAT and ERS are now being successfully integrated (Colesanti et al., 2003), providing invaluable continuous data about deformation effects over large temporal and spatial extents.

Diffraction effects mean that, using a small angle approximation, a radar beam has an angular resolution of $\delta\theta = \lambda / L$ (Young & Freedman, 2000), where L is the physical along-track length of the radar antenna, and λ is the transmitted radiation wavelength.

> *"In traditional (non-SAR) systems, the angular resolution is governed by the ratio of the wavelength of the EM radiation to the aperture size. The image spatial resolution is the angular resolution times the sensor distance from the earth's surface. Therefore, as the sensor altitude increases, the spatial resolution of the image decreases unless the physical size of the aperture is increased"* (Curlander & McDonough, 1991).

This means that two distinct points on the ground can only be resolved if separated by more than $\delta x = R_1 \delta\theta = (R_1 \lambda)/L$, where R_1 is the slant range. Assuming a flat earth, an antenna length of 10m, a nominal incidence angle of 23° (between the radar pulse and the local ellipsoidal normal) and a satellite altitude of 800km, gives a slant range of c.870km, which for ENVISAT's ASAR (lambda=5.66cm) allows resolution of only c.5km. To achieve its supposed ground resolution of c.30m, ENVISAT would require a real antenna several kilometres in length, an obvious impracticality.

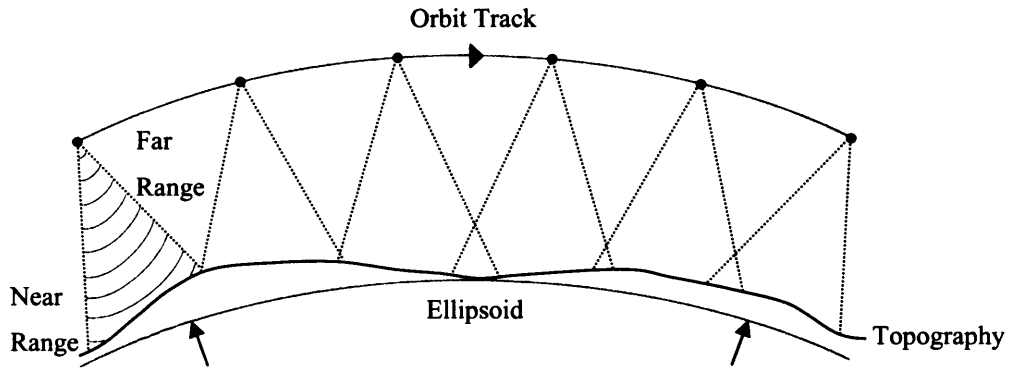

Figure 2-10: The Synthetic Aperture. A single SAR scene of the area between the two arrows may include many thousands of radar pulses transmitted and received by the radar array as it flies over a region. Note however that ENVISAT's near / far ranges are not in the flight direction as it has a side looking radar.

Instead, a synthetic aperture, created by moving a smaller antenna over a large distance, allows a single SAR scene/image of the surface (e.g. between the two arrows in Figure 2-10) to be created by many hundreds/thousands of radar pulses transmitted and received over a significant period of time (when we take the satellite's velocity into account). Received signals traced back to emissions over this area of ground are all synthesised into a single image of that region using sophisticated techniques through the process of focusing (Massonnet & Feigl, 1998). The distance travelled by the sensor during the acquisition of data for a specific region constitutes the synthetic aperture, and is as though the satellite had a real antenna of this length (may be several km). Processing must take into account the fact that ranges are 'slant ranges', measured along the look direction of the radar, and must be corrected for geometric artefacts (such as foreshortening) to allow radar data to be geo-located onto horizontal projections of a region. The local SAR coordinate system (along and across-track) used to display Figure 2-11 can cause mountainous terrain to appear distorted when compared to an optical image of the same area. The mountains in the left-hand image can be seen to slope to the left, caused by the side-looking imaging geometry of the radar system (prone to effects such as layover, shadowing and foreshortening, directly comparable to stereo-photogrammetry). The greyscale represents the amplitude of the returned (back-scattered) microwave signals, and can be used to differentiate vegetation types and surface roughness etc.

Figure 2-11: ENVISAT ASAR data for the Los Angeles area in California (11/09/2004 - Track 2170, Frame 2925), displayed using the local SAR coordinate system (along and across track). The left-hand image is of a type known as quicklook, where the pixels have been re-sampled to 320m x 320m (a multi-look 16 image). The right-hand image shows a detail from the lower right-hand corner of the quicklook image at the original resolution of 5m x 20m (a single-look complex, or SLC, image). Image supplied by Z. Li.

An interferogram produced from two spaceborne SAR scenes / images can be used to recreate topography from stereo parallaxes in the SAR phase data, and can provide information similar to that given by an optical stereo pair. They are usually repeat-pass interferograms, which mean that the two scenes have been collected during different orbits/passes over a region. Interferometry measures small changes in distance to a particular object by comparing the phase shift between two or more subsequent wave returns, and shifts of only a fraction of a wavelength can be detected. Its ability to resolve features therefore depends upon the actual wavelength used. ENVISAT's C-band ASAR array has a wavelength of only 5.66cm, which means that it is theoretically capable of recording surface change at the level of a few millimetres. For DInSAR, the components of the baseline separating the satellite on its two passes over an area will change from near to far range, as will the incidence angles of the radar pulse. What results is knowledge of phase differences to only modulo 2π, and the process of phase unwrapping (similar in concept to that of ambiguity resolution in GPS) allows reconstruction of an 'absolute' deformation field by fixing one point considered far enough away from the main deformation site so as to be fixed. This is a tricky process which carries with it its own complications (Klees & Massonnet, 1999). However, a reference DEM (created from an independent source, or from two separate SAR images of an area) can turn two SAR images into a differential interferogram after flattening of

the individual scenes, and also sidesteps the troublesome process of phase unwrapping for the topography; deformation phase unwrapping is usually simpler (Burgmann et al., 2000).

2.4. DInSAR and Orbit Errors

Figure 2-12 shows the orbital and imaging geometry for repeat-pass InSAR:

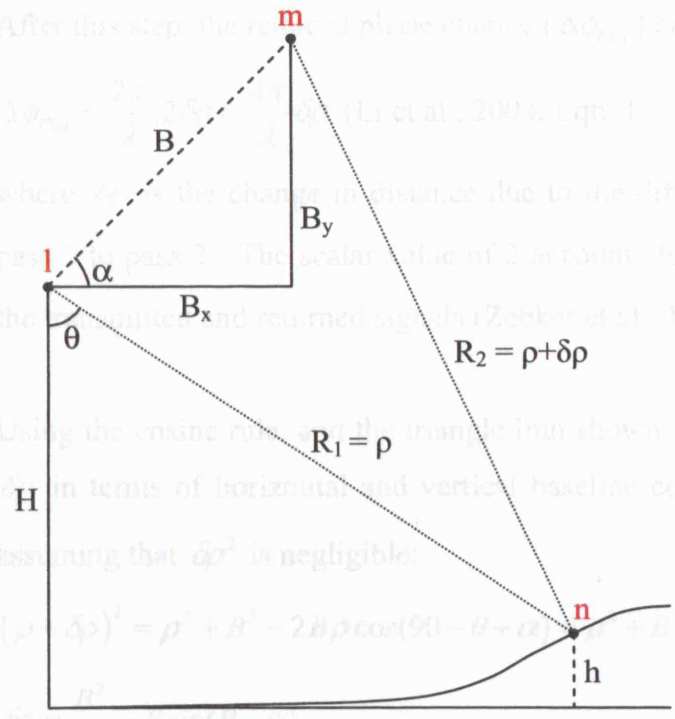

Figure 2-12: SAR Orbit Geometry.

where l and m are the satellite positions at two distinct epochs, n is the point on the ground being imaged on both occasions, B is the 3D baseline separating the satellites which is then resolved into horizontal and vertical components (B_x and B_y respectively), H is the satellite altitude, h is the distance between the ground surface and a reference surface, and R_1 and R_2 are the ranges to point n (where R_2 is larger than R_1 by a small amount $\delta\rho$).

Initial processing removes phase contributions due to the curvature of the Earth by subtracting the expected phase change due to an ellipsoidal surface (see Figure 2-13).

Figure 2-13: Reducing topography from an ellipsoidal to a flat surface.

After this step, the reduced phase change ($\Delta\phi_{Flat}$) can be expressed as:

$$\Delta\phi_{Flat} = \frac{2\pi}{\lambda}.2\delta\rho = \frac{4\pi}{\lambda}\delta\rho \text{ (Li et al., 2004, Eqn. 1)} \quad (2.1)$$

where $\delta\rho$ is the change in distance due to the different positions of the satellite from pass 1 to pass 2. The scalar value of 2 accounts for the fact that $\delta\rho$ is present in both the transmitted and returned signals (Zebker et al., 1994).

Using the cosine rule, and the triangle lmn shown in Figure 2-12 allows us to solve for $\delta\rho$ in terms of horizontal and vertical baseline components (B_x and B_y respectively), assuming that $\delta\rho^2$ is negligible:

$$(\rho+\delta\rho)^2 = \rho^2 + B^2 - 2B\rho\cos(90-\theta+\alpha) = \rho^2 + B^2 - 2B\rho\sin(\theta-\alpha) \quad (2.2)$$

$$\begin{aligned}\delta\rho &= \frac{B^2}{2\rho} - B\sin(\theta-\alpha) \\ &= \frac{B_x^2+B_y^2}{2\rho} - B\sin\theta\cos\alpha + B\cos\theta\sin\alpha \quad (2.3) \\ &= \frac{B_x^2+B_y^2}{2\rho} - B_x\sin\theta + B_y\cos\theta\end{aligned}$$

Substituting this back into equation (2.1) gives:

$$\Delta\phi_{Flat} = \frac{4\pi}{\lambda}\left\{\frac{B_x^2+B_y^2}{2\rho} - B_x\sin\theta + B_y\cos\theta\right\} \quad (2.4)$$

Adding an additional range change due to surface deformation ($\Delta\rho$) gives:

$$\Delta\phi_{Flat} = \frac{4\pi}{\lambda}\left\{\frac{B_x^2+B_y^2}{2\rho} - B_x\sin\theta + B_y\cos\theta + \Delta\rho\right\} \quad (2.5)$$

Due to the sensor geometry (i.e. $2\rho \gg B_x^2 + B_y^2$), we can ignore the first term inside the brackets. After re-arranging to solve for $\Delta\rho$ we can differentiate to find the effect on deformation measurements due to errors in the horizontal and vertical baseline components (Li et al., 2004):

$$\frac{\partial \Delta\rho_x}{\partial B_x} = \sin\theta \tag{2.6}$$

$$\frac{\partial \Delta\rho_y}{\partial B_y} = -\cos\theta \tag{2.7}$$

Noting that:

$$\frac{\delta\Delta\rho}{\delta B_n} \approx \frac{\partial \Delta\rho}{\partial B_n} \tag{2.8}$$

$$\delta\Delta\rho \approx \frac{\partial \Delta\rho}{\partial B_n}\delta B_n \tag{2.9}$$

We can then express changes in surface deformation measurements that result directly from orbit errors in the radial and across-track directions:

$$\delta\Delta\rho_x = \sin\theta.\delta B_x \tag{2.10}$$

$$\delta\Delta\rho_y = -\cos\theta.\delta B_y \tag{2.11}$$

Assuming that the x and y baseline error components are independent, we can chart the impact of horizontal and vertical baseline error on surface deformation for a variety of areal extents (Figure 2-14), where L denotes the length in the across-track direction of the interferogram. Although the across-track extent (swath width) depends upon the mode in which ENVISAT's ASAR is being used, COMET routinely use SAR data with a swath width of 100km or greater. It can be seen from the figure that for such extents, even a 50mm horizontal baseline error can still contribute significantly to image noise (bias).

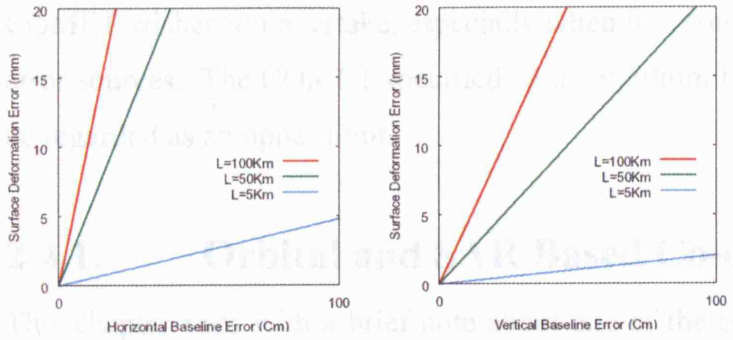

Figure 2-14: The impact of horizontal and vertical baseline error on surface deformation (Image after Li et al., 2004, Fig. 3). L denotes the length of one side of the area being imaged; note that as areal extent increases, baseline accuracy becomes significantly more important.

The two images in Figure 2-14 have been produced by calculating the maximum relative error (far – near). Although the across-track (horizontal) baseline component is obviously dominant, it appears that radial (vertical) baseline error should not be ignored. As is evident from Figure 2-15, we can calculate θ_f and θ_n using the sine rule if we: know the satellite altitude (h≈800km); assume a mid-swath nominal incidence angle (θ) of 23° and; stipulate that distances BC and CD are both 50km (i.e. L/2).

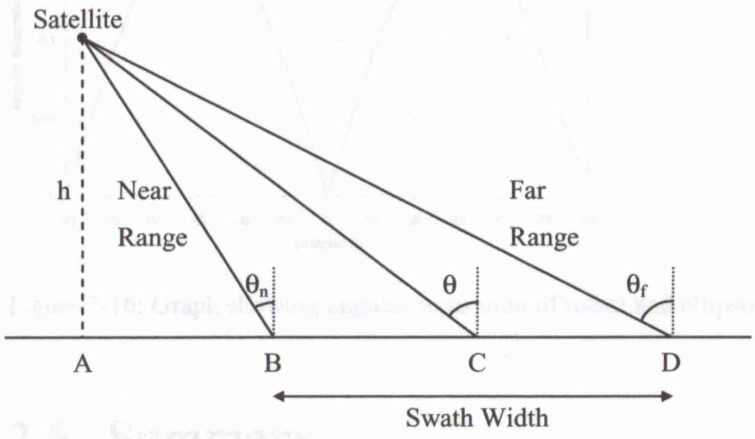

Figure 2-15: Relative surface deformation error for a SAR scene with width BD.

The above-mentioned parameters provide values of θ_f = c. 25.965° and θ_n = c.19.899° for L=100km. Using equations (2.10) and (2.11), the impact upon the estimates of surface deformation is 5mm and 1mm respectively for a horizontal baseline error of 50mm and a vertical baseline error of 30mm. Values of this magnitude are clearly large enough to introduce significant noise into the differential interferogram analysis which

COMET wishes to undertake, especially when it is considered that these are not isolated error sources. The COMET specified value of 50mm for baseline error should therefore be regarded as an upper limit.

2.4.1. Orbital and SAR Based Co-ordinate Systems

This chapter ends with a brief note about one of the common assumptions made when conducting SAR error analysis. Radial and across-track errors for the ERS tandem mission have commonly been used to get a handle on orbit error effects (e.g. Reigber et al., 1996 and Hanssen, 2001), but strictly speaking the radial error should not be applied directly. In SAR sensor geometry, the nadir pointing vector is actually the local geodetic normal at the sub-satellite point, rather than the radial vector (e.g. the ROI_pac SAR processor's sch coordinate system, Buckley, 2000). However, Figure 2-16 shows that as the maximum angular separation of these two vectors is less than 0.2°, this will have no visible effect on the error analysis conducted in section 2.4.

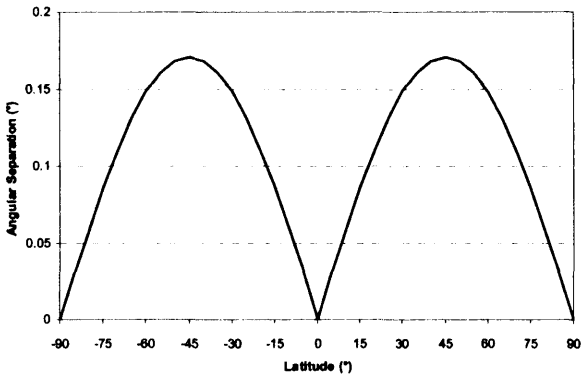

Figure 2-16: Graph showing angular separation of radial and ellipsoidal normal vectors.

2.5. Summary

It has been shown that DInSAR techniques rely heavily upon high quality orbit solutions, and that ENVISAT may well currently be incapable of providing the orbits that COMET requires. The remaining chapters show how it may be possible to improve the accuracy of ENVISAT orbits.

3. Review of Relevant Literature

This section covers several of the most widely known papers either directly or indirectly associated with the subject of non-conservative force modelling. A close reading reveals that many of these are intimately tied to modelling the effects of solar radiation pressure and thermal re-radiation on Global Positioning System (GPS) satellites which, with an altitude of c.20,000 km, are in medium Earth orbit (MEO). Other in-depth studies concentrate on the low Earth orbiting (LEO) Ocean TOPography EXperiment (Topex)/Poseidon altimetry satellite (c.1335km altitude). Both GPS satellites and Topex/Poseidon offer excellent examples of improved NCF modelling resulting in more accurate observations; however, the modelling techniques used are often poorly defined. Also outlined is a technique which specifically aims to be generic in the types of satellite that it is applicable to, and it is this which forms the basis of the present research. In addition, attempts at modelling Earth Radiation Pressure and the timings of entry/exit into Earth's eclipse boundaries are considered.

3.1. GPS Non-Conservative Force Modelling

The first widely used solar pressure model for Block I GPS satellites was developed by Rockwell International, and is commonly referred to as the ROCK4 model. Lichten & Border (1987) report that the model, which accounts only for SRP forces, uses just 13 flat or cylindrical surfaces to represent the spacecraft. This was followed by a similar model, the ROCK42 (S20) model, for Block II/IIA GPS satellites. In both cases, although the shadowing of one component by another is considered, secondary reflections (where radiation reflected from one surface strikes another) are not. In some situations (Fliegel et al., 1992) neglecting these secondary reflections can cause larger errors than if shadowing were ignored entirely. High precision orbit determination with the ROCK4 model appears to require the estimation of scale parameters in each of the spacecraft body-fixed (BFS) X and Z directions and of a constant bias value in the Y direction (Lichten & Border, 1987)[7]. It is not clear how long this model took to develop, but Bar-Sever & Russ (1997), when talking directly of the ROCK models,

[7] The GPS body-fixed Z-axis points from the satellite centre of mass to the geocentre, the Y-axis results from the cross-product of Z and the probe-Sun vector, and X completes the right-handed set.

mentions that development costs for radiation pressure models can reach millions of dollars.

Fliegel et al. and Fliegel & Gallini (1992 & 1996) were responsible for revising the Block I and II/IIA ROCK models to include the effects of thermal re-radiation (denoted as T10 and T20 respectively); a plume shield added to the real GPS satellites to protect the solar panels from becoming contaminated by exhaust waste was also added to the Block II/IIA geometrical model. They estimate that the TRR force may account for almost five percent of the total radiation pressure force on Block I and II/IIA satellites (Fliegel & Gallini, 1996). The authors also developed a new model (T30) for the Block IIR GPS satellites. It is noted that several structures, although relatively small, remain unmodelled, as do secondary intersections and the effect of heat conducted into and through the bus (denoted as Qrates in the current research). While the code to compute the initial model is described as cumbersome, model implementation is straightforward as it uses a short Fourier series with just one argument, the Earth-probe-Sun (EPS) angle. The error of the T10, T20 and T30 models is estimated to be at around the 2-3% level for each, and this can lead to 3-4m of error after 12 hours of orbit prediction if no adjustments are estimated from tracking data. Stochastic parameter estimation is capable of improving this by an average of 8% for non-eclipsing satellites (Vigue et al., 1994a – eclipsing GPS satellites are not central to this literature review as prior to Block IIR, GPS satellites exhibited chaotic attitude behaviour during eclipse seasons, and this contributes significantly to the total error during these periods).

A very different approach to radiation pressure force modelling comes from Bar-Sever & Russ (1997) which, while not costing millions of dollars, does use a full 9 months of tracking data to compute empirical models for eclipsing and non-eclipsing Block II/IIA GPS satellites. Bar-Sever & Russ argue that this technique is capable of modelling the forces which act upon actual satellites, rather than computer simulations, often greatly simplified. In particular, a force acting along the body-fixed Y-axis (known as Y-bias) is recovered which improves orbit predictions, and this is not modelled apriori by the ROCK models. In essence, the operation consists of estimating the parameters of a Fourier series similar to that used in the implementation of the ROCK models. While the EPS angle is retained as the independent argument, to reduce the number of parameters to be estimated the coordinate system is changed to UVW. U points in the

Sun to spacecraft direction, V (identical to the body-fixed Y-axis) is the cross-product of U and the satellite to geocentre vector, and W completes the right-handed set. It is interesting to note that the authors mention that the recovered Y-bias is probably the major contributor to any improvement over the ROCK models, which require Y-bias to be estimated as a stochastic parameter. It is also stated that error levels in the testing of this new model indicate that it can still be improved upon (Bar-Sever & Russ, 1997).

The year 2000 saw an attempt to return to the analytical apriori modelling of several non-conservative force effects on the GPS Block IIR satellites, including SRP, TRR, ERP, Qrates and antenna thrust (Marquis & Krier, 2000). The geometrical model of the satellite is composed entirely of triangles and yet again, although shadowing is considered, secondary reflections are ignored. The shadowing routine breaks individual elements down into smaller and smaller triangles, until only visible triangles remain (Marquis & Krier, 2000), and anecdotal evidence has this as the source of the model's problem. Apparently, the machine running the software would break down elements into so many triangles that it would run out of memory, but instead of reporting an error, the computation would continue to run. The Naval Surface Warfare Centre computed an error for this model of less than 1% for the only Block IIR satellite available at the time (SVN43), and found errors of 12-13% for the ROCK42 model on Block II/IIA satellites. However, this very large value appears highly suspect, and goes against the experiences of other authors (e.g. Vigue et al., 1994a and Bar-Sever & Russ, 1997). In fact, a later admission by Marquis (2003) reveals that the new model has had an unquantifiable impact.

3.2. Topex Non-Conservative Force Modelling

Topex/Poseidon (T/P) has much in common with ENVISAT, in particular it has a very complex bus design, a single solar array, a similar attitude regime and, relative to all of the GPS satellites is both quite large and geometrically complex. T/P has an in-orbit configuration (length, width, height) of c.5.5m x 11.7m x 6.6m, and a mass of c.2500Kg, though these dimensions still do not quite measure up to ENVISAT's deployed size of c.26m x 10m x 5m and mass of c.8000Kg. The T/P non-conservative force modelling program, which addressed the effects of SRP, TRR and ERP (using the Knocke (1989) model), was designed to meet specific operational requirements; being

allowed to contribute a maximum of 6cm to the satellite's total 13cm RMS radial error budget (Marshall et al., 1992). By modern standards however it must be recognised that these are relatively crude goals, Haines et al. (2004) are now routinely achieving 1cm radial errors for Topex/Poseidon's follow on satellite Jason-1, with the aid of NCF models produced at UCL.

The Thermal Radiation Analysis System (TRASYS) and the Systems Improved Numerical Differencing Analyser (SINDA) software used was quite sophisticated for its time, allowing spacecraft to be defined by up to 1000 elements chosen from a set of primitives including rectangles, polygons, discs, cylinders, spheres and cones. Topex/Poseidon's geometrical micromodel included 310 individual surfaces (see Figure 3-1), though all surfaces were unrealistically given the same specular reflectivity coefficient and secondary intersections were ignored. In a manner very similar to Marquis & Krier's (2000) shadowing routine, TRASYS divides individual components into smaller and smaller 'elemental areas'. Implementing the micromodel for orbit determination proved to be too computationally expensive even with a cylindrical eclipse algorithm, as models were produced per nominal orbit with each run taking 1 day to compute the forces for an orbit lasting just 112 minutes. Instead, even though the micromodel is recognised as being the best model available, a box and wing approximation was used for operational orbit determination (Rosborough & Antreasian, 1990 and Marshall et al., 1992) which does not consider shadowing, reflection or conduction, though parameters are adjusted to best fit the measurement residuals. In fact, this move was expected during the development of the micromodel, and its author's state that they wish it to be a standard upon which simpler models can be based (Antreasian & Rosborough, 1992). Unsurprisingly perhaps, the simple model initially failed to meet the now relatively crude mission requirements, and large variability was found in its performance across the different attitudes of the satellite under its sinusoidal yaw regime. The likelihood of this effect had already been noted by Rosborough &Antreasian (1990) – "due to the sinusoidal yaw program that the satellite follows, the array does not point perfectly normal to the Sun resulting in a significant force component not aligned with the Sun direction". Additional work to fine tune the box and wing model offers no hard results about what contribution the NCFs make to the total RMS radial error budget, but instead leaves us with a slightly ambiguous

statement: "In all simulations, macro-model performance has met and often exceeded precision orbit determination error requirements." (Luthcke & Marshall, 1992).

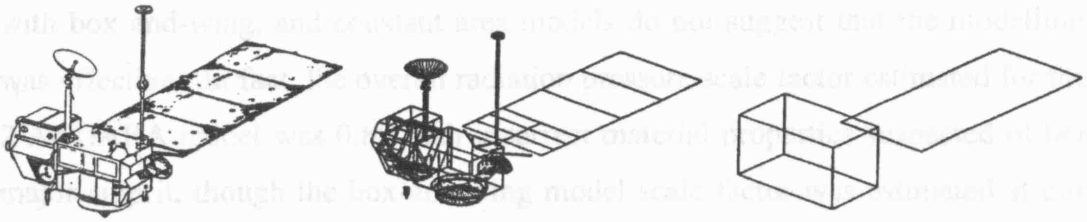

Figure 3-1: From left to right showing: a representation of the real Topex/Poseidon spacecraft, the micromodel approximation and the macromodel approximation (Marshall et al., 1992, Fig. 1).

Further refinements to the model (Kubitschek & Born, 2001) indicate that solar array mis-pointing can contribute significantly to anomalous accelerations experienced during sinusoidal yaw (c.f. ENVISAT, see section 8.1.3). The authors note that although improved radiation pressure models may not substantially affect orbit precision, they do reduce the magnitude of estimated along-track accelerations which may be of use for future gravity field and atmospheric density studies (Kubitschek & Born, 2001).

3.3. Generic Non-Conservative Force Modelling

While some of the techniques outlined in the previous sections may technically be capable of being applied to many different spacecraft, few have demonstrably shown this. The final two methodologies outlined in this chapter however do exactly that.

Doornbos et al. (2002) used the ANGARA (Analysis of Non-Gravitational Accelerations due to Radiation and Aerodynamics) software to model non-conservative forces (SRP, TRR, ERP and atmospheric drag) affecting ERS-2 and ENVISAT satellites. Complex seasonal ERP flux values recovered from ERBE (Earth Radiation Budged Experiment, an in-situ space probe) data are used together with solar flux values and output from atmospheric density models to compute non-conservative force induced accelerations. The computationally intensive technique of Test Particle Monte Carlo (TPMC) is used to perform these calculations along with fairly sophisticated geometric models of each spacecraft (triangulated into panels of approximately equal size (Fritsche et al., 1998)), considering shadowing and multiple 'secondary' reflections until an arbitrary limit is reached. TPMC uses probability density functions to give

properties to representative packets of radiation / atmospheric particles which are 'fired' towards the computer model of the satellite, with the response over all packets being summed. Comparing orbits produced by these TPMC models against orbits computed with box-and-wing, and constant area models do not suggest that the modelling effort was effective. In fact, the overall radiation pressure scale factor estimated for the ERS-2 ANGARA model was 0.85 with incorrect material properties suspected of being the major culprit, though the box-and-wing model scale factor was estimated at only 1.09 (Doornbos et al., 2002). There are only minor differences in the tracking residuals and once-per-revolution estimated accelerations between all three models. Further investigation however reveals that it may be the geometrical model which introduced these problems:

> "*The ENVISAT model was created from scratch, with information found in several technical drawings, illustrations and photographs of the flight model under construction. Because of insufficient data on the complex geometry of several of ENVISAT's instruments, it was not possible to create a geometry model with the same accuracy as that of ERS-2*" (Doornbos, 2001).

Another method which has achieved excellent success with a number of different spacecraft flying at different altitudes is the pixel array technique of Ziebart (2004). In contrast to the other procedures, Ziebart's pixel array discretises the incident radiation rather than the geometrical components (c.f. Marquis & Krier, 2000 & Marshall et al. 1992), which are instead subjected to a ray tracing procedure which 'auto-discretises' components in a stable manner. Spacecraft components are modelled using the following primitives: polygons, circles, rings, cylinders, cones, truncated cones, paraboloids and spheres. The pixel array can be rotated around the satellite and, in order to account for all the likely directions from which a satellite may encounter radiation, is not restricted to a particular plane of the BFS coordinate system. The software (UCL_SRP) can actually be used to model accelerations resulting from SRP, TRR (additional development by Adhya, 2005) and ERP; shadowing is accounted for and it is one of only two methods described here which models secondary intersections. Similar to the ROCK models, the implementation procedure is separated from the model computation, as this is computationally very intensive. In an orbit determination

package, a surface fitted to the modelled accelerations is bi-linearly interpolated for speed and efficiency. This technique has already shown it is capable of achieving good results for orbit determination with Jason-1 (Haines et al., 2004), having a scale factor of only c.1.01. Orbit prediction results for GPS Block IIR satellites (Adhya, 2005) are also very encouraging, where average RMS residuals after integrating a 12 hour orbit are only 0.19m in height, 0.08m across-track and 0.59m along-track, very much improved over the 3-4m error expected from the ROCK models over the same period.

3.4. Earth Radiation Pressure Modelling

Earth radiation pressure is due to reflected (optical shortwave) and emitted (infrared longwave) radiation which has its origin in the re-radiation of solar energy incident upon the Earth's surface. Shortwave radiation is directly reflected (diffuse & specular) and is therefore present only on the daylight side of the Earth. Factors affecting its signature include the relative orientation of the Sun with respect to the Earth, the properties of the land/ocean surfaces which 'see' the Sun, and cloud cover (Montenbruck & Gill, 2001). Longwave Earth radiation, in contrast, is always present to some degree even on the night side of the Earth, and can be thought of as forming a background level of radiation.

Existing models of ERP range from the very simple to the very complex. A prime example of the former is that presented by Fliegel et al. (1992) for GPS satellites. Here, the magnitude of the ERP acceleration is computed by simply scaling the magnitude of the SRP acceleration for a given Sun-Earth-Probe angle; the direction is considered to be purely radial. While this might be a reasonable approximation at the relatively high altitude of GPS satellites, where an inverse distance squared power law will reduce the flux magnitudes to a smooth sine curve, this will not be true for LEO altitudes and important detail will be lost (see Figure 5-22). The model as presented also fails to account for the persistence of the longwave radiation on the night side of the Earth, and instead the curve tends asymptotically to zero in this region, introducing a systematic bias.

Knocke & Ries (1987) developed a more sophisticated and generic ERP model which is still perhaps the most widely used in modern orbit determination packages, including

JPL's GIPSY (Bar-Sever, pers. comm.) and GSFC's GEODYN II (GEODYN source code) software. Knocke (1989) gives a more comprehensive account of their nominal model: the part of the Earth visible from the satellite is divided into only 19 segments, a central cap with its focus at the sub-satellite point, and two adjacent concentric rings, which are divided into 6 and 12 segments respectively; the shortwave and longwave contributions from each segment are generated from purely zonal (i.e. latitude dependent) second degree spherical harmonic terms based on least squares fits to seasonally averaged Earth radiation budget data. However, the division of the visible Earth into only 19 segments is very crude, and makes no attempt to correctly classify the reflective properties of each region due to different geographic surface types (e.g. land, ocean, snow or some mixture of these). The use of averaged data allows only for smooth periodic variations in the flux rather than short term anomalies, and the model makes no allowance for cloud cover which, as the next paragraph notes, can be very important. Finally, it should be noted that the model is designed to treat all satellites as simple spheres, which is probably now not even appropriate for satellites at the GPS altitude, let alone LEO satellites of complex shape which will have very distinctive response functions.

Perhaps the broadest study of the effects of ERP on an artificial Earth orbiting satellite, involving the greatest number of investigators (only a small number of which are discussed here), has focused on the geodetic LAGEOS satellite. Even with a relatively high altitude of approximately 6000km, the LAGEOS orbit has been shown to be affected significantly by the effects of ERP (Métris et al., 1997). Vokrouhlický et al. (1993a and 1993b) develop rather sophisticated models based purely on the theory of radiative transfer, yet make no effort to validate their results using observations of ERP flux values from space; all authors have taken advantage of the simple spherical geometry of LAGEOS. Attempts to recover thermal effects from such models show results which "point to a persisting discrepancy between the theoretical and empirical modelling of the LAGEOS I thermal effects" (Métris & Vokrouhlický, 1996). One useful outcome of these attempts has been to show that the correct treatment of cloud cover is important for ERP modelling (Vokrouhlický et al., 1993a), but this remains a very difficult issue to this day.

3.5. Eclipse Modelling

Earth-orbiting satellites experience partial or total eclipses when they pass through the regions known as the umbra and penumbra. In the penumbra, the total solar irradiance is partially occluded by the Earth, whereas the umbra can be defined as the region on the anti-Sun side of the Earth which is completely devoid of solar radiation. In order to model accurately the forces acting on the satellite due to SRP and TRR it is important to know exactly when the satellite enters or exits a shadow region, as the amount of solar radiation incident on the spacecraft drops dramatically.

It is perhaps surprising that literature on this topic is so sparse, and that the existing material ranges between two extremes. Several techniques use a spherical Earth model, as this allows simple geometric arguments to be developed (Montenbruck & Gill, 2001; Vallado, 2001; Neta & Vallado, 1997; Vokrouhlický et al., 1993c). However, it is certainly worthwhile treating the Earth as an oblate spheroid as it has been shown that with respect to a spherical Earth the main changes occur in the timing of the umbra and penumbra transitions, and in the overall duration of the eclipse periods (Vokrouhlický et al., 1996). Such mistiming has important consequences for the precise numerical integration of orbit trajectories (Woodburn, 2000). The main drawback of implementing such a model is that existing approaches for eclipse boundary determination with a spheroidal Earth are significantly more complex than for a spherical Earth. As a result current models using a spheroidal Earth are more costly to implement in operational software as they are computationally intensive, requiring the use of either a series of rotations (Vokrouhlický et al., 1996) or the solution of a quartic equation (Neta & Vallado, 1997).

As part of the force modelling work undertaken at University College London (UCL) by its Geodesy Research Group, a new treatment of the problem (see section 10) has been developed which yields direct solutions for the eclipse state - whether the satellite is in umbra, penumbra or clear - whilst still accounting for the Earth's polar flattening (Adhya et al., 2004).

3.6. Summary

There have been many different approaches to non-conservative force modelling in the past, and these have met with various degrees of success with a range of different forces and satellites. Ziebart's technique deals with very complex spacecraft and has proven ability in producing operational orbits; the success of this technique is built upon in the following work.

4. Forces Acting on Satellites in Low Earth Orbit

When performing orbit determination we do not make perfect observations of ranges and range rates between tracking stations and LEO spacecraft, nor do we have perfect knowledge of the differential equations that describe their motion; moreover assumptions and simplifications are usually are made to reduce the computational burden encountered when solving these equations (Tapley et al., 2004). Here, the dynamic LEO environment is outlined, as are methods for modelling a particular category of forces (non-conservative).

4.1. The Two-Body Problem

It is interesting that Newton's (1642 - 1727) second law of motion (Eqn. (4.1)), a seemingly innocuous statement which is today taught to most high school students, is essential for an understanding of virtually all modern orbit analysis.

$$\bar{F} = m\bar{a} \tag{4.1}$$

As shown below, it provides a framework upon which the mathematics for expressing the relative acceleration between a planetary body and an orbiting satellite can be built. For convenience, in what follows immediately below the two bodies considered will always be the Earth and ENVISAT.

The gravitational potential (U) between two bodies represented as point masses can be expressed as:

$$U = \frac{Gm_1m_2}{r} \tag{4.2}$$

The gradient of the potential ($\partial U/\partial r$) along the line joining the two bodies gives the magnitude of the gravitational force due to mass m_1 which acts on mass m_2 (Tapley et al., 2004):

$$F_g = -\frac{Gm_1m_2}{r^2} \tag{4.3}$$

Equation (4.3) represents another of Newton's impressive achievements in that this, his inverse square law of gravitation, accurately accounts for the elliptical motion of the planets (Vallado, 2001). To recover the equation of motion, we require the satellite's

acceleration relative to the centre of the Earth in an inertial (non-rotating) reference frame. Hence, in the restricted two-body formulation the gravitational force will act along the inertial unit position vector of the satellite with respect to the Earth, given by $\bar{r}/r$ in Eqn. (4.4).

$$\bar{F}_g = -\frac{Gm_1m_2\bar{r}}{r^3} \tag{4.4}$$

The direction of the relative acceleration vector depends upon the two masses involved; here we can state that it will be in the direction of the Earth, the primary attracting body, as the mass of ENVISAT is negligible by comparison. This calculation is shown below by combining a version of Eqn. (4.4) for each of the Earth and satellite, taking care to respect the relative orientation of the two bodies as shown in Figure 4-1.

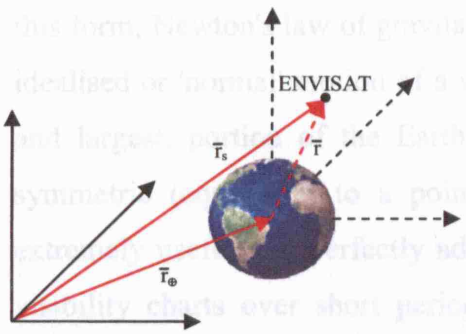

Figure 4-1: Relative position vector of a satellite with respect to the Earth in an inertial reference frame. Solid black lines represent an inertial frame based at the centre of mass of the entire system, which is translated only with respect to the frame at the centre of mass of the Earth (dashed black lines). Solid red lines show the Earth and satellite position vectors, while the dashed red line shows the satellite's position relative to the centre of mass of the Earth.

From Figure 4-1 it can be seen that the position vector from the Earth to the satellite is given by:

$$\bar{r} = \bar{r}_s - \bar{r}_\oplus \tag{4.5}$$

The second derivative of Eqn. (4.5) gives the relative acceleration of the satellite with respect to the Earth:

$$\ddot{\bar{r}} = \ddot{\bar{r}}_s - \ddot{\bar{r}}_\oplus \tag{4.6}$$

Gravitational force exerted by the Earth ($m_\oplus$) upon the satellite (m_s):

$$\bar{F}_{g_s} = m_s\ddot{\bar{r}}_s = -\frac{Gm_\oplus m_s}{r^2}\left(\frac{\bar{r}}{r}\right) \tag{4.7}$$

Gravitational force exerted by the satellite upon the Earth:

$$\bar{F}_{g_\oplus} = m_\oplus \ddot{\bar{r}}_\oplus = \frac{G m_s m_\oplus}{r^2}\left(\frac{\bar{r}}{r}\right) \tag{4.8}$$

Using Eqn.'s (4.1) and (4.6) along with the principle of the superposition of forces allows us to group Eqn.'s (4.7) and (4.8), and to solve for the final relative acceleration vector.

$$\ddot{\bar{r}} = -\frac{G(m_\oplus + m_s)\bar{r}}{r^3} \tag{4.9}$$

Equation (4.9) is Newton's closed analytical solution to the two-body problem; for practical purposes the mass of a satellite can be ignored since it will be smaller by several orders of magnitude compared to that of the Earth or other planetary bodies. In this form, Newton's law of gravitation can be used to compute what is referred to as the idealised or 'normal' motion of a satellite. However, this accounts for only the central, and largest, portion of the Earth's gravity field which is assumed to be spherically symmetric (equivalent to a point mass / monopole (Vallado, 2001)). While it is extremely useful and perfectly adequate for rapidly computing such things as satellite visibility charts over short periods (Leick, 2004), more precise applications require greater attention to detail. Additional perturbing forces introduced by extension of the problem to even three bodies, e.g. by including the Moon, means that there is no longer a closed form analytical solution (Tapley et al., 2004), and numerical integration techniques must be used (e.g. Hairer et al., 1987).

These additional perturbing forces are actually many and varied in nature, but can be categorised into two main groups: gravitational (conservative) and non-gravitational (non-conservative). Conservative forces, which are path independent, effect a change in the balance between the potential and kinetic energy of a system but conserve the total energy. For our purposes, the system includes the satellite, the Sun, Moon, Earth and the other planetary bodies in our solar system. Modern applications demand however that it is now necessary to consider not only the gravitational forces induced by the Moon and other planets, but also changes in the gravity field in near Earth space caused by the Earth's inhomogeneous mass distribution (see Figure 4-2). However, accurate planetary ephemerides (Heafner, 1999) and dedicated satellite gravity recovery missions such as CHAMP (CHAllenging Minisatellite Payload - launched 15/07/2000), GRACE

(Gravity Recovery And Climate Experiment - launched 17/03/2002) and GOCE (Gravity Field and Steady-State Ocean Circulation Explorer - launch scheduled for 2007) mean that conservative forces are generally considered to no longer be a source of significant error in the production of satellite orbits when compared to the effects of unmodelled non-conservative forces.

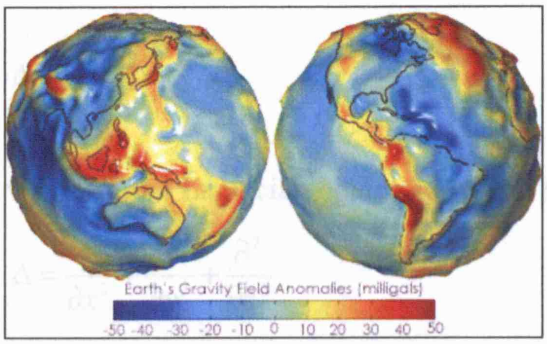

Figure 4-2: GRACE gravity anomalies (http://www.gfz-potsdam.de/pb1/op/grace/index_GRACE.html) – shows the extent to which Earth's gravity field differs from that of a uniform, featureless Earth - based on 111 days of GRACE data.

The modelling of non-conservative forces is still in its infancy and attempts have, until quite recently (Ziebart, 2001b and Adhya, 2005) remained relatively naïve (e.g. Fliegel et al., 1992) or reliant upon 'brute force' (e.g. Bar-Sever & Russ, 1997). These non-conservative forces are path dependent and do not conserve the mechanical energy of the system. The principal non-conservative forces discussed here and which act on Low Earth Orbiting spacecraft, are due to solar radiation pressure, thermal re-radiation, Earth radiation pressure effects, venting of heat produced by payload instrumentation, atmospheric drag and thrust caused by signals emitted from the satellite (e.g. ASAR signal).

The remainder of this chapter, and all of the following chapter, is dedicated to looking in greater detail at these conservative and non-conservative perturbing forces, for which the most complete reference source is the IERS (International Earth Rotation Service) conventions, now updated as of 2003 (McCarthy & Petit, 2003).

4.2. Conservative Forces

4.2.1. Earth Gravity

Since 1937, modern representations of gravity anomalies have been founded upon spherical harmonic expansions (Rapp, 1998), where a harmonic is defined as any function which satisfies Laplace's equation (4.10):

$$\Delta U = 0 \tag{4.10}$$

where Δ, the Laplacian operator, has the form (MacRobert, 1927):

$$\Delta = \frac{\partial^2}{\partial x^2} + \frac{\partial^2}{\partial y^2} + \frac{\partial^2}{\partial z^2} \tag{4.11}$$

and U, in this case, is a model of the Earth's gravitational potential energy.

An instructive example of such a function, given by Heiskanen & Moritz (1967, modified slightly here and reproduced with corrections), is the gravitational potential between two point masses (Eqn. (4.2)) separated by distance r; where r is given by:

$$r = \left(x^2 + y^2 + z^2\right)^{1/2} \tag{4.12}$$

Taking the second derivative of Eqn. (4.2) with respect to the three components (x,y,z) in turn produces the following for x (where each component has the same form):

$$\frac{\partial^2}{\partial x^2}\frac{Gm_1m_2}{(x^2+y^2+z^2)^{1/2}} = \left[\frac{3x^2Gm_1m_2}{r^5} - \frac{Gm_1m_2}{r^3}\right] = \left[\frac{3x^2Gm_1m_2}{r^5} - \frac{Gm_1m_2r^2}{r^5}\right] = \frac{-Gm_1m_2\left(r^2-3x^2\right)}{r^5} \tag{4.13}$$

Summing the second derivatives for each of the three components as indicated by Eqn. (4.11) indeed produces zero, and shows that this function, as so defined, is harmonic. Note however, that the potential for a solid body, i.e. a more realistic consideration of the Earth, is only harmonic at all points outside the attracting mass.

Spherical harmonics differ in that they represent problems in terms of spherical coordinates, where Laplace's equation becomes (Heiskanen & Moritz, 1967):

$$\Delta U = \frac{1}{r^2}\frac{\partial}{\partial r}\left(r^2\frac{\partial U}{\partial r}\right)+\frac{1}{r^2\sin\theta}\frac{\partial}{\partial\theta}\left(\sin\theta\frac{\partial U}{\partial\theta}\right)+\frac{1}{r^2\sin^2\theta}\frac{\partial^2 U}{\partial\lambda^2}=0 \tag{4.14}$$

where r is the radius, θ is the geocentric co-latitude, and λ is the geocentric longitude.

When solving for the potential at a point, solutions for Eqn. (4.14) commonly have the form (Tapley et al., 2004):

$$\begin{aligned} U = {} & \frac{G(m_\oplus + m_s)}{r} - \frac{GM^*}{r}\sum_{n=1}^{\infty}\left(\frac{a_e}{r}\right)^n P_n(\sin\phi)J_n \\ & + \frac{GM^*}{r}\sum_{n=1}^{\infty}\sum_{m=1}^{n}\left(\frac{a_e}{r}\right)^n P_{nm}(\sin\phi)[C_{nm}\cos m\lambda + S_{nm}\sin m\lambda] \end{aligned} \tag{4.15}$$

where M^* is a reference mass, a_e is a reference distance, φ is the geocentric latitude, n is the degree, m is the order and P_{nm} are associated Legendre functions (or Legendre polynomials when m=zero) which can be computed very efficiently using recursive formulations (Heiskanen & Moritz, 1967). J_n, C_{nm} and S_{nm} are spherical harmonic coefficients (see Figure 4-3), though often the Legendre functions and coefficients are normalised ($\bar{C}_{nm}$ and $\bar{S}_{nm}$) to avoid numerical round off errors.

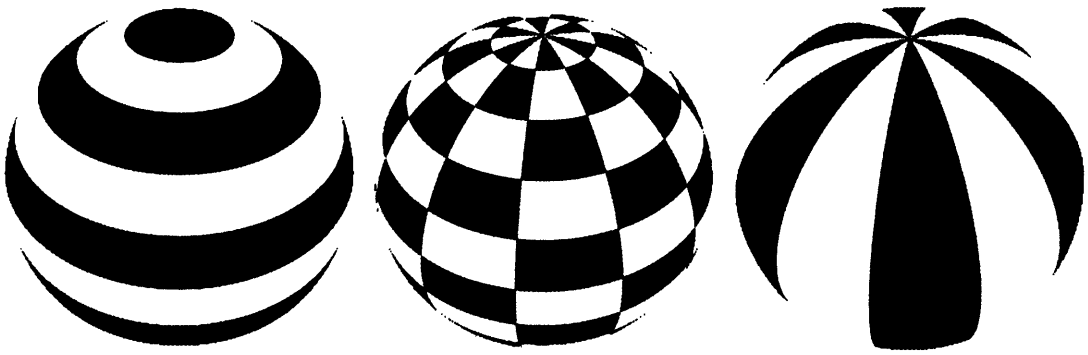

Figure 4-3: The different types of spherical harmonics – respectively zonal (J_n), tesseral (C and S where n≠m) and sectoral (C and S where n=m).

Gravity field modelling has progressed remarkably since the early 1990's, with high resolution dedicated gravity field measurement missions (e.g. CHAMP & GRACE) opening up many new possibilities. Representations of the Earth's gravity field are now

no longer restricted to portraying a static field, and most include secular time variable components (Rapp, 1998). For low flying satellites such as ENVISAT, which are affected more by subtle higher frequency signatures in the gravity field than satellites in medium Earth orbit, these new datasets have also resulted in unprecedented levels of accuracy in precise orbit determination. Willis and Heflin (2004) saw a great improvement when using the GGM01C gravity field (GRACE combined with surface gravity measurements) to degree and order 120 (Willis, P., JPL, pers. comm.) to determine the positions of ground based DORIS stations. Differences in position solutions with respect to independent GPS measurements fell from 12-26mm when using the EGM96 (Lemoine et al., 1998) gravity field to 10-13mm using GGM01C. With direct relevance to ENVISAT, Lemoine (GSFC, pers. comm.) has tested different gravity field models (to degree and order 90) against independent SLR measurements for ENVISAT orbit determination over 68 arcs during 2004 (each arc is typically 4-7 days long), the results are presented below.

The following gravity field models were used in the test:

Model	**Source**
GGM01S	GRACE satellite-only model, 111 days of data to 120x120. UTCSR/GFZ/JPL.
GGM01C	GRACE combination model, GGM01S + surface gravity to 200x200. UTCSR/GFZ/JPL.
GGM02C	GRACE satellite-only model, approx. one-year of data to 160x160. UTCSR/GFZ/JPL.
GRIM5C1	Pre-CHAMP & GRACE combination model, satellites + altimetry + surface gravity to 120x120. GRGS/GFZ.
PGS7777B	Satellite-only model, CHAMP (72 days) + other satellites to 110x110. GSFC.

Table 4-1: Details of different gravity field models tested at GSFC.

Model	Average RMS (cm)
GGM01S	4.77
GGM01C	4.28
GGM02C	4.74
GRIM5C1	4.67
PGS7777B	4.51

Table 4-2: Independent SLR RMS residuals over 2004 using different gravity field models.

Of the fields tested, Table 4-2 clearly shows that GGM01C is the gravity field model of choice for ENVISAT orbit determination. This model has been used to produce the orbit prediction results presented in chapter 11 of this thesis, though after testing for loss of accuracy and in an attempt to reduce computation time, the models were only evaluated to degree and order 70. Accelerations due to this gravity field are shown in Figure 4-4 for ENVISAT over the course of one orbit *without* the central [monopole] force term which would otherwise dominate, in three different coordinate frames. As might be expected, the field produces fairly complicated signatures in the ECI and ECEF frames, while in the HCL frame the accelerations are once and twice per rev, with H dominating.

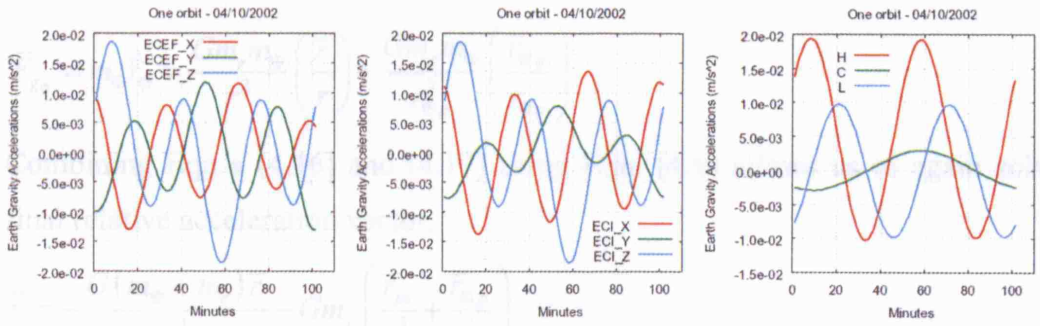

Figure 4-4: GGM01C gravity field induced accelerations experienced by ENVISAT over one orbit (central [monopole] force term excluded).

4.2.2. Third Body Effects (Sun, Moon, Planets)

It is immediately apparent from Figure 4-5 that calculating gravitational accelerations due to third bodies is slightly more complicated than that considered in section 4.1. However, spherical harmonics are not required here and only the monopole term for the

third body needs to be accounted for, due to the distance between these bodies and an Earth orbiting satellite.

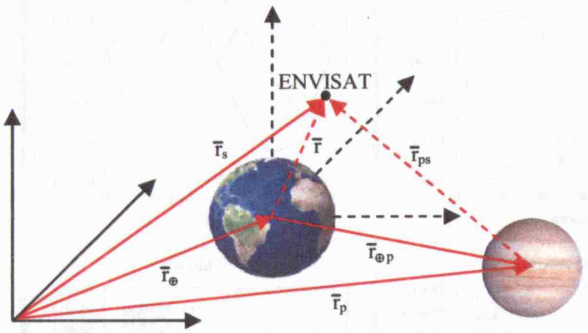

Figure 4-5: Relative position vector of a satellite with respect to the Earth and a third body in an inertial reference frame. Solid black lines represent an inertial frame based at the centre of mass of the entire system, which is translated only with respect to the frame at the centre of mass of the Earth (dashed black lines). Solid red lines show the Earth, third body and satellite position vectors, while the dashed red lines shows the satellite's position relative to the centres of mass of the Earth and the third body.

The acceleration caused by the third body (p) *relative to the* Earth is therefore given by the sum of the gravitational forces exerted by the Earth and (p) upon the satellite (Vallado, 2001):

$$\bar{F}_{g_s} = m_s \ddot{\bar{r}}_s = -\frac{G m_\oplus m_s}{r^2}\left(\frac{\bar{r}}{r}\right) - \frac{G m_p m_s}{r_{ps}^2}\left(\frac{\bar{r}_{ps}}{r_{ps}}\right) \tag{4.16}$$

Plus, the sum of the gravitational forces exerted by the satellite and the third body (p) upon the Earth:

$$\bar{F}_{g_\oplus} = m_\oplus \ddot{\bar{r}}_\oplus = \frac{G m_s m_\oplus}{r^2}\left(\frac{\bar{r}}{r}\right) + \frac{G m_p m_\oplus}{r_{\oplus p}^2}\left(\frac{\bar{r}_{\oplus p}}{r_{\oplus p}}\right) \tag{4.17}$$

Combining Eqn.'s (4.16) and (4.17) using Eqn. (4.6) allows us to again solve for the final relative acceleration vector.

$$\ddot{\bar{r}} = -\frac{G\left(m_\oplus + m_s\right)\bar{r}}{r^3} - G m_p\left(\frac{\bar{r}_{ps}}{r_{ps}^3} + \frac{\bar{r}_{\oplus p}}{r_{\oplus p}^3}\right) \tag{4.18}$$

where the left hand term is the original monopole acceleration given in Eqn. (4.9) (which for practical purposes is of course replaced with the spherical harmonic expansion discussed in section 4.2.1), and the right hand term is the perturbing acceleration due to the presence of a third body.

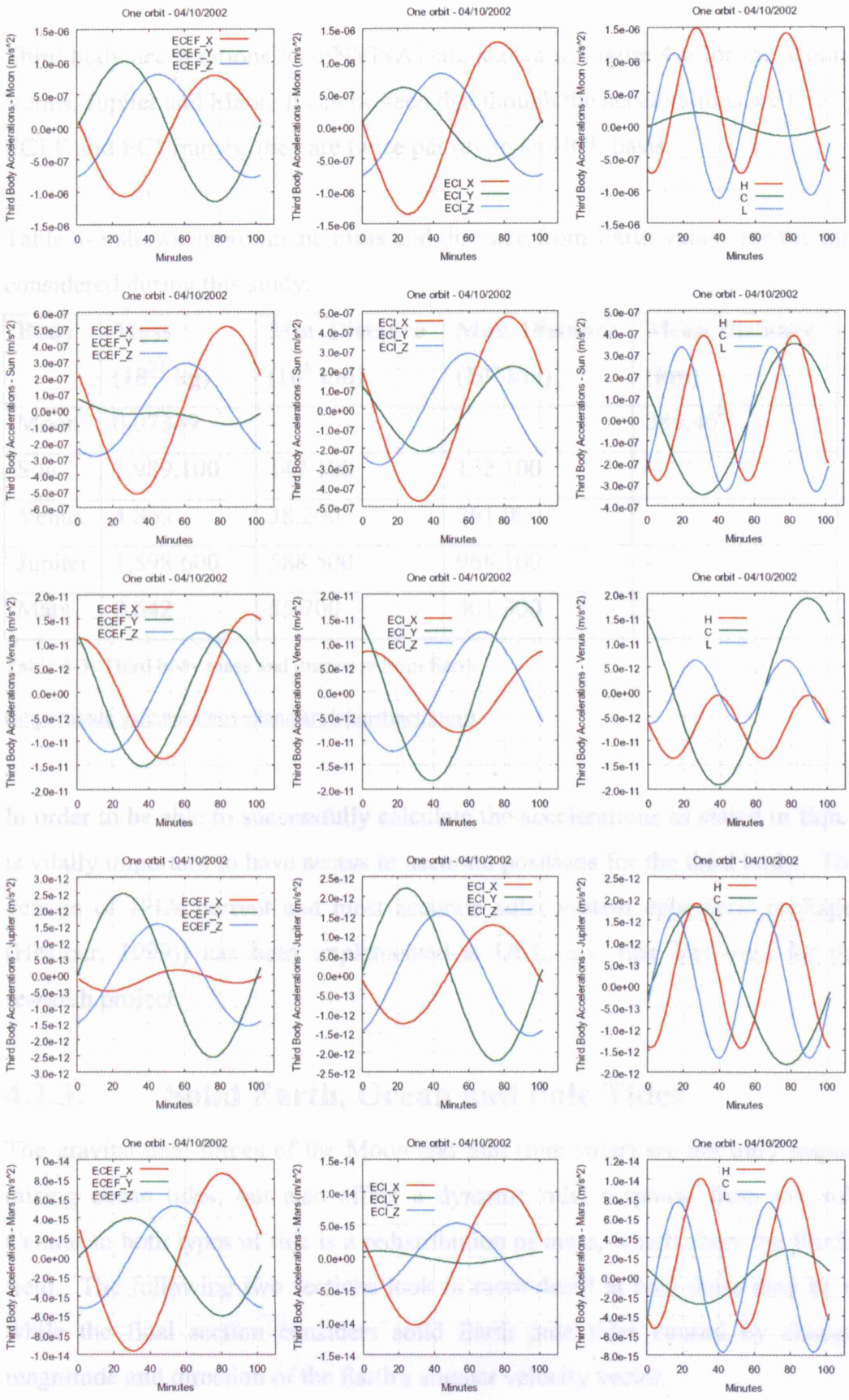

Figure 4-6: Third-body induced accelerations in decreasing order of magnitude for Moon, Sun, Venus, Jupiter and Mars.

Third body accelerations for ENVISAT are shown in Figure 4-6 for the Moon, the Sun, Venus, Jupiter and Mars. It can be seen that though the accelerations are once per rev in ECEF and ECI frames, they are twice per rev in an HCL basis.

Table 4-3 shows approximate mass and distance from Earth values for the third bodies considered during this study.

Body	**Mass (10^{24} kg)**	**Min. Distance (10^6 km)**	**Max. Distance (10^6 km)**	**Mean Distance (km)**
Moon	0.07349	-	-	384,467
Sun	1,989,100	147.100	152.100	-
Venus	4.869	38.200	261.000	-
Jupiter	1,898.600	588.500	968.100	-
Mars	0.642	55.700	401.300	-

Table 4-3: Third body mass and distances from Earth

(http://nssdc.gsfc.nasa.gov/planetary/planetfact.html).

In order to be able to successfully calculate the accelerations as stated in Eqn. (4.18), it is vitally important to have access to accurate positions for the third body. Therefore, a version of JPL's current and most accurate solar system ephemeris package (DE405 (Heafner, 1999)) has been implemented at UCL, and this was used for the current research project.

4.2.3. Solid Earth, Ocean and Pole Tides

The gravitational forces of the Moon and Sun (luni-solar) are not only responsible for raising ocean tides, but also effect a dynamic tidal response from the solid Earth. Central to both types of tide is a redistribution of mass, which alters the Earth's gravity field. The following two sections look in more detail at how these may be modelled, while the final section considers solid Earth pole tides caused by changes in the magnitude and direction of the Earth's angular velocity vector.

4.2.3.1. Solid Earth Tide

The total body tide potential (U_B) at a point ($\bar{r}$) in space relative to the geocentre is given by (Marsh et al., 1988):

$$U_B = \sum_{p=1}^{2} \frac{k_2}{2} \frac{Gm_p a_e^2}{r_{\oplus p}^3} \left[\frac{a_e}{r}\right]^3 \left[3\left[\frac{\bar{r}_{\oplus p} \cdot \bar{r}}{r_{\oplus p} r}\right]^2 - 1\right] \tag{4.19}$$

where the position of the Moon with respect to the geocentre is represented by the subscript p=1 and the Sun by p=2, k_2 is a Love number (in this case the elasticity parameter which reflects the ratio between U_B and U (Eqn. (4.15))) and a_e is the Earth's equatorial radius.

Taking the second derivative with respect to position produces the resultant acceleration at $\bar{r}$ of a satellite due to the luni-solar solid Earth tides ($\ddot{\bar{r}}_{st}$) (Seeber, 2003)[8]:

$$\ddot{\bar{r}}_{st} = \sum_{p=1}^{2} \frac{k_2}{2} \frac{Gm_p}{r_{\oplus p}^3} \frac{a_e^5}{r^4} \left[\left(3 - 15\cos^2\theta\right)\frac{\bar{r}}{r} + \left(6\cos\theta\right)\frac{\bar{r}_{\oplus p}}{r_{\oplus p}}\right] \tag{4.20}$$

where θ is the angle between $\bar{r}$ and $\bar{r}_{\oplus p}$.

As Eqn. (4.20) contains the scalar term $Gm_p / r_{\oplus p}^3$, the Sun's contribution is approximately only one half that of the moon for a LEO satellite. From Figure 4-7 we can see that $\ddot{\bar{r}}_{st}$ contains many different periods, due to the reliance upon θ.

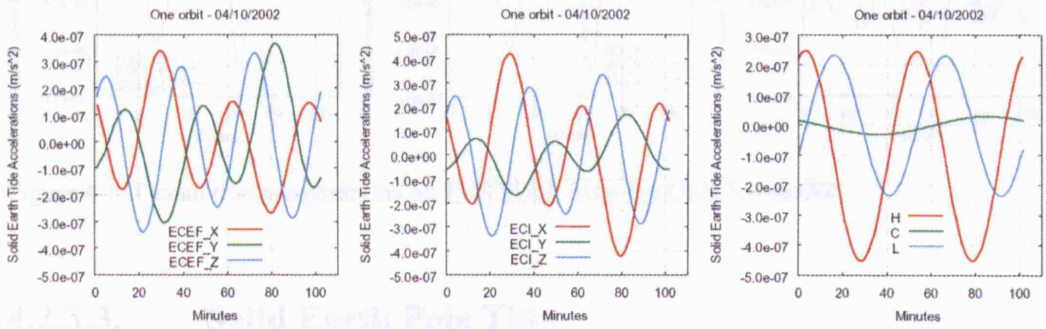

Figure 4-7: Example of ENVISAT Accelerations due to the solid Earth tide.

4.2.3.2. Ocean Tides

Ocean tides, under the influence of Lunar and Solar gravity, cause large mass re-distributions which affect the geopotential. For satellite orbit prediction / determination,

[8] Note: more sophisticated solid Earth tide models are available, e.g. McCarthy & Petit (2003).

dynamic ocean models result in changes to the normalised geopotential coefficients (McCarthy, 1996[9]). These models are difficult to incorporate into satellite orbit software tools and, it has been found, are often insufficiently documented to allow the validation of the model; yet they are also essential when analysing the orbits of LEO satellites (Seeber, 2003). Therefore, the current study took FORTRAN routines used in the SLR SATellite ANalysis, or SATAN, software (G. Appleby, July 2005, pers comm.) and coded them into C++. Identical inputs were then passed to the FORTRAN and C++ routines and the outputs were compared to check that the new code was operating correctly. The University of Texas at Austin's Centre for Space Research produces a set of spherical harmonic coefficients which accord to the IERS conventions, calculated from the Topex altimetry satellite (ftp://ftp.csr.utexas.edu/pub/tide/). SATAN makes use of version 3.0 of this model (although version 4.0 is now available) and allows corrections to be made up to degree 20 and order 10. It can be seen from Figure 4-8 that these accelerations are very complex, and this is largely due to the number and irregular nature of the coastlines that pass beneath ENVISAT as it makes one revolution around the Earth (Seeber, 2003).

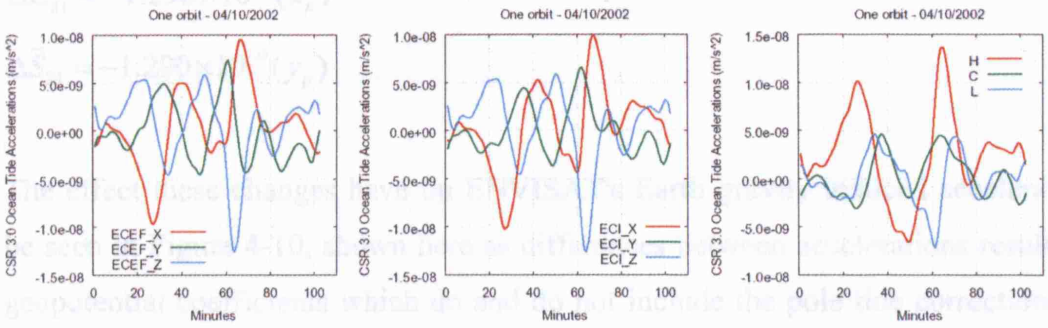

Figure 4-8: Ocean tide accelerations on ENVISAT from the CSR 3.0 model.

4.2.3.3. Solid Earth Pole Tide

A solid Earth pole tide results from changes in the magnitude and direction of Earth's angular velocity vector (Tapley et al., 2004). This movement, termed polar motion, is perhaps most easily thought of as a change in the location of the Earth's spin axis with respect to the crust. The IERS model this behaviour relative to a 'fixed' reference pole

[9] These 1996 conventions were used for the work conducted in this thesis, though more recent conventions are now available (McCarthy & Petit, 2003).

(see Figure 4-9) and, for the nine year period shown, the range of motion does not exceed c.15m in the X or Y directions. The most obvious pattern seen in Figure 4-9 is known as the Chandler period, which has a repeat cycle of approximately 434 days (Leick, 2004).

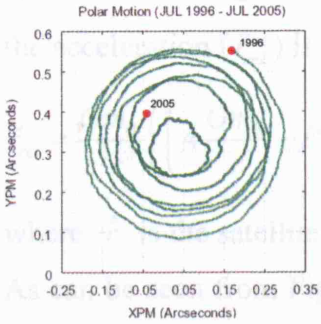

Figure 4-9: Polar Motion (data from http://hpiers.obspm.fr/eoppc/bul/bulb/).

For satellite orbit prediction / determination, as with the ocean tides, the influence of polar motion is usually implemented through changes to the normalised $\bar{C}_{21}$ and $\bar{S}_{21}$ geopotential coefficients (McCarthy, 1996) - see section 4.2.1:

$$\Delta\bar{C}_{21} = -1.290\times10^{-9}(x_p) \tag{4.21}$$

$$\Delta\bar{S}_{21} = -1.290\times10^{-9}(y_p) \tag{4.22}$$

The effect these changes have on ENVISAT's Earth gravity induced accelerations can be seen in Figure 4-10, shown here as differences between accelerations resulting from geopotential coefficients which do and do not include the pole tide corrections. They have a far more uniform signature than that arising from the ocean tides.

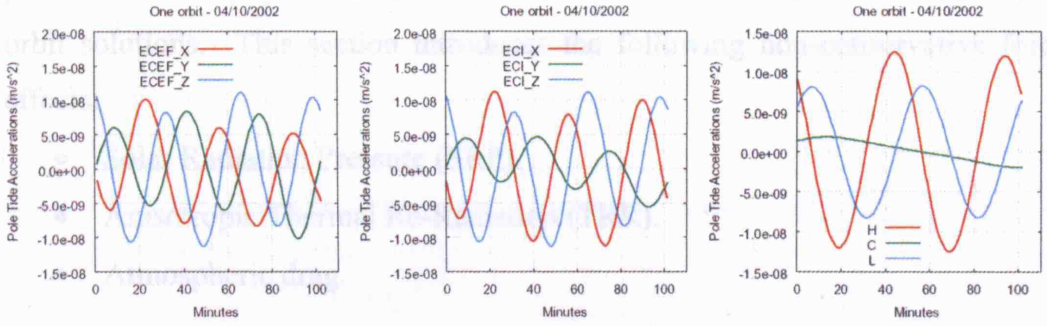

Figure 4-10: Solid Earth Pole Tide Accelerations on ENVISAT.

4.2.4. Relativistic Effects

Newtonian mechanics are fully suited to many applications, but for high precision orbit prediction and estimation, relativistic effects must also be considered. The dominant effect of the curvature of space-time due to the rotation and mass of the Earth is a small advance in the argument of perigee (Tapley et al., 2004). The relativistic correction to the acceleration ($\ddot{\bar{r}}_{rel}$) is given by (Seeber, 2003):

$$\ddot{\bar{r}}_{rel} = \frac{Gm_{\oplus}}{c^2 r^3}\left(\left(4\frac{Gm_{\oplus}}{r} - \dot{r}^2\right)\bar{r} + 4\left(\bar{r}\cdot\dot{\bar{r}}\right)\dot{\bar{r}}\right) \tag{4.23}$$

where $\dot{\bar{r}}$ is the satellite's velocity vector, and c is the speed of light in a vacuum.
As can be seen from Figure 4-11, for a LEO satellite such as ENVISAT this correction will be significant when conducting orbit determination.

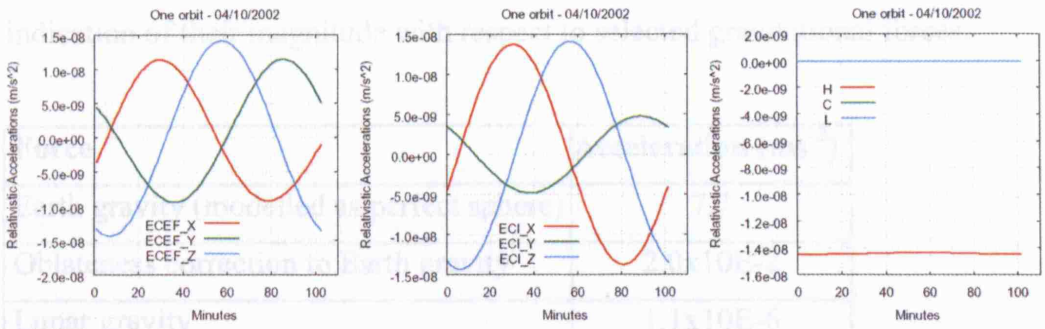

Figure 4-11: Relativistic corrections to ENVISAT accelerations.

4.3. Non-Conservative Forces

Modern precise orbit products rely upon very sophisticated tracking networks, non-linear estimation strategies and hopefully accurate and precise empirical or analytical a priori models of physical force effects. Errors in each of these will affect the resultant orbit solutions. This section introduces the following non-conservative force (NCF) effects:

- Solar Radiation Pressure (SRP).
- Anisotropic Thermal Re-Radiation (TRR).
- Atmospheric drag.

Modelling details and analysis of the three forces mentioned above which pertain specifically to ENVISAT, as well as a discussion of the remaining non-conservative forces:

- Spacecraft internal heat distribution (Qrate).
- Earth Radiation Pressure (ERP).
- Antenna thrust.

are left until the following chapter in order to retain a clear distinction between existing approaches and the significant and fundamental modelling advances made during this project. Note that a major overhaul was also performed on the UCL_SRP software in order to allow it to be run efficiently for the ENVISAT satellite. As the overhaul relates to implementation problems, rather than a redefinition of the fundamental models, further discussion of this difficult issue is left until chapters 5 and 6. However, to put all of these forces in perspective relative to one another, approximate magnitudes for the resultant accelerations caused by the most significant of these force effects on ENVISAT are given, in order of decreasing accelerations, in Table 4-4 along with an indication of their magnitude with respect to selected gravitational forces.

Force	**Acceleration (ms^{-2})**
Earth gravity (modelled as perfect sphere)	7.7
Oblateness correction to Earth gravity	2.0x10E-2
Lunar gravity	1.1x10E-6
Solar gravity	5.7x10E-7
Solid Earth tide, raised by the Moon	2.8x10E-7
Solid Earth tide, raised by the Sun	1.4x10E-7
Solar radiation pressure	6.5x10E-8
Atmospheric drag[10]	2.1x10E-8
ERP effects	1.4x10E-8
Thermal re-radiation	6.2x10E-9
Antenna thrust	4.1x10E-10
Venus gravity	6.3x10E-11

Table 4-4: Approximate values for the most significant accelerations due to non-conservative force effects on ENVISAT in decreasing order.

[10] Drag is strongly dependent upon changes in atmospheric density due to the solar cycle (value here computed for Jan 2003, approximately one half of the way between solar maximum (2000) and solar minimum (2006)) – i.e. the ranking of drag in this table will change over time. A nominal drag coefficient of 2.25 was used.

An order of magnitude calculation allows us to gauge the maximum total displacement (i.e. worst case) due to SRP, ERP and drag induced accelerations over the course of one ENVISAT orbit (c.101 minutes) if these accelerations are considered to act continuously in the same direction (see Table 4-5). A constant acceleration (a) equals a change in velocity ($v-v_0$) divided by the change in time (Δt):

$$a = \frac{v - v_0}{\Delta t} \tag{4.24}$$

This results in a velocity which changes linearly with time. The average velocity (v_a) can therefore be given both by the average of two epoch's velocities:

$$v_a = \frac{v_0 + v}{2} \tag{4.25}$$

and the change in position divided by time:

$$v_a = \frac{x - x_0}{\Delta t} \tag{4.26}$$

We can equate equations (4.25) and (4.26), then substitute in (4.24) after rearranging it to solve for the velocity (v). We end up with equation (4.27):

$$x = x_0 + v_0 \Delta t + \frac{1}{2} a \Delta t^2 \tag{4.27}$$

which shows us that a constant acceleration contributes ($\frac{1}{2} a \Delta t^2$) to a change in position.

Force	Total Displacement after 1 revolution (m)
SRP	1.19
Drag	0.39
ERP	0.26

Table 4-5: Total displacement due to SRP, ERP and drag after one ENVISAT orbit.

These accelerations have traditionally been modelled analytically by very simple flat panel models with averaged values for surface properties, such as existing and widely used 'macro-models' for ENVISAT developed by CNES. The reason for this is that their modelling is made difficult due to: the nature of the interaction between the radiative / particulate fluxes and the complex geometrical shapes of the spacecraft bus and solar array; the fact that surface elements may have widely different surface

properties (often poorly defined) and; computing accurate NCF models can be very numerically intensive. A very large and extremely complex satellite such as ENVISAT presents these difficulties in measures far beyond those tackled by any previous non-conservative force modelling work.

4.3.1. Solar Radiation Pressure and Thermal Re-Radiation - SRP & TRR

4.3.1.1. Solar Radiation Pressure

The 1990's saw renewed interest in modelling of the force on spacecraft buses / payloads resulting from solar radiation pressure both empirically (Bar-Sever & Russ, 1997) and analytically (Fliegel et al., 1992 and Fliegel & Gallini, 1996), especially for Global Positioning System (GPS) satellites where highly accurate predicted orbits are an operational requirement. While these models proved to be superior to their predecessors, the analytical techniques failed to properly account for the complexity of the spacecraft bus due to both the required computational resources and a lack of algorithmic sophistication. However, a more recent attempt (Ziebart, 2001b) produced a technique which theoretically requires no simplification of the bus geometry, and is thus perfectly positioned for use with a complex satellite such as ENVISAT. It is this method which is outlined in the current section; computational requirements meant that certain aspects of this technique had to be extended and developed in a significant manner (see chapters 5 and 6).

The term solar radiation pressure actually describes an exchange of momentum between photons (electromagnetic radiation from the Sun) and the surfaces of a satellite which absorb, re-emit and reflect these photons. For any surface, this leads to direct pressure from absorbed radiation (F_{drp}), and specular (F_{sp}) and diffuse (F_{diff}) pressure from reflected radiation[11] (see Figure 4-12).

[11] Although other reflection models exist (e.g. Nicodemus, 1970), this author is not aware of their required parameters being computed for satellite force modelling activities.

Total radiation pressure is computed by summing the magnitudes of these individual forces (i.e. F_{drp} + F_{sp} + F_{diff}), and this can be decomposed into directions normal ($\bar{F}_n$) and shear ($\bar{F}_s$) to a given surface (Ziebart, 2001b):

$$\bar{F}_n = -\frac{E}{c} A \cos\theta \left[(1+\nu\mu)\cos\theta + \frac{2}{3}\nu(1-\mu) \right] \cdot \hat{n} \tag{4.28}$$

$$\bar{F}_s = \frac{E}{c} A \cos\theta \sin\theta (1-\nu\mu) \cdot \hat{s} \tag{4.29}$$

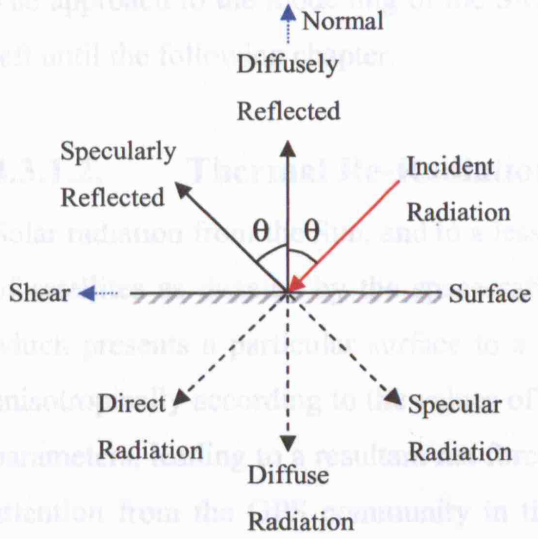

Figure 4-12: Schematic showing direct and reflected radiation pressure acting on a planar surface.

where E is the solar irradiance parameter (1367Wm^{-2} (Frolich & Lean, 1998)), c is the speed of light in a vacuum, A is the surface area, θ is the incidence angle, ν is the reflectivity of the component - the proportion of incident radiation that is reflected (averaged over the whole spectrum), μ is the specularity of the component - the proportion of reflected radiation that is reflected specularly, $\hat{n}$ and $\hat{s}$ are unit vectors normal and shear to the surface respectively, expressed in body fixed coordinates.

The implementation of Ziebart's (2001b) method depends upon the use of a pixel array which discretises the flux incident upon the spacecraft into elements whose size is defined by the user (typically 1, 2 or 5 mm depending upon requirements). The pixel array is positioned orthogonally to a particular Sun-spacecraft direction with respect to a computer model of the satellite (see chapter 6) and the force due to each element is

summed across the array. Most Earth observation satellites such as ENVISAT have a well defined attitude regime (see chapter 8) and this can be used to define a range of Sun directions for the pixel array. The resultant BFS force for each Sun direction is converted to an acceleration (Eqn. (4.1)) and together, all of the data generated can be used to produce a gridded data file of accelerations at regularly spaced (2.5°) intervals of body fixed latitude and longitude. A process of bi-linear interpolation is then used in an orbit integrator to provide the required accelerations.

The approach to the modelling of the SRP forces acting on ENVISAT's solar panels is left until the following chapter.

4.3.1.2. Thermal Re-Radiation

Solar radiation from the Sun, and to a lesser extent the Earth, heats the exposed surfaces of satellites as dictated by the spacecraft's attitude regime. In most cases, a satellite which presents a particular surface to a heat source will re-emit some of this energy anisotropically according to the values of its reflectivity, absorptivity and transmissivity parameters, leading to a resultant net force. As with SRP, thermal re-radiation received attention from the GPS community in the 1990's with varying success (Vigue et al., 1994b, Fliegel & Gallini, 1996), but it was not until much more recently that a generic treatment for all satellites was presented (Adhya, 2005). This last method has been implemented at UCL and is outlined briefly below.

Most of ENVISAT's bus is covered in multi-layer insulation (MLI) (gold coloured components in Figure 4-13) in an attempt to thermally isolate it. The force ($\bar{F}_{MLI}$) due to the thermal emission of radiation from MLI is easily modelled (Eqn. (4.30)) under the assumption of a Lambertian distribution (see section 5.5.4 for more details), and depends upon the fourth power of the surface's absolute temperature (T) and means that the temperatures across the surface must be known or well modelled (see below).

$$\bar{F}_{MLI} = -\frac{2}{3}\frac{\varepsilon_s \sigma T^4}{c} A \cdot \hat{n} \tag{4.30}$$

where ε_s is the surface's emmissivity parameter, σ is the Stephan Boltzmann constant, A is the area, c is the speed of light in a vacuum and $\hat{n}$ is the surface's unit normal.

Figure 4-13: Multi-layer insulation (MLI) covering the ENVISAT bus.

Of course, as this must be integrated across the entire spacecraft, the calculation is performed most efficiently if done simultaneously with the force due to SRP using the pixel array technique mentioned in section 4.3.1.1. Here, the area and surface normal of each insolated spacecraft 'pixel' will already have been generated. For the ENVISAT bus, the surface temperature is calculated for those components which are covered with multi-layer insulation (MLI).

Several assumptions regarding the MLI are made: the interior of the spacecraft (T_{sc}) is kept at 'room' temperature (298K); the MLI has negligible lateral conductivity, and; the MLI emits as a Lambertian diffuser. The study found that the fourth power of the temperature for MLI surfaces can be generated from Eqn. (4.31) (Eqn. 4.34 in Adhya, 2005).

$$T_{MLI}^4 = \frac{\alpha E \cos\theta + \varepsilon_{eff}\sigma T_{sc}^4}{\sigma\left(\varepsilon_{MLI} + \varepsilon_{eff}\right)} \tag{4.31}$$

where α is the absorptivity (1-ν) of the MLI, E is the incident radiation flux (Wm^{-2}), θ is the incidence angle of the radiation flux, ε_{eff} is the effective emmissivity between the MLI and the spacecraft (0.02), and ε_{MLI} is the emmissivity of the MLI (1.0). The values for the emmissivity parameters have been maintained from the study by Adhya owing to the similarity of the MLI used on all the satellites considered (Cavan, N., Rutherford Appleton Laboratories, Oct 2002, pers. comm.).

Solar arrays are typically constructed from a sandwich of several different materials, and must therefore be treated slightly differently from surfaces covered in MLI. Front and rear temperatures are calculated using an energy balance equation which accounts for the properties of the array 'sandwich'. As very limited information about the composition of ENVISAT's solar array is available, the properties used are identical to those given in Adhya (2005). The resultant force ($\bar{F}_{SA}$) is given by Eqn. (4.32) (Eqn. 4.18 in Adhya, 2005).

$$\bar{F}_{SA} = -\frac{2}{3}\frac{\sigma\left(\varepsilon_f T_f^4 - \varepsilon_b T_b^4\right)}{c} A \cdot \hat{n} \tag{4.32}$$

where T_f, T_b, ε_f and ε_b are the temperatures and emissivities of the front and back panel surfaces respectively (surface temperatures are calculated from Eqn. 4.16 and 4.17 given in Adhya[12] (2005), but are not given here).

4.3.2. Aerodynamic Drag

The basic mathematical model for accelerations due to atmospheric drag for satellites at the ENVISAT altitude follows from assuming, as is common practice, that the main [direct] drag force acts anti-parallel to the satellite velocity vector relative to the atmosphere. If v_r is the magnitude of the satellite's velocity (ms^{-1}) relative to the atmosphere and A is the [ram] area of the satellite (m^2) presented to the atmosphere along v_r, then in one second the satellite sweeps out a volume of $v_r A$. Taking ρ as the atmosphere's mass density (Kgm^{-3}) at a certain point in time and space, then the mass of atmosphere (m_a) incident on the satellite during this second will be:

$$m_a = A\rho v_r \tag{4.33}$$

and the momentum transferred to the satellite will be:

$$m_a v_r = A\rho v_r^2 \tag{4.34}$$

The force due to drag acting on a satellite is equal to the rate of change of momentum, which Eqn. (4.1) shows us is also equal to the product of the satellite's mass (m_s) and

[12] N.B. the negative signs in Eqn.s (4.7 & 4.12) in Adyha (2005) are typographical errors, though the resulting expressions (4.16 & 4.17) are correct.

the drag acceleration ($\ddot{\vec{r}}_D$). The acceleration can then be recovered as shown below (Montenbruck & Gill, 2001):

$$\ddot{\vec{r}}_D = -\frac{1}{2} C_D \frac{A}{m_s} \rho v_r^2 \hat{v}_r \tag{4.35}$$

The negative sign indicates that the acceleration is anti-parallel to the unit relative velocity vector ($\hat{v}_r$), which provides the direction of the acceleration. C_D is introduced to model the actual momentum transfer dependent upon the interaction between the satellite and the atmosphere and the factor 0.5 simply provides consistent notation in aerodynamics (can be thought of as scaling the C_D term). C_D typically ranges from 1.5 to 3.0 (Montenbruck & Gill, 2001), and a nominal value of 2.25 has been used in this study, although in actual orbit determination ENVISAT's estimated C_D value has been less than 2.0 and higher than 7.0 (see chapter 11). This is because the formulation of Eqn. (4.34) assumes that both the atmospheric density and the ram area presented to the flux are perfectly known, which is in practice very rarely true (see next chapter for more on this).

4.4. Summary

In this chapter it has been shown that there are many forces (both conservative and non-conservative) which must be considered when computing orbit solutions for Earth orbiting spacecraft. Existing methods for modelling them have been outlined. Some of these forces however remain very difficult to model, particularly for large and complex satellites, and this is tackled in part II of the text.

PART II

5. Advanced Non-Conservative Force Modelling

This section analyses current techniques and proposes alternatives where appropriate for modelling SRP, TRR and aerodynamic drag. New techniques for modelling ERP, Qrates and antenna thrust are outlined in detail. While much of the discussion pertains specifically to ENVISAT, much of it will be seen to largely hold true for LEO satellites in general.

5.1. SRP

5.1.1. Solar Array

ENVISAT's solar array consists of fourteen 5m x 1m segments which form a corrugated surface with a total surface area of $70m^2$. However, each segment is alternately canted at c.+/- 4° with respect to the array's longitudinal axis (see Figure 5-1).

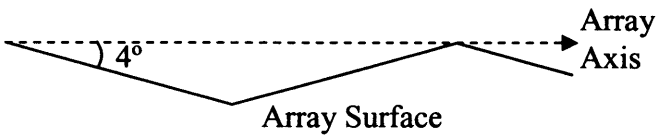

Figure 5-1: Corrugated surface of ENVISAT's solar array.

This has the effect of reducing the total area of the array in the direction normal to the array axis by a small amount (c.$13cm^2$) which will reduce the total force acting upon the whole panel. It also means that a component of the force acting on each segment will be cancelled by that acting on an adjacent segment, thus reducing the total force exerted overall.

Typically, solar panels are treated as single flat plates when calculating the force due to SRP and drag etc. during orbit determination, and it is no different for ENVISAT's solar array in the CNES macromodel. A simple adjustment enables us to model the physical reality of the corrugated surface much more closely. All segments which point in a particular direction can be treated as a single flat plate, so we end up representing ENVISAT's solar array by two 5m x 7m segments which are each canted at +/- 4° with

respect to the array's longitudinal axis. As the orientation of each of these segments remains fixed with respect to both the longitudinal axis and the normal of the total solar array (see section 8.1.3 for how the directions of these two axes can be accurately calculated), key components of the surface normal of each segment (i.e. how far they project along the array's longitudinal and normal axes) can be pre-computed and set as a constant value in order to reduce the computational overhead.

While this is perhaps likely to result in only a small improvement, it is especially important for the calculation of SRP on such a large structure as ENVISAT's solar array which is designed to be optimally Sun-pointing at all times. Most importantly, failure to account for it will result in a systematic bias.

5.1.2. Sanity Check

This section shows how the SRP/TRR model was checked for an arbitrary Sun direction using a simple box-wing model with accelerations calculated analytically. The process is designed to give confidence that the UCL_SRP program (a very complicated piece of software) is producing values in the correct ballpark. More details on how the UCL_SRP model was computed and implemented are given in the following chapters.

The following model setup was adopted in the ENVISAT body-fixed frame:

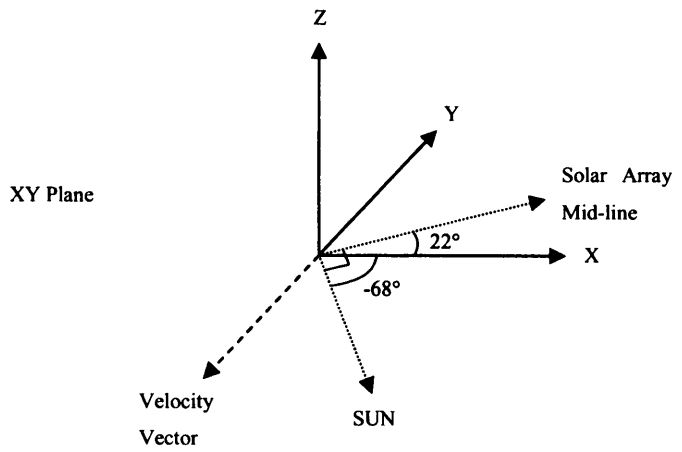

Figure 5-2: Sanity check model setup in the ENVISAT body-fixed frame.

The above diagram shows that the probe-Sun vector has been defined with a longitude of -68° and a latitude of 0°, the Sun is set at a distance of 1AU from the satellite.

This ensures that the Sun direction is normal to the solar array, and means that only one side and one end panel of the box best fitted to the bus can be seen (see Figure 5-3):

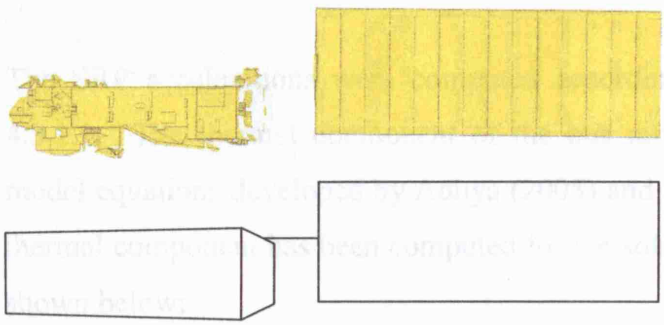

Figure 5-3: Relative geometries of the precise UCL and box-wing ENVISAT models for the sanity check.

The following gives an outline of the differences which are most likely to be apparent between the two models. The ASAR array will contribute a negative X acceleration from its canted surface which can be seen, as will the faceted surfaces of those instruments on the underside of the payload module; though these effects may be matched by the larger overall area of the best fitted box face. A negative Z component will also be introduced by the ASAR array which will not feature at all in the analytical model. As noted above in the previous section (5.1.1), treating ENVISAT's solar array as two separate segments, instead of a single flat plate as in the box-wing model, should have the effect of reducing the total overall acceleration.

The analytical calculations were performed with the following additional parameters:

ENVISAT Mass	8040.8 Kg
Bus Reflectivity	0.41
Bus Specularity	0.5
Array Reflectivity	0.25
Array Specularity	0.85

Table 5-1: Table of model parameters

For the bus, the box model has been considered to be completely covered in MLI and this does indeed constitute its major component, for which the above parameters were used. No optical parameters were directly available for the solar array, and therefore those which had been used to good effect on the earlier UCL JASON model (Adhya,

2005) were employed. Also, because these two LEO satellites had similar launch dates and are both of European origin, it seems reasonable to expect that the individual solar panels are of similar design.

The SRP accelerations were computed according to the equations given in section 4.3.1.1. The thermal component of the bus model was computed from the generic model equations developed by Adhya (2005) and reproduced here in section 4.3.1.2, no thermal component has been computed for the solar array in either case. The results are shown below:

UCL_SRP	X	Y	Z
Bus SRP & TRR	-5.87432E-09	2.00142E-08	-8.92849E-12
Array SRP	-1.83799E-08	4.54755E-08	-3.26979E-16
Sum	-2.42542E-08	6.54898E-08	-8.92816E-12

Box-Wing	X	Y	Z
Bus SRP & TRR	-6.56596E-09	1.93142E-08	0.00000E+00
Array SRP	-1.84155E-08	4.55800E-08	0.00000E+00
Sum	-2.49815E-08	6.48943E-08	0.00000E+00

Table 5-2: Comparison of UCL_SRP and analytical box-wing computations.

As can be seen when comparing these values, the numbers produced are very similar, and differ in the manner predicted above. This gives confidence that the modelling process has been correctly performed from start to finish.

5.2. TRR

5.2.1. ASAR array

The only significant instrument not considered for ENVISAT when calculating a thermal force is the ASAR array (see Figure 5-4), for which no information about the materials used to construct it were available from the Astrium data set.

Figure 5-4: Undeployed ASAR antenna in the clean room before launch.

The following outlines additional reasons for not considering the ASAR instrument in the present TRR analysis. The array (c.1.3m x 10m) is constructed from 20 honeycomb tiles each with 16 sub-arrays, i.e. 320 main elements. The tiles are mounted on five rigid carbon-fibre reinforced plastic (CFRP) frames which deploy after launch to form a single planar surface, and each tile is affixed to its own radiating panel (ESA, 2002). Every tile is individually monitored and compensated for changes in temperature, as this affects the stability of the radio frequency produced by the antenna (Torres, 2002). To improve thermal stability, the antenna uses a system of passive thermal control assisted by active heaters to distribute heat evenly across the array (Boisvert et al., 1997). Without further information on these systems it is impossible to state what, if anything, the net thermal output of the array amounts to.

However, to gauge the possible effects of neglecting this contribution to the total non-conservative force budget, the following calculation is carried out. The ASAR array is treated as a grey body whose emissivities are equal to its absorptivities (Incropera & DeWitt, 2002) with values of c.0.85 and 0.93 for the front and back surfaces respectively, a thickness of 0.1m, a conductivity value for the CFRP of 4.2Wm-1K-1 (Tanaka et al., 2001), a solar flux of 1368Wm-2 and an average ERP flux of 275 Wm-2. The results obtained are shown in Table 5-3.

T_f (K)	T_b (K)	Force (N/m^2)	Acc per unit area m/s^2
331.930	313.288	-1.714E-07	-2.132E-11

Table 5-3: Nominal TRR force from the ASAR antenna.

Across the array, it appears therefore that such a force may be non-negligible, however, there is great uncertainty in this calculation due to the un-quantified effect of the heating elements mentioned above. For this reason, and due to lack of contradictory evidence, this study assumes that the ASAR antenna radiates thermal energy in a controlled isotropic manner, and *is* therefore taken to produce a negligible net thermal force. However, this assumption *should* be re-evaluated in the future when further information comes to light.

5.3. Combined SRP & TRR

As solar radiation is the main contributing factor to both SRP and TRR, it is essential that the position of the Sun is well known (using DE405), and also the degree to which the Sun is obscured from the satellite by the Earth's shadow (an eclipse). For this reason, a new eclipse function (see chapter 10) was developed (Adhya et al., 2004) to correctly determine eclipse period boundaries when modelling the Earth as an oblate spheroid. The present pixel array algorithm, as explained previously, has been modified to produce combined SRP and TRR bus accelerations and therefore improvements to the efficiency of the UCL_SRP software using the block modelling technique outlined in chapter 6 impacts dramatically upon the computation of both. Although the solar panel contributions for each are calculated independently, the figure below (Figure 5-5) shows the combined SRP and TRR accelerations for the bus and panel over the course of one orbit. Only in the HCL frame are these accelerations capable of being adequately modelled using a once-per-rev empirical parameterisation (see Ziebart et al., 2003 for more on this topic).

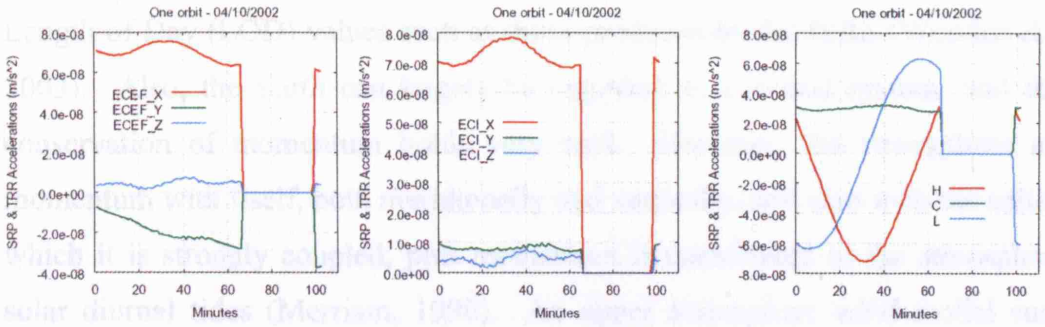

Figure 5-5: SRP and TRR accelerations over one ENVISAT orbit.

The section to the right of each graph in Figure 5-5 where the acceleration drops to zero can be easily explained when the output of the eclipse function is examined. Figure 5-6 shows that at this time the satellite was in eclipse behind the Earth, and gives some indication how critical the correct calculation of eclipse period boundaries is.

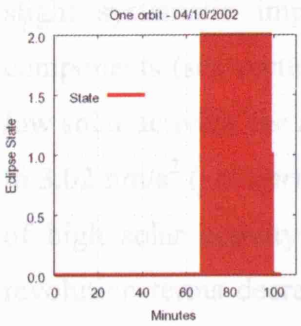

Figure 5-6: Eclipse states over one ENVISAT orbit (0.0 = full phase, 1.0 = penumbra, 2.0 = umbra) generated using the algorithm described in section 10.

5.4. Aerodynamic Drag

To first order, mainly because of the very high velocity of LEO satellites, the assumption is made that the atmosphere co-rotates with the Earth, and ($\overline{v}_r$) is given by Eqn. (5.1) (Montenbruck & Gill, 2001).

$$\overline{v}_r = \overline{v} - \overline{\omega}_\oplus \times \overline{r} \tag{5.1}$$

$\overline{\omega}_\oplus$ is the Earth's angular velocity vector $\left(0.0 \quad 0.0 \quad 0.7292\times10^{-4}\right)^T$ in radians per second, based upon the length (LOD) of one sidereal day (86164.0989 seconds, Aoki et al., 1982). Observed/estimated LOD values vary irregularly at the millisecond level, and so should have little impact upon the relative velocity vector on a day to day basis. Applications which depend upon this parameter should, at the very least, use daily Length of Day (LOD) values such as those produced by the IERS (Wooden & Gambis, 2003). Also, the Earth can largely be regarded as a closed system, and the law of conservation of momentum holds very well. However, the atmosphere exchanges momentum with itself, both meridionally and vertically, and also with the solid Earth to which it is strongly coupled; plus momentum is contributed to the atmosphere by the solar diurnal tides (Merriam, 1990). An upper atmosphere wind model such as the Horizontal Wind Model 93 (HWM-93, Hedin et al., 1996) can help to model the small dynamic effects of these high altitude 'winds', although it is based mainly on data taken up to an altitude of only 120km. In fact, errors of up to 20m/s have been recorded at

altitudes of just 90km (Drob & Picone, 2000) and Aylward et al. (2000) suggests that HWM-93 is insufficiently detailed to be of much use at the ENVISAT altitude. However, although this model has only a small effect, orbit estimation for the ERS-2 satellite by Doornbos et al. (2002) which includes HWM-93 is stated as showing a slight systematic improvement in the estimated once per revolution acceleration components (see section 11.2.1.1.5 for more on once per revolution terms). In fact, at low solar activity, the along-track once per revolution terms actually increase from 2.96 to 3.02 nm/s^2 (i.e. *apriori* modelling is degraded) when HWM-93 is included. At times of high solar activity we see a very different story, with the along-track once per revolution terms decreasing sharply from 13.68 to 12.88 nm/s^2 upon the inclusion of HWM-93 (Doornbos et al., 2002, Table 3). In a fashion similar to the ocean tide model, this study uses a C++ routine derived from Hedin's original FORTRAN source code[13] checked for identical output against supplied test data.

Of critical importance for this drag acceleration model is the atmospheric density value. When discussing the atmospheric models available almost 16 years ago, Hedin notes that their data tables:

> "*extend from 90 to 2000 km...However, it should be remembered...that the best data coverage is in the 150 to 600 km region. At higher altitudes, the model simply extrapolates, assuming no temperature gradient and diffusive equilibrium. Both of these assumptions will begin to break down at greater altitudes in the exosphere*", (Hedin, 1989).

In fact, through comparison with satellite accelerometer measurements, a quantitative assessment of the errors in empirical density models available in 1989 for the relatively low altitude region between 150-250km puts the standard error at +/-15% (Marcos, 1989). It is mentioned that improved models require "more realistic indicators of solar and geomagnetic activity, comprehensive measurement programs and continued development of thermospheric general circulation models" (Marcos, 1989). Now, one and a half decades later, and this situation is still only in the very initial stages of change. In 2002, Doornbos et al. mention that poor density modelling for the orbits of the ERS-2 satellite is reflected through large variations in the estimated drag coefficient,

[13] http://uap-www.nrl.navy.mil/models_web/hwm/hwm_home.htm

which will expand and contract to soak up deficiencies in the density parameter. The dominant along-track nature of the drag force also implies that such mis-modelling may result in erroneous estimation of along track accelerations. Clearly however, some sort of density model is required, although no single model appears to perform best in all cases (Doornbos et al., 2002, Willis et al., 2004, Lathuillere et al., 2002).

For this study the NASA Marshall Engineering Thermosphere model version 2.0 (MET V2) was chosen; it works within the error bounds stated by Marcos, is relatively simple to use, and was specifically designed for use in operational satellite drag applications (Owens, 2002). Again, C++ routines derived from original FORTRAN source code (Co-developer W. Vaughan, pers. comm.) were checked for identical output against supplied test data. As inputs, MET V2 requires the satellite's altitude, latitude and longitude, as well as the current epoch to the nearest minute, a flag defining the type of geomagnetic index to be used (Kp or a_p, single global indices), a daily solar radio noise flux (F10.7[14]), a 162-day average of F10.7 (taken over six solar rotation periods of 27 days each) and a value for the three hourly geomagnetic activity index[15]. The main driver for the density computed by MET V2 is the geomagnetic activity index value, which was used in its Kp form for this project. These global indices are binned across all of the possible values of the Earth's magnetic field, and range from 0 to 9 (Mayaud, 1980). The top left image in Figure 5-7 shows the mass density output of MET V2, with a discontinuity which is clearly coeval with a change in the geomagnetic index at a 3 hour boundary. The top right image shows the behaviour of Kp (Geo) over the course of one day where the stepped changes are clearly visible.

[14] F10.7 data from: ftp://ftp.ngdc.noaa.gov/STP/SOLAR_DATA/SOLAR_RADIO/FLUX/ with the inputs having to be scaled by 1/10, as instructed, before use.

[15] Geomagnetic index data from:
ftp://ftp.ngdc.noaa.gov/STP/GEOMAGNETIC_DATA/INDICES/KP_AP/

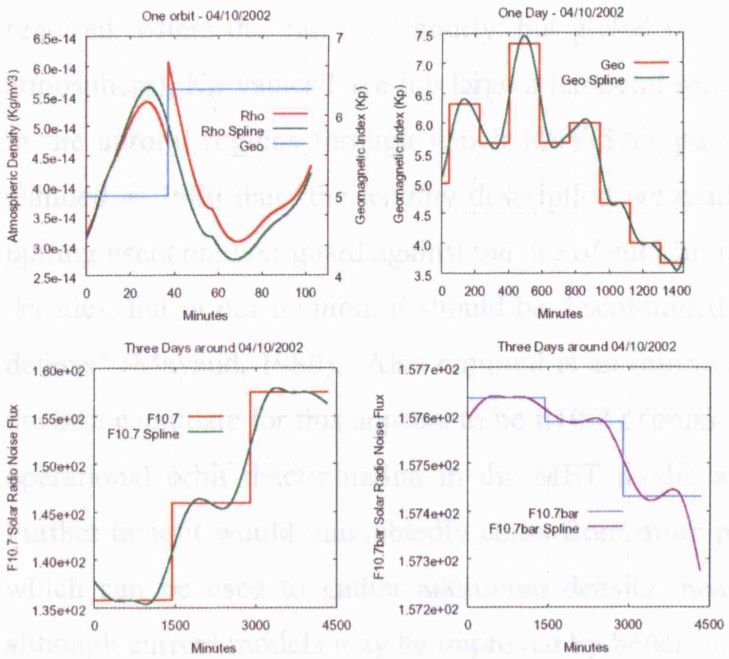

Figure 5-7: Atmospheric mass density from MET V2 and its associated input parameters.

Solar ultraviolet electromagnetic radiation (EUV) has a strong impact on the density of the atmosphere, but is not measurable from the surface of the Earth. F10.7, the 10.7cm solar radio flux, can be measured from the ground and is well correlated with solar EUV activity, for which it is currently used as a proxy within most atmospheric models (Owens, 2002). The two F10.7 parameters (daily & average) are valid for a period of one day, and their step pattern is shown in the two bottom images in Figure 5-7. In order to assess the effect of mass density discontinuities on orbit integration, cubic splines (Giordano et al., 2003) were fitted to all three parameters (Kp, F10.7, F10.7bar), and the combined effect of this smoothing process is seen in the green line in the top left hand image marked as "Rho spline", which lacks the discontinuity of the red line. The splines were forced to match observed values at hour boundaries except in the case of a discontinuity, in which case an average was used. However, upon integrating two orbits from identical initial conditions with the same force models, where one used raw Kp and F10.7 values and the other smoothed values, it was found that the orbit differences proved to be negligible.

It seems that drag modelling will improve significantly only with a similar improvement in the density modelling of the exosphere, and the following can only echo the comment by Marcos given above. It seems that higher resolution geomagnetic index data are

required, where the current 3 hourly, but global (i.e. one value for the planet's entire atmosphere), Kp values have too large a temporal resolution and are not well modelled in the auroral regions through which ENVISAT passes each orbit. In fact, Mayaud claimed in 1980 that "the lengthy description we made of the Kp index was aimed at putting users on their guard against the use of such an index; it was very useful for some decades, but in our opinion, it should be discontinued relatively quickly because of its defects" (Mayaud, 1980). Also required is an improved proxy for solar EUV activity; the best candidate for this appears to be E10.7 (Tobiska, 2003) which is being tested for operational orbit determination in the MET model at Marshall Space Flight Centre. Further benefit would undoubtedly come from more probes at relatively high altitudes which can be used to gather additional density measurements. Note however, that although current models may be improved by better input parameters, it us unlikely that such a static model will ever be able to capture all the detail in a highly non-linear and dynamic atmosphere.

Despite the inclusion of the various atmospheric models mentioned above, the mathematical formulation of drag accelerations presented above is still relatively crude. The drag coefficient will almost never fully account for the ways in which the atmospheric particles are reflected / re-emitted from the spacecraft (Wachman, 1962) and the [ram] profile of the spacecraft used to calculate the area is considered as a flat plate, analogous to the flat plates used in simplistic radiation pressure models. One development would be to consider more detailed ram profile area models, as this value directly scales the aerodynamic force, and a possible new approach to this problem is outlined in Appendix 14. More sophisticated general models of aerodynamic drag have attempted to make use of normal and tangential accommodation coefficients which describe the degree of energy transfer between incident particles and spacecraft components reflected in the directions normal and tangential to the surface of that component (Cook, 1965). Resultant accelerations derived from changes made to these parameters, decomposed in to a drag and a lift force - where the lift force acts normal to the drag force, can be significant. However, these are often unsuccessful as there is currently no way of reproducing orbital conditions in the laboratory, and these coefficients are extremely difficult to accurately estimate / measure (Stark, 1986). It is instructive to note that the GEODYN II software (current release 07/2005 source code, and Long et al., 1989) does not include routines to estimate a lift coefficient. Modern

orbit determination software performs a piecewise re-estimation of the drag coefficient (often every 3-6 hours depending upon the orbital altitude) to account for changes in atmospheric density as the satellite orbits the planet (Lemoine, F. (GSFC) & Willis, P. (JPL) pers comm.).

The atmosphere at the ENVISAT altitude is sufficiently rarefied that the mean free path, the distance a molecule travels before impinging upon another molecule, is large enough so that we do not have to consider the effect of impacts between incident and reflected molecules. The exosphere, the region of atmosphere inhabited by ENVISAT, is therefore said to exhibit a regime called free molecule flow (Schamberg, 1959). However, this does not mean that the interaction between such a flow and a complex satellite such as ENVISAT will be correctly modelled using the flat plate assumption implicit in the above model. For this reason, the current study originally intended to follow a more sophisticated drag modelling pathway, more complex even than the SRP technique, utilising the method of Direct Simulation Monte Carlo or DSMC (Bird, 1995) which has been shown to have good results for orbiters entering the Martian atmosphere (Moss et al., 1997) and for the space shuttle (LeBeau & Lumpkin, 2001).

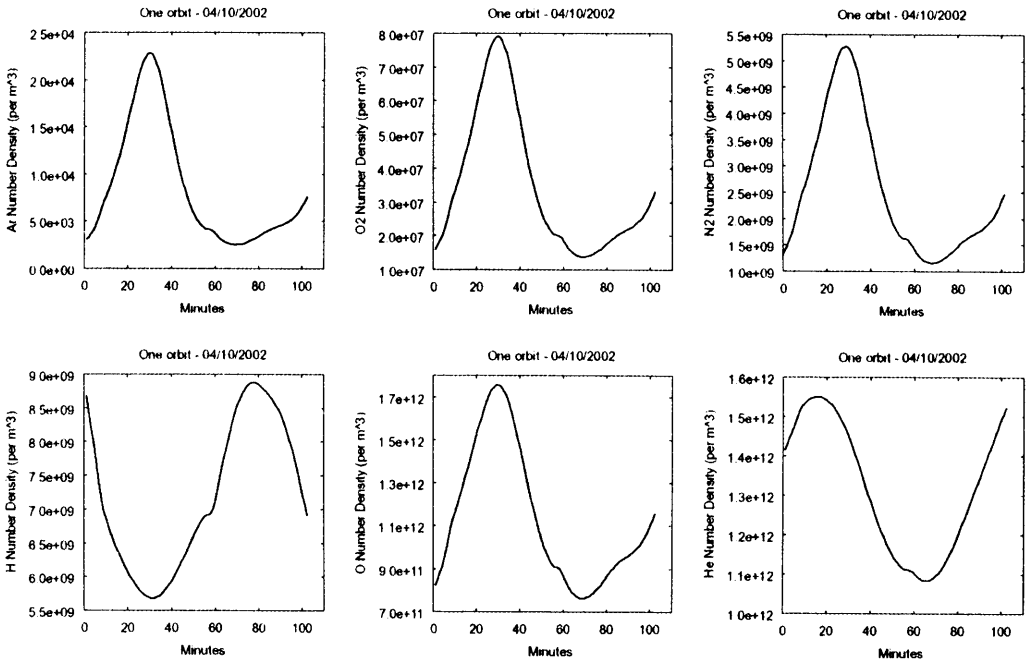

Figure 5-8: Atmospheric number densities from MET V2 over one ENVISAT orbit.

DSMC uses statistical mechanics to describe the behaviour of a gas[16], thus avoiding the massive computational resources required to individually trace the paths of all atmospheric particles incident upon ENVISAT. ENVISAT has a maximum ram profile of c.85m^2 and a velocity of c.7.5km/s, resulting in a volume of 6.4x10^{5}m^3 being swept out every second. With a minimum atmospheric number density of c.1.9x10^{12}/m^3 along the ENVISAT orbit track on 04/10/2002 (from MET V.2 model, summing minimum contribution of each gas species shown in Figure 5-8), a molecule by molecule approach would require a total number of c.1.2x10^{18} particles to be tracked per second, far more than is practicable with most currently available computer resources. Instead, DSMC traces only a small number molecules to represent the gas mixture as a whole with velocities generated by a probability distribution function (for a free-molecular / ideal gas regime, this is a Maxwell distribution (Mandl, 1971)) and making use of models of interaction dynamics.

Even though only a sub-set of actual particles is used, it is still an inherently complex calculation to numerically integrate the effects of even a rarefied gas striking a body of complex structural design. Figure 5-9 shows the discretisation of the computational

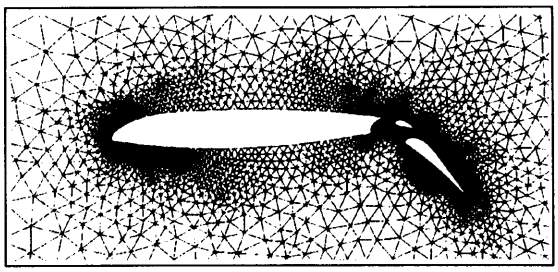

Figure 5-9: Adaptive 2D triangular mesh fitted to an aerofoil. From Shewchuk (1999 (Fig. 2.43)).

domain around an aircraft's wing, which is sub-divided most intensively in regions of high density gradients to account for a higher probability of inter-molecular collisions. Note that for ENVISAT, a 3D mesh is required, and the automatic and optimal generation of these types of volume mesh are still the subject of intense research.

---

[16] Note, drag modelling must also consider the mass of each atmospheric particle, e.g. although monatomic oxygen and helium have similar number densities, an oxygen atom has a mass almost four times greater than that of a helium atom and so will result in greater drag.

An alternative to DSMC is Test Particle Monte Carlo (TPMC), which does not attempt to challenge the free molecular flow assumption, i.e. does not consider the possibility of inter-particle collisions between the incident and reflected flow fields. The Analysis of Non-gravitational Accelerations Due to Radiation and Aerodynamics (ANGARA) force modelling package (Fritsche et al., 1998) utilises the TPMC procedure, and has been used to generate surface forces / accelerations for ENVISAT (Doornbos, 2001). However, orbit determination for ENVISAT by the Department of Earth Observation and Space systems (DEOS) at Delft, using these ANGARA drag accelerations, places only third in a table of six orbit determination centres, measured in terms of RMS SLR residuals over 35 days (see Table 2-1).

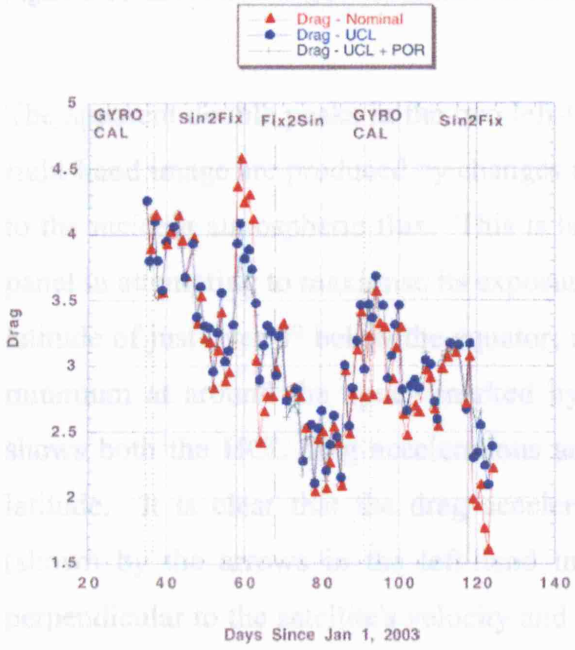

Figure 5-10: Estimated Drag Coefficients for the JASON satellite over a c.6month period using GIPSY-OASIS II (Ziebart et al., 2005).

In fact, new data has recently come to light which suggests that the choice of radiation pressure model can have a marked effect upon the stability of estimated drag parameters (see Figure 5-10). This in turn, implies that the assumed errors in the atmospheric density models may not be as large as first feared, but result in part from aliasing due to the mis-modelling of other forces. To assess this further, the current study uses the drag acceleration model in Eqn. (4.35), and plots both estimated drag coefficients and along track empirical accelerations for ENVISAT over the entire year of 2004 (see chapter 11), as computed with both the NOM and UCL radiation pressure models.

The following plots (Figure 5-11) show ENVISAT drag accelerations over the course of one orbit.

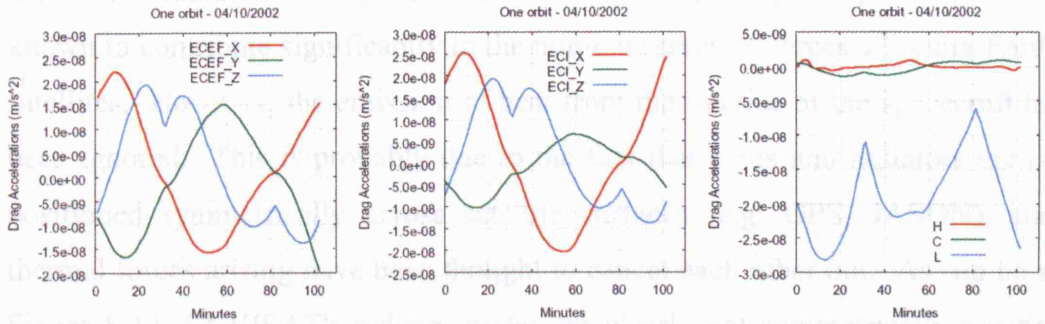

Figure 5-11: ENVISAT drag accelerations over the course of one orbit.

The apparent double peaks in the two left-hand images, and the very sharp peaks in the right-hand image are produced by changes in the ram profile of the satellite with respect to the incident atmospheric flux. This is largely dominated by the rotation of the solar panel in attempting to maximise its exposure to the Sun, which at this time of year has a latitude of just over 4° below the equator; it is for this reason that the drag force is at a minimum at around the epoch marked by arrows in the figure below. Figure 5-12 shows both the HCL drag accelerations and the total ram profile area plotted against latitude. It is clear that the drag acceleration reaches a minimum near the equator (shown by the arrows in the left-hand image) when the solar array normal is near perpendicular to the satellite's velocity and the array's minimum area is presented to the atmosphere. The dual peaks in ECEF and ECI Z drag accelerations can be similarly explained, although the solar array area only dominates until being offset by additional changes in the orientation of the bus.

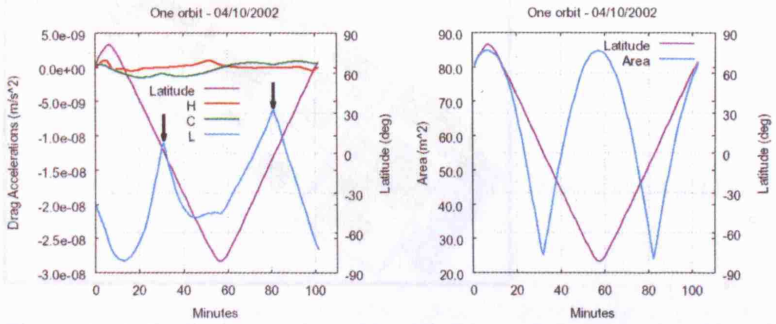

Figure 5-12: Relationship between drag accelerations, ram profile and latitude.

5.5. Bus Internal Heat Flow Modelling - Qrates

5.5.1. Qrate Retrieval

Thermal re-radiation (TRR) for bus sections and solar arrays of spacecraft has long been known to contribute significantly to the non-conservative forces affecting Earth orbiting satellites. However, the emission of heat from the interior of the spacecraft has largely been ignored. This is probably due to the fact that vents and radiators are commonly positioned symmetrically across satellite surfaces (e.g. GPS, JASON), and so any thermal forces arising have been thought to cancel each other out. As can be seen from Figure 5-13, ENVISAT's radiator nodes are clearly not symmetrically positioned over the satellite's surface, a situation likely to result in a net thermal force; this is due to the requirement to position all of ENVISAT's scientific hardware in such a tightly controlled space (Robson, 2004, Astrium, pers. comm.). EADS Astrium (UK) was responsible for the thermal design of ENVISAT's internal components, and has extremely sophisticated beginning-of-life (BOL) and end-of-life (EOL) thermal models for this satellite's bus (their most complex to date). Andrew Robson, head of the thermal engineering section at EADS Astrium, was kind enough to house this author for three days during February 2004. During this time, Astrium's proprietary Thermica software was used to identify those ENVISAT components where thermal venting from scientific instrument hardware on the interior of the bus would occur (see Figure 5-13). Both BOL and EOL thermal models were computed, allowing the change in the thermal emissions (known at Astrium as Qrates) to be estimated over the lifetime of the satellite for those surfaces identified previously.

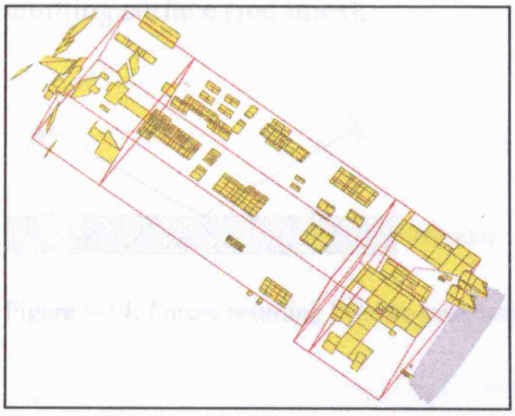

Figure 5-13: Radiating surfaces identified (superimposed on outline of bus).

A record of the identified radiator nodes was maintained by means of unique numbers corresponding to comment line values in the Astrium spacecraft geometry file. Routines were programmed which selected the identified nodes from the geometry file and automatically converted them into a UCL userfile format, in order that the node selection and identification procedure could be verified visually (as in Figure 5-13).

Once verified, the surface unit normals of the selected radiator nodes were computed and Thermica Qrates (linear heat flow values) of each radiator node for the BOL and EOL models were used to scale these normal vectors. A total Qrate vector ($\overline{q}$) was computed for each of the BOL and EOL models by simply summing the vectors for each node.

5.5.2. Qrate Acting Normal to Surface

> "*The energy flows in the thermal model results are not only normal to the surface. In terms of emissions only, it is fair to assume an even hemispherical [Lambertian] distribution from the surface*" (Robson, 2004, pers. comm.).

This implies an azimuthally symmetric emission of radiation which decays as the cosine of the angle made with respect to the surface normal (i.e. a co-latitude, see section 5.5.3), described by a Lambertian distribution function (Chapman, 1974). However, as shown in Figure 5-14 the effect of any radiation travelling parallel to the surface (blue lines) will be cancelled out by radiation acting in the opposite direction. Therefore, we need only be interested in that fraction of the total radiation which acts normal to the emitting surface (red lines).

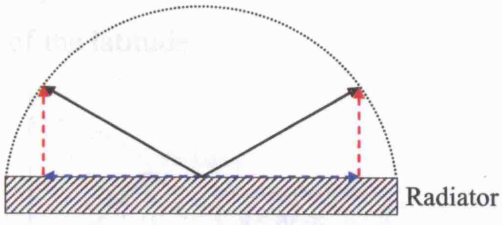

Figure 5-14: Forces resulting from an even hemispherical distribution.

The following sections show how it is possible to recover this fraction of the total radiation after defining a differential area element for the surface of a sphere.

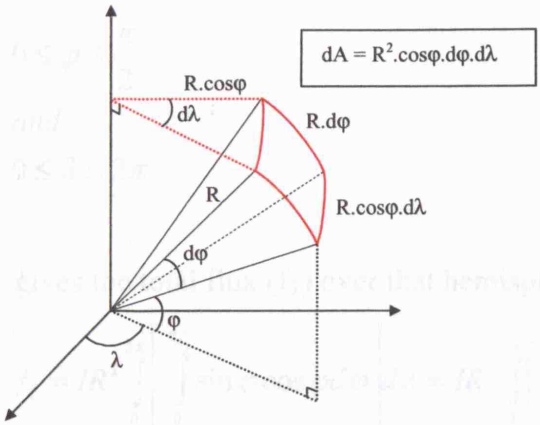

Figure 5-15: Differential area element on the surface of a sphere.

It can be shown that this gives the correct result for the surface area (SA) of a sphere (i.e. $4\pi R^2$):

$$SA = 2R^2 \int_0^{2\pi} \left[\int_0^{\pi/2} \cos\varphi d\varphi \right] d\lambda = 2R^2 \int_0^{2\pi} [\sin\varphi]_0^{\pi/2} d\lambda \qquad (5.2)$$
$$= 2R^2 [\lambda]_0^{2\pi} = 4\pi R^2$$

5.5.3. Integrating for Total Flux Using a Lambertian Distribution.

For an area element (dA), the flux emitted through it is: $I \sin\varphi dA$, where I is the intensity of radiation in the direction perpendicular to the surface. The Lambertian distribution function specifies that the intensity in a specific direction (I(θ)), usually expressed in Wm^{-2}, falls off as the cosine of the co-latitude or (see Figure 5-16) the sine of the latitude.

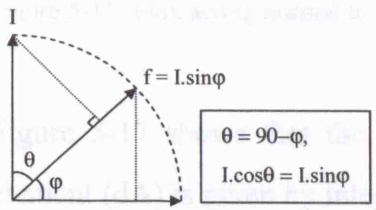

Figure 5-16: The Lambertian distribution function.

Integrating this function over a hemisphere, with integration limits of:

$$0 \le \varphi \le \frac{\pi}{2}$$
$$\text{and} \qquad (5.3)$$
$$0 \le \lambda \le 2\pi$$

gives the total flux (f_T) over that hemisphere:

$$f_T = IR^2 \int_0^{2\pi} \left[\int_0^{\pi/2} \sin\varphi \cos\varphi d\varphi \right] d\lambda = IR^2 \int_0^{2\pi} \left[-\frac{\cos 2\varphi}{4} \right]_0^{\pi/2} d\lambda \qquad (5.4)$$
$$= \frac{1}{2} IR^2 [\lambda]_0^{2\pi} = \pi IR^2$$

where use is made of the trigonometric identity: $\sin\varphi\cos\varphi = \frac{1}{2}\sin 2\varphi$

5.5.4. Integrating for Flux Using a Lambertian Distribution.

Each flux vector over a hemisphere can be broken down in to components both shear and normal to the emission surface. The flux vector can therefore be modified before integration to account only for emission normal to the surface:

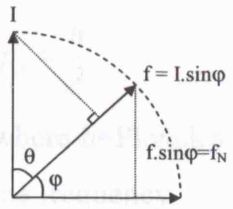

Figure 5-17: Flux acting normal to the emitting surface.

Figure 5-17 shows that the flux emitted normal to the surface (f_N) through an area element (dA) is given by integrating: $f \sin\varphi dA = I \sin^2 \varphi dA$

$$f_N = IR^2 \int_0^{2\pi} \left[\int_0^{\pi/2} \sin^2\varphi \cos\varphi d\varphi \right] d\lambda = IR^2 \int_0^{2\pi} \left[\frac{1}{3}\sin^3\varphi \right]_0^{\pi/2} d\lambda$$
$$= \frac{1}{3} IR^2 [\lambda]_0^{2\pi} = \frac{2}{3}\pi IR^2 \tag{5.5}$$

Comparing f_N to f_T shows that the vector ($\bar{q}_n$) describing the flux normal to the surface, the net Qrate vector, is simply two thirds of the total flux, i.e.:

$$\bar{q}_n = \frac{2}{3} f_T \hat{n} \tag{5.6}$$

where $\hat{n}$ is the unit surface normal.

5.5.5. Qrates as Accelerations

This section shows how the net Qrate vector can be represented as a force / acceleration for orbit prediction / determination purposes. The net Qrate vector has units of Watts (W), the SI unit of power - or the time rate at which work is done (i.e. energy per second (s)).

A photon is the quantum of electromagnetic radiation used to measure the heat emitted from the spacecraft bus and its momentum (p_λ) is frequency dependent (Young & Freedman, 2000):

$$p_\lambda = \frac{h}{\lambda} \tag{5.7}$$

where h=Planck's constant, and λ (the wavelength) equals the speed of light divided by the frequency.

The energy of a single photon is therefore given by:

$$E_\lambda = p_\lambda c \tag{5.8}$$

As it represents the time rate at which work is done, we can say that the magnitude of our net Qrate vector ($\bar{q}_n$) is given by:

$$|\bar{q}_n| = \frac{2}{3} f_T = \frac{2}{3} \frac{\sum E_\lambda}{s} \tag{5.9}$$

where $\sum E_\lambda$ represents the sum of all photons (including a spectrum of characteristic wavelengths) emitted from the surface element, and the time (s) equals one second.

By the conservation of momentum, we can relate Eqn. (5.8) and (5.9) to see that in one second the momentum transfer is given by:

$$\frac{2}{3}\sum p_\lambda = \frac{2}{3}\frac{\sum E_\lambda}{sc} = \frac{|\bar{q}_n|}{c} \tag{5.10}$$

Newton's second law tells us that force is equal to the rate of change of momentum, where m_s is the mass of the satellite:

$$F = \frac{|\bar{q}_n|}{c} = m_s a \tag{5.11}$$

The resultant acceleration is given by:

$$\bar{a} = \frac{-\bar{q}_n}{m_s c} \tag{5.12}$$

where we note that the acceleration acts in the direction opposite to the emission of the radiation.

5.5.6. Calculating the Qrate Acceleration for ENVISAT

As the epochs are known for which the BOL and EOL models are valid, for orbit prediction / determination it is then a simple matter of evaluating the current timetag and linearly interpolating between the net Qrate vectors as these times. Changes in the mass of the ENVISAT satellite can easily be accounted for as they are a matter of public record[17].

The following example shows the effect that neglecting this force can have on ENVISAT.

BOL: Friday March 1, 2002. At 01:07.59[18].

EOL: Thursday March 1, 2007. At 01:08.00[19].

---

[17] ENVISAT mass history available from http://nng.esoc.esa.de/envisat/mass.env

[18] http://www.bnsc.gov.uk

[19] Based on an assumed life of 5 years, Robson, 2004, Astrium, pers. comm.

In the body-fixed frame, the net Qrate vectors ($\bar{q}_n$) for these two epochs are:

	X	Y	Z
BOL (Watts)	-145.504	217.166	320.668
EOL (Watts)	-142.029	265.511	424.859

Table 5-4: BOL and EOL net Qrate vectors.

On 15/12/2003, approximately half-way between ENVISAT's launch and the present day (c.1.8 years after launch), ENVISAT's mass was 8040.805 (kg). Linearly interpolating between the EOL and BOL vectors, and applying equation (5.12) gives the following results for 15/12/2003:

	X	Y	Z
$\bar{q}_n$ (Watts)	-144.253	234.570	358.177
$\bar{a}$ (ms^{-2})	5.984E-11	-9.731E-11	-1.486E-10

Table 5-5: Net Qrate and acceleration vector for ENVISAT on 15/12/2003.

After the EOL epoch has passed, all Qrates are simply fixed to the EOL value.

The acceleration vector (see Figure 5-18) acts primarily in the –Z direction; looking again at Figure 5-13 we can see that this is to be expected as the majority of ENVISAT's radiating surfaces are on the +Z side of the bus. After one day (using $0.5*|\bar{a}|t^2$), the –Z component of the acceleration in Table 5-5 alone results in a total displacement of approximately 0.55m if considered as a constant acceleration. This can only get larger as ENVISAT's thermal output increases over the course of its life and its mass decreases.

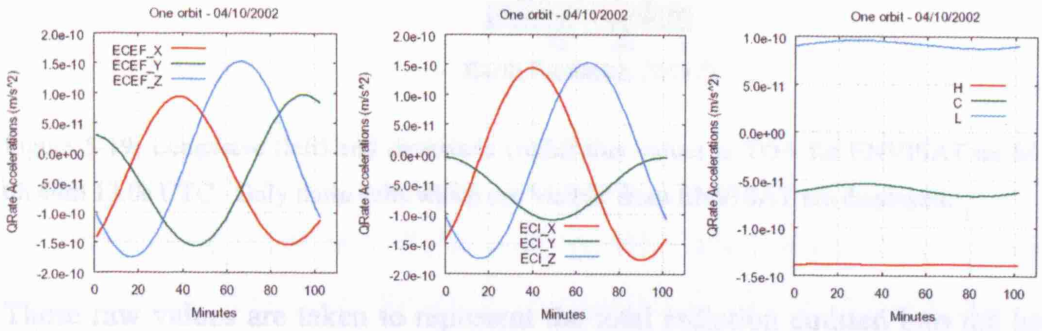

Figure 5-18: Qrate accelerations over one orbit.

5.6. Earth Radiation Pressure - ERP

Earth radiation is comprised of both reflected optical shortwave and emitted infrared longwave radiation. Shortwave radiation is directly reflected (diffuse & specular) solar radiation, and is therefore present only on the daylight side of the Earth. It has a strong temporal dependence since it is affected not only by the relative orientation of the Sun with respect to the Earth and the satellite, but also by Earth rotation (i.e. the surface properties of the hemisphere seen by the satellite) and cloud cover (Montenbruck & Gill, 2001). The longwave component, in contrast, is always present to some degree and can be thought of as forming a background level of radiation.

In the current study, a new technique developed at UCL (Ziebart et al., 2004) is used to generate ERP flux values along a nominal satellite orbit trajectory. The flux values are derived from monthly total-sky averages (i.e. averages of cloudy and non-cloudy measurements) of longwave and shortwave data from the CERES (Clouds and the Earth's Radiant Energy System) in-situ space probes. Raw longwave and shortwave data (see Figure 5-19) are based on a grid spaced at 2.5°x2.5° resulting in 10,368 cells, and measured values are interpolated to the top of the atmosphere (TOA, 30km above WGS84).

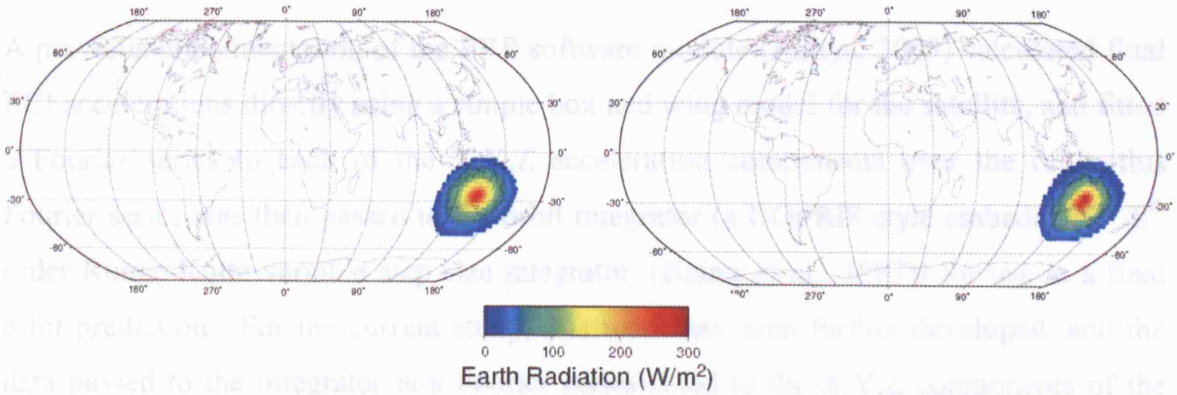

Figure 5-19: Longwave (left) and shortwave (right) flux values at TOA for ENVISAT on 04/10/2002 at 0h 44m 13.0s UTC. Only those cells which are 'visible' from ENVISAT are displayed.

These raw values are taken to represent the total radiation emitted into the hemisphere above the cell. For a particular epoch, TOA radiation values from each grid cell visible to the satellite (i.e. unit normal at centre of cell is <90° from the cell to satellite vector) are mapped under an assumption of Lambert scattering (see section 5.5.3) and scaled for

the satellite altitude (falls off as the inverse square of the distance). The final flux vector is, of course, simply the sum of the individual fluxes contributed by each visible cell.

The ERBE and CERES probes provide us with a total intensity (I_T) in (Wm^{-2}), and so from one grid cell with area dA the total flux (f_T) will be:

$$f_T = I_T dA \tag{5.13}$$

As shown in detail in Eqn. (5.4), the total flux can also be expressed in terms of the intensity (I) normal to the cell ($f_T = \pi I r^2$). Note, care should be taken here in the case of ERP because although the flux has now reached the satellite altitude (a sphere of radius r), the area of the emitting grid cell must be calculated using the Earth radius. Solving for I from these two equations (see Eqn. (5.14)) allows us to then map the radiation flux onto the satellite direction (f_S) with a Lambertian distribution function (see Eqn. (5.15)).

$$I = \frac{I_T dA}{\pi r^2} \tag{5.14}$$

$$f_S = \frac{I_T dA \cos\theta}{\pi r^2} \tag{5.15}$$

where θ is the satellite's co-latitude.

A previous implementation of the ERP software module (Adhya, 2005) calculated final ECI accelerations directly using a simple box and wing model for the satellite, and fitted a Fourier series to each of the X,Y,Z acceleration components over the orbit; this Fourier series was then passed to the orbit integrator (a DOPRI8 style embedded $7^{th}/8^{th}$ order Runge-Kutta variable step size integrator, (Hairer et al., 1987)) for use in a final orbit prediction. For the current study, this work has been further developed, and the data passed to the integrator is a Fourier series fitted to the X,Y,Z components of the ERP flux vector. This flux vector is used to scale the precise SRP/TRR model (see section 4.3.1) which has been extended to accommodate a larger range of flux input directions (from [+13° to +43°] to [-18° to +43°] with respect to the BFS YZ plane) than is required for a pure SRP model (see section 9). Figure 5-20 charts the separation of ERP vectors computed as shown above and ENVISAT's BFS YZ plane under its stellar yaw steering attitude regime. It shows that the new range covered by the UCL SRP/TRR model is adequate, allowing for some overlap.

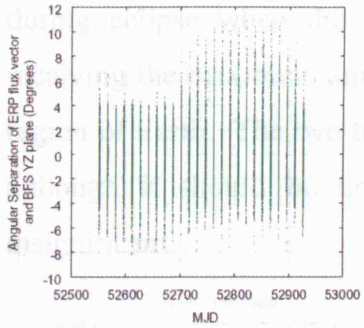

Figure 5-20: Separation of ERP flux vectors and ENVISAT's BFS YZ plane.

Figure 5-21 shows a graphic representation of all locations covered by the pixel array under the chosen range. The gray shaded area denotes the coverage attained by pixel arrays in the BFS XY plane separated by 2.5°; the 'grey area' is then itself replicated every 2.5° by a rotation around the BFS X axis until all possible input directions are covered.

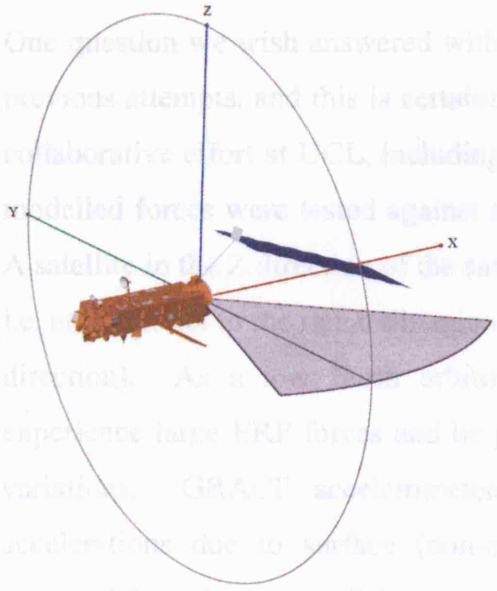

Figure 5-21: Pixel array locations for the UCL SRP and TRR model.

As can be seen from Figure 5-22, these accelerations are large and have very complex signatures which are not easily modelled by a simple once-per-rev empirical parameterisation. The HCL plot on the right-hand-side also shows the latitude of the satellite, and we can see that there are peaks in the H value which correspond with crossing the equator (noting that at this epoch, the Sun has a geocentric latitude of c.4°). For the first peak, the satellite is directly between the Sun and the Earth, and is receiving a maximum amount of both shortwave and longwave radiation. The second peak occurs

during eclipse when the shortwave radiation falls to zero but the satellite is still receiving the maximum amount of 'background' longwave radiation from the equatorial region of Earth. The two troughs occur when the satellite is crossing the polar regions, although it should be noted that even here the accelerations are by no means insignificant.

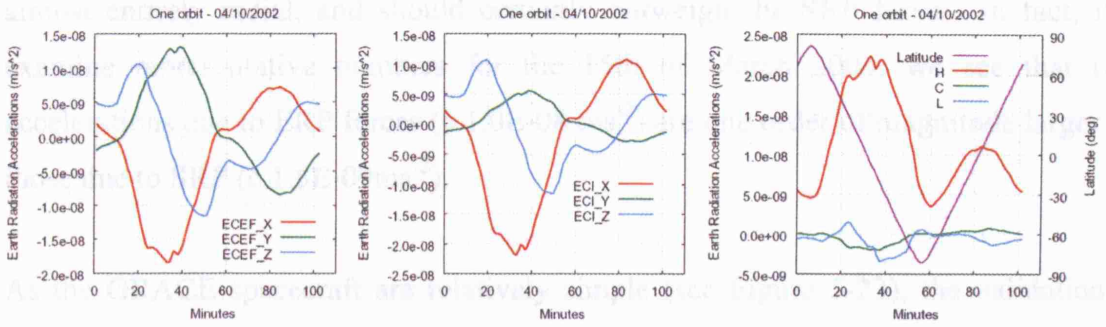

Figure 5-22: ERP accelerations for ENVISAT.

5.6.1. Validating UCL ERP

One question we wish answered with any new technique is whether it fares better than previous attempts, and this is certainly true for the new UCL ERP model. As part of a collaborative effort at UCL, including work performed by M. Ziebart and M. Gulamali, modelled forces were tested against accelerometer measurements onboard the GRACE A satellite in the Z direction of the satellite's BFS (BFS Z for GRACE is nadir pointing, i.e. anti-parallel to the radial direction, where ERP forces act principally along the radial direction). As a low Earth orbiting satellite (altitude c.500km), GRACE A will experience large ERP forces and be particularly sensitive to their temporal and spatial variations. GRACE accelerometers have been specifically designed to measure accelerations due to surface (non-conservative) forces in order that these can be removed from the gravity field recovery process.

On 15th March 2004, GRACE A was flying near its terminator, i.e. the orbit plane is almost perpendicular to the Sun direction, which is represented by its having a beta angle close to +/-90° (between -82.6° and -81.6° over this day). The beta angle is the "acute angle between the Sun vector and the orbit plane. It is defined as positive if the Sun vector forms an acute angle with the orbit normal, and negative otherwise." (Bar-Sever et al., 1996). This means that on the day of the 15th, the SRP contribution to the radial force will be relatively small, as the Sun really only 'sees' one side of the GRACE satellite, and thus acts almost entirely out of the orbital plane. Radial TRR forces have

not been modelled as they will most likely only be a fraction of the SRP radial force, though of course ERP will exert some thermal influence over the nadir facing panel of GRACE. Drag will also be very small as the GRACE A satellite is pitched forward at only c.1°, and therefore most of the drag force will act anti-parallel to the velocity vector, or almost orthogonal to the radial direction. The ERP force will however be almost entirely radial, and should certainly outweigh the SRP force. In fact, if we examine representative numbers for the 15th of March 2004, we see that radial accelerations due to ERP forces (c.1.0E-08 ms^{-2}) are one order of magnitude larger than those due to SRP (c.1.5E-09ms^{-2}).

As the GRACE spacecraft are relatively simple (see Figure 5-23), the validation test compares accelerometer data to accelerations modelled using the plate macromodel outlined in Bettadpur (2004b). SRP forces were computed using a standard solar irradiance scaled for the actual Sun-satellite distance, while ERP forces were based upon two independent sources: the first used flux values from the new UCL CERES based ERP software; the second used flux values from the earlier algorithm by Knocke (1989).

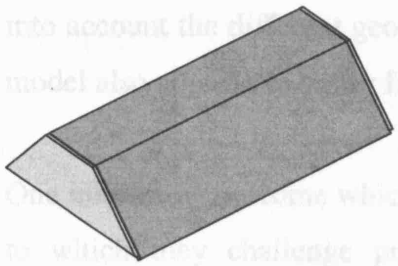

Figure 5-23: Schematic representation of a GRACE spacecraft

Over the course of the first 12 hours of the day, these accelerations were summed, projected onto the BFS Z direction, and then plotted (see Figure 5-24) alongside level 1B (ACC1B) accelerometer measurements[20]. Orbit data was kindly provided by Willy Bertiger of JPL.

[20] http://isdc.gfz-potsdam.de

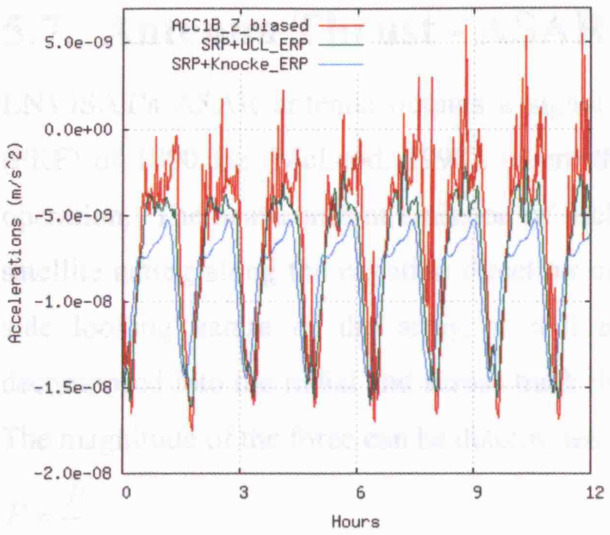

Figure 5-24: GRACE A accelerometer BFS Z measurements compared to modelled accelerations on 15/03/2004.

As can be seen, the UCL results match the accelerometer measurements much more closely than the Knocke results. It can also be seen that the Knocke results suffer from being purely zonal (i.e. latitude dependent), and so accelerations for each orbit (period = c.90 minutes) over these 12 hours have exactly the same pattern, while UCL results take into account the different geographical scene types 'seen' by the satellite. The Knocke model also appears to suffer from a slight phase error.

One interesting outcome which applies to both the UCL and Knocke results is the extent to which they challenge published accelerometer biases (Bettadpur, 2004a). As mentioned above, for this orbit configuration ERP is expected to be the dominant radial force and so the summed acceleration should act radially, or in the negative BFS Z direction. This is correctly represented by the modelled values in Figure 5-24. Raw accelerometer values scaled and biased according to Bettadpur (2004a) however are still all positive, i.e. they suggest that the satellite is being drawn towards the Earth by the ERP acceleration, which is clearly incorrect. To overlay the data for comparison purposes, an additional and relatively large bias of 1.743E-8ms^{-2} had to be added to the original ACC1B Z bias of 5E-7ms^{-2}. Note that the published scale and bias terms are only officially applicable until November 1, 2003 (Bettadpur, 2004a) and that these values should be determined during gravity estimation.

5.7. Antenna Thrust - ASAR Power Output

ENVISAT's ASAR antenna outputs a signal at a nominal pulse repetition frequency (PRF) of 1800 Hz (McLeod, 1998), where the power is dependent upon its mode of operation. The near-constant emission of such a signal will cause a recoil force on the satellite acting along the negative direction of the ASAR array normal. Owing to the side looking nature of the array, it will result in an acceleration which can be decomposed into the radial and across track directions with respect to the orbital plane. The magnitude of the force can be determined from the following (c.f. Eqn. (5.8)):

$$F = \frac{P}{c} \tag{5.16}$$

where F is force, P is power, and c the velocity which in this case is equal to the speed of light in a vacuum (Young & Freedman, 2000).

The power output of ENVISAT's ASAR array has a minimum value (Low Rate Background Regional Mission (LR BRM)) which never falls below 645W and can be as high as 1365W during a high rate mission (Torres et al., 1999). High rate missions do follow a schedule but can also be requested by users. Although it is possible to access further information on the operation mode of the array[21] as well as any periods of unavailability[22], this data is not provided in a format particularly useful for orbit prediction / determination (G. Scarpino - ESA Earth Observation Missions Helpdesk Team, pers comm.). For these reasons, an average signal power value of 1000W has been used in the current study, which results in a force of c.3.3×10^{-6}N and an acceleration with constant magnitude of c.4.1×10^{-10}ms^{-2}. Figure 5-25 shows the resultant accelerations over the course of one orbit.

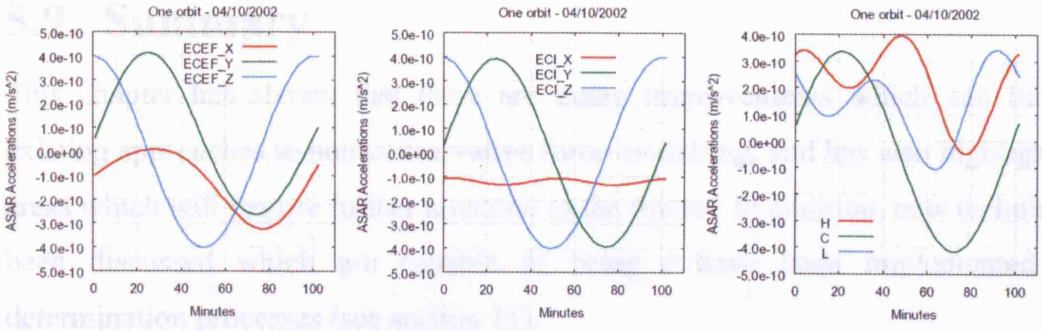

Figure 5-25: ENVISAT ASAR antenna induced accelerations over one orbit.

[21] http://earth.esa.int/services/catalogues.html

[22] http://envisat.esa.int/instruments/availability/

5.8. Mass Scaling

The UCL_SRP software computes the accelerations for when the spacecraft is at 1 astronomical unit (AU) from the Sun using a nominal mass, which for ENVISAT was chosen arbitrarily at an early point in its on-orbit lifespan to be 8040.8Kg. When the model is used in a precise orbit determination process, the output is scaled by $(1AU/ps)^2$, where ps is the actual probe-Sun distance at the epoch of the model call. Due to the effects of the perturbing forces under discussion here the semi-major axis of ENVISAT's orbit requires adjustment every 30-40 days. This is performed via an in-plane Stellar Fine Control Manoeuvre (SFCM), in which the thrusters fire along the velocity direction and use $\approx$ 0.1Kg of fuel. Approximately three times per year a more significant adjustment to the orbit occurs in order to alter its inclination using an out-of-plane Orbit Control Manoeuvre (OCM), where thrusters fire roughly perpendicular to the orbit plane and use $\approx$ 6-7 Kg of fuel[23].

Section 5.5.5 has already stated that the masses of ENVISAT are a publicly available resource, and from the beginning of life to 07/01/2005, this data shows that ENVISAT's mass decreased from 8106.4 to 8010.4Kg, which is only a change in total mass of c.1%. The departure from the nominal mass used to compute the model is much smaller, and is not likely to be significant. However, because a modelling accuracy of <1% has already been achieved by the UCL group for the JASON satellite (Haines et al., 2004), and due to a desire to be physically accurate, this study rescales all SRP and TRR accelerations to the stated mass for that epoch.

5.9. Summary

This chapter has shown that there are many improvements which can be made to existing approaches to non-conservative force modelling, and has also highlighted some areas which will require further attention in the future. In addition, new techniques have been discussed which are capable of being / have been implemented in orbit determination processes (see section 11).

[23] http://envisat.esa.int/instruments/availability/_manoeuvre.html, 08/06/2004

6. Block Modelling

High precision non-conservative force models have previously been computed only for satellites consisting of only 100-200 structural components, which are relatively simple when compared to ENVISAT. This chapter outlines a discretisation technique which allows existing algorithms to be extended to spacecraft one order of magnitude larger and more complex than previously attempted.

6.1. Why Block Modelling?

With a marked increase in the power of desktop computers, it is now possible to adopt an approach to modelling satellite geometry which retains almost all of the necessary information of the as-built structure. This represents a significant improvement over much simpler methods still in use today, often referred to as macro- or box-and-wing models. A Centre National d'Etudes Spatiales (CNES) macromodel (Restitution d'Orbites Department, CNES, 2002) appears typical of this type, and hopes to model ENVISAT's extremely complicated structure with a 6 panel bus (or 6+2 when explicitly taking the ASAR array into account) and a separate solar array. Alternative approaches have attempted to represent spacecraft structures by resolving the surface into a number of triangular facets (e.g. Marquis & Krier, 2000 and Koppenwallner et. al., 1995). The ability of this triangular facet method to model the geometry will of course depend upon the structural complexity of the satellite and, for a satellite as complex as ENVISAT, a very large number of facets would be required in order to faithfully represent the geometry. This can make the resultant model unwieldy in computational terms. A reduction in the number of facets may mean that subtle effects of geometric detail are not fully reproduced, and this can lead to a reduction in the accuracy of the resultant model. For a structure like ENVISAT, an overly simplistic approach may lead to unexpected and undesirable results. The approach adopted here follows Ziebart (2001a) in using a series of geometric primitives (see Section 7.1) to represent structural elements such as parabolic radio antennas and other scientific instruments. Ziebart's software, here referred to as UCL_SRP, was made available to this project at the source code level.

Historically, it is likely that model simplification occurred mainly because of the computational resources required to assess the effect of a vast number of photons or atmospheric particles striking a large number of components, and not simply because the modelling is conceptually difficult. However, with ENVISAT, we are still faced with computational resource issues owing to its oversized dimension. The ENVISAT bus model produced at UCL from the data set provided by Astrium still has 1059 of these primitive components, and the solar array adds another 73. Prior to this study, the largest computation using the UCL_SRP software was for GPS-IIR satellites which uses only 182 individual components, and has a smaller frontal surface area (8m x 8m). By virtue of the software's original design, the pixel array is square; for the ENVISAT bus at *one* EPS angle, including the ASAR antenna, this gives a maximum pixel array size of 10.2m x 10.2m. At a pixel resolution of 5mm, that results in more than 4.15 million pixels. If each pixel is tested at least once against each component, this means 1059 x 4,150,000 = c.4.4 billion calculations. Many multiples of this would be required to compute a complete model, though the number of calculations will be less for some EPS angles as the profile the satellite presents to the array changes. By way of comparison, GPS-IIR requires a maximum of only 2.5 million pixels with a 5mm resolution, equating to c.450 million calculations (182 x 2,500,000) for a single EPS angle. A complete 5mm / 5° GPS-IIR model still took c.10 days to perform on an AMD Athlon 1800 processor desktop PC. To make computing an ENVISAT model a viable proposition, a way was sought to speed up this testing process. The approach adopted builds two additional models around the existing precise geometry which shall be known here as the block and überblock models of the spacecraft. These extra models are constructed in a pre-processor step which still only takes a few seconds to complete, so as not to interfere with the running of the main function of the software. The block model is composed of cuboids which are best fitted to discrete sections of the spacecraft defined as component groups; a complete block model will include all of the precise spacecraft components. Block modelling procedures are extensively documented in the remaining sections of this chapter, but an overview of the block model testing process is outlined below (see Figure 6-1):

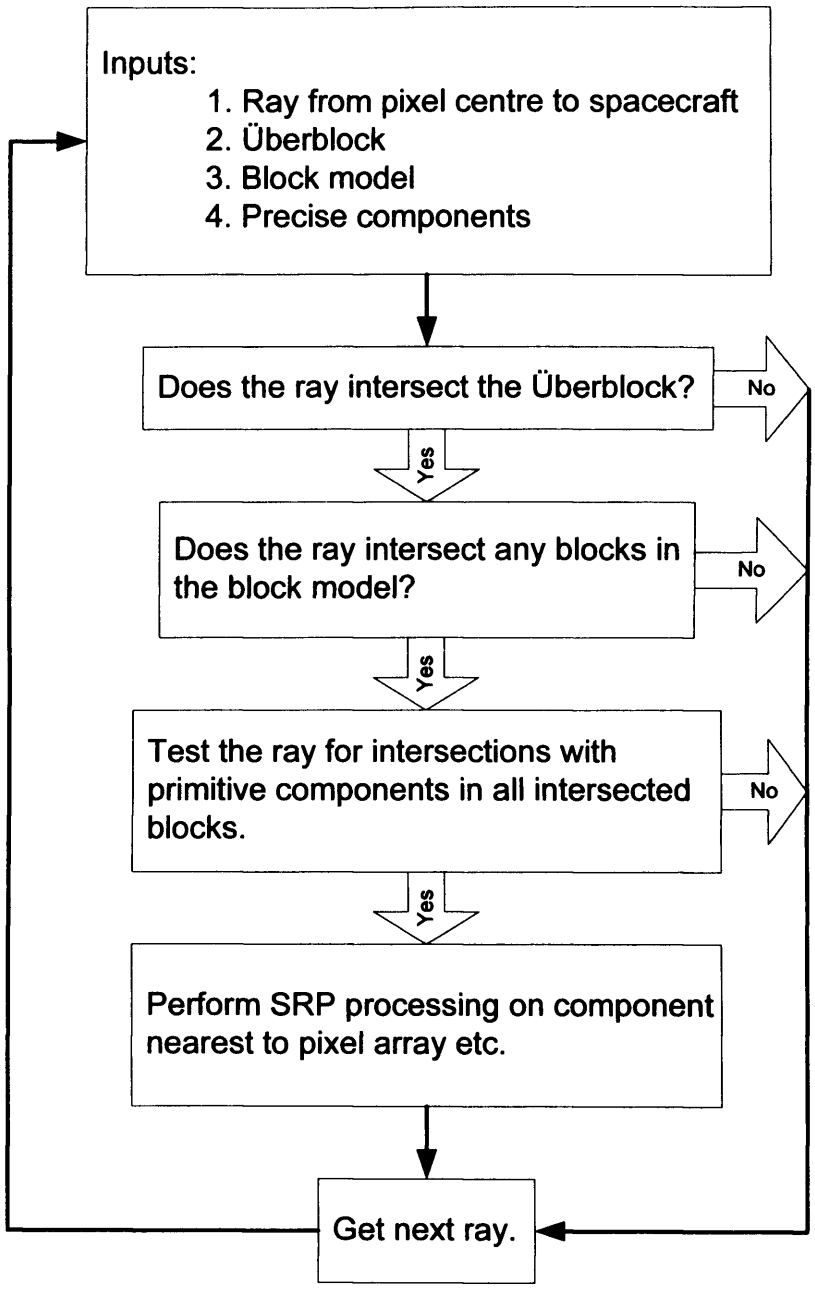

Figure 6-1: Block Modelling Process Flowchart.

The überblock model consists of a single cuboid best fitted to the block model, whose surface area is a minimum and which contains completely all facets of the block model. In the case of ENVISAT, this very simple first überblock test may not eliminate many unnecessary calculations at certain attitudes of the satellite relative to the pixel array owing to it having an almost square bounding box, so most pixels will intersect with the überblock:

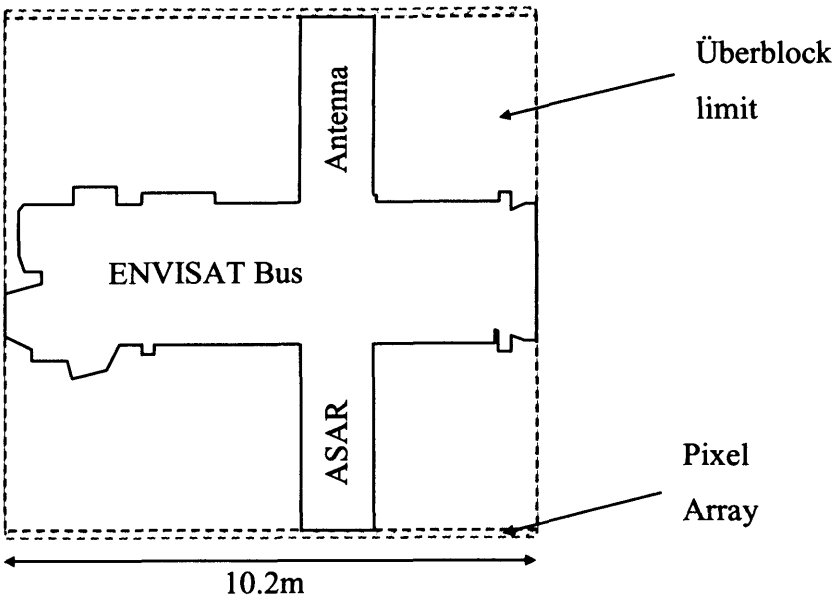

Figure 6-2: Unused pixels shown against the maximum possible ENVISAT bus surface area

In the case of satellites with non-square bounding boxes such as GPS-IIR, the überblock model will present a significant saving. However, the block model *will* have a deep impact on the number of computations that need to be performed for ENVISAT, and this can be seen by the amount of 'dead-space' (shown as a dotted area in Figure 6-2 above). The ENVISAT userfile contains a total of 16 component groups, meaning that a rapid ray-in-box algorithm (see Section 6.2.4 below) need only check the pixels in the 'dead-space' for intersections against 16 boxes, rather than against the full 1059 components contained within the precise model. As the ray-in-box test is a relatively simple procedure to implement, the boxes form a hierarchical testing structure. This form of testing is the basis of collision detection in a lot of modern computer games software (Barequet & Sariel, 2001). This block modelling technique reduced the computation time for a 5mm / 5° GPS-IIR model from c.10 days to just 15 hours on the PC mentioned above.

6.2. Block Creation

Individual elements of the spacecraft model may be arbitrarily oriented with respect to the absolute spacecraft reference frame (Body Fixed System – BFS), making it difficult to directly compute a bounding box. A very basic algorithm for fitting a box to a group of components may therefore consist of only the following statement:

"Create a local object coordinate system (OCS) having one axis aligned with the longest distance between any two nodes of the object and calculate the minimum and maximum X,Y,Z object coordinates in this new frame"

Note that this does not account for the fact that a rotation around this "longest dimension" axis may reduce the volume of the box depending upon how the object lies in the directions of the remaining axes (see Section 6.2.3 for more on this). Nor does it explicitly specify the transformation (a translation and series of rotations) from BFS to OCS. Such a transformation would need to be applied to the coordinates of a ray or particle if we hope to understand how it interacts with the bounding box in the local frame.

An efficient implementation of the algorithm described below should hold the translation and rotation matrices in RAM along with the min/max XYZ block coordinates in the OCS. Vectors representing light rays for SRP modelling and positions of particles for atmospheric drag modelling are thus easily transformed using the available matrices and can then be tested against the already available transformed box coordinates, making each test very fast. In UCL_SRP, each particle is processed sequentially, and only proceeds to the next level in the überblock-block-precise test hierarchy if an intersection is generated at the previous level. The procedure used to generate the rotation matrices required to align the BFS and OCS frames is outlined in Section 6.2.1; defining an OCS for the different types of geometric primitives is discussed further in Section 6.2.2.

6.2.1. Transformations

If two sets of coordinate axes (e.g. $\bar{x},\bar{y},\bar{z}$ and $\bar{p},\bar{q},\bar{r}$) share a common origin but one system is rotated with respect to the other, then a single rotation about a fixed axis will bring the two systems into alignment, where all points on this fixed axis remain unaffected by the rotation. This is Euler's fundamental theorem on rigid body rotation (Battin, 1999).

If $\bar{v}$ is any vector in the $\bar{x},\bar{y},\bar{z}$ system, then we can define angles α,β,γ which are the angles between $\bar{v}$ and the $\bar{x},\bar{y},\bar{z}$ axes respectively (see Figure 6-3, which shows an arbitrary vector $\bar{v}$ and its relationship to $\bar{x},\bar{y},\bar{z}$).

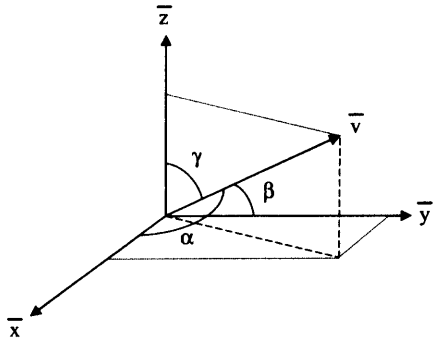

Figure 6-3: Direction cosines

If we define unit vectors along $\bar{x},\bar{y},\bar{z}$ as $i_{\bar{x}},i_{\bar{y}},i_{\bar{z}}$, then we can describe $\bar{v}$ in terms of these unit vectors:

$$\bar{v} = xi_{\bar{x}} + yi_{\bar{y}} + zi_{\bar{z}} \tag{6.1}$$

Clearly, the scalar components are given by:

$$\begin{aligned} x &= v\cos\alpha \\ y &= v\cos\beta \\ z &= v\cos\gamma \end{aligned} \tag{6.2}$$

Unit $\bar{v}$ will then be:

$$i_{\bar{v}} = \cos\alpha i_{\bar{x}} + \cos\beta i_{\bar{y}} + \cos\gamma i_{\bar{z}} \tag{6.3}$$

The scalar terms in $i_{\bar{v}}$, known as direction cosines, are normally defined as $l = \cos\alpha$, $m = \cos\beta$ and $n = \cos\gamma$ to give:

$$i_{\bar{v}} = li_{\bar{x}} + mi_{\bar{y}} + ni_{\bar{z}} \tag{6.4}$$

This can be extended to define a second frame, whose axes $\bar{p},\bar{q},\bar{r}$ can also be treated as vectors in terms of their positions with respect to $\bar{x},\bar{y},\bar{z}$:

$$\begin{aligned} i_{\bar{p}} &= l_1 i_{\bar{x}} + m_1 i_{\bar{y}} + n_1 i_{\bar{z}} \\ i_{\bar{q}} &= l_2 i_{\bar{x}} + m_2 i_{\bar{y}} + n_2 i_{\bar{z}} \\ i_{\bar{r}} &= l_3 i_{\bar{x}} + m_3 i_{\bar{y}} + n_3 i_{\bar{z}} \end{aligned} \tag{6.5}$$

Our arbitrary vector $\bar{v}$ can be expressed in terms of projections along the axes of the two different frames, and the descriptions will be equivalent:

$$\bar{v} = x\bar{i}_{\bar{x}} + y\bar{i}_{\bar{y}} + z\bar{i}_{\bar{z}} = p\bar{i}_{\bar{p}} + q\bar{i}_{\bar{q}} + r\bar{i}_{\bar{r}} \tag{6.6}$$

We can then expand the above identity using (6.5):

$$\begin{aligned}\bar{v} = x\bar{i}_{\bar{x}} + y\bar{i}_{\bar{y}} + z\bar{i}_{\bar{z}} = p\left[l_1\bar{i}_{\bar{x}} + m_1\bar{i}_{\bar{y}} + n_1\bar{i}_{\bar{z}}\right] + \\ q\left[l_2\bar{i}_{\bar{x}} + m_2\bar{i}_{\bar{y}} + n_2\bar{i}_{\bar{z}}\right] + \\ r\left[l_3\bar{i}_{\bar{x}} + m_3\bar{i}_{\bar{y}} + n_3\bar{i}_{\bar{z}}\right]\end{aligned} \tag{6.7}$$

Expanding further and grouping like terms gives:

$$\begin{aligned}\bar{v} = x\bar{i}_{\bar{x}} + y\bar{i}_{\bar{y}} + z\bar{i}_{\bar{z}} = \left(pl_1 + ql_2 + rl_3\right)\bar{i}_{\bar{x}} + \\ \left(pm_1 + qm_2 + rm_3\right)\bar{i}_{\bar{y}} + \\ \left(pn_1 + qn_2 + rn_3\right)\bar{i}_{\bar{z}}\end{aligned} \tag{6.8}$$

Equating like with like:

$$\begin{aligned}x &= \left(pl_1 + ql_2 + rl_3\right) \\ y &= \left(pm_1 + qm_2 + rm_3\right) \\ z &= \left(pn_1 + qn_2 + rn_3\right)\end{aligned} \tag{6.9}$$

This can be rearranged into matrix form:

$$\begin{bmatrix}x\\y\\z\end{bmatrix} = \begin{bmatrix}l_1 & l_2 & l_3\\ m_1 & m_2 & m_3\\ n_1 & n_2 & n_3\end{bmatrix}\begin{bmatrix}p\\q\\r\end{bmatrix} = \bar{R}.\begin{bmatrix}p\\q\\r\end{bmatrix} \tag{6.10}$$

where the rotation matrix $\bar{R}$ is given by:

$$\bar{R} = \begin{bmatrix}i_x.i_p & i_x.i_q & i_x.i_r\\ i_y.i_p & i_y.i_q & i_y.i_r\\ i_z.i_p & i_z.i_q & i_z.i_r\end{bmatrix} \tag{6.11}$$

The reverse operation, the rotation from $\bar{x},\bar{y},\bar{z}$ to $\bar{p},\bar{q},\bar{r}$ can be obtained with the transpose of $\bar{R}$:

$$\begin{bmatrix} p \\ q \\ r \end{bmatrix} = \begin{bmatrix} l_1 & m_1 & n_1 \\ l_2 & m_2 & n_2 \\ l_3 & m_3 & n_3 \end{bmatrix} \begin{bmatrix} x \\ y \\ z \end{bmatrix} = \bar{R}^T . \begin{bmatrix} x \\ y \\ z \end{bmatrix} \tag{6.12}$$

The rotation matrix becomes even simpler if $\bar{x}, \bar{y}, \bar{z}$ is defined with an origin at (0,0,0) and the following unit axes:

$$\begin{aligned} i_{\bar{x}} &= (1,0,0) \\ i_{\bar{y}} &= (0,1,0) \\ i_{\bar{z}} &= (0,0,1) \end{aligned} \tag{6.13}$$

Then:

$$\bar{R} = \begin{bmatrix} x_{i_{\bar{p}}} & x_{i_{\bar{q}}} & x_{i_{\bar{r}}} \\ y_{i_{\bar{p}}} & y_{i_{\bar{q}}} & y_{i_{\bar{r}}} \\ z_{i_{\bar{p}}} & z_{i_{\bar{q}}} & z_{i_{\bar{r}}} \end{bmatrix} \tag{6.14}$$

The values are simply the direction cosines of the second frame relative to the reference frame. Now, we are in a position to be able to easily transform points from one coordinate system to another (i.e. OCS to BFS).

6.2.2. Low-Level Block Creation

It is of course important that any algorithm is robust, and can cope with component groups containing a wide range of different primitives. Circles and rings can be ignored for block modelling purposes because, at present, they are always associated with a panel or primitive component (e.g. end cap for a cylinder) when used in UCL_SRP, and do not actually alter the extents of the underlying panel or primitive component. For all other elements, excluding polygons, a box is first fitted locally to the primitive using the following method (the natural extension of this procedure to groups of primitives is detailed in section 6.2.3):

A vector $\bar{y}'$, defined as running from the object's first end-point to the second end-point, is a good choice for a local axis because it is an axis of rotational symmetry for these primitives. If $\bar{v}_1$ is the vector to the first end-point and $\bar{v}_2$ is the vector to the second end-point, then:

$$\bar{y}' = \bar{v}_2 - \bar{v}_1 \tag{6.15}$$

A further two vectors can be thought of as completing the local axis triad. They are calculated in the following ways (where a 'hat' denotes a unit vector):

When $\overline{y}'$ lies along one of the reference frame axes $(\overline{x},\overline{y},\overline{z})$, then the following outlines a quick procedure to assign $\overline{x}'$ and $\overline{z}'$ for cones, cylinders, paraboloids etc., where *radius* is the radius of the component (the largest radius in the case of a truncated cone); see Figure 6-4 for a graphical representation of this.

If $\hat{y}' = \hat{x}$:

$$\overline{x}' = \begin{bmatrix} 0 \\ radius \\ 0 \end{bmatrix} \tag{6.16}$$

$$\overline{z}' = \begin{bmatrix} 0 \\ 0 \\ -radius \end{bmatrix} \tag{6.17}$$

If $\hat{y}' = \hat{y}$:

$$\overline{x}' = \begin{bmatrix} radius \\ 0 \\ 0 \end{bmatrix} \tag{6.18}$$

$$\overline{z}' = \begin{bmatrix} 0 \\ 0 \\ radius \end{bmatrix} \tag{6.19}$$

If $\hat{y}' = \hat{z}$:

$$\overline{x}' = \begin{bmatrix} radius \\ 0 \\ 0 \end{bmatrix} \tag{6.20}$$

$$\overline{z}' = \begin{bmatrix} 0 \\ -radius \\ 0 \end{bmatrix} \tag{6.21}$$

Otherwise:

$$\overline{x}' = \overline{z} \times \overline{y}' \tag{6.22}$$

$$\overline{z}' = \overline{x} \times \overline{y}' \tag{6.23}$$

In this case, the $\bar{x}'$ and $\bar{z}'$ vectors must now be normalised and multiplied by the component's radius:

$$\bar{x}' = radius * \hat{x}' \tag{6.24}$$

$$\bar{z}' = radius * \hat{z}' \tag{6.25}$$

For example, in the case of a cylinder:

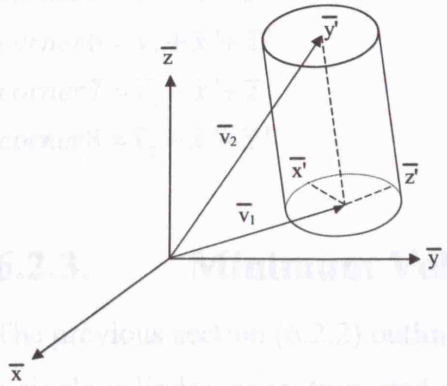

Figure 6-4: Cylinder local coordinate system

The corners of the best fitting box can now be calculated using simple vector addition and subtraction (see Figure 6-5):

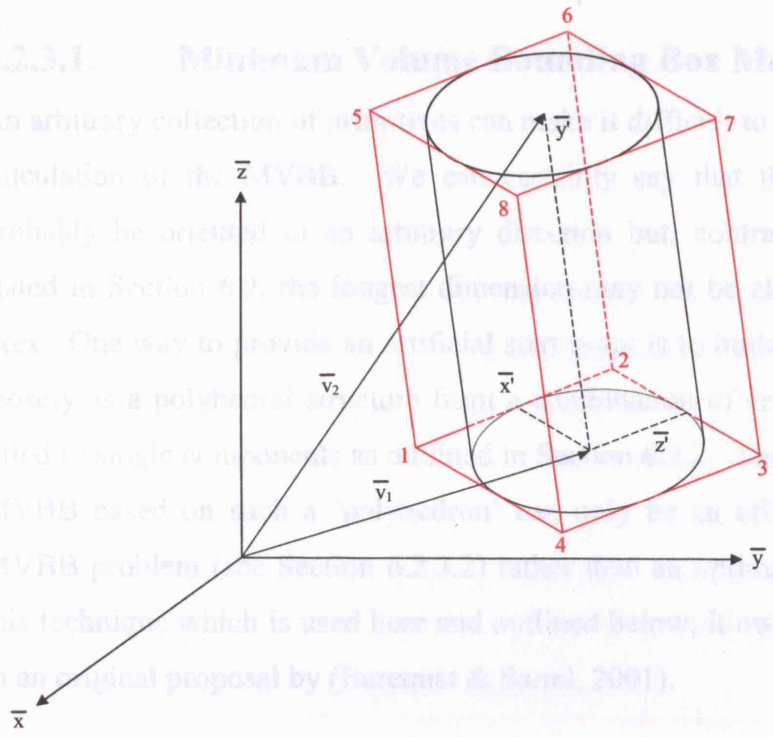

Figure 6-5: Fitting a box to a cylinder

where:

$$
\begin{aligned}
corner1 &= \overline{v}_1 + \overline{x}' - \overline{z}' \\
corner2 &= \overline{v}_1 + \overline{x}' + \overline{z}' \\
corner3 &= \overline{v}_1 - \overline{x}' + \overline{z}' \\
corner4 &= \overline{v}_1 - \overline{x}' - \overline{z}' \\
corner5 &= \overline{v}_2 + \overline{x}' - \overline{z}' \\
corner6 &= \overline{v}_2 + \overline{x}' + \overline{z}' \\
corner7 &= \overline{v}_2 - \overline{x}' + \overline{z}' \\
corner8 &= \overline{v}_2 - \overline{x}' - \overline{z}'
\end{aligned}
\tag{6.26}
$$

6.2.3. Minimum Volume Bounding Box (MVBB)

The previous section (6.2.2) outlined the method used to create a best fitting box around a single cylinder, cone, truncated cone or paraboloid. However, it is very unlikely, and also inefficient, to simply fit a box to a single primitive. The reason for this procedure becomes clear if we regard it as an intermediate step in the process of defining a minimum volume bounding box (MVBB) for a collection of primitives which contain polygonal and non-polygonal elements.

6.2.3.1. Minimum Volume Bounding Box Method

An arbitrary collection of primitives can make it difficult to define the start point for the calculation of the MVBB. We can certainly say that the resulting box will most probably be oriented in an arbitrary direction but, contrary to the simple algorithm stated in Section 6.2, the longest dimension may not be aligned with one of the OCS axes. One way to provide an artificial start point is to build what can be regarded very loosely as a polyhedral structure from a combination of original polygons, and blocks fitted to single components as outlined in Section 6.2.2. This does however mean that a MVBB based on such a 'polyhedron' can only be an efficient approximation to the MVBB problem (see Section 6.2.3.2) rather than an optimal volume solution, yet it is this technique which is used here and outlined below; it owes something of its creation to an original proposal by (Barequet & Sariel, 2001).

The blocks output by the Low-Level Block Creation can be interpreted as 6 polygonal faces, and are added to any polygons in the original component group, the result is a set containing only polygons. One edge of each polygon in the set is then arbitrarily chosen

as a baseline, and using another vertex of this polygon, three mutually orthogonal unit vectors are established which can be used to form a local coordinate system:

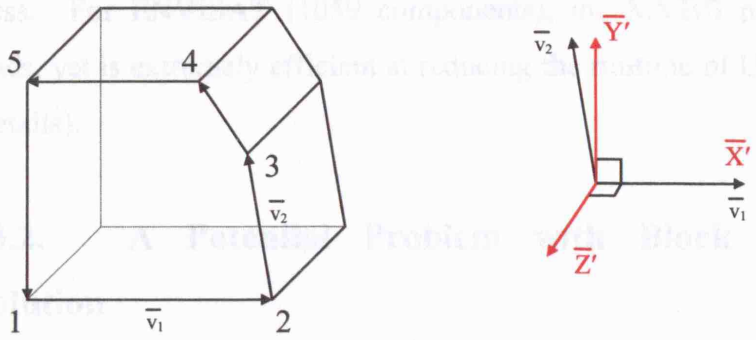

Figure 6-6: MVBB

A copy of this polygon set is created, and the coordinates of the point at the beginning of the baseline are used to transform the entire system to the origin. Then, the three unit vectors are used to rotate the coordinates of every polygon in the set (see Section 6.2.1) so that the OCS is brought into alignment with the reference frame. It is then a simple matter to scroll through all these coordinates checking for minimum and maximum X,Y and Z values. When these are found, the volume of the resulting bounding box is found from:

$$(\text{maxX}-\text{minX})*(\text{maxY}-\text{minY})*(\text{maxZ}-\text{minZ}) \tag{6.27}$$

This result is stored, along with the minimum and maximum X,Y and Z values, and the translation and rotation parameters. Immediately prior to storage, 1mm is subtracted from each of the min values, and 1mm is added to each of the max values in order to avoid problems with numerical rounding when calculating intersections – if this is not done, then a ray or particle may be thought to not intersect a component when in fact it does so but with grazing incidence. Each other polygon is then given the opportunity to have one of its edges be the baseline, and the one generating the minimum volume overall is chosen as the basis for the block model. This is a simple matter which follows Equation (6.26) very closely, and is not explicitly given again here.

6.2.3.1.1. A Brief Note About Coding

As different satellites will require different numbers of component groups, the software was made generic by allowing the memory for the individual block information to be

allocated dynamically at run time. The arrays created use Standard Template Library (STL) lists, which are optimised for fast access in an attempt to speed up the testing process. For ENVISAT (1059 components), the MVBB process takes less than 5 seconds, yet is extremely efficient at reducing the runtime of UCL_SRP (see section 6.1 for details).

6.2.3.2. A Potential Problem with Block Modelling and its Resolution

However, the approach given in Section 6.2.3.1 can still be problematic, as the following simple example of fitting a MVBB to a box created from several polygons and a cylinder shows. Figure 6-7 shows a planimetric view of this possible configuration, looking at the XY plane with the cylinder sitting atop the box. The ideal situation is shown in the left image, where the cylinder's bounding box is aligned with that of the polygonal box. The procedure described in Section 6.2.2 above will actually create the situation shown in the right hand pane, where the cylinder's box is aligned with the reference frame owing to $\overline{y}'$ and $\overline{z}$ being parallel. Although this shows that an optimally placed MVBB is not always produced using the method adopted here, the effort required to resolve such issues, especially when we begin to consider more complex groupings of different primitives, probably outweighs both the effort required to implement the solution, and to compute it (O'Rourke, 1985).

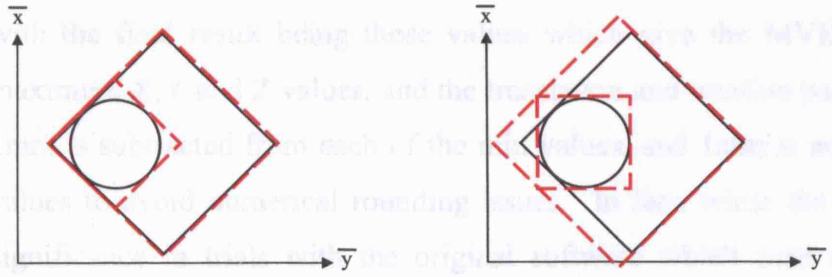

Figure 6-7: Problems with MVBB

6.2.3.3. Überblock Modelling

The überblock modelling approach is similar to the above but differs in that its base 'polyhedron' is created directly from the combined output of the earlier block modelling procedure for all component groups instead of using the original primitive components.

Although this has the possibility of slightly increasing the size of the best fitting box overall, it has significant benefits in terms of performance. The number of points is dramatically reduced and the local coordinate system is easily defined.

According to Figure 6-8, corner 1 of each block in turn is considered as a potential false origin, and its vector is subtracted from all other points. The appropriate choice of vectors to box corners makes it a simple matter to form the local coordinate system, with the 2nd, 5th and 4th points of each box being chosen as pointing along the $\bar{x}', \bar{y}', \bar{z}'$ axes respectively.

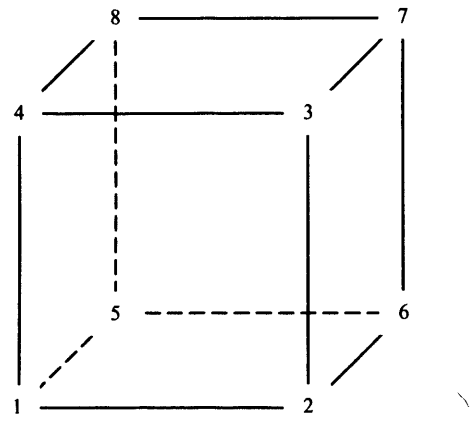

Figure 6-8: Block Corner Numbering Conventions

Again, the minimum and maximum X,Y and Z values are calculated in the OCS frame, with the final result being those values which give the MVBB. The minimum and maximum X,Y and Z values, and the translation and rotation parameters are stored after 1mm is subtracted from each of the min values, and 1mm is added to each of the max values to avoid numerical rounding issues. In fact, while the überblock was of great significance in trials with the original software which used a square pixel array, it became somewhat redundant after a rectangular pixel array technique was implemented. Normal block modelling however remains a very valuable procedure.

6.2.4. Ray-in-Box Test Procedure

Figure 6-1 shows that an initial test checks to see whether any rays or particles intersect with or lie inside the überblock, if no rays or particles do then it is evident that nothing can have struck the spacecraft. Those particles which do intercept the überblock are

then tested against the more detailed block model. Again, if no particles strike any of the blocks, then the satellite is not hit at all. Those that do strike any blocks are then tested against the precise geometry of only those components *which lie inside those blocks*. This dramatically reduces the number of tests which need to be made, thus increasing the computational efficiency of the software; as long as on average each block is fitted to more than 6 precise components, because each box will have 6 polygonal faces! For this reason, the software has been modified so that a user can choose whether or not to use the block modelling procedure, and can turn it off if the disadvantages outweigh the benefits (reliance placed here upon user experience).

A rapid algorithm used to determine whether any rays or particles lie inside the überblock or individual component group blocks, referred to here as the ray-in-box test, differs from the point-in-polygon test (Taylor, 1994) used by Ziebart (2001b) to determine the intersections of pixel rays with generic n-sided polygons. This fast browsing procedure is outlined below:

Light rays within the UCL_SRP software are represented by two points (moving from $\overline{p}_1$ to $\overline{p}_2$) along their trajectory. This provides us with all the information that we need for a unique solution to move along the line in any direction and at any distance. $\overline{p}_1$ can be thought of as taking us to the line, and a scalar (k) multiple of a normalised $\overline{p_1 p_2}$ vector will take us along the line. As each block carries with it the information to transform one of its corners to the origin and to bring each of its edges parallel with the axes of the reference frame, we can easily apply this transformation to the vectors that describe the light ray or particle trajectory. The algorithm's speed is also increased by the fact that the transformed box is already described by a sequence of only six numbers stored in RAM, meaning that only the vectors defining the light ray need to be transformed. The six numbers which describe the box are the minimum and maximum X, Y and Z values in the transformed frame.

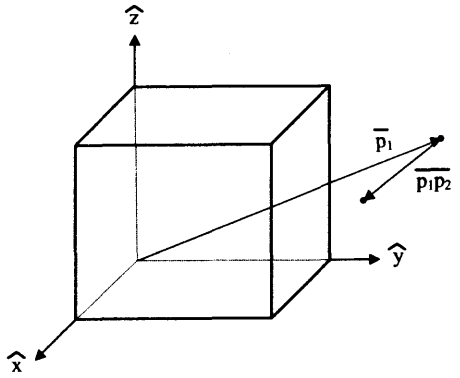

Figure 6-9: Ray-in-box intersection

We can then project the $\overline{p_1p_2}$ vector from $\overline{p}_1$ until it makes contact with the faces with those minimum and maximum X, Y and Z values in turn. As an example, the procedure for the minimum X face is given below:

$$p_1.x + k(p_1p_2.x) = \min X \tag{6.28}$$

Solving for k, gives:

$$k = (\min X - p_1.x) / p_1p_2.x \tag{6.29}$$

To get the intersection point ($\overline{IP}$) with the plane of constant minX:

$$\overline{IP} = \overline{p}_1 + k\left(\overline{p_1p_2}\right) \tag{6.30}$$

If and only if $\min Y \le IP.y \le \max Y$ and $\min Z \le IP.z \le \max Z$, then the ray passes through the box. If these conditions are not met then the same procedure is continued with the remaining faces, either stopping when the conditions are satisfied or proceeding through all the tests with no intersection point being found.

6.2.4.1. Resolution of a Potential Problem with Ray-in-Box Tests

It may appear that if $p_1p_2.x = 0$ (also for y and z when considering other faces), then a problem might arise as you would be dividing by zero when solving for k. However, a line passing through the box must intersect at least two faces, and can intersect a maximum of all six faces if passing through opposing corners of the box. Therefore, in the case of a 'divide by zero' (actually a test for $|p_1p_2.x|$<1E-15 due to round-off error

restrictions etc.), the test for that face should be stopped and the procedure continued against the other faces. Remember also that the box's size has already been increased by 1mm in each direction, so if any rays happen to strike the box with grazing incidence yet fail these tests, it is likely that they would not have struck the original and slightly smaller box anyway.

6.3. Summary

A simple technique has been outlined which dramatically reduces the computation time for the production of SRP and TRR models. It has been shown how this can be applied even when a spacecraft is described by a large number of geometric primitives and details several simple considerations which can be used to further improve efficiency. A graphical tool which helps to validate the success of the automated block modelling process, as well as offering many other useful innovations for the quality control of satellite models used in non-conservative force modelling, is outlined in section 7.

7. Managing Complexity

This chapter describes the development of a sophisticated generic software application for viewing and interrogating the geometric primitive descriptions of satellites produced at UCL during the course of this, and subsequent, non-conservative force modelling work. As more and more complicated satellites are considered, a tool such as this is vital to ensure the correct operation of embedded algorithms and also allows users to check the accuracy of their text based satellite descriptions before generating final force models, and proved central to the work conducted on ENVISAT. A brief description of how to use this software can be found in Appendix B.

7.1. Geometric Primitives

7.1.1. Primitive Definitions

The geometric primitives used in this study allow all components of the ENVISAT satellite to be modelled accurately. They include: convex and non-convex polygons, circles, rings, cones, truncated cones, parabolas with both inward and outward facing normals, spheres and cylinders.

The following figures (mostly reproduced from Ziebart, 2002) show these different primitives with all of the parameters which must be specified when creating a new component of each type:

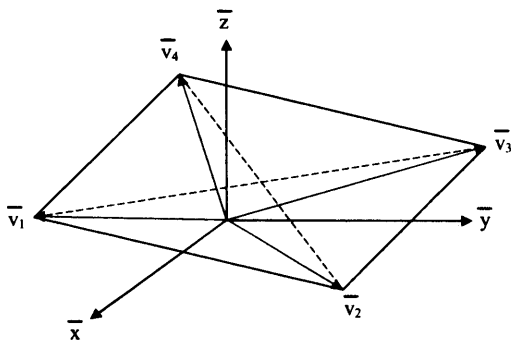

Figure 7-1: Polygonal component

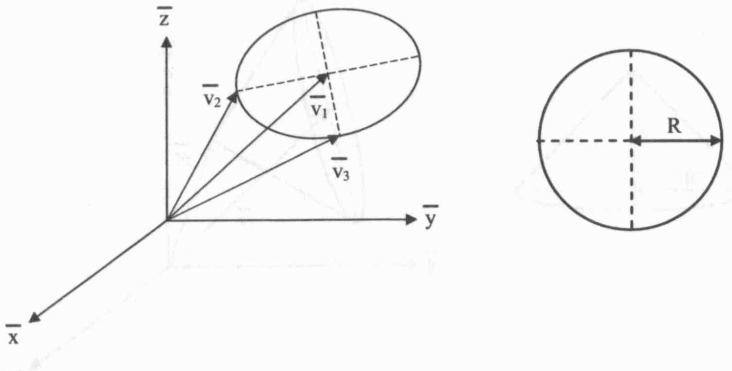

Figure 7-2: Circle component

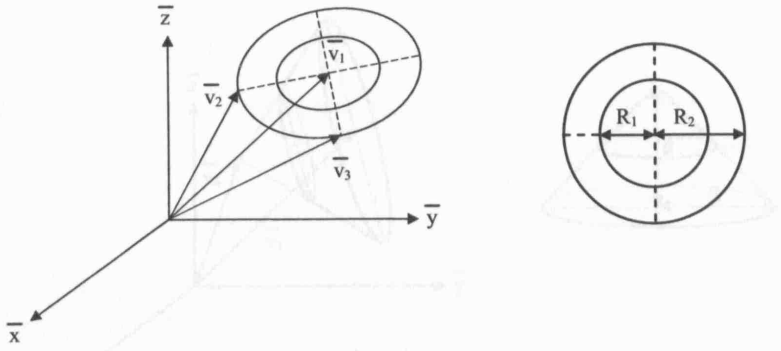

Figure 7-3: Ring component

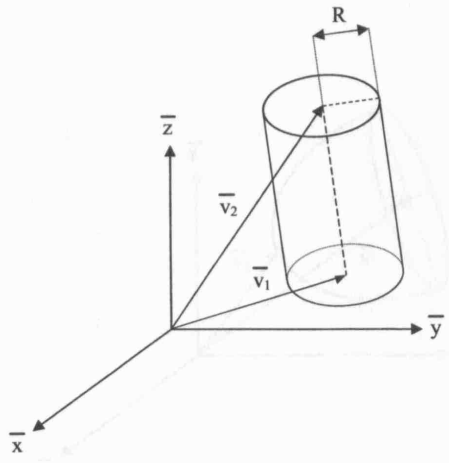

Figure 7-4: Cylinder component

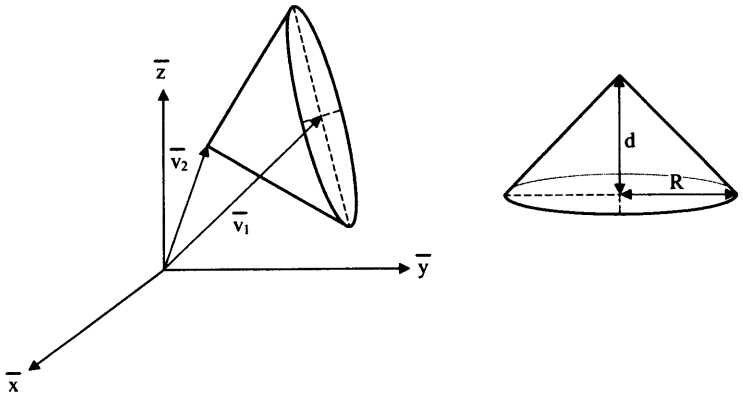

Figure 7-5: Cone component

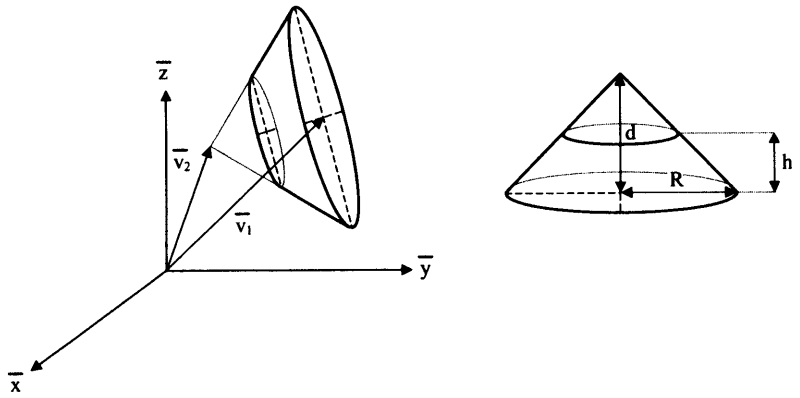

Figure 7-6: Truncated cone component

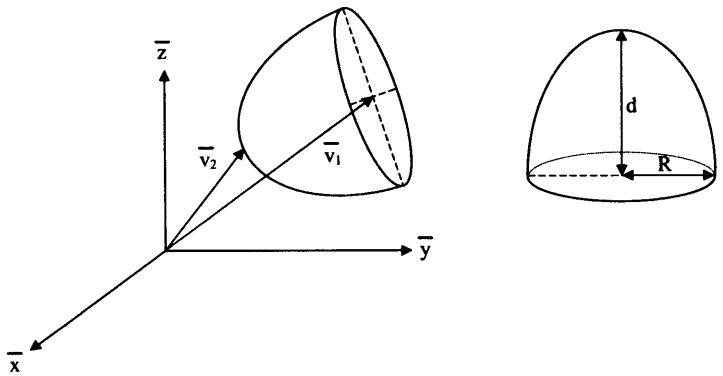

Figure 7-7: Paraboloid component

For polygonal components an additional parameter specifying the total number of vertices is required. Polygon, circle and ring surface vertices must be given according to the following winding rule: when looking along the surface normal towards the

component's active (i.e. outward facing) surface, the vertices should be numbered in an anti-clockwise order (see Figure 7-1 and Figure 7-8).

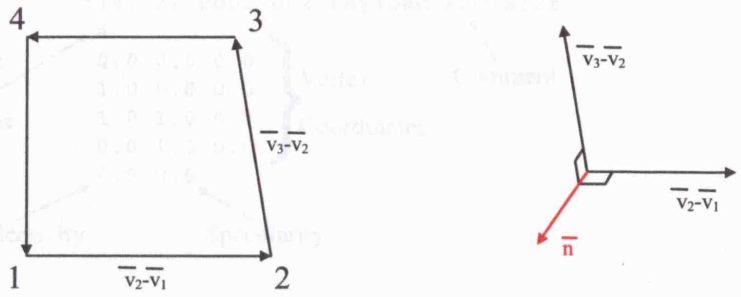

Figure 7-8: Surface normal generation

This requirement then provides a simple means for the surface normal to be computed by the software for these primitives:

$$\hat{n} = \frac{(\overline{v}_2 - \overline{v}_1) \times (\overline{v}_3 - \overline{v}_2)}{\left|(\overline{v}_2 - \overline{v}_1) \times (\overline{v}_3 - \overline{v}_2)\right|} \tag{7.1}$$

This is always valid unless dealing with a non-convex polygon where at least one internal angle is >180°.

The supporting document (Ziebart, 2002) which describes these primitives also includes textual examples of the definition of each type of primitive in the ASCII text format used by UCL_SRP. In order to perform the block modelling, an integer identifier was added to this file format to represent each component group. For example, a polygonal component might be described thus:

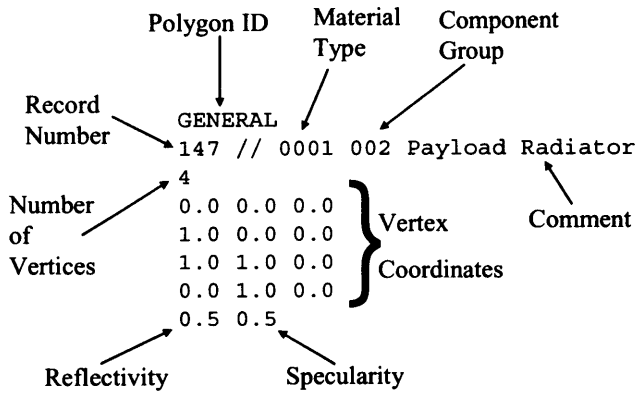

7.2. The Viewer

The viewer software was written using Microsoft's Visual C++ 6.0, and utilises the OpenGL Application Program Interface (API) (Wright & Sweet, 2000) for displaying the graphics shown below. The following sub-sections detail the application's functionality.

7.2.1. Initial Display

Open access to accurate structural and material property data can be very difficult to achieve as manufacturers, who spend millions of pounds designing and building satellites, obviously want to avoid handing over this sort of information to their competitors. The thermal engineering section of EADS Astrium (UK), a major partner in the manufacture of the ENVISAT satellite, generously offered this project a copy of their ENVISAT model (a neutral input file in .VIF format, for use with Astrium's proprietary Thermica software), along with accompanying text describing the exact file format. In order to be able to use this with UCL's non-conservative force modelling software, an initial step involved writing a conversion tool to transform the .VIF file to UCL's preferred format (see section 7.1.1). The converted file contained 2642 components, all of which required some form of validation. A decision was taken to develop a generic software application for viewing and interrogating the geometric primitive descriptions of satellites produced at UCL during the course of this, and subsequent, non-conservative force modelling work. It is important to state that the reason for covering this in some detail is because without this tool, it is likely that the results achieved by the research conducted during this thesis would not have been

possible. Figure 7-9 and Figure 7-10 show images of the converted EADS Astrium data prior to any cleaning.

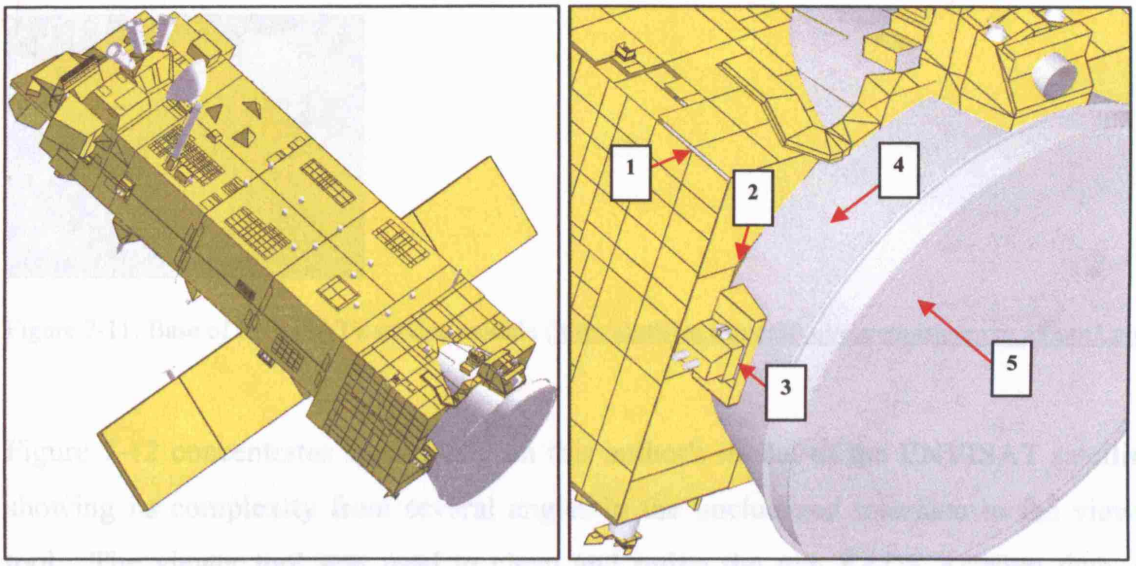

Figure 7-9: Left hand image shows raw converted EADS Astrium VIF data. Right hand image shows problems with imported data: numbered items 1-3 show gaps in the data, 4 & 5 highlight radiator data which has been completely omitted in the EADS Astrium data (see Figure 7-11 for a photograph of this section of the actual satellite). Graphics generated by the author's viewing tool.

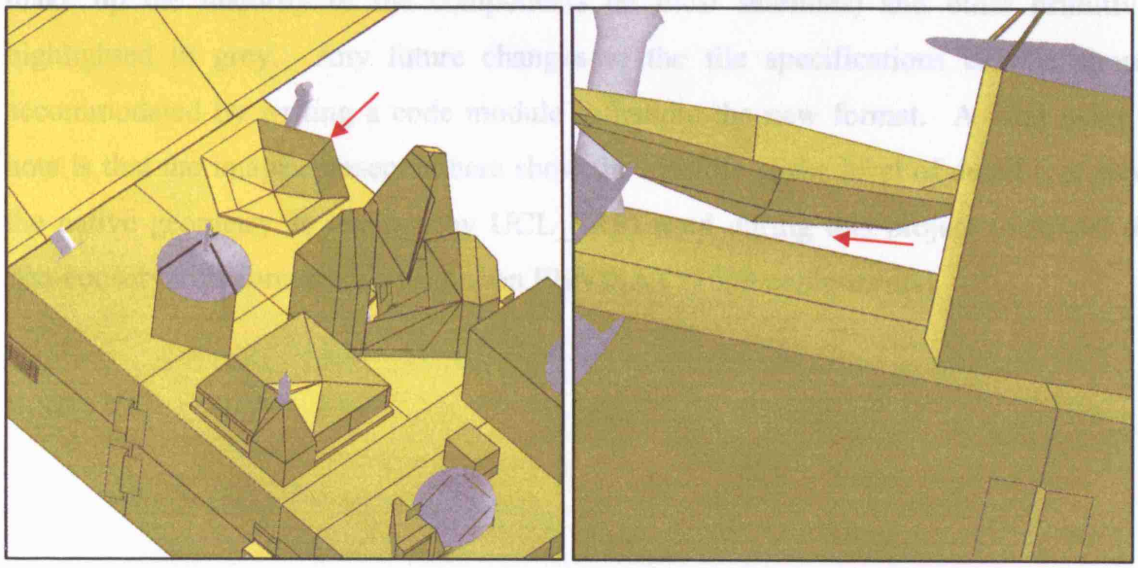

Figure 7-10: Left hand image shows raw converted EADS Astrium VIF representation (polygonal facets) of ENVISAT's RA2 antenna; the right hand image shows that it is missing a support for its base.

The left hand image of Figure 7-9 allows us to see that, due to thermal modelling requirements, many components of the EADS Astrium model are highly segmented, while the right hand image, and both images in Figure 7-10, show that there are

imperfections and important omissions in the data. As shown in Figure 7-11, there are actually some highly specular surfaces on the base of ENVISAT's service module, which are potentially very important for accurate NCF induced accelerations modelling.

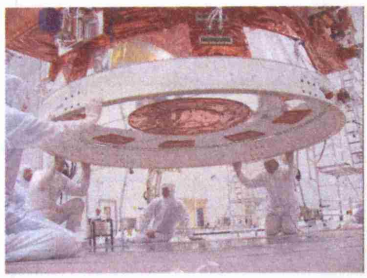

Figure 7-11: Base of ENVISAT's service module (http://dutlsisa.lr.tudelft.nl/sis/envisat/envi_album3.ppt).

Figure 7-12 concentrates specifically on this author's model of the ENVISAT satellite, showing its complexity from several angles in the uncluttered interface to the viewer tool. The viewer tool was used to clean and refine the raw EADS Astrium data, as evidenced by the smooth lines and non-segmented surface of the model displayed here. ASCII text descriptions of satellites (see section 7.1.1) can be opened directly using this tool, and are displayed on screen with polygonal components in yellow (these tend to make up the majority of the components on most satellites) and other primitives highlighted in grey. Any future changes to the file specifications can be simply accommodated by writing a code module to handle the new format. A vital point to note is that the images presented here show the satellite at the level of detail (i.e. show the native geometry as retained by UCL_SRP) used during this project to model the non-conservative forces which act upon ENVISAT (1059 components).

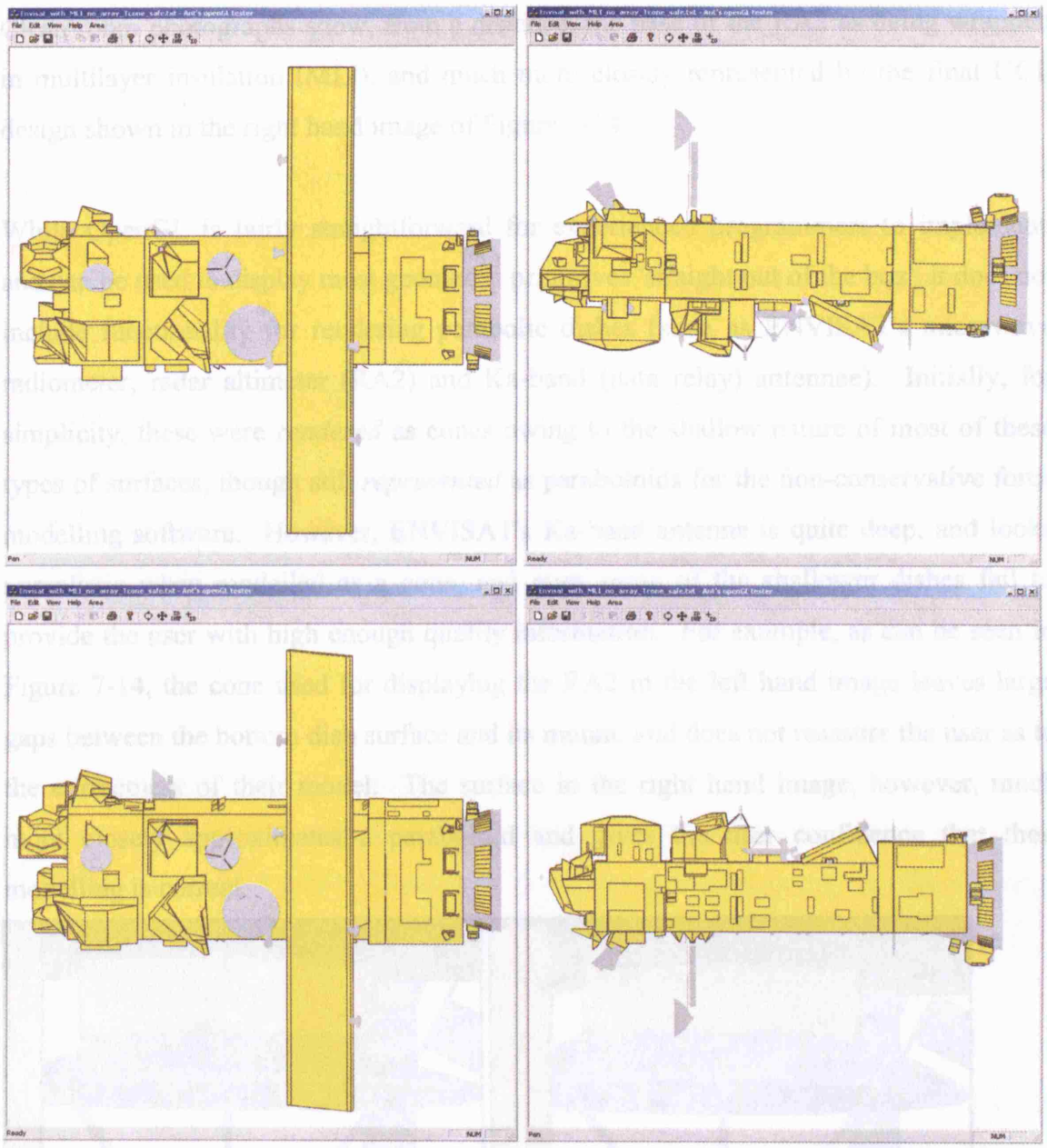

Figure 7-12: General views of the cleaned ENVISAT satellite model.

Figure 7-13 clearly demonstrates that ENVISAT's radar altimeter is a parabolic dish, rather than a series of polygonal facets as used in the Astrium dataset (Figure 7-10).

Figure 7-13: ENVISAT's RA2 antenna

(http://envisat.esa.int/instruments/tour-index/ra2/ra2_antenna.htm).

Clean room photographs show, from a distance, the base of the RA2 as being wrapped in multilayer insulation (MLI), and much more closely represented by the final UCL design shown in the right hand image of Figure 7-14.

While OpenGL is fairly straightforward for experienced programmers to implement, and can be used to display most geometric primitives 'straight out of the box', it does not include functionality for rendering parabolic dishes (such as ENVISAT's microwave radiometer, radar altimeter (RA2) and Ka-band (data relay) antennae). Initially, for simplicity, these were *rendered* as cones owing to the shallow nature of most of these types of surfaces, though still *represented* as paraboloids for the non-conservative force modelling software. However, ENVISAT's Ka-band antenna is quite deep, and looks unrealistic when modelled as a cone, and even some of the shallower dishes fail to provide the user with high enough quality information. For example, as can be seen in Figure 7-14, the cone used for displaying the RA2 in the left hand image leaves large gaps between the bottom dish surface and its mount, and does not reassure the user as to the correctness of their model. The surface in the right hand image, however, much more closely approximates a paraboloid and gives the user confidence that their modelling is correct.

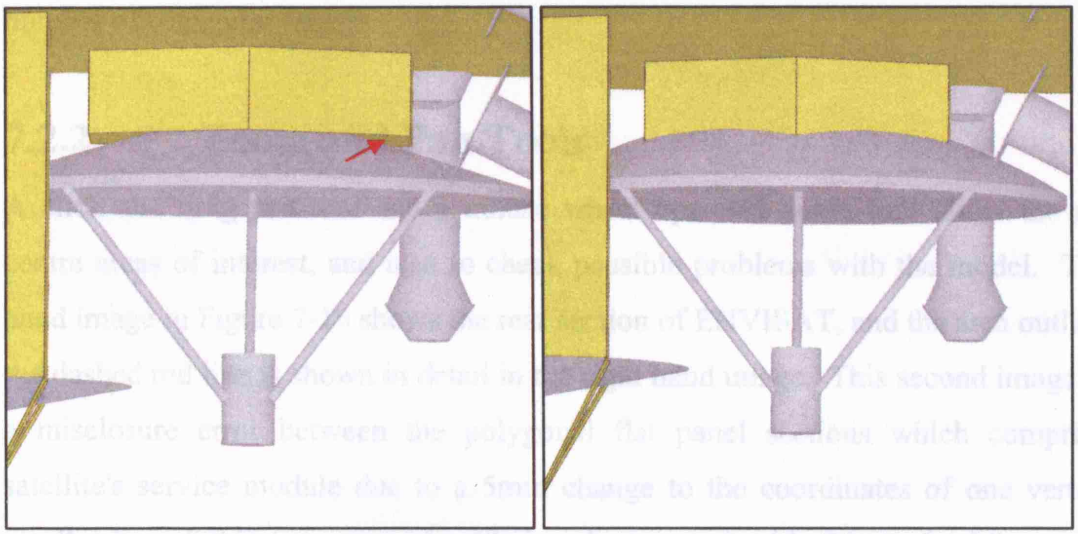

Figure 7-14: Left hand image shows ENVISAT's RA2 antenna displayed as a cone, whilst the right hand image uses a surface which much more closely approximates a paraboloid.

"*The Triangle is the primitive of choice for the OpenGL programmer*" (Wright & Sweet, 2000).

Although it is not possible for computers to render true curved surfaces due to the discrete pixel (picture element) nature of computer monitors, large numbers of triangles with appropriate lighting schemes can be used to closely approximate a parabolic dish (see Figure 7-15).

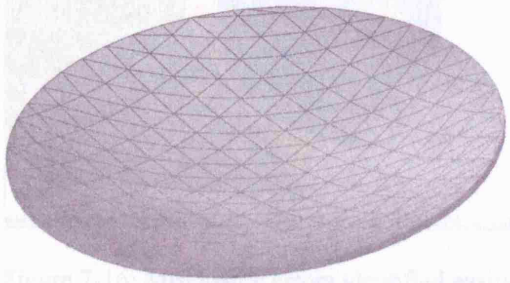

Figure 7-15: Paraboloid, rendered in satellite viewer, showing surface facets.

The effect demonstrated here was achieved by an algorithm which generates a series of regular points over the surface of the paraboloid, with variable resolution depending upon the real size of the dish. These 'seed' points are then used as the vertices of a large number of triangular facets.

7.2.2. Zoom and Pan Tools

A click and drag pan tool and a mouse wheel operated zoom tool allow the user to centre areas of interest, and also to check possible problems with the model. The left hand image in Figure 7-16 shows the rear section of ENVISAT, and the area outlined by the dashed red line is shown in detail in the right hand image. This second image shows a misclosure error between the polygonal flat panel sections which comprise the satellite's service module due to a 5mm change to the coordinates of one vertex. A small error of this type was identified and corrected with this tool while reviewing UCL's model of the JASON altimetry satellite.

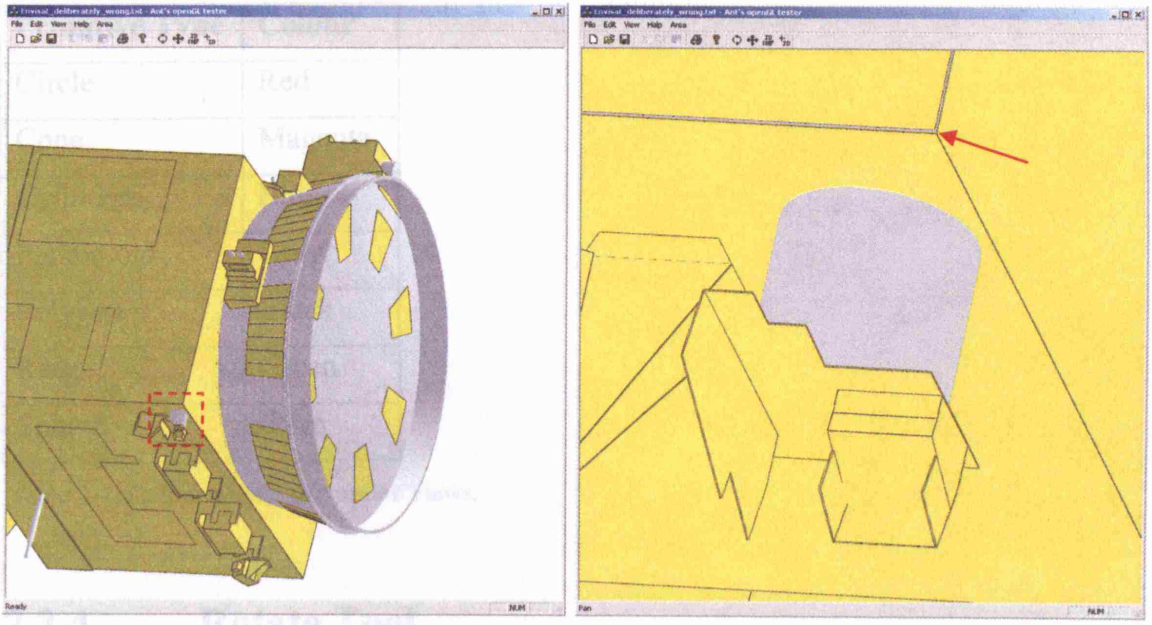

Figure 7-16: Misclosure errors identified easily using the zoom and pan tools.

7.2.3. Outline Tool

Readers paying close attention to Figure 7-11 and Figure 7-16 will notice that it appears as though the UCL model has also neglected the circle of MLI in the centre of the service module's base. However, use of the outline tool shows that this is not the case (see Figure 7-17), but is in fact only because this inner circle sits inside an outer ring, shown in the same colour in the fully rendered model.

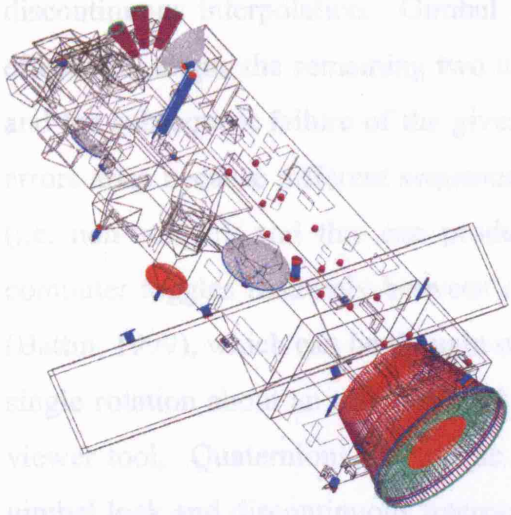

Figure 7-17: Outline representation of the ENVISAT satellite.

In order to allow individual primitives to be distinguished, the following colour palette is used:

Primitive Type	Colour
Circle	Red
Cone	Magenta
Cylinders	Blue
Paraboloid	Grey
Polygon	Black
Ring	Green
Sphere	Cyan

Table 7-1: Colour palette for outline views.

7.2.4. Rotate Tool

The rotate tool uses a virtual trackball, as outlined by Shoemake (1992), to translate 2D mouse movements into 3D manipulations of the underlying spacecraft geometry. It allows the user, without restriction, to rotate a model to any orientation. As indicated in Figure 7-18, upon activation of the rotation tool a sphere drawn in outline is displayed to provide a frame of reference for the user, as well as lines representing the origin and three body fixed axes of the coordinate system used to describe the geometry (red = +X, blue = +Y, purple = +Z). Euler angle (3 axis rotation matrix) based animation / motion systems suffer from the problem of 'gimbal lock' (Watt & Watt, 1992) and discontinuous interpolation. Gimbal lock occurs when a 90° rotation about one axis effectively aligns the remaining two axes, resulting in a loss of one degree of freedom and the subsequent failure of the given rotation sequence. Discontinuous interpolation errors arise because different sequences of Euler rotations can arrive at the same result (i.e. non-unique), and this can produce unexpected erratic motion on screen as the computer toggles randomly between different solutions. Instead, quaternion operators (Battin, 1999), which can be thought of as defining rotations in a manner equivalent to a single rotation about an arbitrary axis in space, were implemented by the author in the viewer tool. Quaternions are unique in that their use makes it possible to avoid both gimbal lock and discontinuous interpolation errors. Rotations described by quaternions are given by simply multiplying the current rotation quaternion by the quaternion expressing the incremental change in rotation as the user moves their mouse, thus

requiring far fewer operations than the equivalent matrix product, saving time and reducing numerical round-off error[24].

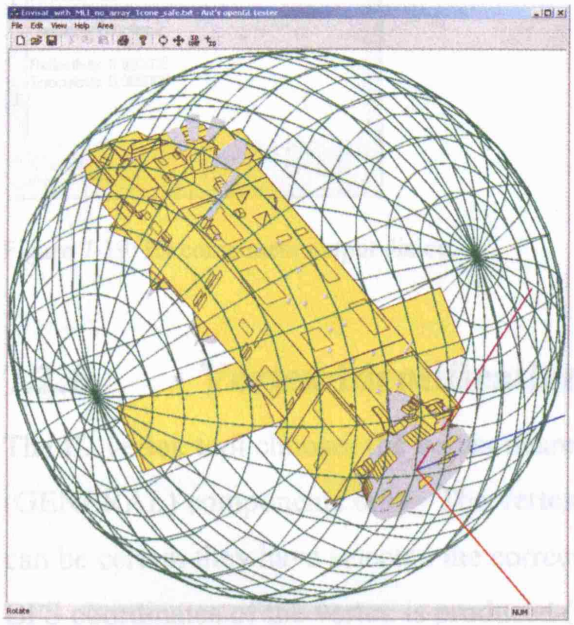

Figure 7-18: The rotation tool in action.

This tool enables users to become very familiar with a satellite, and the ability to manipulate a complete rendered model of the satellite can aid in understanding the satellite for force modelling purposes.

7.2.5. Component Identification

The ID component tool makes use of a feature of OpenGL known as the depth buffer (or Z buffer) which places components in order of their on-screen visibility for rendering purposes, i.e. so that the correct [parts of each] component is rendered no matter what the viewing geometry. The depth buffer can be interrogated for a given area, in this case defined as a pixel selected by the user, and the details of the component at the top of the list are output to screen (see Figure 7-19). It is very useful when dealing with large models because it allows users to trace problems seen on screen back to a specific record number (Recnum) in the userfile for any component type. Component type, group number (for block modelling, see chapter 6) and material properties are also shown.

---

[24] Downs, L. Using Quaternions to Represent Rotation. http://www.genesis3d.com/~kdtop/Quaternions-UsingToRepresentRotation.htm.

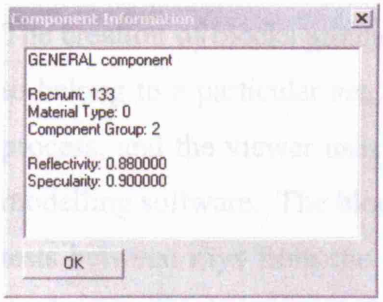

Figure 7-19: ID component output dialog.

7.2.6. Vertex Identification

The ID vertex tool chooses the vertex nearest to the mouse selection point for polygonal (GENERAL) components only. The vertex identified is highlighted in red so that users can be certain they have selected the correct point, and an output window containing the BFS coordinates of the vertex is produced (see Figure 7-20). Vertex coordinates are tab separated, which mean they can be easily copied and pasted into a program such as Microsoft Excel for further manipulation if necessary. This tool can improve the speed and efficiency of model development. For example, as soon as two opposing panel sections on part of a spacecraft bus are in place, remaining panels can easily be added by selecting corners of the existing panels in the appropriate order and pasting their coordinates directly into the userfile. Such enhancements can also help to reduce the incidence of misclosure errors.

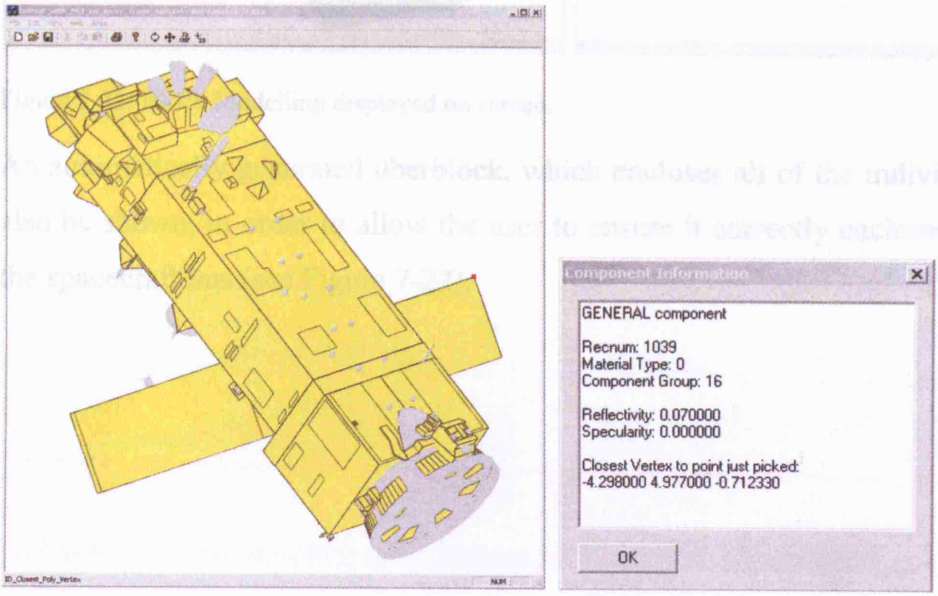

Figure 7-20: Point selected for vertex ID, and the output dialog.

7.2.7. Block Modelling Display

The creation of blocks around component groups (a set of primitives declared by a user to belong to a particular set, often a discrete area of model space) is a fully automated process, and the viewer uses exactly the same algorithms for this purpose as the force modelling software. The blocks are created to increase the efficiency of the intersection tests between rays from the pixel array and components of the spacecraft model (see section 6 for in-depth information about block creation and intersection testing processes). The component groups are created as the userfile is loaded, and to check the success of this operation the user can view all of the blocks (see Figure 7-21). If required, all of the precise components can be removed from the display.

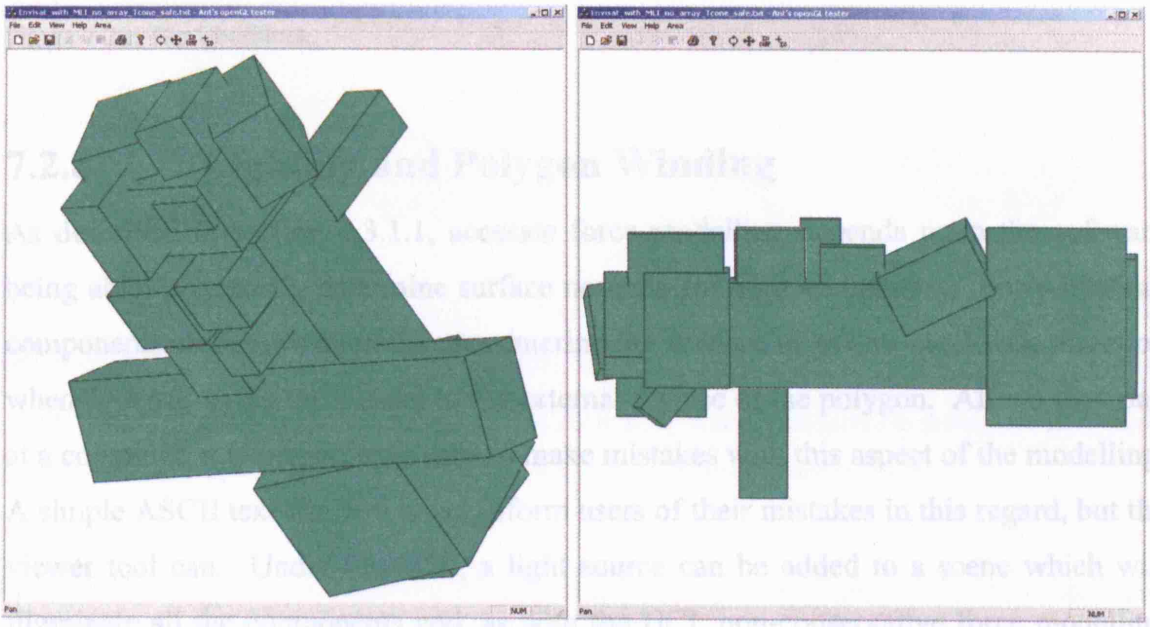

Figure 7-21: Block Modelling displayed on screen.

An automatically generated überblock, which encloses all of the individual blocks, can also be shown, in order to allow the user to ensure it correctly encloses all elements of the spacecraft bus (see Figure 7-22).

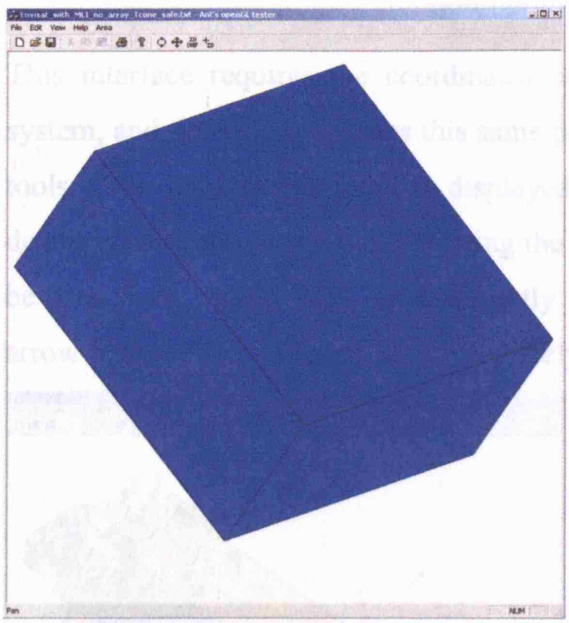

Figure 7-22: The Uberblock.

7.2.8. Lighting and Polygon Winding

As described in section 4.3.1.1, accurate force modelling depends upon the software being able to correctly determine surface normals for each component. For polygonal components, this relies upon the user entering the vertices in an anti-clockwise direction when 'looking' along the normal to the external surface of the polygon. After a long day at a computer, it is surprisingly easy to make mistakes with this aspect of the modelling. A simple ASCII text file will never inform users of their mistakes in this regard, but the viewer tool can. Under OpenGL, a light source can be added to a scene which will illuminate all the components and, as with the UCL non-conservative force modelling software, considers anti-clockwise winding as defining the direction in which the surface normal of the polygon issues. A light source is added through the use of a simple user interface (see Figure 7-23).

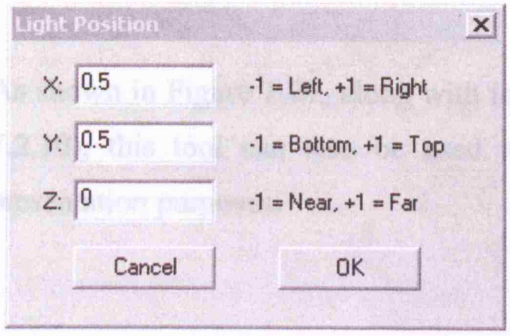

Figure 7-23: The user interface for positioning a light source.

This interface requires the coordinates of the light in a viewer window coordinate system, and the light maintains this same position even when using the pan and rotation tools. The light source itself is displayed on screen as a 'push pin', with a red head denoting its origin, and a tail indicating the direction in which the light is acting. As can be seen from Figure 7-24, an incorrectly wound radiator panel (identified by the red arrow in the left hand image) is immediately apparent.

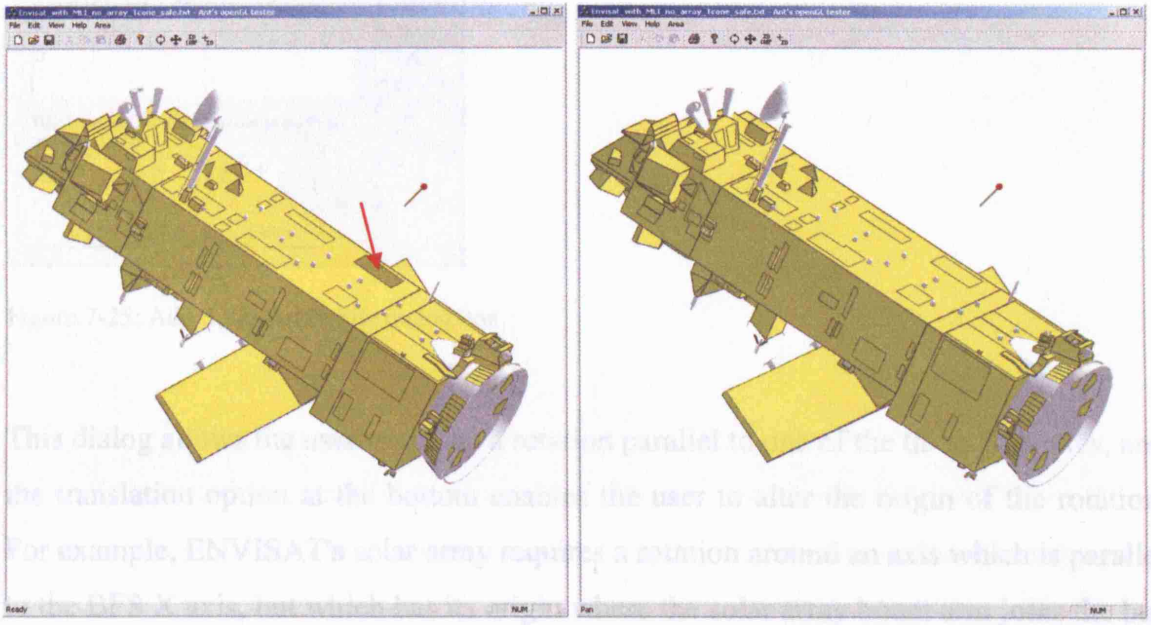

Figure 7-24: The lighting tool can help to identify incorrectly wound polygons, as shown in the left hand image. The right hand image shows the satellite after the problem has been corrected.

It should be noted that shadowing is not accounted for; all surfaces which 'face' the light source are lit, even if other components are 'in the way' (e.g. see components on the underside of the bus in Figure 7-24). *Prima facia* this may seem slightly unusual, but is almost unnoticeable as the tool is particularly good at helping to identify components which behave differently from adjacent ones.

As shown in Figure 7-27, along with in-built image generation capabilities (see section 7.2.10), this tool can also be used to produce some stunning looking images for presentation purposes.

7.2.9. Adding a Solar Array

Although the UCL non-conservative force modelling software is usually operated with the spacecraft bus only, it can be helpful for a user to see the spacecraft bus together with the satellite's solar array. Choosing "Add Solar Array File" from the File menu displays the dialog seen in Figure 7-25.

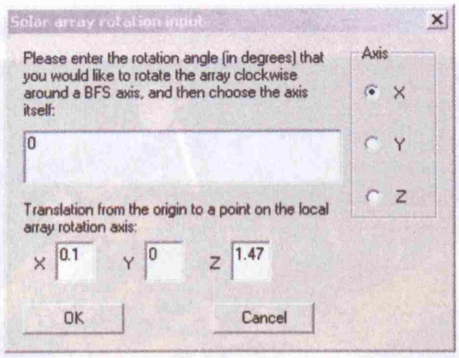

Figure 7-25: Add Solar Array File dialog box.

This dialog allows the user to define a rotation parallel to one of the three BFS axes, and the translation option at the bottom enables the user to alter the origin of the rotation. For example, ENVISAT's solar array requires a rotation around an axis which is parallel to the BFS X axis, but which has its origin where the solar array boom arm joins the bus (see Figure 7-26). This is so that the user can investigate possible modelling problems which may arise when the solar array is in different positions.

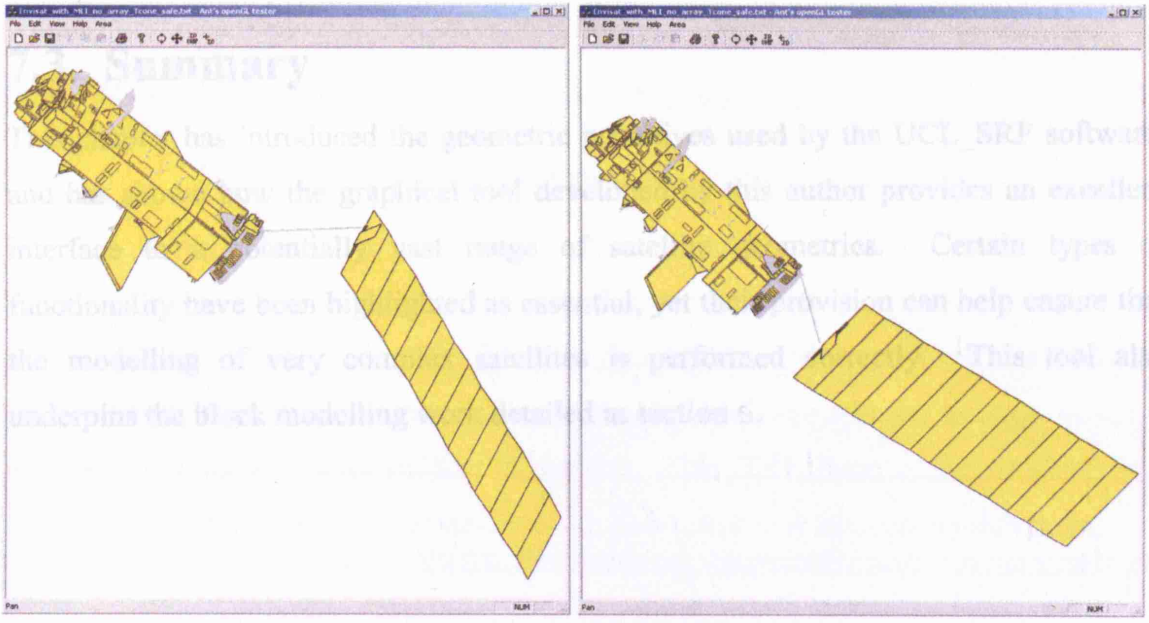

Figure 7-26: ENVISAT's solar array added at two different rotation angles.

7.2.10. Images

The software was written to enable the output of view images for inclusion in reports and model documentation; saved images preserve all facets of the view, including lighting. The background can be toggled between black and white in the viewer and, as can be seen from the two images in Figure 7-27, a black background can be used to great effect.

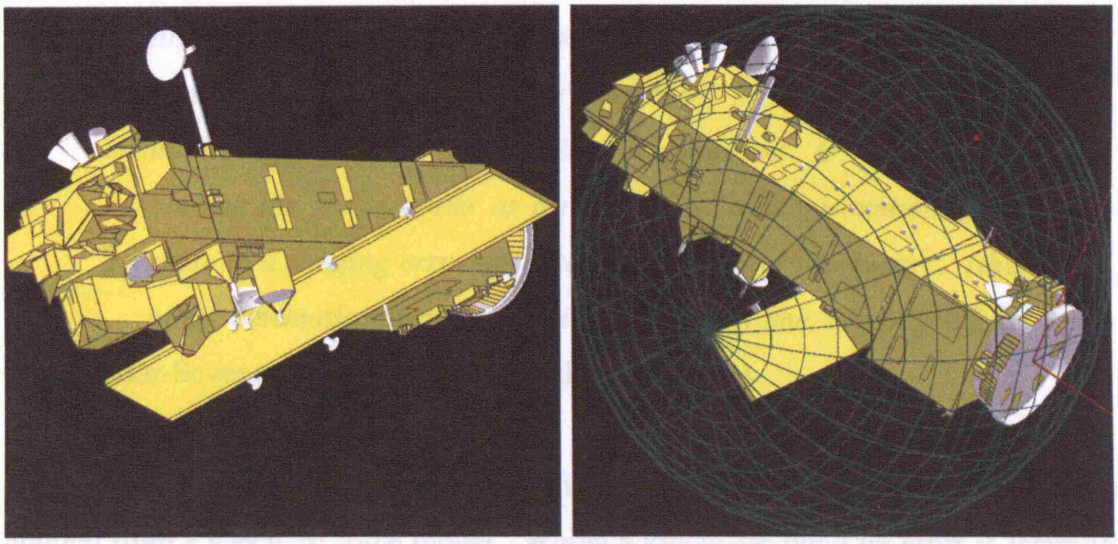

Figure 7-27: Bitmap images saved from the viewer with lighting and other information preserved.

7.2.11. Area Tool

This tool is still under development, but is discussed in greater detail in Appendix A.

7.3. Summary

This chapter has introduced the geometric primitives used by the UCL_SRP software, and has shown how the graphical tool developed by this author provides an excellent interface to a potentially vast range of satellite geometries. Certain types of functionality have been highlighted as essential, yet their provision can help ensure that the modelling of very complex satellites is performed correctly. This tool also underpins the block modelling work detailed in section 6.

8. Satellite Attitude

A satellite's attitude model defines such things as the pointing directions of the body-fixed axes and the normal(s) to the solar array(s). An incorrect attitude model will give rise to both dynamic and kinematic errors, described below for a GPS satellite:

> "*Dynamically, the solar pressure and heat radiation forces on the satellite are mismodeled, in both magnitude and direction, since they depend strongly on the satellite's attitude ... Kinematically, the mismodelling of the radiometric measurement is two-fold ... misplacing the phase center as a result of attitude mismodelling can give rise to a ranging error of up to 10cm for some receivers ... [the] ... other kinematic effect is the mismodeling of the wind-up effect*" (Bar-Sever et al., 1996, square brackets are mine).

Removal of dynamic errors is very important to ensure that the correct force vector is applied from a specified force model. Whilst a kinematic wind up error is inapplicable to ENVISAT's DORIS antenna, as the radio signal is not circularly polarised, the dynamic effects and the mis-location of the phase centre of ENVISAT's DORIS antenna caused by attitude mismodelling are identical to those mentioned above. For these reasons a correct attitude model is extremely important for precise ENVISAT orbit determination and prediction.

8.1. The Satellite Body-Fixed Systems

8.1.1. The Satellite Reference System

Not only is ENVISAT a large and geometrically complex satellite, but it also has a complicated attitude model which is outlined in the ENVISAT "Mission Conventions Document" (Alvarez, 1997). The True of Date (TOD) (Alvarez, 1997 and Vallado, 2001) inertial coordinate system is adopted as the reference system, through which a nominal body-fixed system (nBFS) is derived. The TOD frame is the standard ECI frame (i.e. J2000) rotated to account for Earth precession and nutation, in that order:

$$\overline{ECI}_{TOD} = \overline{NU}\ \overline{PR}\ \overline{ECI}_{J2000} \tag{8.1}$$

where $\overline{\overline{NU}}$ and $\overline{\overline{PR}}$ are, respectively, the rotation matrices for nutation and precession which take us from the J2000 epoch of definition (12 noon, 01/01/2000 UT1) to the current epoch. Alvarez provides a simplified model of precession and nutation (1997) which performs within specified mission tolerances, but not as well as a precise model based on IERS conventions (McCarthy, 1996) which was used here, see Section 8.1.2.1.

In the Mission Conventions Document, the nBFS is referred to as the Satellite Reference System (Alvarez, 1997). If a satellite has a TOD position ($\overline{r}$) and velocity ($\overline{v}$), the unit nBFS ($\hat{x}, \hat{y}, \hat{z}$) in terms of the TOD frame is given by:

$$\hat{z} = \frac{\overline{r}}{|\overline{r}|} \tag{8.2}$$

$$\hat{x} = \frac{\overline{r} \times \overline{v}}{|\overline{r} \times \overline{v}|} \tag{8.3}$$

$$\hat{y} = \hat{z} \times \hat{x} \tag{8.4}$$

Hence, $\hat{y}$ is approximately aligned with the negative velocity vector, and the nBFS is similar to the conventional HCL basis.

8.1.2. The Satellite Relative Reference System

The satellite's velocity in an inertial reference system combined with the Earth's rotation (the effect of which varies with latitude) introduces a frequency (Doppler) shift in the received SAR data. This effect is reduced by applying yaw-steering which shifts the antenna beam forwards and backwards from 0° at the poles to c.+/-4° at the equator (Hanssen, 2001) with respect to the nBFS by rotations principally about the Z axis. This is implemented in ENVISAT's main operational flight mode which is called Stellar Yaw Steering Mode (SYSM), where the attitude of the satellite is determined with respect to a 'fixed' star catalogue by very accurate star tracking sensors. This serves two purposes: first, the body-fixed Z axis, through roll (about the local Y axis) and pitch (about the local X axis) rotations, is aligned with the local geodetic normal - defined as the line normal to the WGS84 ellipsoid which also passes through the satellite centre of mass (Alvarez, 1997) (see Section 8.1.2.1). Second, the body-fixed Y axis is brought

anti-parallel to the ground track velocity vector by a yaw rotation (about the local Z axis) in order to minimise the Doppler shift in the signal due to Earth rotation (Alvarez, 1997) (see Section 8.1.2.2). This series of rotations transforms the satellite Reference System into the Satellite Relative Reference System (nBFS into BFS). The model is determined by the following parameters:

Cx = +0.1672°
Cy = -0.0501°
Cz = +3.9130°

These parameters are given in degrees, and must then be converted to radians before being used in the following equations[25] which give the roll (ROTroll), pitch (ROTpitch) and yaw (ROTyaw) rotation angles respectively, where the argument of latitude (Ulat), is the sum of the argument of perigee (ω) and the true anomaly (ν):

$$ROTroll = Cy.\sin(Ulat) \tag{8.5}$$

$$ROTpitch = Cx.\sin(2*Ulat) \tag{8.6}$$

$$ROTyaw = Cz.\cos(Ulat).\left[1-\frac{(Cz.\cos(Ulat))^2}{3}\right] \tag{8.7}$$

Due to ENVISAT's near spherical orbit (eccentricity = 0.001165), the argument of perigee is poorly determined and varies wildly over the course of an orbit, making it a poor choice of parameter. However, Ulat remains stable as it represents the angle between the current satellite position and the direction of the ascending node (see Figure 8-1).

[25] ftp://spike.cst.cnes.fr/pub/ENVIS/README_nominal_attit

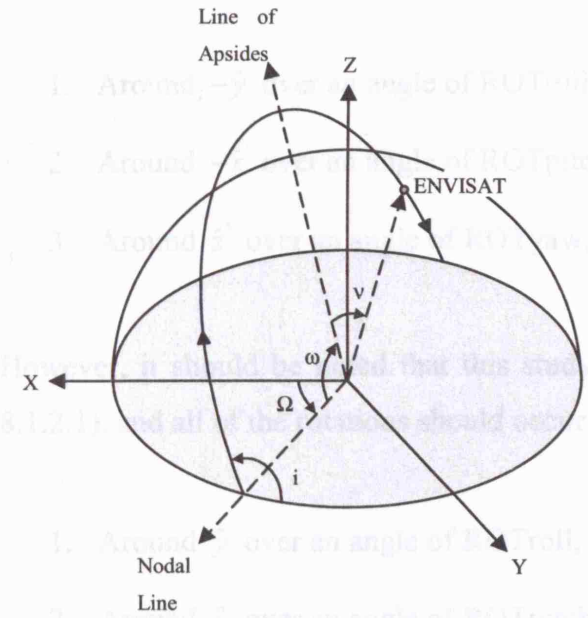

ν: True Anomaly

ω: Argument of Perigee

Ω: Right Ascension of the Ascending Node

i: Inclination

Ulat: argument of latitude (ω + ν)

Figure 8-1: The orbit in space

As can be seen from Figure 8-2 the yaw rotations result in a sinusoidal oscillation of the satellite about the local geodetic normal. An argument of latitude of 0° corresponds to the ascending node, and a positive yaw angle at this point means a counter-clockwise rotation when looking along the local Z axis towards the origin. At the descending node (Ulat=180°), the reverse is true, and the satellite reaches its maximum yaw clockwise around the local Z axis.

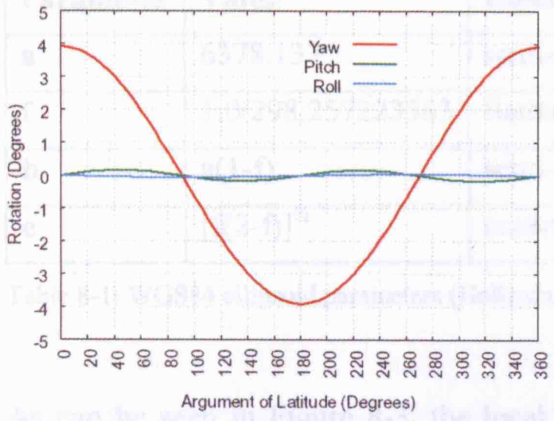

Figure 8-2: Yaw, pitch and roll rotations in SYSM

Alvarez (1997) explains that under SYSM, the rotations should be performed in the following order:

1. Around $-\hat{y}$ over an angle of ROTroll, transforming $(\hat{x},\hat{y},\hat{z}) \rightarrow (\hat{x}',\hat{y},\hat{z}')$
2. Around $-\hat{x}'$ over an angle of ROTpitch, transforming $(\hat{x}',\hat{y},\hat{z}') \rightarrow (\hat{x}',\hat{y}',\hat{z}'')$
3. Around $\hat{z}''$ over an angle of ROTyaw, transforming $(\hat{x}',\hat{y}',\hat{z}'') \rightarrow (\hat{x}'',\hat{y}'',\hat{z}'')$

However, it should be noted that this study found these to be *incorrect* (see Section 8.1.2.1), and all of the rotations should occur around positive axes, i.e.:

1. Around $\hat{y}$ over an angle of ROTroll, transforming $(\hat{x},\hat{y},\hat{z}) \rightarrow (\hat{x}',\hat{y},\hat{z}')$
2. Around $\hat{x}'$ over an angle of ROTpitch, transforming $(\hat{x}',\hat{y},\hat{z}') \rightarrow (\hat{x}',\hat{y}',\hat{z}'')$
3. Around $\hat{z}''$ over an angle of ROTyaw, transforming $(\hat{x}',\hat{y}',\hat{z}'') \rightarrow (\hat{x}'',\hat{y}'',\hat{z}'')$

8.1.2.1. Local Geodetic Normal

While the yaw rotations dominate the model, it is the roll and pitch rotations which initially align the Z axis with the local geodetic normal. For ENVISAT, the local geodetic normal is defined as the line normal to the WGS84 ellipsoid which also passes through the satellite centre of mass, and all that is required is the determination of the direction of this vector in space. The WGS84 ellipsoid has the following properties:

Parameter	Value	Description
a	6378.137	semi-major axis
f	1.0/298.257223563	flattening
b	a(1-f)	semi-minor axis
e	$[f(2-f)]^{1/2}$	eccentricity

Table 8-1: WGS84 ellipsoid parameters (Hofmann-Wellenhof et al., 2001)

As can be seen in Figure 8-3, the local geodetic normal is the surface normal of the ellipsoid at the sub-satellite point, and does not necessarily pass through the centre of the ellipsoid of revolution. (N) is the distance from the Earth's spin axis along the geodetic normal to the surface of the ellipsoid, while (h) (the geodetic/ellipsoidal

height) is the distance along the normal from the surface of the ellipsoid to the satellite. The longitude (λ) of the normal is determined easily and, with (N) and (h) defined, a very simple iterative technique allows the solution of a non-linear trigonometric expression for the local geodetic normal's latitude (φ) (Leick, 1995).

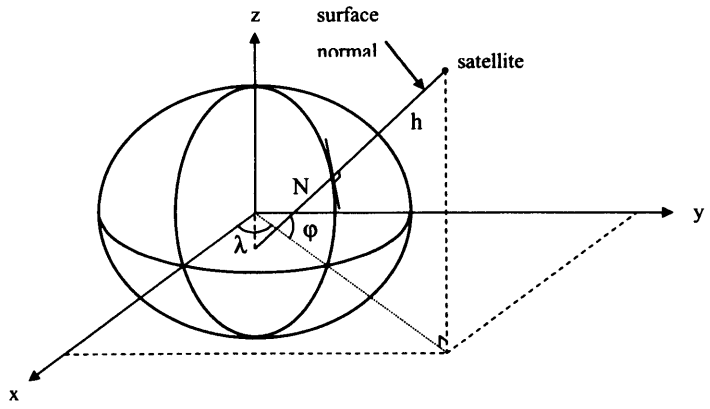

Figure 8-3: Local geodetic normal (Leick, 1995, Figure 6.7)

From Figure 8-3, where x,y,z are geocentric Earth fixed Cartesian coordinates, it can be seen that:

$$\lambda = \tan^{-1}\left(\frac{y}{x}\right) \tag{8.8}$$

$$\varphi = \tan^{-1}\left(\frac{(N+h)\sin\varphi}{\sqrt{x^2+y^2}}\right) \tag{8.9}$$

Equation (8.9) can also be expressed as:

$$\varphi = \tan^{-1}\left(\frac{z}{\sqrt{x^2+y^2}}\left(1+\frac{e^2 N\sin\varphi}{z}\right)\right) \tag{8.10}$$

To solve for the latitude, an approximate value for the satellite's Cartesian (z) coordinate (z_0) is first calculated under the assumption that (h) is initially zero:

$$z = \left[N\left(1-e^2\right)+h\right]\sin\varphi \tag{8.11}$$

$$z_0 = N\left(1-e^2\right)\sin\varphi \tag{8.12}$$

Substituting (8.12) into (8.10) and rearranging, gives an initial value for the latitude (φ_0):

$$\begin{aligned}\varphi_0 &= \tan^{-1}\left(\frac{N\sin\varphi}{\sqrt{x^2+y^2}}\right)\\ &= \tan^{-1}\left(\frac{z_0}{\left(1-e^2\right)\left(\sqrt{x^2+y^2}\right)}\right)\end{aligned} \tag{8.13}$$

This value is substituted into the right-hand side of equation (8.9), where:

$$N = \frac{a}{\sqrt{1-e^2\sin^2\varphi_i}} \tag{8.14}$$

Relatively few iterations over successive solutions for (8.14) and (8.9) yield a final value for the latitude, which allows a unit vector for the local geodetic normal to be recovered.

The effect of performing the rotations from nBFS to BFS under SYSM as described by Alvarez (see above), in comparison with the correct rotations, is shown through a calculation of the angular separation between the BFS Z axis and the local geodetic normal (Figure 8-4) over the course of one orbit. Although a maximum misalignment of ~0.35°, which results from using the published model, might not appear particularly significant, it far exceeds the stated mission pointing performance of better than 0.07° on each axis (Alvarez, 1997). Communication with the ESA-ESTEC ENVISAT System Division (B. Duesmann, pers. comm., 09/02/04), suggests that this is a typographic error in the Mission Conventions Document, as pointing performance monitoring conducted by ESA is within tolerance limits. However, this could have potentially significant implications for anyone attempting to use this information to process data from ENVISAT's scientific payload instruments.

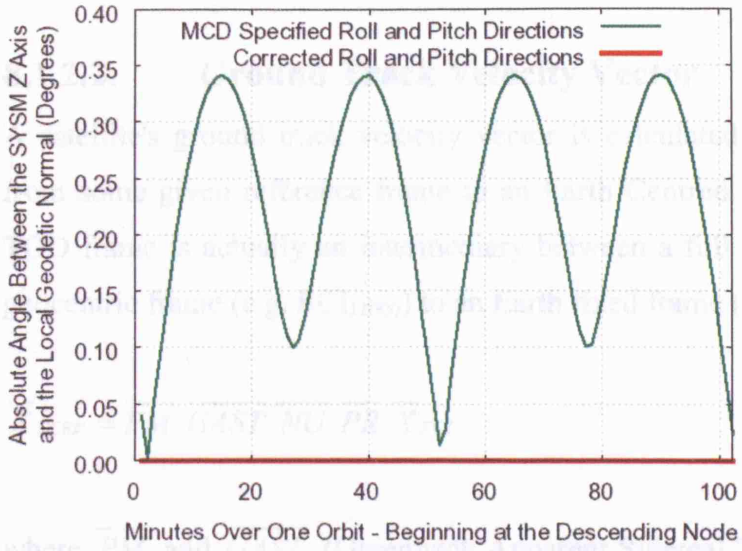

Figure 8-4: Absolute angle separating the local Z axis and the local geodetic normal under different rotation conventions

It is worth mentioning that the use of an approximate model for precession and nutation as specified in the Mission Conventions Document (Alvarez, 1997) does detrimentally affect ENVISAT's pointing performance, but not in a significant manner, and the angular separation of the local Z axis and the local geodetic normal is still well within specified tolerances (see Figure 8-5). This same test was performed for the ground track velocity vector with similar results (see section 8.1.2.2).

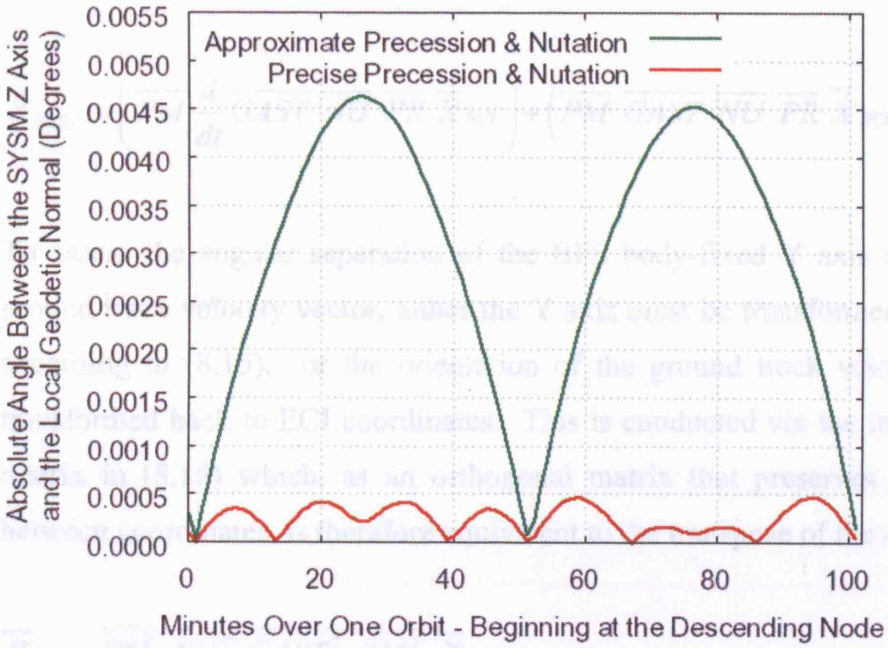

Figure 8-5: Angle between the body-fixed Z axis and the local geodetic normal computed using approximate (Alvarez, 1997) and precise (McCarthy, 1996) precession and nutation parameters

8.1.2.2. Ground Track Velocity Vector

A satellite's ground track velocity vector is calculated by a series of transformations from some given reference frame to an Earth Centred Earth Fixed (ECEF) frame; the TOD frame is actually an intermediary between a full conversion from a non-rotating geocentric frame (e.g. ECI_{J2000}) to an Earth fixed frame (i.e. ECEF) (Vallado, 2001):

$$\overline{X}_{ECEF} = \overline{PM}\ \overline{GAST}\ \overline{NU}\ \overline{PR}\ \overline{X}_{ECI} \tag{8.15}$$

where $\overline{PM}$ and $\overline{GAST}$ (Greenwich Apparent Sidereal Time) are, respectively, rotation matrices which account for polar motion and Earth rotation. Although approximate polynomial expressions exist which allow all of these rotation matrices to be populated, for this study more precise values were used following the well defined standards of the International Earth Rotation Service (IERS) (McCarthy, 1996). The velocity transformation requires the time derivative of equation (8.15) (Vallado, 2001), for which nutation, precession and polar motion can be considered constants, as they change over much larger time scales than do GAST and the satellite position. Hence, through application of the product rule, a velocity ($\dot{\overline{X}}$) can be transformed from ECI to ECEF by:

$$\dot{\overline{X}}_{ECEF} = \left(\overline{PM}\,\frac{d}{dt}\overline{GAST}\ \overline{NU}\ \overline{PR}\ \overline{X}_{ECI}\right) + \left(\overline{PM}\ \overline{GAST}\ \overline{NU}\ \overline{PR}\ \dot{\overline{X}}_{ECI}\right) \tag{8.16}$$

To assess the angular separation of the BFS body-fixed Y axis against the satellite's ground track velocity vector, either the Y axis must be transformed to the ECEF frame according to (8.15), or the orientation of the ground track velocity vector must be transformed back to ECI coordinates. This is conducted via the inverse of the rotation matrix in (8.15) which, as an orthogonal matrix that preserves distance and angles between coordinates, is therefore equivalent to the transpose of the original matrix:

$$\overline{X}_{ECI} = \overline{PR^T}\ \overline{NU^T}\ \overline{GAST^T}\ \overline{PM^T}\ \overline{X}_{ECEF} \tag{8.17}$$

Under the attitude model described above, the alignment of the BFS body-fixed Y axis against the ground track velocity vector fares slightly worse than the corrected Z axis' alignment with the geodetic normal (see section 8.1.2.1). As can be seen from Figure 8-6, the present study shows that the angular separation is sometimes as large as ~0.2° (specified tolerance = 0.07°). This is perhaps more likely to be due to the empirical nature of the attitude model which appears to have concentrated on Z axis pointing, rather than the attitude and orbit control system (AOCS) on-board the satellite. The AOCS uses gyros, star trackers, reaction wheels and magnetorquers to control satellite pointing when in SYSM, and has a much higher accuracy (see Table 8-2). What can be seen in Figure 8-6 is therefore far more likely to represent a failure of the empirical attitude model used to represent the satellite's orientation, rather than actual mis-pointing of ENVISAT. Any deviation of the model from reality can potentially have important consequences for force modelling.

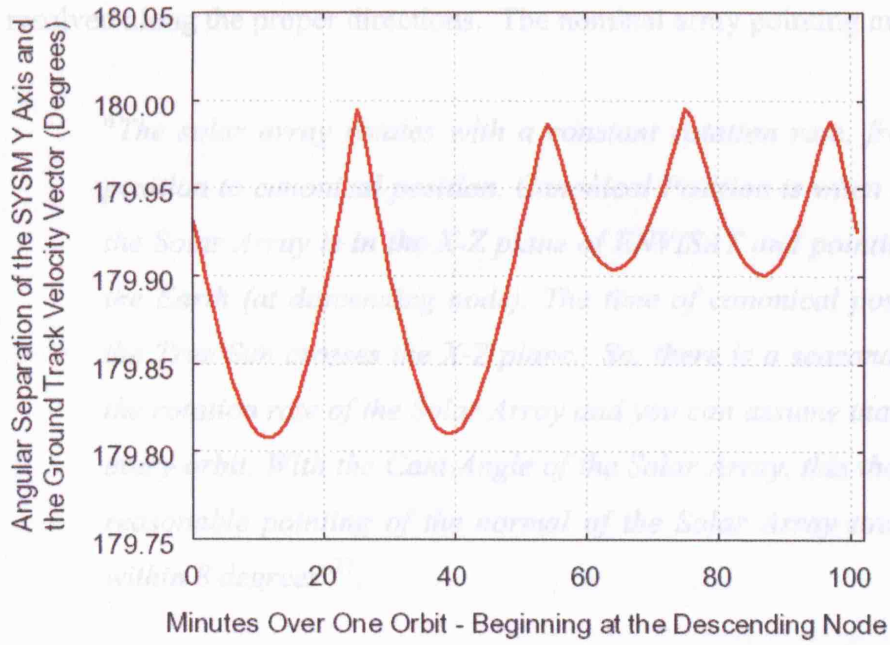

Figure 8-6: Angular separation of the local Y axis and the ground track velocity vector

Satellite Axis	Max. Depointing DOY 334-328
X-axis	25 mdeg
Y-axis	20 mdeg
Z-axis	15 mdeg

Table 8-2: Satellite mispointing due to AOCS[26]

8.1.3. Solar Array Pointing

With a surface area of $70m^2$, ENVISAT's solar array forms a significant component of the non-conservative force model in terms of SRP and TRR. As with the bus, it is not only important to correctly model the distinct surfaces of the array (see section 5.1.1). The array's attitude must also be modelled correctly, in order that the accelerations are resolved along the proper directions. The nominal array pointing model is as follows:

> *"The solar array rotates with a constant rotation rate, from canonical position to canonical position. Canonical Position is when the normal to the Solar Array is in the X-Z plane of ENVISAT and pointing away from the Earth (at descending node). The time of canonical position is when the True Sun crosses the X-Z plane. So, there is a seasonal variation in the rotation rate of the Solar Array and you can assume that it is updated every orbit. With the Cant Angle of the Solar Array, this then results in a reasonable pointing of the normal of the Solar Array towards the Sun within 8 degrees"*[27].

Such a model is not trivial to implement in orbit determination software as it will inevitably require some sort of iterative propagation of the orbit forwards and backwards to determine the points at which the true Sun crosses the XZ plane in order that the solar array rotation rate can be calculated on a once per revolution basis.

---

[26] Rudolph A. ENVISAT Validation Workshop, ESRIN, 9-13/12/2002, page 14. http://envisat.esa.int/workshops/validation_12_02/opening/rudolph.htm

[27] ftp://spike.cst.cnes.fr/pub/ENVIS/README_nominal_attit

Discussion with ESA's Flight Dynamics department (Duesmann, 2004, pers. comm.) revealed the following [slightly ambiguous] information: "Flight Dynamics calculates the parameters once per day based on the best predicted orbit, but uplinks them to ENVISAT twice per day as part of their operational tasks". To reduce computational overhead, an analytical model has been developed during the course of this research which should closely approximate the pointing behaviour of the actual solar array.

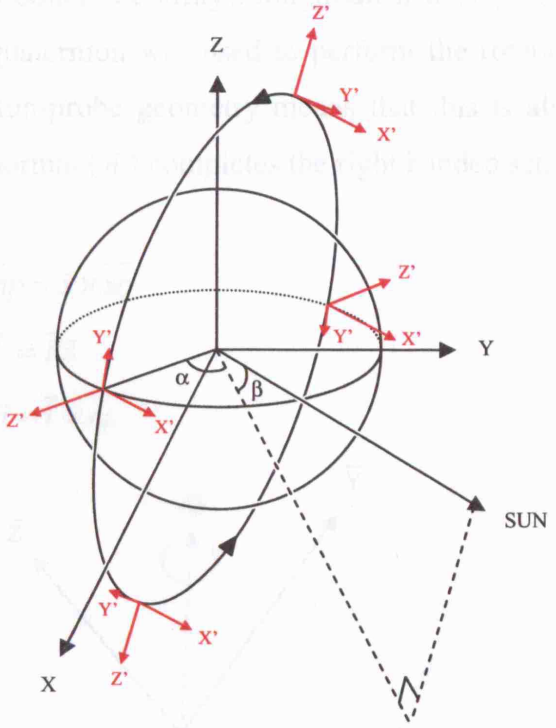

Figure 8-7: BFS axis directions over the course of one complete orbit

During the course of one orbit, the BFS X axis points in a near constant [across-track] direction in space, while the Y and Z axes make one full revolution around the X axis (see Figure 8-7). The solar array maintains a fixed angle of ~22° with respect to the BFS X axis. These two constraints mean that the array's local longitudinal axis will sweep out a cone with a half angle of 22° around the BFS X axis over one orbit. It also seems sensible to conclude that the array pointing scheme is designed to optimise power output from the array (i.e. the array normal should point towards the Sun as much as possible), and it was with this in mind that the new analytical model was developed.

At any point, the array should attempt to maximise the angle between its normal and the Sun-probe vector. This is the case if the array's longitudinal axis lies on the opposite

side of the cone to the Sun, and also lies in a plane containing the Sun-probe vector and the BFS X axis (thus passing through the full diameter of the cone). The cross-product ($\overline{np}$) of the BFS X axis ($\overline{x}$) and the Sun-probe direction ($\overline{sp}$) gives a vector which is normal to the plane containing both of these vectors. $\overline{np}$ can be used as a rotation axis around which the BFS X axis can be rotated 22° anti-clockwise by a matrix $\overline{R}$ to produce the array's longitudinal axis ($\overline{l}$); although, in the software implementation a quaternion was used to perform the rotation. The persistence of the BFS X axis and Sun-probe geometry means that this is always an anti-clockwise rotation. The array normal ($\overline{n}$) completes the right handed set.

$$\overline{np} = \overline{x} \times \overline{sp} \tag{8.18}$$

$$\overline{l} = \overline{R}\overline{x} \tag{8.19}$$

$$\overline{n} = \overline{l} \times \overline{np} \tag{8.20}$$

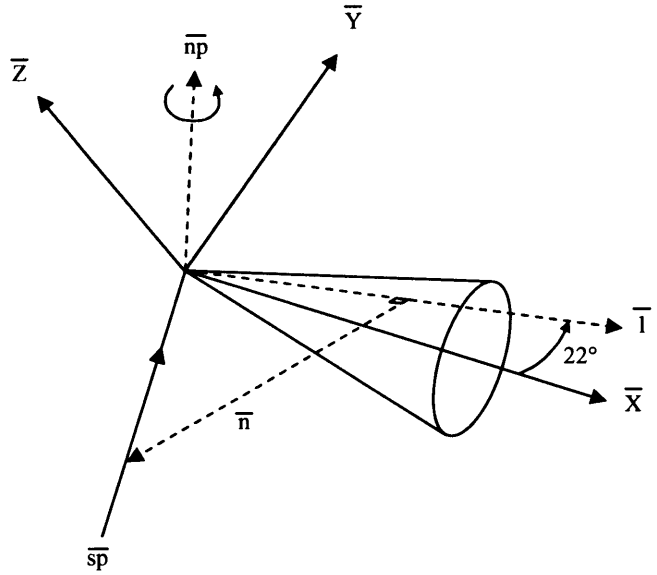

Figure 8-8: Finding the optimal array normal

These three vectors ($\overline{l}, \overline{np}, \overline{n}$) form a local array axis system which can be used to resolve the accelerations due to SRP and TRR. If $\overline{n}$ vectors are computed at each epoch (t) over the course of one ENVISAT orbit, a plot of the angular separation between each consecutive vector pair with the mean removed (i.e. separation between $\overline{n}$ at t_i and t_{i-1}) demonstrates that there is high degree of consistency in the rotation rate produced by this method (see Figure 8-9).

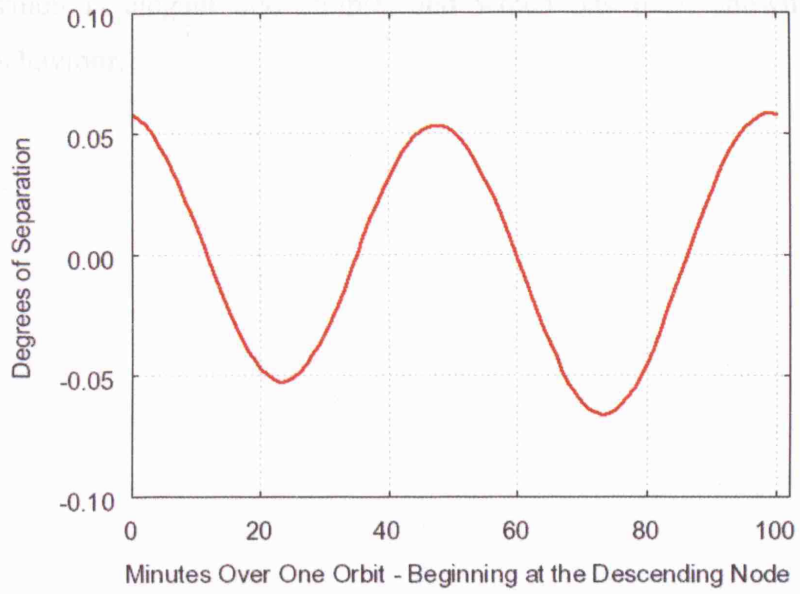

Figure 8-9: Chart showing the number of degrees which separate consecutive array normal axis ($\overline{n}$) vectors each minute (mean removed) over the course of one orbit, using the above algorithm for array pointing

Although this series displays an obvious periodicity influenced by the sinusoidal yaw regime, it has a very narrow range of c.0.1°. This is exactly what we should expect, because it means that the physical reality of the constant rotation rate of ENVISAT's solar array is being adhered to (see nominal array pointing model definition at beginning of this section). Also, owing to the algorithm's design, we can be certain that overall the array will try to maximise the area it presents to the Sun, as should the array pointing model which is actually in use by ENVISAT. It should be noted however, that the solar array is a critical component which will dominate the SRP force field. Any errors in the pointing of the solar array normal will map into errors in this force field which may not be absorbed by estimated once per revolution soak-up parameters.

8.2. Summary

It is important to implement satellite attitude models correctly otherwise a variety of problems will result when computing orbit solutions. We have seen that care should be taken when using published models, as it is possible for them to be either incorrect, and/or dramatically over simplified. In this section ENVISAT's bus attitude model has

been corrected and validated, and a new solar array attitude model has been developed which is elegant and simple, and which has been shown to conform to expected behaviour.

9. SRP and TRR Model Computation

This chapter outlines those regions of ENVISAT's body-fixed coordinate space for which model values must be computed, and additional procedures implemented to allow this process to be undertaken.

9.1. Defining the Computational Zone

9.1.1. Nominal Pointing Values

Computing a Solar Radiation Pressure and Thermal Re-radiation model for a satellite of complex shape is highly computationally intensive, and requires a thorough investigation into all the possible configurations of Sun-probe geometry as noted in Figure 5-21. For ENVISAT, this allows computation to be targeted upon those regions of the body-fixed coordinate space for which model values must be computed. As already mentioned in chapter 8, ESA/ESTEC quote a remarkably naive value for the pointing of the solar array normal:

> *"With the Cant Angle of the Solar Array, this then results in a reasonable pointing of the normal of the Solar Array towards the Sun within 8 degrees"*[28].

This follows from a basic geometric argument (see Figure 9-1) using the cant angle of the solar array (fixed at 22° with respect to the BFS X axis, angle (c)), and a mean local solar time at the descending node of 10_{AM} (an offset of 2 hours from the Sun at the equator, equivalent to 30°, angle (a)). It can be seen that under these conditions, with the BFS X axis orthogonal to the plane of the orbit, the equatorial angular separation between the Sun vector and the solar array normal is fixed at 8° (angle (e)).

[28] ftp://spike.cst.cnes.fr/pub/ENVIS/README_nominal_attit

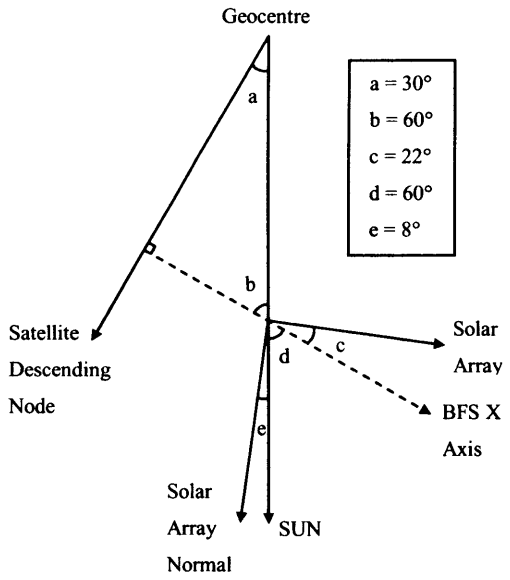

Figure 9-1: Simple geometric model of the equatorial angular separation between the Earth-Sun vector and the solar array normal

Far more accurate results given below (Figure 9-2) have been generated using the nBFS attitude model described in chapter 8, in conjunction with over one year of precise ENVISAT orbit data supplied by ESA (Michiel Otten, ESA/ESTEC, pers. comm., 22/01/2004) and JPL DE405 Sun positions. The opportunity was also taken at this point to investigate further into why a cant angle of 22° was chosen for the solar array. Integer cant angles from 20-30° were tested for angular separation between the resultant array normal and the Sun vector, which showed that a value of 24° minimises the angular separation, as plotted in Figure 9-2 against the actual cant angle value of 22°. It can be seen that during the summer months, when it is possible to achieve 0° of separation, a cant angle of 22° outperforms a 24° value, while at all other times 24° performs better. With these results in mind, whilst it has not been possible to confirm the reasons for choosing a cant angle of 22° for the solar array, it is suggested here that this is perhaps a trade-off between optimal pointing and some limitations in the design of the satellite, such as an excessive torque on the array boom arm if canted at 24°.

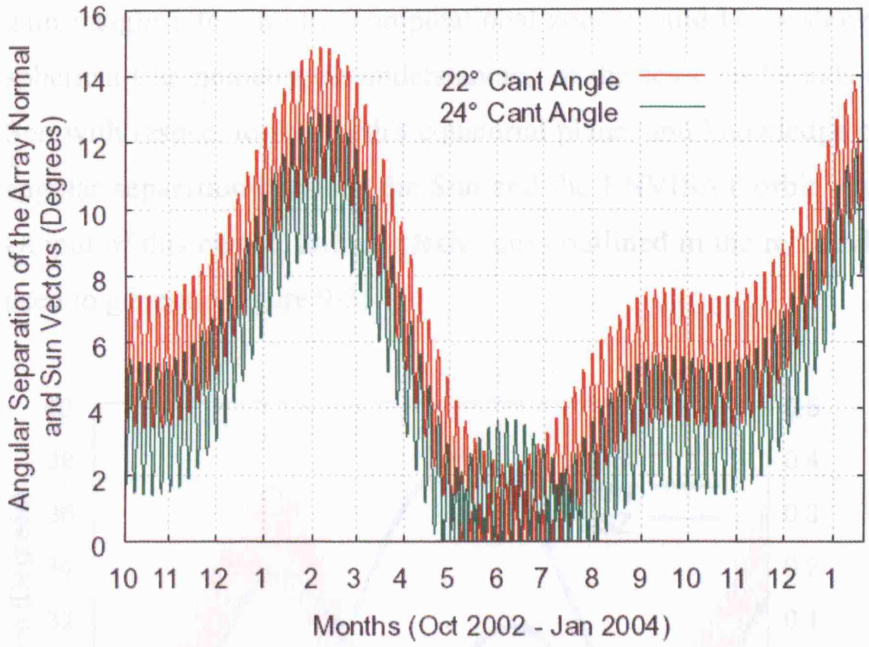

Figure 9-2: Figure showing the angular separation of the array normal and the Sun vector across 15 months of precise orbit data under SYSM and for two different cant angles

The values shown here clearly demonstrate that the actual range of pointing values for ENVISAT's solar array are almost twice as large as the 8° quoted. The fixed angle between the solar array normal and the BFS X axis means that this significantly alters the size of the region for which an SRP/TRR model needs to be computed. The maximum ESA/ESTEC value of 8° solar array mis-pointing suggests that model values should cover angles of between 22°-30° with respect to the angular separation of the Sun vector and the ENVISAT main BFS YZ plane (which lies in the plane of the orbit), while values from this study propose that any model must cover a much larger region of at least +20° to +37° (see Figure 9-3). In fact, the originally computed model covered the zone from +13° to +43° to both mitigate the impact of any unforeseen orientations and to limit any 'drift' from the 'truth' in a continuous surface model (using Golden Software's[29] Surfer program) fitted to the discrete calculated data points for each BFS axis. However, this was extended to -18° to +43° to allow its use with the ERP model as outlined in section 5.6. Negative angles denote regions in the negative BFS X half-space, while positive angles are located in the positive BFS X half-space. As the difference between the nominal coverage and the region outlined here is much larger than 4°, it can not be put down to the oscillation of the BFS axes caused by SYSM. To

[29] www.goldensoftware.com

gain insight into why the computational zone should be as shown requires some basic spherical trigonometry, an understanding of the seasonal bounds on the elevation of the Sun with respect to the Earth's equatorial plane, and knowledge of the actual equatorial angular separation between the Sun and the ENVISAT orbit plane (see section 9.1.2). Output of this nature, utilising techniques outlined in the remainder of this chapter, was used to generate Figure 9-3:

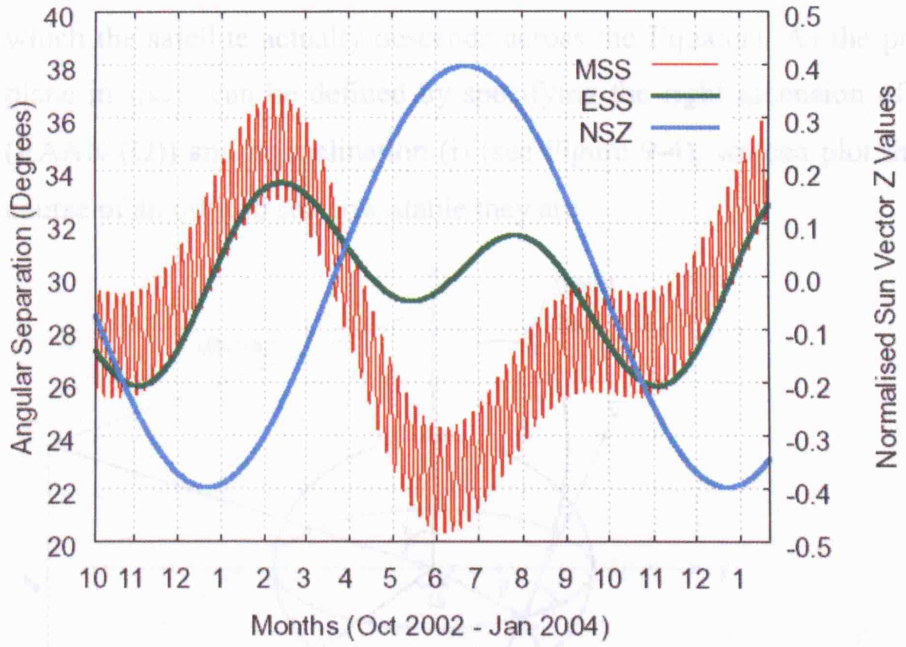

Figure 9-3: Minimum separation of the ECI Sun vector and the ENVISAT's nBFS YZ plane. Left-Hand Y Axis: MSS = Minimum Angle Separating Sun Vector and BFS YZ plane, ESS = Equatorial Separation of Sun and Orbit Plane. Right-Hand Y Axis: NSZ = Normalised Sun Vector Z Values.

9.1.2. The Equatorial Angular Separation between ENVISAT's Orbit Plane and the Sun's Local Hour Angle Vector

A technique for generating the required equatorial separation requires two inputs which are easily calculated for any one epoch:

- An ECI vector which lies in both ENVISAT's instantaneous orbital plane and in the Earth's equatorial plane – here, an ECI vector in the direction of the descending node is used.
- An ECI vector which corresponds to the local hour angle of the Sun

9.1.2.1. ECI Vector in the Direction of ENVISAT's Descending Node

In order to recover the equatorial separation of ENVISAT's orbital plane and the Sun, we will use an ECI vector pointing from the geocentre to ENVISAT's descending node. It is instructive to see how well an instantaneous descending node vector (computed at any point on orbit) reflects the position of the actual descending node (the point at which the satellite actually descends across the Equator). As the position of an orbital plane in space can be defined by specifying the right ascension of its ascending node (RAAN (Ω)) and its inclination (i) (see Figure 9-4), we can plot these values over the course of an orbit to see how stable they are.

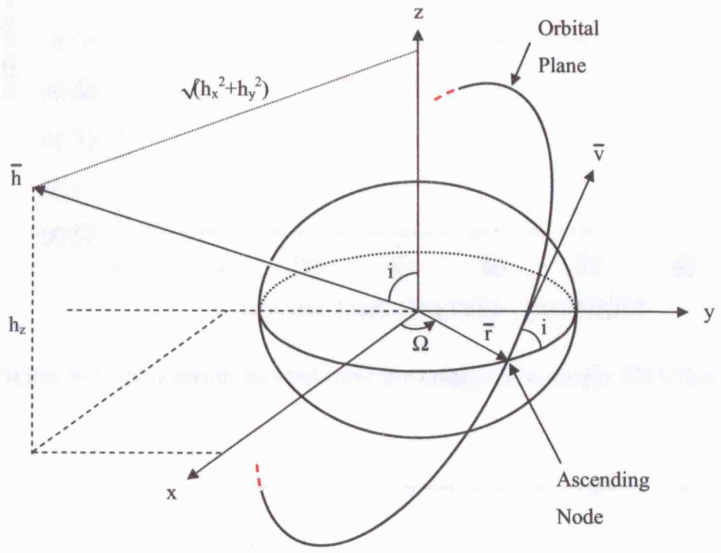

Figure 9-4: RAAN (Ω) and inclination (i)

An ascending node is that point on orbit where the satellite crosses the equator when moving from South to North and its RAAN is the angle to the node measured in the equatorial plane from the ECI X axis (angle is positive to the East). The cross-product of the position ($\bar{r}$) and velocity ($\bar{v}$) vectors gives the angular momentum vector ($\bar{h}$), and this is used to compute the orbit's inclination (equivalent to the angle the orbit plane makes with respect to the equatorial plane):

$$\bar{h} = \bar{r} \times \bar{v} \tag{9.1}$$

$$i = \tan^{-1}\left(\frac{\sqrt{\left(h_x^2 + h_y^2\right)}}{h_z}\right) \tag{9.2}$$

Over the course of a single orbit, ENVISAT's inclination and right ascension of the ascending node (RAAN) are very stable (varying less than 0.1° in both cases), as can be seen from the following two figures produced from ENVISAT precise orbit data (orbit data courtesy of Michiel Otten, ESA).

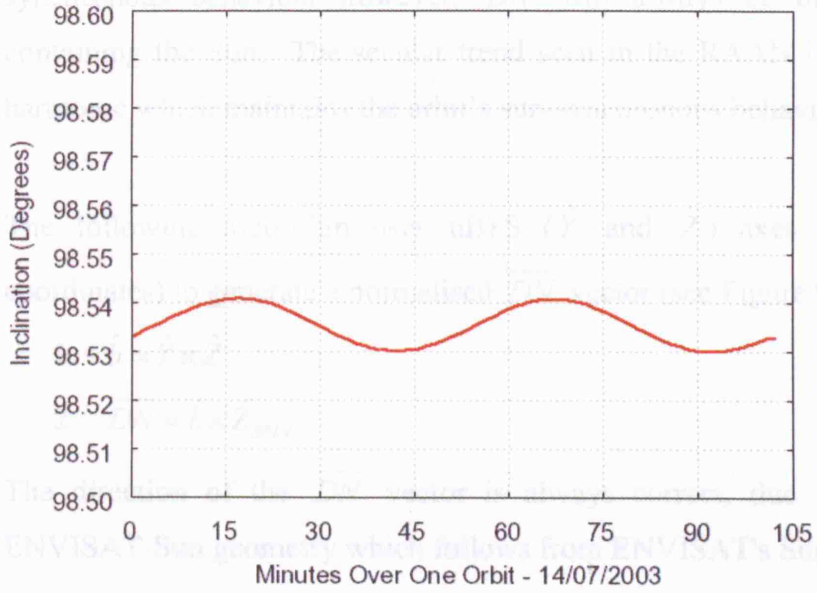

Figure 9-5: inclination plotted over the course of a single ENVISAT orbit at one minute intervals

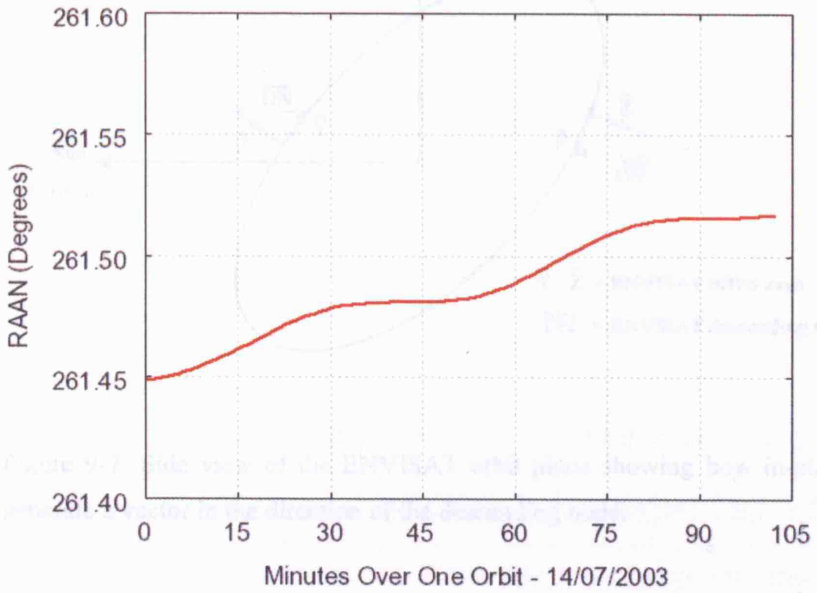

Figure 9-6: RAAN plotted over the course of a single ENVISAT orbit at one minute intervals

This means that at any point on an orbit, a vector in the direction of the descending node ($\overline{DN}$) generated from the in-plane nBFS ($\hat{Y}$ and $\hat{Z}$) axes (given in terms of ECI coordinates) will represent the whole orbit very well, with an accuracy bounded by the level of variation in the RAAN and inclination. Speaking generally $\overline{DN}$ lies along the intersection between the orbital plane and the equatorial plane, its direction however depends upon the orbital geometry of a particular satellite. With ENVISAT's Sun-synchronous behaviour however, $\overline{DN}$ will always be oriented in the half-space containing the Sun. The secular trend seen in the RAAN is due to the second zonal harmonic which maintains the orbit's sun-synchronous behaviour (see section 1.2).

The following algorithm uses nBFS ($\hat{Y}$ and $\hat{Z}$) axes (given in terms of ECI coordinates) to generate a normalised $\overline{DN}$ vector (see Figure 9-7):

1. $\hat{b} = \hat{Y} \times \hat{Z}$
2. $\overline{DN} = \hat{b} \times \hat{Z}_{SPIN}$

The direction of the $\overline{DN}$ vector is always correct, due to the persistence of the ENVISAT-Sun geometry which follows from ENVISAT's Sun synchronous orbit.

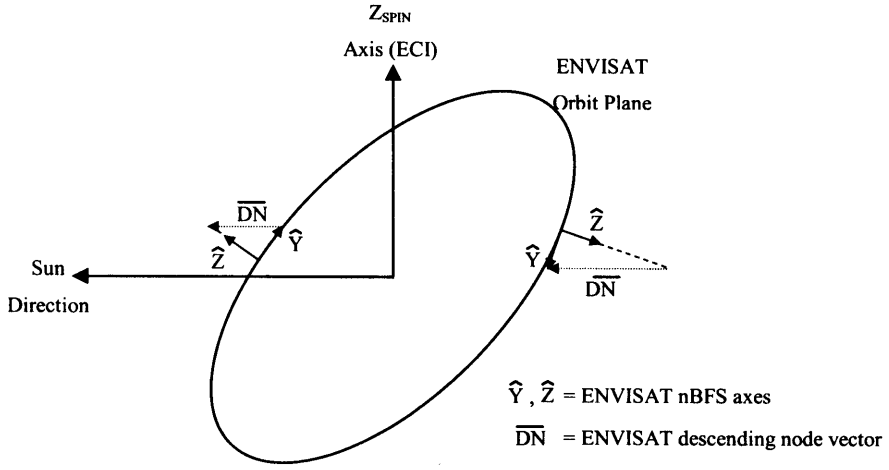

Figure 9-7: Side view of the ENVISAT orbit plane showing how in-plane nBFS axes can be used to generate a vector in the direction of the descending node.

9.1.2.2. ECI Vector Corresponding to the Sun's Local Hour Angle

If $\hat{S}$ is the normalised ECI Sun vector, then the ECI vector which corresponds to the local hour angle ($\overline{S}_{LHA}$) is just $\hat{S}$ projected vertically onto the Earth's equatorial plane:

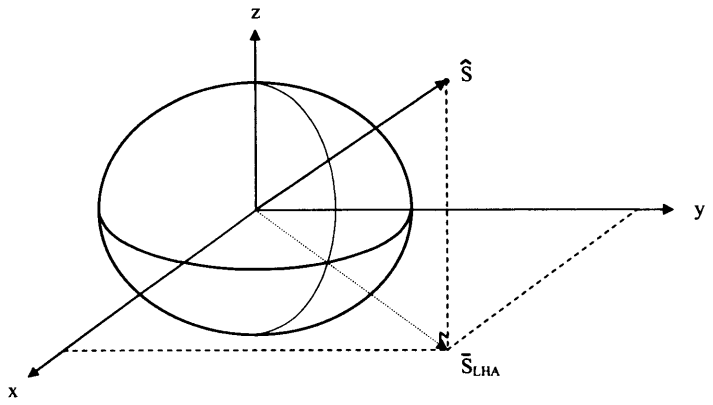

Figure 9-8: Sun's local hour angle

$$\overline{S}_{LHA} = \begin{bmatrix} \hat{S}_x \\ \hat{S}_y \\ 0 \end{bmatrix} \tag{9.3}$$

9.1.2.3. Calculating the Angular Equatorial Separation

It is then a trivial matter to construct an algorithm which calculates the angular equatorial separation (ESS) from the normalised $\overline{DN}$ vector:

1. $ESS = \cos^{-1}\left(\overline{DN}.\hat{S}_{LHA}\right)$

To generate the results shown in Figure 9-3, this calculation was performed for all of the ENVISAT orbit data mentioned in Section 9.1.1 using JPL DE405 Sun positions.

9.1.3. Calculating the Minimum Angular Separation of the Sun Vector and ENVISAT's orbit [nBFS YZ] plane

The following diagrams make use of the knowledge that the ENVISAT orbit plane has an inclination of approximately 98.55°. This gives a value for theta of 81.45° (180°-98.55°) in Figure 9-9, and a theta of 98.55° in Figure 9-10. Note that the line b' in both

figures is intended to represent the minimum angular separation between ENVISAT's orbit plane and the Sun, and is therefore orthogonal to ENVISAT's orbit plane; all solid lines shown are great circles.

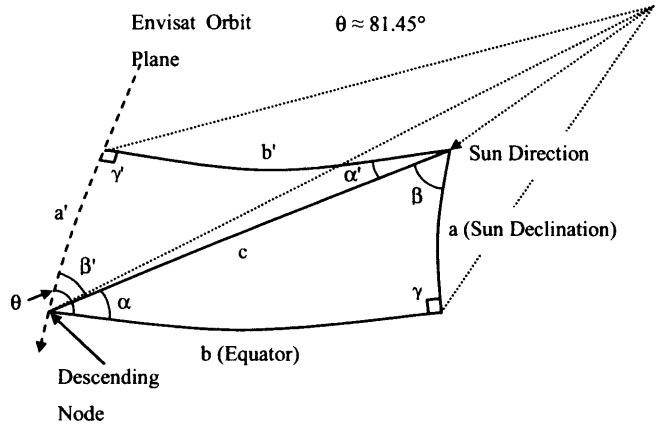

Figure 9-9: ENVISAT's orbit with the Sun above the equator

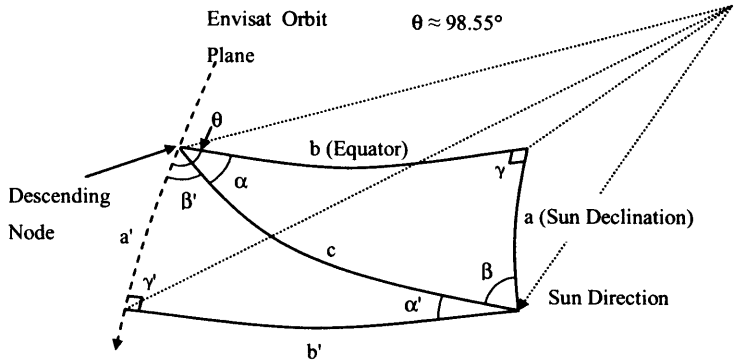

Figure 9-10: ENVISAT's orbit with the Sun below the equator

To recover b', we can just use some simple spherical trigonometry:

$$\cos c = \cos a \cos b + \sin a \sin b \cos \gamma \tag{9.4}$$

As $\cos \gamma = 0$:

$$c = \cos^{-1}(\cos a \cos b) \tag{9.5}$$

$$\frac{\sin a}{\sin \alpha} = \frac{\sin c}{\sin \gamma} \tag{9.6}$$

As $\sin \gamma = 1$

$$\alpha = \sin^{-1}\left(\frac{\sin a}{\sin c}\right) \tag{9.7}$$

$$\beta' = \theta - |\alpha| \tag{9.8}$$

$$\frac{\sin c}{\sin \gamma} = \frac{\sin b'}{\sin \beta'} \tag{9.9}$$

$$b' = \sin^{-1}(\sin c \sin \beta') \tag{9.10}$$

A summary of the results of these calculations (at the peaks/troughs of the main curve shown in Figure 9-3) can be seen in Table 9-1 below, whilst the fit to the whole dataset is shown in Figure 9-11. It is clear that the ESA model, which allows a separation of only 22° to 30°, will most definitely not fit the data.

Equatorial Separation (°)	**Unit Sun Vector, Z Value**	**Minimum Separation From Orbit Data (°)**	**Minimum Separation From Spherical Trig (°)**
26.0	-0.25	25.5-29.5	27.2
33.5	-0.25	33.0-37.0	34.5
29.0	0.35	21.0-25.0	23.4
31.5	0.35	23.0-27.0	25.6

Table 9-1: Spherical trig calculation values

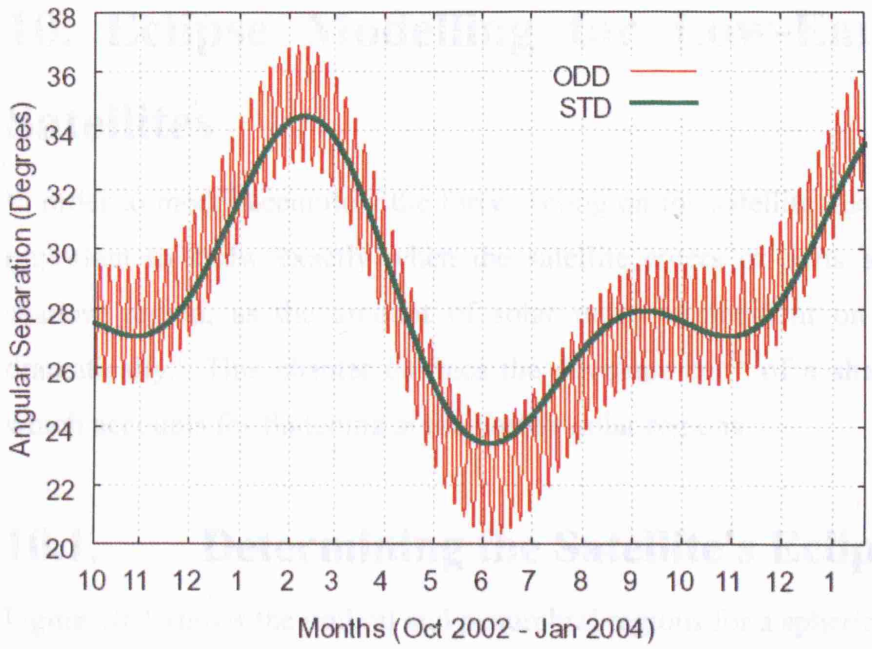

Figure 9-11: Spherical trigonometry against orbit data derived values. ODD = Orbit data derived minimum angle separating Sun vector and BFS YZ plane, STD = spherical trigonometry derived minimum angle separating Sun vector and BFS YZ plane.

9.2. Summary

Studying only those regions of the body-fixed coordinate system which require forces to be modelled can provide a simple way of reducing the computational overhead when computing force models. However, it has also been clearly demonstrated that over simplifying the determination of these regions can be disastrous.

10. Eclipse Modelling for Low-Earth Orbiting Satellites

In order to model accurately the forces acting on the satellite due to SRP and TRR it is important to know exactly when the satellite enters or exits a penumbral / umbral shadow region, as the amount of solar radiation incident on the spacecraft drops dramatically. This chapter outlines the development[30] of a shadow boundary model which accounts for flattening at the Earth's polar regions.

10.1. Determining the Satellite's Eclipse State

Figure 10-1 shows the umbral and penumbral regions for a spherical Earth. In reality the Earth is flattened, with the polar radius being about 0.3% smaller than the equatorial radius. If the Earth's oblateness is taken into account, the boundaries of the shadow regions are altered.

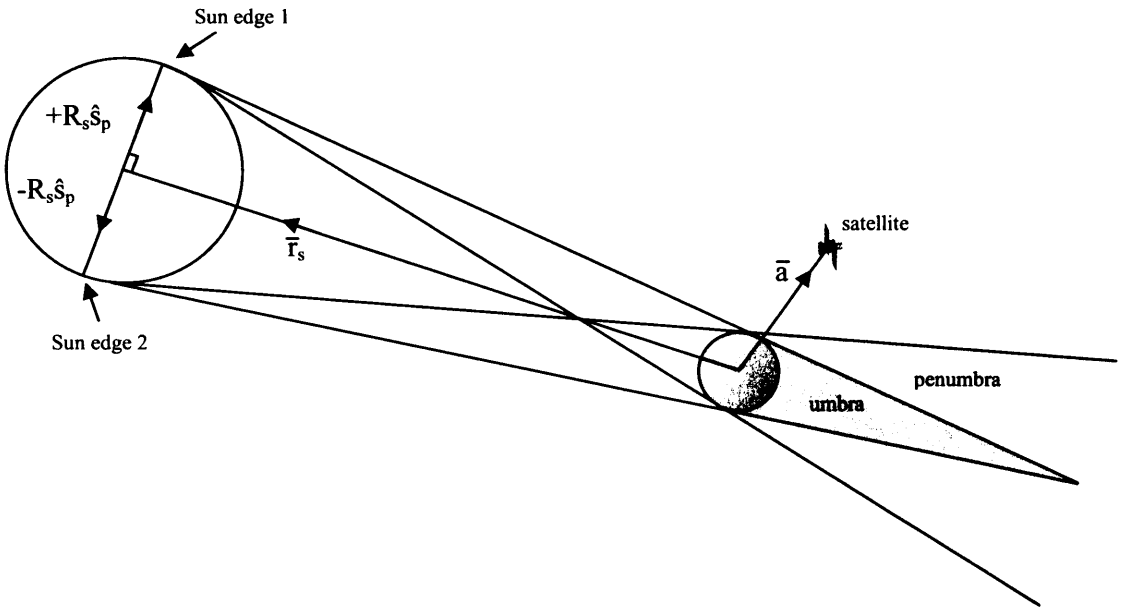

Figure 10-1: Lines forming shadow region boundaries in a plane defined by the Sun centre, the geocentre and the satellite

An instantaneous plane is defined by the geocentre, the Earth-Sun vector $\bar{r}_s$ and the Earth-spacecraft vector $\bar{a}$. In this two-dimensional space the Sun is modelled as a

[30] In collaboration with Dr Sima Adhya, UCL.

circle. The unit vector orthogonal to the Earth-Sun vector is used to find the two required "edges" of the Sun in an Earth Centred Inertial (ECI) coordinate frame (see Figure 10-1). The vectors $\bar{r}_{s1}$ and $\bar{r}_{s2}$ can be defined as the lines from the geocentre to Sun-edge 1 and Sun-edge 2 respectively. The method is based upon tests that determine whether or not lines from the Sun edges to the spacecraft intersect the Earth. If an intersection occurs, *and* the distance from the Sun to this intersection point is less than the Sun-spacecraft distance, then the satellite is either in the penumbra or the umbra.

The actual calculations of the intersection points are carried out using 3-D geometry, with the surface of the Earth being mathematically approximated by the equation of a spheroid:

$$\frac{x^2+y^2}{p^2}+\frac{z^2}{q^2}=1 \tag{10.1}$$

where x, y, z are the ECI coordinates of a point in space on the surface of the spheroid, p is the equatorial radius and q is the polar radius.

The two lines between the spacecraft and the Sun can be defined as follows:

$$\frac{x-a_1}{b_1}=\frac{y-a_2}{b_2}=\frac{z-a_3}{b_3} \tag{10.2}$$

where (a_1, a_2, a_3) are the x, y, z components of the position vector of the spacecraft ($\bar{a}$), and (b_1, b_2, b_3) are the x, y, z components of the vector from either Sun-edge 1 or Sun-edge 2 to the spacecraft ($\bar{b}$). Vectors $\bar{a}$ and $\bar{b}$ can be obtained for a specific epoch, from precise ephemerides or a numerical integration, and hence the lines are defined. In the plane, rays of light starting at the Sun edges and making tangents with the Earth define the full phase/penumbra and penumbra/umbra boundaries, as shown in Figure 10-2.

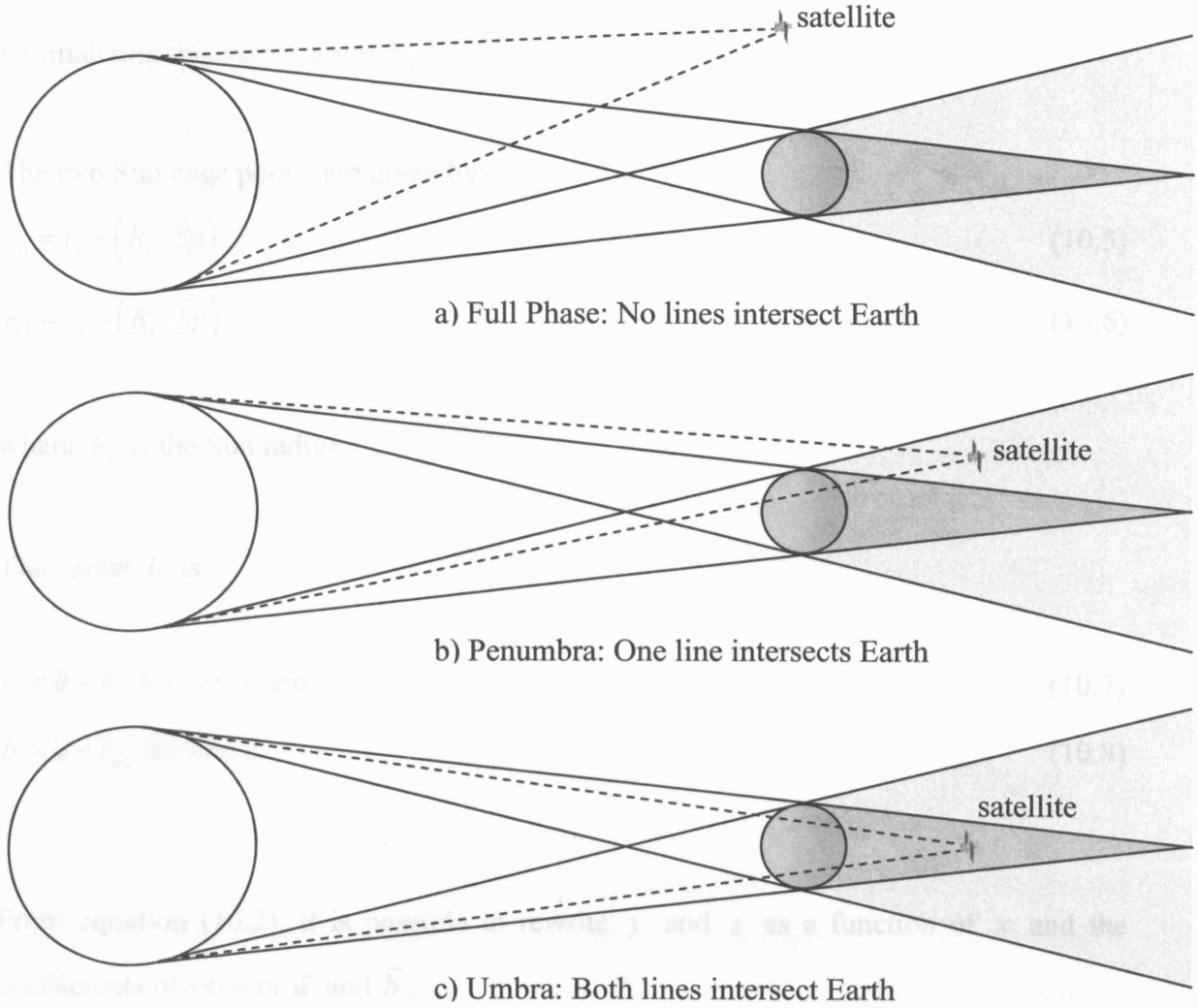

Figure 10-2: Diagram of a satellite in full phase and a satellite in eclipse

To determine $\hat{S}_p$:

The cross product between $\overline{r}_s$ and $\overline{a}$ is taken to give a vector ($\overline{r}_i$) normal to the plane.

$$r_i = r_s \times a \tag{10.3}$$

Taking the cross product of $\overline{r}_i$ with $\overline{r}_s$ gives the vector that lies in the plane and is perpendicular to $\overline{r}_s$, which is $\overline{S}_p$.

$$\overline{S}_p = \overline{r}_s \times \overline{r}_i \tag{10.4}$$

Normalizing this vector gives $\hat{S}_p$.

The two Sun edge points are given by:

$$\overline{r}_{s1} = \overline{r}_s + \left(R_s \cdot \hat{S}p\right) \tag{10.5}$$

$$\overline{r}_{s2} = \overline{r}_s - \left(R_s \cdot \hat{S}p\right) \tag{10.6}$$

where R_s is the Sun radius.

The vector $\overline{b}$ is:

$$\overline{b} = \overline{a} - \overline{r}_{s1} \text{ for line 1 and} \tag{10.7}$$

$$\overline{b} = \overline{a} - \overline{r}_{s2} \text{ for line 2} \tag{10.8}$$

From equation (10.2), it is possible to rewrite y and z as a function of x and the coefficients of vectors $\overline{a}$ and $\overline{b}$.

$$y = \frac{b_2}{b_1}(x - a_1) + a_2 \tag{10.9}$$

$$z = \frac{b_3}{b_1}(x - a_1) + a_3 \tag{10.10}$$

Now y and z can be substituted into equation (10.1) to yield a quadratic in x:

$$\frac{x^2 + \left[\frac{b_2}{b_1}(x - a_1) + a_2\right]^2}{p^2} + \frac{\left[\frac{b_3}{b_1}(x - a_1) + a_3\right]^2}{q^2} = 1 \tag{10.11}$$

$$q^2x^2 + q^2\left[\frac{b_2}{b_1}(x - a_1) + a_2\right]^2 + p^2\left[\frac{b_3}{b_1}(x - a_1) + a_3\right]^2 = p^2q^2 \tag{10.12}$$

$$Ax^2 + Bx + C = 0 \tag{10.13}$$

In this quadratic:

$$\begin{aligned} A &= b_1^2 q^2 + q^2 b_2^2 + p^2 b_3^2 \\ B &= -2b_2^2 q^2 a_1 + 2b_1 b_2 q^2 a_2 - 2p^2 b_3^2 a_1 + 2p^2 b_1 b_3 a_3 \\ C &= q^2\left[b_1^2 a_2^2 + b_2^2 a_1^2 - 2b_2 b_1 a_1 a_2\right] + p^2\left[b_1^2 a_3^2 + b_3^2 a_1^2 - 2b_3 b_1 a_1 a_3\right] - b_1^2 p^2 q^2 = 0 \end{aligned} \tag{10.14}$$

The real solutions to this quadratic equation give the x-coordinates of the points of intersection of the spheroid and the Sun-edge to spacecraft line.

For a real solution to exist:

$$B^2 - 4AC \geq 0 \tag{10.15}$$

If equation (10.15) is satisfied, an intersection takes place. A negative value has no physical meaning, but shows that no intersection occurs. If there is no intersection, then the satellite is in full phase. Lines from both Sun edges to an instantaneous satellite position are tested in this manner. Once the value of x is obtained, it can be substituted into equation (10.2) to solve for the y and z coordinates of the intersection point; equivalent equations can be generated to yield quadratics in y and z. Full coordinates of the intersection point are required in order to calculate its distance from the Sun. If this distance is larger than the distance between the Sun and the spacecraft, then the satellite is automatically assigned a state of full phase. In all other cases, the following conditions are regarded:

- If both lines have real solutions, then the spacecraft is in the umbra.
- If only one of the lines has real solutions the spacecraft is in the penumbra.
- If there are no real solutions then the spacecraft is in full phase.

The algorithm written to carry out this function takes a UTC timetag and the position vector of the satellite as inputs. The corresponding Sun positions are retrieved for each

epoch from an ephemeris file (JPL DE405), and the test for intersection points is carried out. A specified integer value is returned depending upon the result of the computation; the program calling the function uses this integer value to determine if a change of state has occurred.

10.2. Results

The method above describes a way of determining whether the satellite is in full phase, penumbra or umbra at a particular epoch. This algorithm can be used with positions interpolated from precise ephemerides (as used here), or from an integrated orbit position for prediction purposes. Precise orbit determination requires an accurate timetag for when a change of state occurs (Woodburn, 2000), as this is important when calculating the correct solar flux for use in modelling many non-conservative forces. In order to predict the exact crossing time, iteration between the satellite's position and its state will be required. The iteration process is efficient as the method shares much of the geometric simplicity of its spherical Earth counterparts, thus also making its implementation very straightforward. The algorithm could be easily incorporated into both fixed-step and adaptive-step size orbit integrators. Its impact upon precise orbit determination will of course rely upon the choice of step size in a fixed-step integrator.

Preliminary analyses were conducted using precise ENVISAT orbit and photometric data provided by the satellite laser ranging (SLR) facility at Herstmonceux. In this instance, photometry is simply the observation and counting of solar photons reflected from the spacecraft, which can be sorted from laser pulses during simultaneous SLR observations on the basis of amplitude and duration by a median filter (Otsubo et al., 2004). Obviously, as the satellite enters eclipse, there will be less sunlight incident upon it, resulting in fewer photon counts; though this will also depend to a small degree upon the viewing geometry from the SLR station. The photometry data shown in Figure 10-3 for ENVISAT (a LEO satellite), and Figure 10-4 for Glonass (a MEO satellite) are quite typical for the satellites tested. A decision was made to use only the ENVISAT photometry to test the efficacy of the algorithm because, as can be seen from the figures, the Glonass eclipse transition occurs over a much longer time period. It is also expected that atmospheric refraction will have a greater impact on the higher altitude satellites, and therefore the algorithm cannot as yet, be used with confidence for

these satellites. However, the Herstmonceux SLR team is currently tracking Russian Etalon satellites, which are covered in corner cube reflectors and orbit with an altitude of approximately 19,000km, in an attempt to try to assess the effect of atmospheric refraction on eclipse transition times.

To estimate the time of onset of shadow transition, a low order polynomial is fitted to a short period of pre-event photometric data. This function is extrapolated and residuals from the photometry data are computed. When the modulus of the residuals become larger than 3*RMS of the post-fit residuals, the event is assumed to be underway. The precision of this process is estimated to be about 1 second of time, and the epochs of the photometry data are known much more accurately than that due to the counter being slaved to an atomic clock.

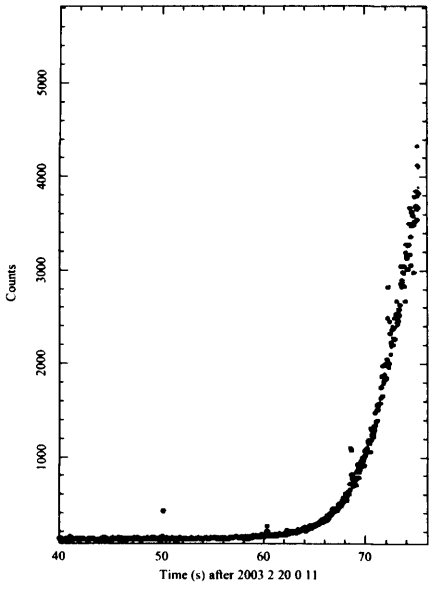

Figure 10-3: ENVISAT Photometry Plot - emergence from eclipse (Reproduced by kind permission of the NERC Space Geodesy Facility at Herstmonceux, E. Sussex)

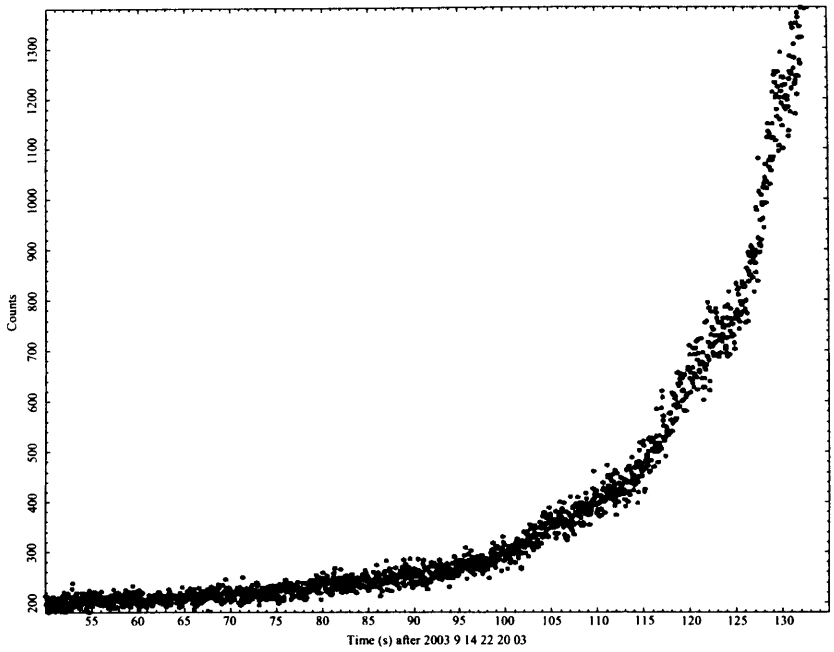

Figure 10-4: Glonass photometry plot - emergence from eclipse (Reproduced by kind permission of the NERC Space Geodesy Facility at Herstmonceux, E. Sussex)

Table 10-1 shows the time offsets for a series of eclipse entry/exit times between ENVISAT photometric observations and three different Earth models. A small root mean square (RMS) value for these time offsets suggests a greater degree of accuracy in the model. The spheroidal model uses the algorithm described here with p=6378.137 km and q=6356.752 km (Montenbruck & Gill, 2001)[31], the spherical model uses p =q=6378.137 km and the International Earth Rotation Service (IERS) model uses a spherical Earth with p=q=6402.0 km (McCarthy, 1996). The data indicate that with standard values for the Earth radii, the above spheroidal algorithm can determine shadow crossing times which demonstrate a significant improvement over comparable spherical models for a low Earth orbiting satellite when tested against photometric observations.

For low Earth orbiting satellites, an incorrect transition point will introduce a systematic bias over many orbit revolutions. Certain orbital geometries may mean that satellites

[31] The values of p and q could perhaps be adjusted to better account for the effects of refraction etc., but this was not performed in the current study.

will be subject to a difference of several minutes spent in eclipse when comparing those predicted by a spherical Earth model against those from the current algorithm.

Date	Time from Photometry	Spheroid (seconds)	Sphere (seconds)	IERS (seconds)
17/02/2003	20:36:59	-4	2	12
17/02/2003	22:17:31	-0.5	6	15
18/02/2003	21:45:52	-4	-1	8
17/03/2003	20:53:54	2	8	17
18/03/2003	20:22:15	-2	4	12
18/03/2003	22:02:53	-5	1	10
20/03/2003	20:59:19	2	8	17
21/03/2003	22:08:14	0	6	14
23/03/2003	21:04:44	3	9	18
24/03/2003	20:33:02	2	8	16
27/03/2003	20:38:28	2	8	16
27/03/2003	22:19:04	1	7	16
07/04/2003	21:31:58	2	7	16
	RMS	2.649383	6.379052	14.67337

Table 10-1: Eclipse entry / exit time offsets between different models and ENVISAT photometry

In terms of efficiency, the algorithm developed here runs 13.4 times faster than an alternative oblate Earth technique (Vokrouhlický et al., 1996) when determining 1 million eclipse states on a dual processor AMD Athlon 2200+ machine.

10.3. Summary

The main operational software requirements for the computation of precise orbit trajectories are accuracy and efficiency. An important part of this must be the correct determination of eclipse shadow boundary transition times, as these boundaries control the periods over which SRP and TRR non-conservative force models should be applied. A review of the publicly available literature on this subject suggests that current methods are either accurate or efficient, but not both. By modelling the Earth as a spheroid, the above method retains the physical complexity inherent in the problem, yet the algorithm is as simple computationally as techniques which model the Earth as a sphere; this results in a highly efficient approach. Initial results point to the ability of

this algorithm to be able to determine shadow crossing times to within 1 second for low Earth orbiting satellites when compared to photometric observations (ENVISAT). This means that any errors in the SRP and TRR modelling which could occur as a result of incorrect eclipse transition times should be minimised if this algorithm is used for LEO satellites.

PART III

11. Results and Analysis

This chapter outlines the extensive testing of the models developed during the course of this study. Tests were performed both at UCL and by staff at NASA's Goddard Space Flight Centre. Analysis of measurement residuals and once-per-revolution estimated accelerations is conducted over one year of orbits.

11.1. UCL Orbit Prediction Results

In this text, the term "orbit prediction" refers to the process of numerically integrating a trajectory from initial conditions (XYZUVW) taken from a precise orbit. ENVISAT precise orbits are produced during "orbit determination" which also incorporates many thousands of DORIS and/or SLR observations into each orbit solution. The orbit predictions performed for this study use a set of models which describe the conservative and non-conservative forces acting upon the spacecraft. It should again be emphasised that during the prediction process NO observational data was used. RMS height, cross and along track 'errors' have been generated by differencing against the precise orbit used to seed the integrator. Although such tests will not conclusively tell us about the precision of the force models, as the precise orbits themselves contain some errors, they do allow a relative assessment of their accuracy and fidelity.

The following information describes the integrator and the force models used:

- An 8th order embedded Runge-Kutta integrator with adaptive step-size control set to a 1 second increment.
- Eclipse determination with the Earth modelled as an oblate spheroid, using the technique documented in chapter 10.
- High order (70x70) GRACE gravity field coefficients, with associated Legendre polynomials generated by a numerically stable recursive formulation.
- Periodic variations to the gravity field coefficients generated using the pole, solid Earth and ocean tides.
- Third body accelerations including the Sun, Venus, the Moon, Mars and Jupiter, with planetary positions generated using the JPL DE405 ephemerides.
- General relativistic forces.

- International Earth Rotation Service conventions are used to compute exact frame transformations.
- All of the non-conservative force models discussed in chapter 4.

The most subtle effects of the GRACE gravity field are only experienced when the harmonics are expanded to degree and order 120 (Willis, 2004, pers comm.). However, such an expansion is more computationally expensive and, for the level of precision required here (millimetric) it was found that expansion to degree and order 70 was sufficient.

Precise orbit data was generously supplied by Michiel Otten from the Navigation Support Office at the European Space Operations Centre (ESOC). 12^{th} order polynomials were fitted to the raw data, provided at an epoch rate of one second, allowing precise positions and velocities to be interpolated for arbitrary epochs. HCL differences were only evaluated once every minute.

Adjustments to the initial conditions which improve the fit to the precise orbits, both $[\Delta X,\Delta Y,\Delta Z,\Delta U,\Delta V,\Delta W]^T$ and $[\Delta X,\Delta Y,\Delta Z,\Delta U,\Delta V,\Delta W,\Delta Cd]^T$, were estimated using the variational technique described in Appendix C. All results shown below arise from integrating over 101 minutes, roughly one ENVISAT orbit. Note however that when a drag coefficient was also estimated a 3 hour integration was required to stabilise the solution, though results are taken over only the first 101 minutes of this period.

Orbit integrations were performed every 15 days for a period of just over one year (see Table 11-1).

Orbit No.	Date	Orbit No.	Date	Orbit No.	Date
1	04/10/2002	10	16/02/2003	19	01/07/2003
2	19/10/2002	11	03/03/2003	20	16/07/2003
3	03/11/2002	12	18/03/2003	21	31/07/2003
4	18/11/2002	13	02/04/2003	22	15/08/2003
5	03/12/2002	14	17/04/2003	23	30/08/2003
6	18/12/2002	15	02/05/2003	24	14/09/2003
7	02/01/2003	16	17/05/2003	25	29/09/2003
8	17/01/2003	17	01/06/2003	26	14/10/2003
9	01/02/2003	18	16/06/2003		

Table 11-1: Integrated orbit numbers and their respective epochs.

Integration for orbit 6 showed unusually large residuals, and these have been traced to an orbit inclination manoeuvre on the morning in question. Results for orbit 6 are therefore not included in the figures and tables below. These figures show HCL (height, across, and along track) RMS residuals over the integration period, for cases where non-conservative force models have been completely removed (No NCF) and where all the force models have been utilised (NCF). Comparison of the performance of the UCL NCF models against the NOM box and wing NCF macromodel is performed in the section on orbit determination (see section 11.2). Additional images show cases where both of these original trajectories have been adjusted, and where the NCF case has been adjusted using two different parameter sets. All summary statistics are given in metres.

The left hand image in Figure 11-1 showing height residuals demonstrates quite clearly the improvement gained upon inclusion of non-conservative force models, while the right hand image dramatically illustrates how close it is possible to come to the precise orbit after integrating over a distance of almost 45000 km.

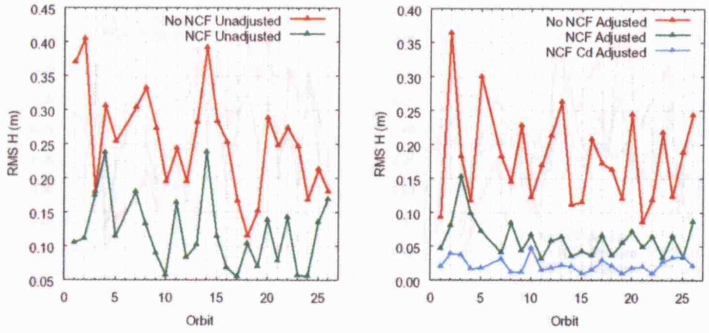

Figure 11-1: RMS height residuals over one orbit.

Note however that the general pattern of the residuals for all cases is quite similar, which suggests that either these errors are unrelated to non-conservative forces, or that there is an unidentified component to non-conservative force models which has not been fully addressed.

	No NCF Unadjusted	No NCF Adjusted	NCF Unadjusted	NCF Adjusted	NCF Cd Adjusted
Min	0.1157	0.0853	0.0549	0.0312	0.0097
Max	0.4050	0.3648	0.2386	0.1534	0.0476
Range	0.2893	0.2795	0.1837	0.1222	0.0379
Average	0.2531	0.1798	0.1193	0.0609	0.0226

Table 11-2: Summary statistics for the height residuals (in metres).

The across track residuals tell a particularly interesting story, in that it appears as though the introduction of the non-conservative force models described here remove the effects of an annual signal. As can be seen by cross-referencing with Figure 11-6, it appears as though the drag modelling may contribute significantly to this effect as large adjustments to the drag coefficient appear to correlate quite well with the apparent trough in the first half of the year's orbits for the case with no NCF models. It is also during this first half of the year that the case with no NCF models appears to have improved across-track residuals, even after adjustment.

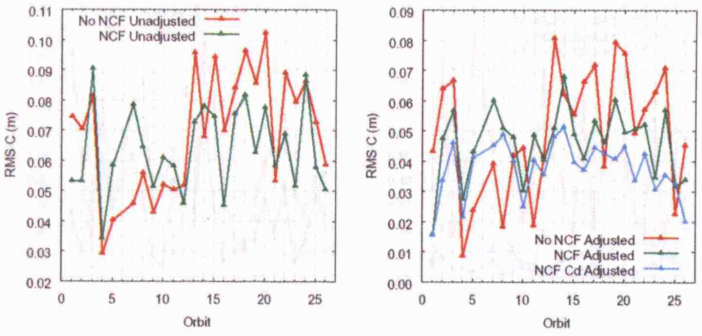

Figure 11-2: RMS across-track residuals over one orbit.

	No NCF Unadjusted	No NCF Adjusted	NCF Unadjusted	NCF Adjusted	NCF Cd Adjusted
Min	0.0295	0.0087	0.0344	0.0159	0.0156
Max	0.1024	0.0808	0.0905	0.0679	0.0513
Range	0.0729	0.0721	0.0561	0.0520	0.0357
Average	0.0693	0.0500	0.0638	0.0459	0.0376

Table 11-3: Summary statistics for the across-track residuals (in metres).

Adjusted no NCF across-track residuals change quite markedly throughout the year, having a range of c.73mm and a maximum of over 8cm. The spread of residuals for the Cd adjusted NCF case is far more compact, with a range of just c.36mm. However, attention should also be given to the NCF adjusted case (with no adjustment for Cd), as the spread of residuals has a range of just c.52mm with a maximum of c.68mm. These results are particularly significant for the current research as they demonstrate the effect that NCF models can have on across track residuals.

The along-track residuals tell a very similar story to the height residuals, showing clear improvements upon the introduction of NCF models, which perform exceptionally well after a full parameter set adjustment. It also appears that certain periods show clear trends in the pattern of the residuals for the NCF cases (particularly orbits 21 – 25).

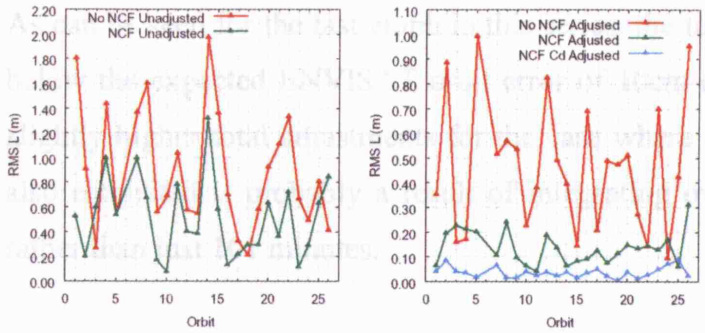

Figure 11-3: RMS along-track residuals over one orbit.

	No NCF Unadjusted	No NCF Adjusted	NCF Unadjusted	NCF Adjusted	NCF Cd Adjusted
Min	0.2107	0.0964	0.0802	0.0419	0.0061
Max	1.9760	0.9924	1.3182	0.3117	0.0890
Range	1.7653	0.8960	1.2380	0.2698	0.0829
Average	0.8912	0.4646	0.5139	0.1378	0.0382

Table 11-4: Summary statistics for the along-track residuals (in metres).

The following images show the individual components of the adjustments to the initial conditions which again appear to behave in a very similar fashion for all cases, which is especially apparent in the Z direction.

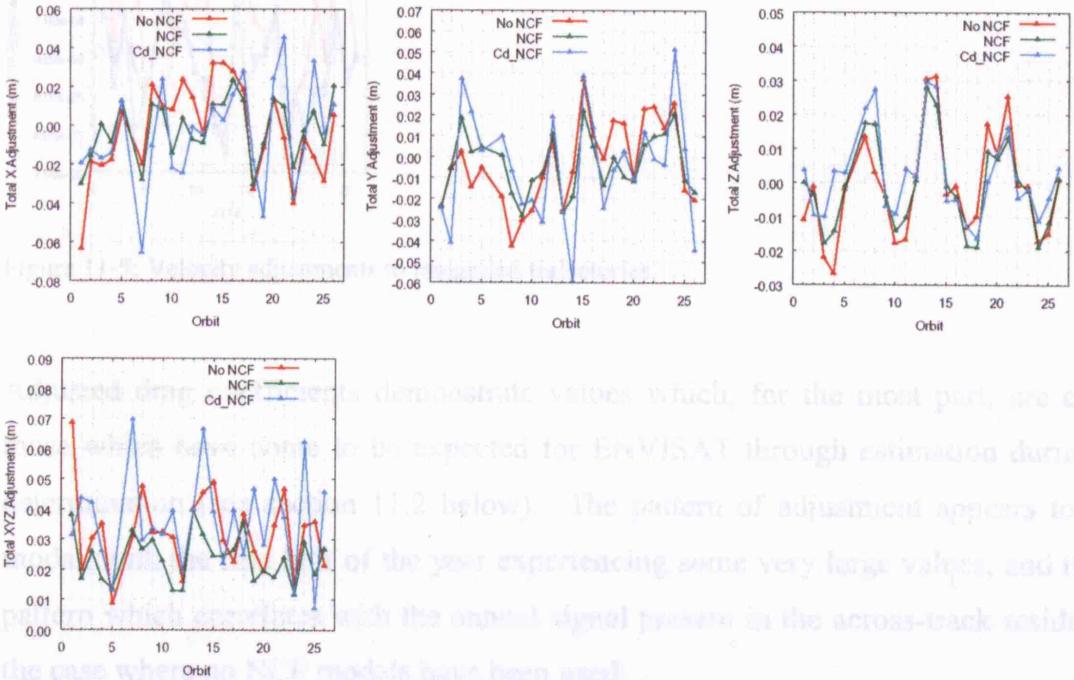

Figure 11-4: Positional adjustments to integrated trajectories.

As can be seen for the last graph in this series, the total XYZ adjustment is always well below the expected ENVISAT orbit error of 10cm (as outlined in section 2.2.2). The slightly higher total adjustments for the case where changes to the drag coefficient are also estimated is probably a result of integrating over the longer duration of 3 hours rather than just 101 minutes.

The velocity adjustments (Figure 11-5) are very small, almost always remaining below the level of one tenth of a millimetre per second, and again follow very similar patterns in all cases.

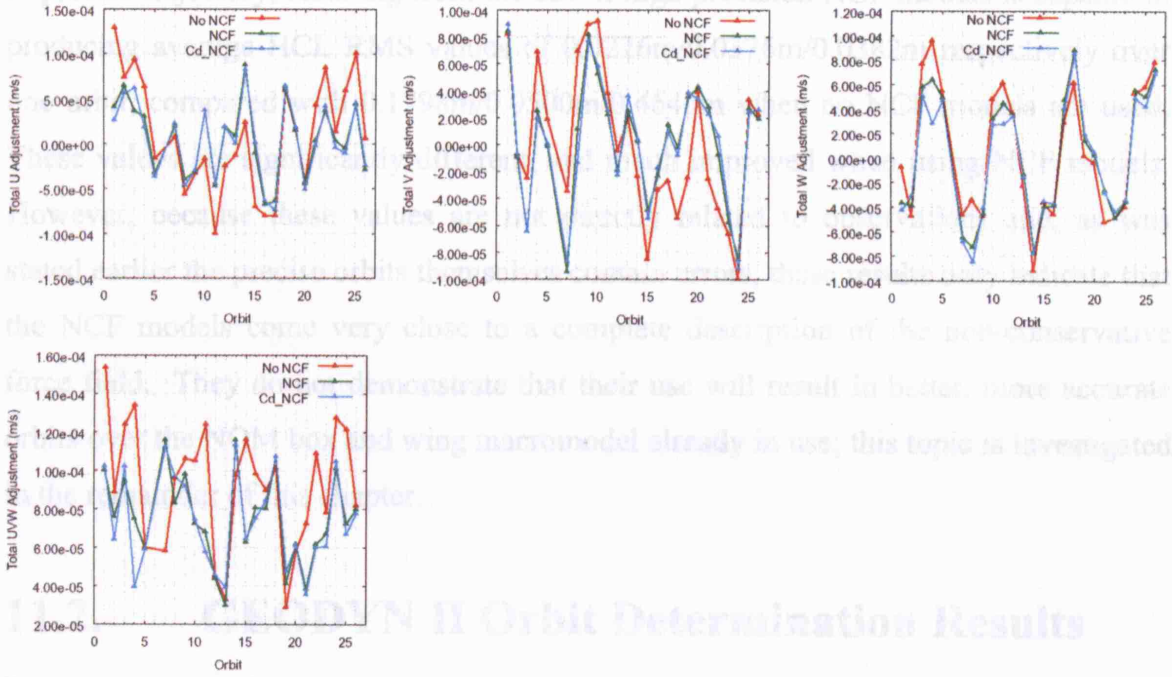

Figure 11-5: Velocity adjustments to integrated trajectories.

Adjusted drag coefficients demonstrate values which, for the most part, are close to those which have come to be expected for ENVISAT through estimation during orbit determination (see section 11.2 below). The pattern of adjustment appears to be bi-modal, with the first half of the year experiencing some very large values, and it is this pattern which correlates with the annual signal present in the across-track residuals for the case where no NCF models have been used.

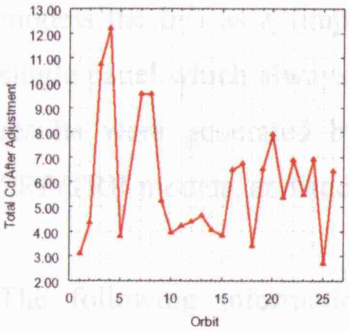

Figure 11-6: Total drag coefficient after adjustment (Nominal Cd = 2.25).

A precise trajectory, resulting from the use of high precision NCF models is capable of producing average HCL RMS values of 0.0226m/0.0376m/0.0382m respectively over one orbit, compared with 0.1798m/0.0500m/0.4646m when no NCF models are used. These values are significantly different, and much improved when using NCF models. However, because these values are not directly related to observations and, as was stated earlier the precise orbits themselves contain errors, these results only indicate that the NCF models come very close to a complete description of the non-conservative force field. They do not demonstrate that their use will result in better, more accurate orbits over the NOM box and wing macromodel already in use; this topic is investigated in the remainder of this chapter.

11.2. GEODYN II Orbit Determination Results

During a visit to NASA's Goddard Space Flight Centre (GSFC) over the Easter period of 2005, FORTRAN code written at UCL to model the ENVISAT attitude and non-conservative accelerations (due to solar radiation pressure, thermal re-radiation, Qrates and ASAR antenna thrust) was incorporated into GSFC's GEODYN II orbit determination software. GEODYN II was used to produce two different sets of orbits, the first uses only DORIS data to compute the solution, allowing SLR measurements to be used as truly independent observations. DORIS only orbit arcs were computed over the whole of the year of 2004 (04/01/2004 - 01/01/2005) by Frank Lemoine (GSFC). Nine selected arcs over 2003 and 2004 were also computed using a full DORIS and SLR dataset to generate the solutions. This study compares results from the UCL model against those achieved with a nominal (NOM) ENVISAT macromodel[32], which

[32] ftp://ftp.cls.fr/pub/ids/satellites/macromodels/en1mod.pdf

models the bus as a simple box consisting of six flat plates, and the solar array as a single panel which always points with its normal in the direction of the Sun. The UCL results were generated by replacing only the nominal bus/solar array attitude and SRP/TRR models, and adding in Qrate accelerations and antenna thrust.

The following information describes the general configuration of the GEODYN software as used in this analysis. A table of parameters, both fixed and estimated, are given in Table 11-5 below:

Parameter	Fixed	Estimated
SRP scale factor (Cr)	1.0	-
Macromodel parameters	Nominal values	-
Initial State (XYZUVW)	-	✓
Drag coefficient (Cd) – every six hours	-	✓
1CPR along-track (1 per day)	-	✓
1CPR across-track (1 per day)	-	✓
DORIS system timing bias	-	Apriori=0.0
DORIS pass-by-pass range-rate bias	-	✓
DORIS pass-by-pass troposphere bias	-	✓

Table 11-5: Parameters fixed and estimated during GEODYN ENVISAT orbit determination during this study.

Earth radiation pressure accelerations were modelled using the older Knocke & Ries (1987) model rather than the UCL approach (see section 5.6) as this new technique is not yet available as an operational service. Drag acceleration modelling again followed Eqn. (4.35) using the UCL attitude model to define the relative velocity vector, but used MSIS86 rather than the MET V2 atmospheric model for density terms. The effect of different gravity fields on computed ENVISAT orbits has been detailed in Table 4-2, and that which gave the best results (GGM01C) was used for the orbit determination results to degree and order 120. The IERS 2003 conventions (McCarthy & Petit, 2003) have been used to describe Earth tide effects, and JPL's GOT00.233 ocean tide model for all constituents was used to degree and order 30 including ocean loading for station geometric corrections. ITRF 2000 was used as the definition for the SLR station coordinates, while the DORIS station coordinate set was produced by Pascal Willis (NASA JPL) and John Ries (Texas A&M) (Willis & Ries, 2005). Atmospheric gravity

[33] http://sealevel.jpl.nasa.gov/science/invest-ray.html

terms were produced every 6 hours by the National Centers for Environmental Prediction's[34] (NCEP) model to degree and order 50.

11.2.1. DORIS Only Orbit Results 2004

11.2.1.1. Model Values

During the orbit determination process, NOM and UCL model values for solar radiation pressure, ERP and drag, decomposed along the HCL directions, are output to GEODYN "telem" files. As the ERP and drag models were identical for both the NOM and UCL cases, any differences in the final orbits must result from either differences in the remaining non-conservative forces between the two models, and/or changes in the modelled attitude of the satellite's solar array (the bus attitude model should be identical).

GEODYN "telem" data was available for ten 4-7 day arcs over the study period, and these are detailed in the following table:

Arc	Start	Arc	Start
1	04/01/2004	6	11/07/2004
2	11/01/2004	7	03/10/2004
3	04/04/2004	8	10/10/2004
4	11/04/2004	9	19/12/2004
5	04/07/2004	10	26/12/2004

Table 11-6: DORIS only arc epochs.

11.2.1.1.1. Modelled SRP Values

Owing to ENVISAT's Sun-synchronous orbit, the SRP scale factor (Cr) will be strongly correlated with estimated once-per-rev accelerations. Therefore this scale factor was fixed to unity for both models and GEODYN "telem" SRP accelerations can be compared like for like. Modelled SRP accelerations show the largest differences of all as can be seen in Figure 11-7, where the output accelerations are shown in full for each available arc. The Y-axis scales for both the NOM and UCL cases have been set to cover the same range of values.

[34] http://www.ncep.noaa.gov/

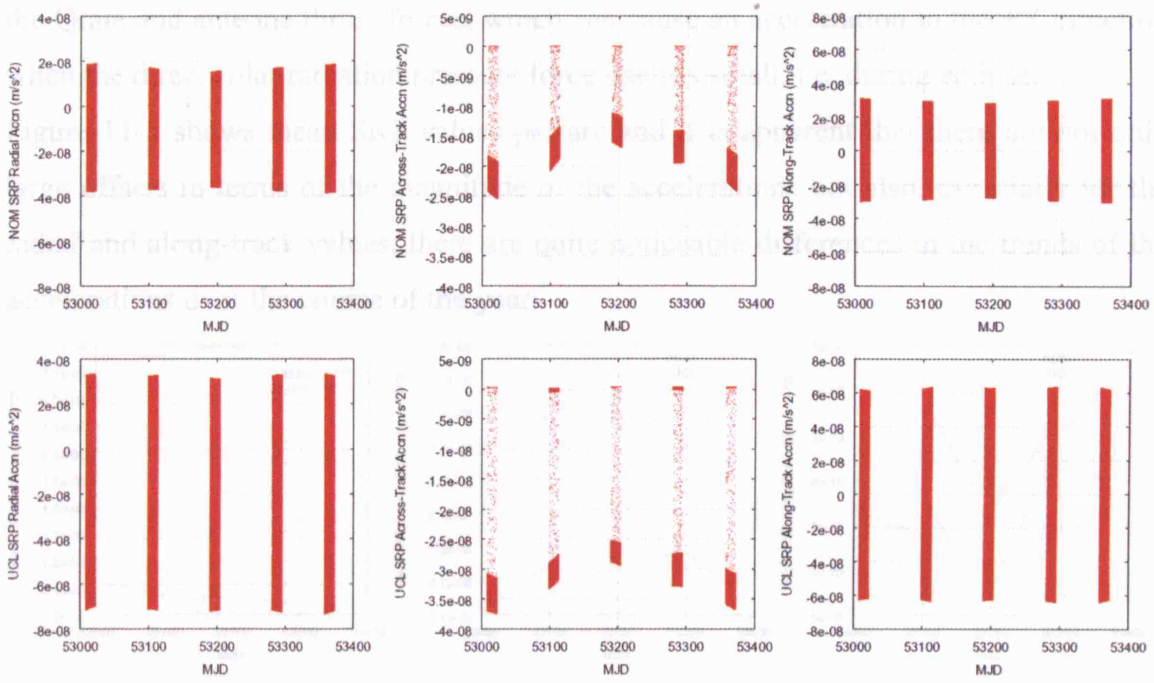

Figure 11-7: Output SRP accelerations for the NOM and UCL cases over the year of 2004.

It is immediately apparent that the total magnitude of the UCL SRP accelerations is almost twice that of the NOM SRP accelerations and in fact, post-fit estimation of Cr by Frank Lemoine (GSFC, pers comm.) gives a value for the macromodel of close to 1.991. Table 11-7 gives some general statistics for the modelled SRP accelerations.

	Min_Radial	**Max_Radial**	**Range_Radial**	**Avg_Radial**
SRP_NOM	-3.856E-08	1.878E-08	5.734E-08	-1.035E-08
SRP_UCL	-7.350E-08	3.334E-08	1.068E-07	-1.933E-08
	Min_Across	**Max_Across**	**Range_Across**	**Avg_Across**
SRP_NOM	-2.548E-08	0.000E+00	2.548E-08	-1.229E-08
SRP_UCL	-3.744E-08	3.126E-10	3.775E-08	-2.080E-08
	Min_Along	**Max_Along**	**Range_Along**	**Avg_Along**
SRP_NOM	-3.033E-08	3.103E-08	6.136E-08	5.150E-10
SRP_UCL	-6.419E-08	6.372E-08	1.279E-07	3.042E-10

Table 11-7: SRP model statistics for the NOM and UCL cases over 2004 (all values in m/s^2).

Apart from the sheer difference in the size of the modelled accelerations, another significant feature of the UCL model is that it shows a small but still important acceleration in the positive across track direction, while the NOM model goes no higher than zero. One of the reasons for this is that the GEODYN "telem" UCL 'SRP' accelerations also contain a thermal force component and very minor contributions from

the Qrate and antenna thrust forces, which can cause an acceleration in the +X direction when the direct solar radiation pressure force itself is small, i.e. during eclipse.

Figure 11-8 shows mean SRP values per arc and it is apparent that there are not only large offsets in terms of the magnitude of the accelerations but also, especially for the radial and along-track values, there are quite noticeable differences in the trends of the accelerations over the course of the year.

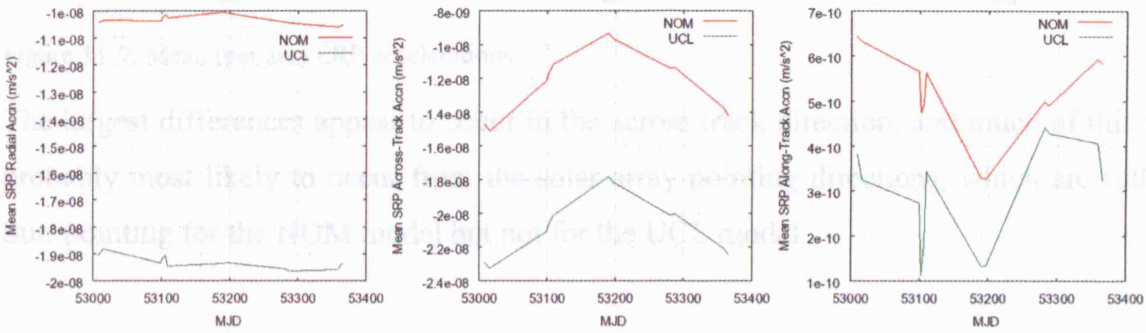

Figure 11-8: Mean (per arc) SRP accelerations.

11.2.1.1.2. Modelled ERP Values

As might be expected, due to the use of the same ERP model for the two orbit solutions, only very small differences are evident due to slight variations in position and attitude for a given epoch.

	Min_Radial	Max_Radial	Range_Radial	Avg_Radial
ERP _NOM	2.377E-09	2.043E-08	1.805E-08	8.443E-09
ERP _UCL	2.378E-09	2.042E-08	1.805E-08	8.443E-09
	Min_Across	**Max_Across**	**Range_Across**	**Avg_Across**
ERP _NOM	-6.863E-10	6.564E-10	1.343E-09	1.701E-10
ERP _UCL	-6.797E-10	6.599E-10	1.340E-09	1.720E-10
	Min_Along	**Max_Along**	**Range_Along**	**Avg_Along**
ERP_NOM	-2.986E-09	6.850E-09	9.836E-09	8.808E-10
ERP _UCL	-2.986E-09	6.849E-09	9.835E-09	8.807E-10

Table 11-8: ERP model statistics for the NOM and UCL cases over 2004 (all values in m/s^2).

The following figure confirms this, by showing ERP values averaged over each arc (each arc nominally between 4-7 days in length) and displayed for the NOM and UCL cases over the year of 2004.

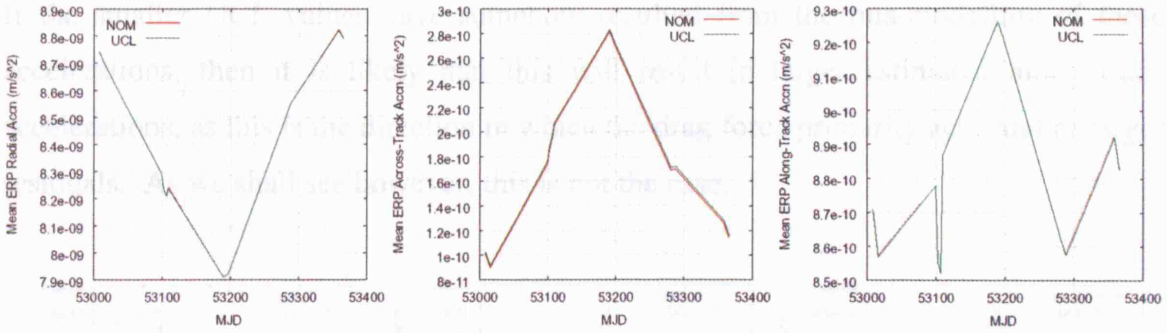

Figure 11-9: Mean (per arc) ERP accelerations.

The largest differences appear to occur in the across track direction, and much of this is probably most likely to occur from the solar array pointing directions, which are fully Sun-pointing for the NOM model but not for the UCL model.

11.2.1.1.3. Modelled Drag Values

Modelled atmospheric drag accelerations for the two cases however are quite different particularly in the along and across-track directions. This is to be expected as these will be heavily dependent upon changes in the attitude of the solar array; the NOM array normal is fixed at 8° off the Sun direction, while the UCL array normal can have a separation from the Sun direction of between c.0-15° using the model defined in section 8.1.3. It may also be true that the larger NOM accelerations are a result of aliasing through the mis-modelling of other forces such as SRP (see below for more on this).

	Min_Radial	**Max_Radial**	**Range_Radial**	**Avg_Radial**
DRA_NOM	-1.106E-11	2.608E-11	3.714E-11	1.639E-12
DRA_UCL	-1.065E-11	2.510E-11	3.575E-11	1.563E-12
	Min_Across	**Max_Across**	**Range_Across**	**Avg_Across**
DRA_NOM	-1.267E-09	4.583E-10	1.726E-09	-9.272E-11
DRA_UCL	-1.220E-09	4.412E-10	1.661E-09	-8.838E-11
	Min_Along	**Max_Along**	**Range_Along**	**Avg_Along**
DRA_NOM	-2.256E-08	-5.508E-10	2.201E-08	-5.625E-09
DRA_UCL	-2.205E-08	-5.156E-10	2.153E-08	-5.360E-09

Table 11-9: Drag model statistics for the NOM and UCL cases over 2004 (all values in m/s^2).

Table 11-9 shows that the ranges of the modelled UCL drag accelerations are systematically smaller than those of the NOM model, as are the maximum, minimum and average values. The figure below shows the mean drag accelerations for each arc.

The fact that the range of the Cd coefficients is smaller for the UCL orbits implies that: 1. the atmospheric neutral density is slightly more stable than has been previously assumed, and 2. that the modelled atmospheric densities may represent the physical state of the atmosphere marginally better than is currently believed (see section 4.3.2). Estimated Cd values for the whole of 2004 can be seen in Figure 11-11, alongside are 6 hourly Cd estimates over just one 7 day arc.

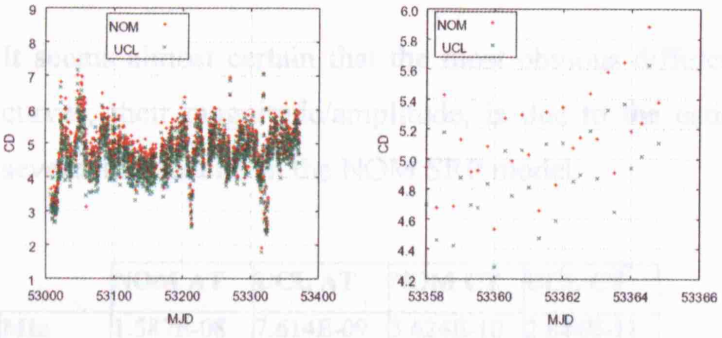

Figure 11-11: Estimated Cd – the left-hand image shows NOM and UCL Cd values over 2004, the right-hand image shows these values over a single 7 day arc beginning on the 19/12/2004.

11.2.1.1.5. Estimated General Along and Across Track Accelerations

GEODYN II estimates once per revolution along and across-track accelerations in a least squares sense (minimises the sum of the squared observation residuals) using the following Fourier series (where θ is the argument of latitude):

$$\ddot{r} = a_1 \cos\theta + b_1 \sin\theta = c_1 \sin(\theta + \varphi) \tag{11.1}$$

The amplitude of the resultant accelerations, which can be seen across the whole of 2004 in Figure 11-12, is given by (Stroud, 1996):

$$|\ddot{r}| = \sqrt{\left(a_1^2 + b_1^2\right)} \tag{11.2}$$

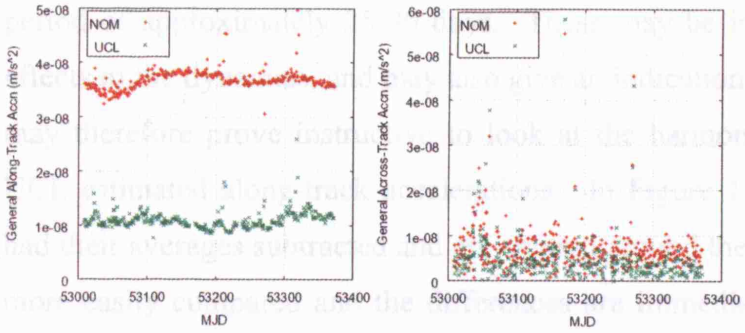

Figure 11-12: General along and across-track acceleration amplitudes over 2004.

It seems almost certain that the most obvious difference between the two along track curves, their magnitude/amplitude, is due to the estimated values having to soak up severe deficiencies in the NOM SRP model.

	NOM AT	UCL AT	NOM CT	UCL CT
Min	1.587E-08	7.614E-09	3.624E-10	2.844E-11
Max	4.969E-08	2.593E-08	5.458E-08	5.771E-08
Range	3.381E-08	1.831E-08	5.422E-08	5.768E-08
Average	3.606E-08	1.110E-08	6.938E-09	4.810E-09

Table 11-11: Summary statistics for estimated NOM and UCL along-track (AT) and across-track (CT) general acceleration magnitudes (all values in units of m/s^2).

It is apparent that the UCL values are much reduced in magnitude on average in both the along and across-track directions, and the along-track values particularly are much reduced in range; this is a testament to the improved fidelity and accuracy of the UCL models. Section 11.2.1.1.3 mentions that larger estimated UCL along-track accelerations would be expected if the UCL NCF model were wrong, but that is certainly not the case! This is supported by results from a very early test of the model in GEODYN II which predicted a four day arc using both NOM and UCL models, in which no once per revolution terms were estimated. Weighted RMS SLR residuals were on the order of 4m for the NOM model, but only c.70cm for the UCL model.

The NOM along-track magnitudes also display a rather irregular and unidentifiable pattern, while the UCL values show a more coherent structure with both a shallow long wavelength annual signal plus reasonably clear shorter wavelength signals with a repeat

period of approximately 25-30 days. These may be indicative of further unmodelled effects in the dynamics, and may also give an indication of *what* may be unmodelled. It may therefore prove instructive to look at the harmonic signatures of the NOM and UCL estimated along-track accelerations. In Figure 11-13 below, both datasets have had their averages subtracted and are centred around the origin in order that they can be more easily compared and the differences are immediately apparent, being somewhat highlighted by the change in the scale of the y-axis with respect to Figure 11-12.

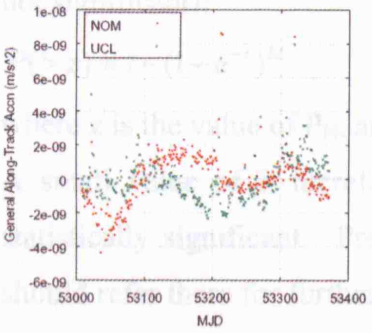

Figure 11-13: Comparison of the NOM and UCL estimated along-track acceleration amplitudes after the mean of each time series has been removed.

A traditional approach to numerically recovering the periods apparent to the eye in these data series would be to plot a periodogram (power v_s frequency) using a fast Fourier transform (FFT). However, a FFT operates under the assumption that the data passed to it is sampled at regular time intervals. Here, we are hampered by the fact that while the data spans 364 days, only 325 samples are available for analysis due to there being several missing arcs. Attempts to interpolate missing data or to pad the time series with zeros are common, but not rigorous, and can lead to spurious powers at low frequencies (Press et al., 2002). Instead, Press et al. (2002) offer an alternative, the Lomb-Scargle method, which evaluates sine and cosine terms only at times when data is available and also makes it simple to generate significance levels for any peaks in the resultant power spectrum ($P_N(\omega)$):

$$P_N(\omega) \equiv \frac{1}{2\sigma^2}\left\{\frac{\left[\sum_j (h_j - \bar{h})\cos\omega(t_j - \tau)\right]^2}{\sum_j \cos^2\omega(t_j - \tau)} + \frac{\left[\sum_j (h_j - \bar{h})\sin\omega(t_j - \tau)\right]^2}{\sum_j \sin^2\omega(t_j - \tau)}\right\} \qquad (11.3)$$

where P_N is the spectral power, ω is the angular frequency (=$2\pi f$, f=frequency), h_j represents the individual data values, $\bar{h}$ is the mean of these data values, σ^2 is the variance of the data, t_j is the time at measurement j, τ is defined by $\tan(2\omega\tau)=\sum_j \sin 2\omega t_j / \sum_j \cos 2\omega t_j$.

As $P_N(\omega)$ has an exponential distribution with a unit mean, significance levels can be generated from the following which assumes the null hypothesis (i.e. a particular peak is not significant):

$$P(>z) \equiv 1-(1-e^{-z})^M \tag{11.4}$$

where z is the value of P_N, and M is the number of frequencies evaluated.

A small value of P therefore indicates that the power of a particular frequency is statistically significant. Press et al. (2002) outline the technique in full, and readers should refer there for further details. Figure 11-14 and Figure 11-15 display the results of the Lomb-Scargle algorithm for the NOM and UCL values. For both cases, the periods are shown only for those frequencies which exceed a significance level of 0.05 (i.e. a confidence level of 95%). The NOM data may reflect a seasonal influence in its c.95 day period, but the remaining periods do not immediately suggest a physical explanation. Accelerations from the UCL model have a very long period of c.454 days, though this may possibly be somewhat spurious as the data only covers 364 days. The other periods may result from seasonal and monthly variations in a force such as drag.

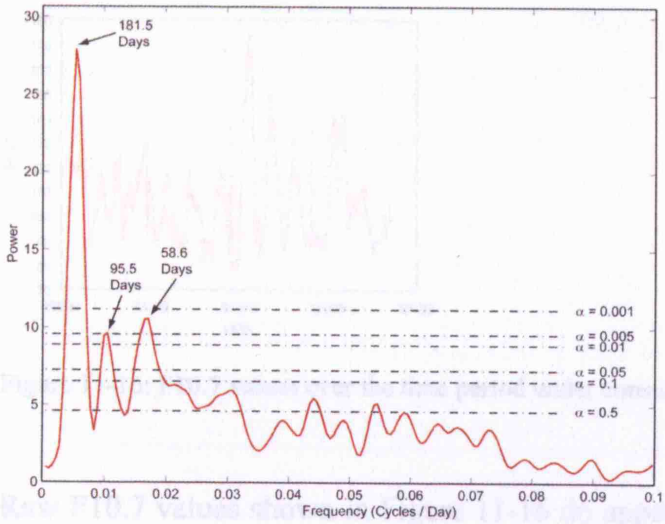

Figure 11-14: Lomb-Scargle normalised periodogram of NOM general along-track accelerations. Alpha values indicate significance levels.

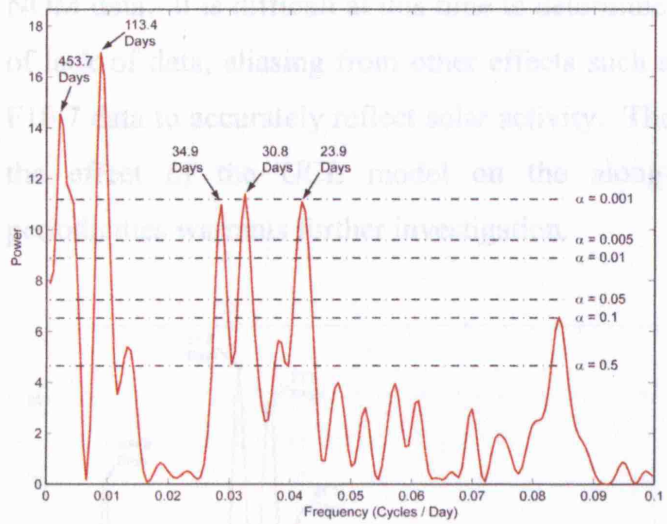

Figure 11-15: Lomb-Scargle normalised periodogram of UCL general along-track accelerations. Alpha values indicate significance levels.

One of the problems however in identifying exactly what is responsible for these periodicities is that they may come from sources for which we currently have only incomplete data, such as the solar radio noise flux F10.7 index used as a proxy for solar extreme ultraviolet flux (the activity of which is linked to the solar differential rotation period of c.25-35 days (Forbes et al., 2006)). It is important to consider F10.7 however, as this is an input into atmospheric density models which will significantly affect the modelled drag force.

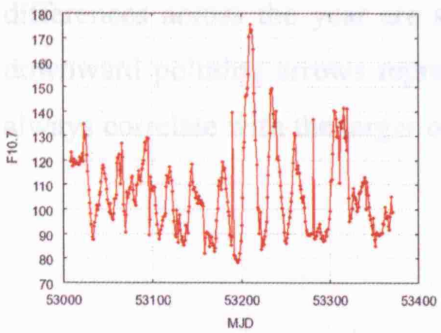

Figure 11-16: F10.7 values over the time period under consideration.

Raw F10.7 values shown in Figure 11-16 do appear to have similar periods to the UCL estimated along-track accelerations, and at first glance its power spectrum (Figure 11-17) has many similarities to that of the UCL accelerations. There are however also

obvious differences, and the c.60 day period may correspond to a similar period in the NOM data. It is difficult at this time to determine whether these differences are a result of lack of data, aliasing from other effects such as ERP, or simply the inability of the F10.7 data to accurately reflect solar activity. Though I believe that this data show that the effect of the UCL model on the along-track accelerations magnitude and periodicities warrants further investigation.

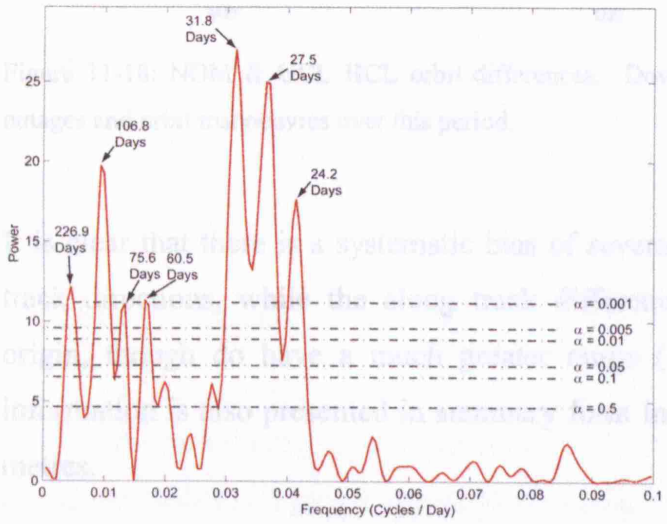

Figure 11-17: Lomb-Scargle normalised periodogram of F10.7. Alpha values indicate significance levels.

11.2.1.1.6. HCL Orbit Differences

The vector separating the 2004 orbits produced with the NOM and UCL models was calculated every 2 minutes, and then decomposed into the HCL directions. The differences across the year are shown in Figure 11-18, where it can be seen that the downward pointing arrows representing DORIS outages and orbit manoeuvres do not always correlate with the larger orbit differences.

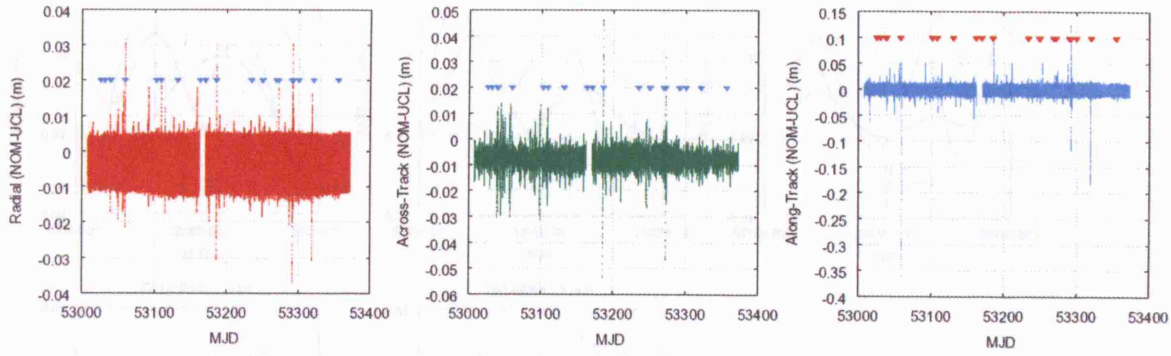

Figure 11-18: NOM & UCL HCL orbit differences. Downward pointing arrows indicate all DORIS outages and orbit manoeuvres over this period.

It is clear that there is a systematic bias of several millimetres in the radial and across track directions, while the along track differences are more symmetrical about the origin, though do have a much greater range (note the scales of the plots). This information is also presented in summary form in Table 11-12, where all values are in metres.

	Radial (H)	Across (C)	Along (L)
Min	-0.0371	-0.0535	-0.3593
Max	0.0315	0.0462	0.1242
Range	0.0686	0.0998	0.4835
Average	-0.0028	-0.0079	-0.0005
RMS	0.0057	0.0086	0.0090

Table 11-12: Summary statistics for NOM-UCL HCL differences (all values in units of metres).

The next set of plots (Figure 11-19) show HCL differences over single orbits for which GEODYN "telem" data exists. These orbits begin at the point when the argument of latitude is closest to zero, and so should be 'synchronised' with each other.

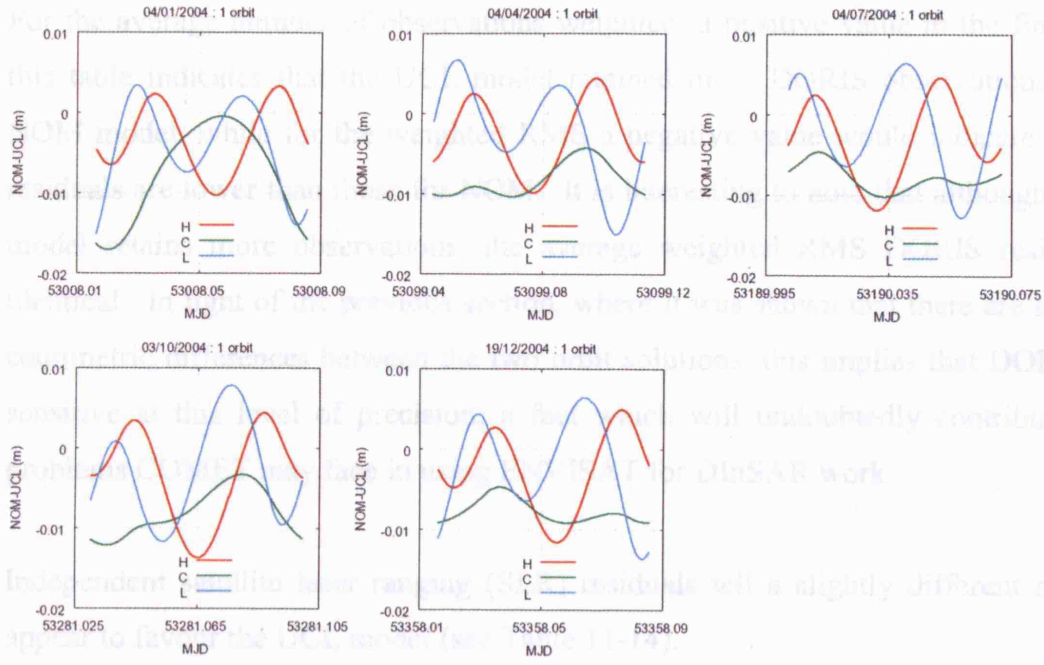

Figure 11-19: Single orbit HCL differences.

The height differences remain remarkably similar throughout, while clear changes in phase, amplitude and period appear in the across and along-track differences throughout the year.

11.2.1.1.7. DORIS and SLR Residuals

The following table (Table 11-13) shows the average number of DORIS observations retained by each model scheme (i.e. values are the averages for all arcs determined over 2004), and also average RMS DORIS residuals for 2004[35], where each RMS value is computed per arc.

	No. Obs	No. Wtd.	Wtd. RMS (cm/s)
NOM	25911.4203	25504.0725	0.0545
UCL	25911.4203	25506.7391	0.0545
UCL-NOM	0.0000	2.6667	0.0000

Table 11-13: Average DORIS RMS residuals.

[35] Onboard software updates cause a significant improvement in DORIS residuals after 12th October 2004.

For the average number of observations weighted, a positive value in the final row of this table indicates that the UCL model retained more DORIS observations than the NOM model, while for the weighted RMS a negative value would indicate that UCL residuals are lower than those for NOM. It is interesting to note that although the UCL model retains more observations, the average weighted RMS DORIS residuals are identical. In light of the previous section, where it was shown that there are systematic centimetric differences between the two orbit solutions, this implies that DORIS is not sensitive at this level of precision; a fact which will undoubtedly contribute to any problems COMET may face in using ENVISAT for DInSAR work.

Independent satellite laser ranging (SLR) residuals tell a slightly different story, and appear to favour the UCL model (see Table 11-14).

	No. Obs.	No. Wtd.	Wtd. RMS (m)
NOM	854.8261	853.5797	0.0515
UCL	854.8261	853.5797	0.0502

Table 11-14: Average SLR RMS residuals.

Although there is no difference in the number of observations retained, this is not particularly surprising as there are far fewer SLR observations compared to DORIS. However, the UCL SLR residuals show a systematic improvement of over 1mm RMS. A plot of the RMS residuals (Figure 11-20) over all of the arcs investigated reveals that the UCL residuals are generally smaller than the NOM values by between 0-2mm.

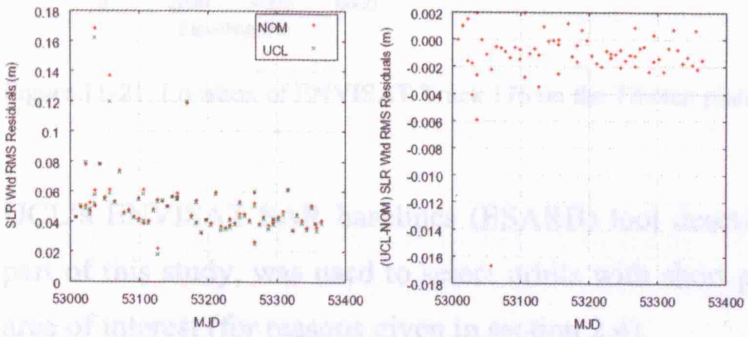

Figure 11-20: SLR weighted RMS residuals for the NOM and UCL orbits.

11.2.2. DORIS & SLR COMET Baseline Orbit Results

In order to investigate the effect of upgrading the non-conservative force models on SAR Interferometry, a small group of "best possible" orbits solutions using combined DORIS and SLR observations were computed. These most closely represent the type of ENVISAT orbit solutions in use by the SAR community at the present time. Both NOM and UCL orbits will be used to process SAR interferograms over the region of interest, for which COMET has chosen the Tibetan plateau and the Himalayas, the most active intracontinental mountain range on Earth. The extent of the SAR imagery recoverable from orbit track 176, shown in Figure 11-21 which covers this area, is over c.100km wide and c.1300km in the along-track direction. At the time of writing, it has not been possible to conduct the SAR interferometry tests, so the present section concentrates on analysing the combined orbit solutions themselves.

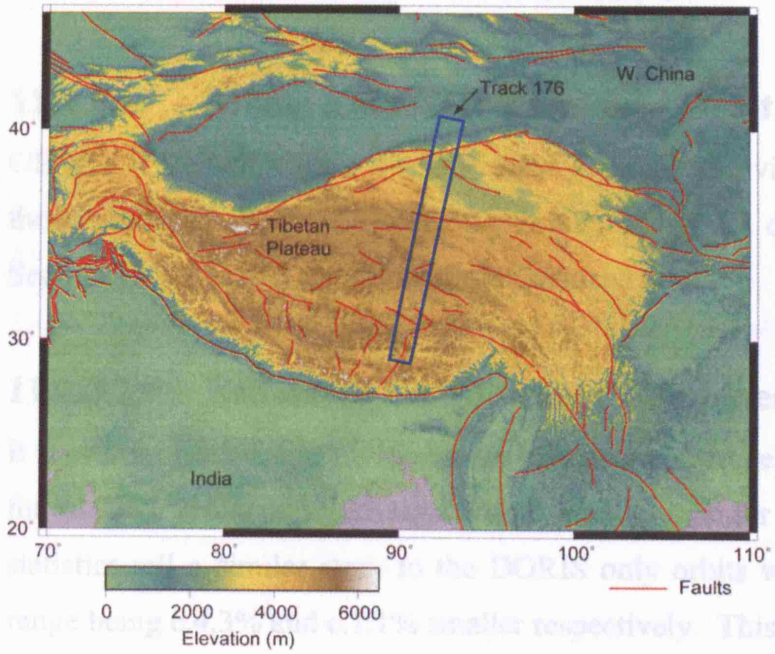

Figure 11-21: Location of ENVISAT Track 176 on the Tibetan plateau[36].

UCL's ENVISAT SAR baselines (ESARB) tool described in Appendix D, written as part of this study, was used to select orbits with short perpendicular baselines over the area of interest (for reasons given in section 2.4).

[36] Image information provided by Dr Tim Wright, University of Oxford.

Baseline Group 1	Baseline Group 2
11/05/2003	06/04/2003
11/01/2004	15/06/2003
30/05/2004	20/07/2003
	28/09/2003
	07/12/2003
	15/02/2004

Table 11-15: DORIS & SLR orbit groups.

The remaining sections highlight specific details concerning the NOM and UCL orbits, in a manner similar to section 11.2.1 of this chapter.

11.2.2.1. Model Values for Combined Orbit Solutions

GEODYN "telem" values for SRP, ERP and drag are virtually indistinguishable from those produced for the DORIS only orbits, which are discussed in detail above (see Section 11.2.1.1) and so will not be reproduced here.

11.2.2.2. Estimated Cd Values for Combined Orbit Solutions

It is evident from Table 11-16 that the maximum, average and range of values estimated for the UCL orbits are again significantly smaller than for the NOM case. The summary statistics tell a similar story to the DORIS only orbits with the UCL Cd average and range being c.4.3% and c.1.1% smaller respectively. This group of orbits, which extend the period of investigation to cover much of 2003, provide further support for the assertion above that: 1. the atmospheric neutral density is not as chaotic as has been previously assumed, and 2. that the modelled atmospheric densities may better represent the physical state of the atmosphere than is currently believed.

	NOM	UCL
Min	2.685	2.492
Max	6.961	6.721
Range	4.276	4.229
Average	4.456	4.266

Table 11-16: Drag coefficient statistics for the NOM and UCL orbits.

11.2.2.3. HCL Orbit Differences for Combined Orbit Solutions

The systematic bias on the order of 1cm in the radial, across and along-track directions, first identified in Section 11.2.1.1.6, can be seen to persist (Table 11-17 & Figure 11-22).

	Radial (H)	Across (C)	Along (L)
Min	-0.0153	-0.0427	-0.0304
Max	0.0084	0.0240	0.0183
Range	0.0237	0.0666	0.0487
RMS	0.0055	0.0102	0.0078

Table 11-17: Summary statistics for NOM-UCL HCL DORIS & SLR differences (all values in metres).

Larger differences also occur, and these again do not appear to correlate fully with DORIS outages and / or orbit manoeuvres.

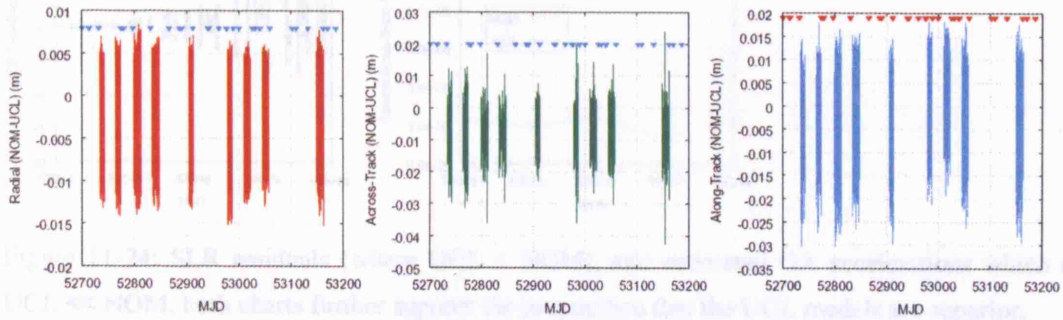

Figure 11-22: NOM & UCL HCL DORIS & SLR orbit differences. Downward pointing arrows indicate all DORIS outages and orbit manoeuvres over this period.

Differencing over MJD's 52976 and 52977 produced very large HCL values (NOM-UCL), which reach up to 1.2m along track (see Figure 11-23), a signature which also appears in the height differences. In this case, it does appear that the large differences

can be traced to a DORIS outage: coverage stops at 03/12/2003 07:28, and does not pick up again until 04/12/2003 at 00:00.

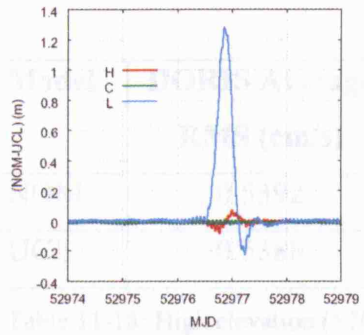

Figure 11-23: HCL differences (NOM-UCL) during DORIS data outage.

Determining which orbit is more accurate over the outage period is difficult[37], as the main source of tracking data has failed, and SLR data is very sparse. However, if it could be proven that either the NOM or UCL orbits were more accurate during these situations, then this might be very useful for applications which require near real-time operational orbits, such as altimetry. As mentioned in section 11.2.1.1.5, early tests in GEODYN II suggest that the UCL model will produce more accurate orbits when tracking data is unavailable and, as shown in Figure 11-24, the UCL orbits appear to results in smaller SLR residuals and estimated along-track accelerations than the NOM orbits.

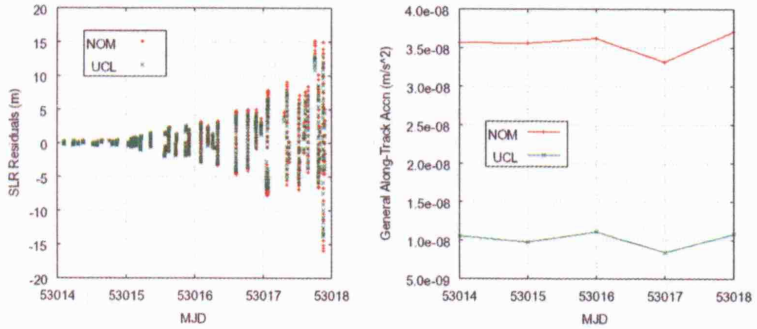

Figure 11-24: SLR residuals (where UCL < NOM), and estimated GA accelerations which show that UCL << NOM, both charts further support the proposition that the UCL models are superior.

11.2.2.4. DORIS and SLR Residuals for Combined Orbit Solutions

All of the residuals show small but systematic improvements when using the UCL model compared with the NOM model. In particular, high elevation SLR fits (using

[37] Altimeter crossovers may provide a method for assessing the accuracies of orbits during such periods.

only SLR data > 70° elevation), which give a more direct measure of radial orbit error, show a 1mm RMS improvement in the residuals when the UCL model is used.

Model	DORIS Average RMS (cm/s)	SLR Average RMS (m)	SLR Average RMS > 70° (m)
NOM	0.5392	0.0188	0.0195
UCL	0.5388	0.0182	0.0185

Table 11-18: High elevation (>70°) DORIS and SLR residuals.

11.3. Summary

This chapter has shown that high precision non-conservative force models can result in more accurate orbits and can dramatically reduce the size of estimated soak-up parameters which should result in less aliasing into observations made by the satellites and can also improve attempts to reconstruct the neutral atmospheric density. These results have now led to this model being included in JPL's GIPSY-OASIS II software (June 2006), for which tests will be conducted in the near future.

12. Conclusions and Future Work

This concluding chapter begins with a review of the work conducted throughout this research project. Next, the principal conclusions and implications of results arising from this work are presented, and finally future areas of research are considered.

12.1. Review

The problem statement presented in section 1.1 proposes that a priori high-precision analytical modelling of non-conservative forces for low Earth orbiting satellites will:

- reduce the need for soak-up parameters
- reduce aliasing
- improve the overall accuracy of final orbit solutions.

The following questions shape the way the research to address these problems is conducted:

- How can we efficiently compute high precision non-conservative force models for very large and complex low Earth orbiting satellites?
- What effect do high precision non-conservative force models have on once-per-revolution empirical 'soak-up' parameters?
- Do these high precision models improve overall orbit accuracy?

Part I of the thesis begins with a detailed investigation of how orbital errors can impact upon synthetic aperture radar measurements such as those made by ENVISAT, our test case satellite. This provides a concrete example of how poor knowledge of a satellite's position (i.e. due to unmodelled effects) can impact directly upon the quality of any resultant observations. It is also shown that current ENVISAT orbits are almost certainly incapable of providing the level of accuracy required by the InSAR community (50mm across track). A literature review highlights some severe deficiencies in current approaches to non-conservative force modelling, yet also singles out one technique that serves to underpin many of the developments made during this research (UCL_SRP - Ziebart, 2004). Chapter 4 outlines the conservative and non-conservative forces which affect LEO satellites. Existing methods used during this

research for modelling certain non-conservative forces (SRP, TRR and atmospheric drag) are described in detail.

Part II of the thesis focuses specifically upon improvements made to existing methods which allow the extremely efficient and highly precise modelling of very large and complicated satellites. Advanced techniques for modelling additional non-conservative forces (Qrates, ERP and Antenna thrust) are introduced. Details of block modelling methods (a rapid ray intersection rejection procedure), are given and implemented, without which the modelling of radiation pressure forces on a satellite such as ENVISAT is computationally prohibitive. A graphical tool is developed which provides an interface to a potentially unlimited number of satellites. The software contains functionality critical to ensure high levels of quality control when modelling complicated spacecraft, and can also aid in rapid model development for any satellite. Chapter 8 investigates ENVISAT's published attitude model, noting its importance in defining the pointing directions of the body-fixed axes, the normal to the solar array, and the location of the phase centre of ENVISAT's DORIS antenna. Deficiencies in the published attitude model are corrected and additional components are developed and validated, the revised attitude model is then used to demarcate those regions of ENVISAT's body-fixed coordinate space over which non-conservative force model values are computed. A new eclipse boundary algorithm is developed which models the Earth as an oblate spheroid, especially important for the accurate modelling of SRP and TRR forces acting on a satellite. Tests prove that it performs significantly better in terms of efficiency and accuracy than existing published models

In Part III, results of extensive testing of the models developed during the course of this study, performed both at UCL and by staff at NASA's Goddard Space Flight Centre, are presented and analysed. High precision non-conservative force models are shown to result in more accurate orbits and dramatically reduce the size of estimated soak-up parameters. The attitude, SRP, TRR, Qrate and antenna thrust models developed herein have now been included in NASA JPL's GIPSY-OASIS II software as a direct result. The principal conclusions of this study are now presented in the following section.

12.2. Conclusions

We are now in a position to directly address the problem statement presented in section 1.1:

- The viewer tool developed during this research ensures high levels of quality control and allows more rapid model development during the geometric modelling phase for large and complicated LEO spacecraft.
- Block modelling tools can reduce model runtime (i.e. the time taken to compute the initial model) by an order of magnitude, from several days to several hours, giving researchers more freedom to experiment with different configurations.
- The viewer and block modelling tools have already shown good results when applied to other satellites including GPS-IIR satellites (Adhya, 2005) which have an orbital altitude of c.20,000 km (medium Earth orbit).
- The high precision non-conservative force models have demonstrated a capacity for significantly reducing the size of once-per-revolution empirical 'soak-up' parameters. Average along-track accelerations for ENVISAT have been reduced from 3.606E-08 m/s^2 to just 1.110E-08 m/s^2 (i.e. reduced by a factor of 3), while average across-track accelerations have been reduced from 6.938E-09 m/s^2 to 4.810E-09 m/s^2 (i.e. reduced by a factor of c.3/2). In section 3.3 it was noted that an alternative non-conservative force modelling software (ANGARA) produced very limited differences in tracking residuals and once-per-revolution estimated accelerations compared to a box-and-wing model (Doornbos et al., 2002). This contrasts markedly with the results achieved for ENVISAT during the current study.
- ENVISAT's atmospheric drag model in GEODYN II remained unaltered, yet the other UCL models (SRP, TRR, Qrate, antenna thrust, attitude), computed solely by this author during the current research project, reduced aliasing into the drag coefficient term. The absolute range of drag coefficient values was reduced by 2.8%, whilst the average drag coefficient value was reduced by 4.6%.
- The new UCL ENVISAT models, developed by this author during the current project, result in more accurate final orbit solutions. More DORIS observations are retained and independent satellite laser ranging shows that UCL RMS residuals are systematically smaller than those generated by use of the previous

model (developed by CNES, referred to here as the NOM model) by between 1-2mm.

Orbit prediction proved to be a good test of model fidelity, presaging the performance of the new UCL ENVISAT models during orbit determination in GEODYN II. In fact, the prediction results suggest that there is more mileage to be had from the complete suite of ENVISAT models, as it was not possible to incorporate the Earth Radiation Pressure (ERP) models into GEODYN during the time at hand. Modelled SRP is almost double that produced by the NOM model; alongside an estimated scale factor of 1.991 for the NOM model this is additional evidence that the UCL model is accurately delivering the higher fidelity SRP accelerations in the radial, across-track and along-track directions.

Independent SLR residuals favour the UCL model, but HCL orbit differences are systematically different at a level of only c.1cm RMS. When considered in tandem with the dramatic differences between the sizes of estimated once-per-revolution empirical soak-up parameters these results may appear to be somewhat disappointing. However, they do confirm that improved non-conservative force models can improve orbit accuracy, and can provide greater confidence in the final orbit solutions. Also, it suggests that perhaps the level of accuracy achieved by the ENVISAT orbits is limited by the capabilities of the current DORIS tracking network. The GRACE gravity mission's GPS derived orbit radial accuracy is only marginally worse than ENVISAT's, and yet they fly at an altitude which is 300km lower and will be subject to greater ERP and drag forces. DORIS provides orbits with a radial accuracy of about 2.5cm RMS for the JASON satellite at 1300km, whilst GPS tracking produces 1cm radial orbits for JASON when tested using independent laser ranging.

12.3. Further Work

Neutral atmospheric density models have been shown in this study to be less problematic than was once thought, as large estimated along-track accelerations (approximately parallel to the direction of the drag force) and the ranges of estimated drag coefficients are at least partly due to the aliasing of other mis-modelled effects. However, it is likely that atmospheric drag modelling is one area in which advances

could result in significant improvements to the accuracy of final orbit solutions for LEO satellites. Atmospheric density models still perform rather poorly at an altitude of 800km, and significant variations in the pattern of estimated drag coefficient values during orbit prediction and orbit determination tests appear to show that the atmospheric model used fails to capture temporal variation in the neutral atmosphere. Greater effort should be put into researching new drag modelling techniques to take account of the fact that the impact surfaces are not simply flat plates, and the international space weather community should produce new geomagnetic indices with increased spatial and temporal resolution. Observed periodicities in the along-track accelerations estimated for the UCL model may offer additional information about future modelling requirements. Additional work could be conducted during periods of higher solar activity than that experienced during 2004 in order to further test the efficacy of the UCL model.

The ERP models described in this thesis make use of monthly averaged CERES measurements of longwave and shortwave radiation emitted and reflected by the Earth in the form of 'total-sky' (cloudy and non-cloudy) data. These models would no doubt benefit tremendously from an instantaneous global coverage of satellites making the required measurements. In particular, we would be able to more accurately model the effect of cloud cover on shortwave radiances. One benefit that it is possible to realise in the very near future is the inclusion of these new ERP models in an orbit determination package such as GEODYN II or GIPSY-OASIS II.

It is recommended that in-depth analysis of altimetry crossover residuals will provide a means to independently check different orbit solutions, and thus help to assess the quality of non-conservative force models. Such testing may also be used during periods of tracking data outages (e.g. DORIS, see section 11.2.2.3) to evaluate orbits wholly or largely reliant upon prediction techniques. However, it should be borne in mind that relevant space agencies are often reluctant to supply geophysical data obtained during such periods.

Ideally a standard CAD format such as STEP or IGES should be used to capture satellite geometry. This would vastly increase the number of software packages able to read and display the contents, and allow for easier transfer of information between

agencies and research groups. The biggest problem at the present time however is the issue of how best to represent attribute metadata for component details such as group, optical properties and general comments. CAD data specifications are improving in this regard all the time however, and it is likely that such a step may be possible in the next few years.

12.3.1. A Final Comment

It appears as though we can attribute much of ENVISAT's lack of required orbit accuracy to the tracking system it uses, with its relatively poor observing geometry and problems due to the frequency bias in the DORIS antenna. For InSAR specialists, the good news lies in the fact that dedicated SAR missions are currently being developed, several by the Chinese, and one by the Germans called TerraSAR-X. TerraSAR-X is an X-band (3.1cm wavelength) satellite which should be delivering data as early as 2006, and which will use GPS observables for positioning. It should not be forgotten that high precision non-conservative force models are still important for determining the orbits of LEO satellites using GPS; in fact, UCL models contributed to JPL breaking through the 1cm radial orbit accuracy for JASON.

13. References

Adhya, S., A. Sibthorpe, M. Ziebart and P. Cross. 2004. "An Oblate Earth Eclipse state Algorithm for Low Earth Orbiting Satellites", in *Journal of Spacecraft and Rockets* **41** (1). Pp. 157-159.

Adhya, S. 2005. *Thermal Re-Radiation Modelling for the Precise Prediction and Determination of Spacecraft Orbits*. PhD thesis, University College London. 208 pages.

Alvarez, L. J. 1997. ENVISAT-*1 Mission CFI Software Mission Conventions Document 2.0*. GMV / European Space Agency (ESA): PO-IS-ESA-GS-0561. 55 pages.

Antreasian, P.G. and G.W. Rosborough. 1992. "Prediction of Radiant Energy Forces on the Topex/Poseidon Spacecraft," in *Journal of Spacecraft and Rockets* **29**(1). Pp. 81-90.

Aoki, S., B. Guinot, G.H. Kaplan, H. Kinoshita, D.D. McCarthy and P.K. Seidelmann. 1982. "The New Definition of Universal Time" in *Astronomy and Astrophysics* **105**. Pp. 359-361.

Aylward, A, M. Smith and D. Hunter. 2000. *Modelling the Effects of Thermospheric Winds*. Logica Final Report, 502.EC23733/FR. 67 pages.

Barequet, G. and H-P. Sariel. 2001. "Efficiently Approximating the Minimum-Volume Bounding Box of a Point Set in Three Dimensions," in *Journal of Algorithms* **38**(1). Pp. 91-109.

Bar-Sever, Y., and W.I. Bertiger, E.S. Davis, J.A. Anselmi. 1996. "Fixing the GPS Bad Attitude: Modeling GPS Satellite Yaw During Eclipse Seasons," in *Navigation*: Journal of the Institute of Navigation **43**(1). Pp. 25-39.

Bar-Sever, Y. and Russ, K.M. 1997. *New and Improved Solar Radiation Models for GPS Satellites Based on Flight Data: Final Report.* JPL, RF-182/808. 30 pages.

Battin, R.H. 1999 (Revised Ed.). *An Introduction to the Mathematics and Methods of Astrodynamics.* American Institute of Aeronautics and Astrodynamics (AIAA), (USA). 799 pages.

Bawden, G.W., W. Thatcher, R.S. Stein, K.W. Hudnut and G. Peltzer. 2001. "Tectonic Contraction Across Los Angeles After Removal of Groundwater Pumping Effects," in *Nature* **412**. Pp. 812-815.

Bettadpur, S. 2004a (January 21). *Recommendation for a-priori Bias & Scale Parameters for Level-1B ACC Data (Release 00).* GRACE TN-04-02. http://podaac.jpl.nasa.gov/grace/documentation (downloaded 06/07/2005). 2 pages.

Bettadpur, S. 2004b (August 2, Rev. 4.2). *GRACE Product Specification Document.* GRACE 327-720. http://podaac.jpl.nasa.gov/grace/documentation (downloaded 06/07/2005). 77 pages.

Beutler, G., E. Brockmann, W. Gurtner, U. Hugentobler, L. Mervant, M. Rothaker, and A. Verdun. 1994. "Extended Orbit Modeling Techniques at the CODE Processing Center of the International GPS Service for Geodynamics (IGS)" in *Manuscripta Geodetica* **19**. Pp. 367-386.

Bird, G.A. 1995. *Molecular Gas Dynamics and the Direct Simulation of Gas Flows.* Clarendon Press (Oxford). 458 pages.

Boisvert, P., S. Rheault, P. Theophanous, A. Lebru, S. Harvey and R. Kerner. 1997. *Verification of ENVISAT ASAR Active Antenna Thermal Design by a Thorough Sensitivity Analysis.* SAE 27th International Conference on Environmental Systems, Nevada, July, 1997. http://mail.robobank.co.kr/qa/files/tmg-sp97.pdf (downloaded 01/11/2002). 10 pages.

Buckley, S.M. 2000. *Radar Interferometry Measurement of Land Subsidence.* PhD Thesis. The University of Texas at Austin (Austin).

Burgmann, R., P.A. Rosen, E.J. Fielding. 2000. "Synthetic Aperture Radar Interferometry to Measure Earth's Surface Topography and Its Deformation," in *Annual Review of Earth Planetary Science* **28**. Pp. 169-209.

Chapman, A. J. 1974 (3rd Ed.). *Heat Transfer.* Macmillan (USA). 653 pages.

Closa, J. 1998. *ESA Document ES-TN-APP-APM-JC01.* http://earth.esa.int/rootcollection/sysutil/ORB_QL.html

Colesanti, C., F. De Zan, A. Ferretti, C. Prati and F. Rocca. 2003. "Generation of DEM with Sub-Metric Vertical Accuracy from 30' ERS-ENVISAT Pairs," in *Proceedings of FRINGE Workshop 2003*, ESA SP-550.

Cook, G.E. 1965. "Satellite Drag Coefficients," in *Planetary Space Science* **13**. Pp. 929-946.

Cunningham, L.E. 1970. "On the Computation of the Spherical Harmonic Terms Needed During the Numerical Integration of the Orbital Motion of an Artificial Satellite", in *Celestial Mechanics* **2**. Pp. 207-216.

Curlander, J.C. and R.N. McDonough. 1991. *Synthetic Aperture Radar: Systems and Signal Processing.* John Wiley & Sons (New York). 672 pages.

Doornbos, E. 2001. *Modelling of Non-Gravitational Forces for ERS-2 and ENVISAT.* MSc Thesis, DEOS, The Netherlands. 98 pages.

Doornbos, E., R. Scharroo, H. Klinkrad, R. Zandbergen and B. Fritsche. 2002. "Improved Modelling of Surface Forces in the Orbit Determination of ERS and ENVISAT," in *Canadian Journal of Remote Sensing* **28** (4). Pp. 535-543.

Drob, D.P., and J.M. Picone. 2000. *Statistical performance measures of the HWM-93 and MSISE-90 empirical atmospheric models and the relation to infrasonic CTBT monitoring*. Proceedings of the 22nd Annual DoD/DOE Seismic Research Symposium: Planning for Verification of and Compliance with the Comprehensive Nuclear-Test-Ban Treaty (CTBT), No. 0703, (New Orleans). 8 pages.

ESA (European Space Agency). 2002. *ASAR Product Handbook 1.0.* http://envisat.esa.int/dataproducts/ (downloaded 25/09/2002). 586 pages.

Feynman, R. 2005. *The Very Best of the Feynman Lectures* (Audio CD). Basic Books.

Fliegel, H.F., T.E. Gallini and E.R. Swift. 1992. "Global Positioning System Radiation Force Model for Geodetic Applications," in *Journal of Geophysical Research* **97**(B1). Pp. 559-568.

Fliegel, H.F. and T.E. Gallini. 1996. "Solar force modelling of Block IIR Global Positioning System satellites," in *Journal of Spacecraft and Rockets* **33**(6). Pp. 863-866.

Forbes, J.M., S. Bruinsma and F.G. Lemoine. 2006. "Solar Rotation Effects on the Thermospheres of Mars and Earth," in *Science* **312**. Pp. 1366-1368.

Fritsche, B., M. Ivanov, A. Kashkovsky, G. Koppenwallner, A. Kudryavtsev and G. Zhukova. 1998. *Radiation Pressure Forces on Complex Spacecraft: Executive Summary*. Hypersonic Technology Göttingen (Germany) and Institute of Theoretical and Applied Mechanics (Russia), HTG-Report-98-2. 75 pages.

Frolich, C., and J.Lean. 1998. "The Sun's Total Irradiance: Cycles, Trends and Related Climate Change Uncertainties since 1976," in *Geophysical Research Letters* **25**(23). Pp. 4377-4380.

Giordano, F., M.Weir, and W. Fox. 2003 (3rd Ed.). *A First Course in Mathematical Modelling*. Thomson, Brooks/Cole (USA). 538 pages.

Goni, G.J. and J.A. Trinanes. 2003. "Ocean Thermal Structure Monitoring Could Aid in the Intensity Forecast of Tropical Cyclones," in *EOS Transactions* **84**(51). Pp. 573-580.

Haines, B., Y. Bar-Sever, W. Bertiger, S. Desai and P. Willis. 2004. "One-Centimeter Orbit Determination for Jason-1: New GPS-Based Strategies," in *Marine Geodesy* **27** (1-2). Pp. 299-318.

Hairer, E., S.P. Norsett and G. Wanner. 1987. *Solving Ordinary Differential Equations I: Nonstiff Problems*. Springer-Verlag (Germany). 480 pages.

Hanssen, R.F. 2001. *Radar Interferometry: Data Interpretation and Error Analysis*, Kluwer Academic Publishers (The Netherlands). 308 pages.

Heafner, P.J. 1999. *Fundamental Ephemeris Computations*. Willmann-Bell Inc. (USA). 320 pages.

Hedin, A.E. 1989. "The Atmospheric Model in the Region 90 to 2000 km," in *Advances in Space Research* **8**(5-6). Pp.9-25.

Hedin, A.E., E.L. Fleming, A.H. Manson, F.J. Schmidlin, S.K. Avery, R.R. Clark, S.J. Franke, G.J. Fraser, T. Tsuda, F. Vial and R.A. Vincent. 1996. "Empirical wind model for the upper, middle and lower atmosphere," in *Journal of Atmospheric and Terrestrial Physics* **58** (13). Pp. 1421-1447.

Heiskanen, W.A. and H. Moritz. 1967. *Physical Geodesy*. W.H. Freeman & Co. (USA). 364 pages.

Hofmann-Wellenhof, B., H. Lichtenegger and J. Collins. 2001 (5th Revised Edition). *GPS: Theory and Practice*. Springer-Verlag (New York). 382 pages.

Hugentobler, U., and G. Beutler. 2003. "Strategies for Precise Orbit Determination of Low Earth Orbiters Using the GPS" in *Space Science Reviews* **108**. Pp. 17-26.

Incropera, F.P. and D.P. DeWitt. 2002 (4th Ed.). *Introduction to Heat Transfer*. John Wiley & Sons (USA). 892 pages.

Klees, R. and D. Massonnet. 1999. "Deformation Measurements Using SAR Interferometry: Potential and Limitations", in *Geologie en Mijnbouw* **77**. Kluwer Academic Publishers (The Netherlands). Pp. 161-176.

Knocke, P. 1989. *Earth Radiation Pressure Effects on Satellites*. PhD Thesis, University of Texas at Austin, Centre for Space Research (CSR-89-1). 216 pages.

Knocke, P.C. and J.C. Ries. 1987. *Earth radiation pressure effects on satellites*. Technical Memorandum CSR-TM-87-01, The University of Texas at Austin (Texas). 53 pages.

Koppenwallner, G., D. Johannsmeier, H. Klinkrad, M. Ivanov, A. Kashkowski. 1995. *A Rarefied Aerodynamics Modelling System for Earth Satellites (RAMSES)*, Oxford University Press (Oxford). Pp. 1366-1372.

Kubitschek, D.G. and G.H. Born. 2001. "Modelling the Anomalous Acceleration and Radiation Pressure Forces for the TOPEX / POSEIDON Spacecraft," in *Philosophical Transactions A of the Royal Society* **359**. Pp. 2191-2208.

Lathuillere, C. M. Menvielle, J. Lilensten, T. Amari and S.M. Radicella. 2002. "From the Sun's Atmosphere to the Earth's Atmosphere: An Overview of Scientific Models Available for Space Weather Developments," in *Annales Geophysicae* **20**(7). Pp. 1081-1104.

LeBeau, G.J., and F.E. Lumpkin. 2001. "Application Highlights of the DSMC Analysis Code (DAC) Software for Simulating Rarefied Flows," in *Computer Methods in Applied Mechanics and Engineering* **191**. Pp. 595-609.

Leick, A. (1995). *GPS Satellite Surveying*, Wiley-Interscience (USA).

Leick, A. 2004 (3rd Ed.). *GPS Satellite Surveying*. John Wiley & Sons Inc. (USA). 434 pages.

Lemoine, F.G., S.C. Kenyon, J.K. Factor, R.G. Trimmer, N.K. Pavlis, D.S. Chinn, C.M. Cox, S.M. Klosko, S.B. Luthcke, M.H. Torrence, Y.M. Wang, R.G. Williamson, E.C. Pavlis, R.H. Rapp and T.R. Olson. 1998. *The development of the joint NASA/GSFC and NIMA (National Imagery and mapping Agency) geopotential model EGM96.* NASA/TP-1998-206861. NASA Goddard Space Flight Centre (GSFC). 575 pages.

Li, Z. 2005. *Correction of Atmospheric Water Vapour Effects on Repeat-Pass SAR Interferometry Using GPS, MODIS and MERIS Data.* PhD Thesis, University College London. 222 pages.

Li, Z., L. Jingnan and X. Caijun. 2004. "Error Analysis in InSAR Data Processing," in *Geomatics and Information Science at Wuhan University* **29**(1). Pp. 72-76.

Lichten, S.M. and J.S. Border. 1987. "Strategies for High-Precision Global Positioning System Orbit Determination," in *Journal of Geophysical Research* **92**(B12). Pp. 12,751-12,762.

Long, A.C, J.O. Cappellari Jr, C.E. Velez and A.J. Fuchs (Eds.). 1989. *Goddard Trajectory Determination System (GTDS): Mathematical Theory, Revision 1.* Computer Sciences Corporation & NASA GSFC (USA).

Luthcke, S.B. and J.A. Marshall. 1992. *Nonconservative Force Model Parameter Estimation Strategy for TOPEX/Poseidon Precision Orbit Determination.* NASA Technical Memorandum TM-104575, 39 pages.

MacRobert, T.M. 1927. *Spherical Harmonics: An Elementary Treatise on Harmonic Functions with Applications.* Methuen & Co. Ltd. (UK). 302 pages.

Mandl, F. 1971. *Statistical Physics.* John Wiley & Sons Ltd. (UK). 379 pages.

Marcos, F.A. 1989. "Accuracy of Atmospheric Drag Models at Low Satellite Altitudes," in *Advances in Space Research* **10**(3-4). Pp. 417-422.

Marquis, W. 2003. "Increased Navigation Performance from GPS Block IIR," in *Navigation* **50**(4). Pp. 219-233.

Marquis, W. and C. Krier. 2000. *Examination of the GPS Block IIR Solar Pressure Model. ION GPS 2000*, 19-22 September 2000, Salt Lake City, UT. Pp. 407-415.

Marsh, J.G., F.J. Lerch, B.H. Putney, D.C. Christodoulidis, D.E. Smith, T.L. Felsentreger, B.V. Sanchez, S.M. Klosko, E.C. Pavlis, T.V. Martin, J.W. Robbins, R.G. Williamson, O.L. Colombo, D.D. Rowlands, W.F. Eddy, N.L. Chandler, K.E. Rachlin, G.B. Patel, S. Bhati, D.S. Chinn. 1988. "A New Gravitational Model for the Earth from Satellite Tracking Data: GEM-T1," in *Journal of Geophysical Research* **93**(B6). Pp. 6169-6215.

Marshall, J.A., S.B. Luthcke, P.G. Antreasian and G.W. Rosborough. 1992. *Modeling Radiation Forces Acting on TOPEX/Poseidon for Precision Orbit Determination.* NASA Technical Memorandum TM-104564. 75 pages.

Massonnet, D. and K. Feigl. 1998. "Radar Interferometry and its Application to Changes in the Earth's Surface," in *Reviews of Geophysics* **36**(4). Pp. 441-500.

Mayaud, P.N. 1980. *Derivation, Meaning, and Use of Geomagnetic Indices.* Geophysical Monograph 22, American Geophysical Union (USA). 154 pages.

McCarthy, D.D. (Ed.). 1996. *IERS Conventions (1996).* IERS Technical Note No. 21. Central Bureau of IERS, Observatoire de Paris. 95 pages.

McCarthy, D.D. and G. Petit (Eds.). 2003. *IERS Conventions (2003).* IERS Technical Note No. 32. http://www.iers.org/iers/publications/tn/tn32/. 127 pages.

McLeod, I. 1998. *ENVISAT-1 Products Specifications Volume 8: ASAR Products Specifications.* ESA report PO-RS-MDA-GS-2009. http://atmos.af.op.dlr.de/documents/esadocs/envisat_prod_spec/vol_08.pdf (downloaded 09/08/2005).

Merriam, J.B. 1990. "Atmospheric Excitation of the Earth's Rotation Rate", in *Variations in Earth Rotation*, D. McCarthy and W. Carter (Eds.). IUGG Vol. 9. American Geophysical Union (USA). 205 pages.

Métris, G., and D. Vokrouhlický. 1996. "Thermal Force Perturbations of the LAGEOS Orbit: the Albedo Radiation Part," in *Planetary and Space Science* **44** (6). Pp. 611-617.

Métris, G., D. Vokrouhlický, J.C. Ries and R.J. Eanes. 1997. "Nongravitational Effects and the LAGEOS Eccentricity Excitations," in *Journal of Geophysical Research* **102** (B2). Pp. 2711-2729.

Montenbruck, O. and E. Gill. 2001 (2nd Ed.). *Satellite Orbits: Models Methods Applications*. Springer-Verlag (Germany). 369 pages.

Moss, J.N., R.G. Wilmoth and J.M. Price. 1997. *DSMC Simulations of Blunt Body Flows for Mars Entries*. 32nd AIAA Thermophysics Conference, Atlanta, Georgia, AIAA Paper 97-2508. http://techreports.larc.nasa.gov/ltrs/PDF/1997/aiaa/NASA-aiaa-97-2508.pdf (downloaded 14/01/2004).

Neta, B. and D. Vallado. 1997. "On Satellite Umbra/Penumbra Entry and Exit Positions," in *Advances in the Astronautical Sciences 95(II): Spaceflight Mechanics 1997,* edited by K. Howell, et al., Advances in the Astronautical Sciences (AAS) Publication. Pp. 715-724.

Nicodemus, F.E. 1970. "Reflectance Nomenclature and Directional Reflectance and Emissivity," in *Applied Optics* **9**. Pp. 1474-1475.

O'Rourke, J. 1985. "Finding Minimal Enclosing Boxes," in *International Journal of Computer and Information Science* **14**(3). Pp. 183-199.

Otsubo, T., R.A. Sherwood, P. Gibbs and R. Wood. 2004. "Spin Motion and Orientation of LAGEOS-2 from Photometric Observation," in *IEEE Transactions on Geoscience and Remote Sensing* **42**(1). Pp. 202-208.

Otten, M, and H. Boomkamp. 2003. *Estimation of the Absolute Orbit Accuracy of ENVISAT.* http://nng.esoc.esa.de/envisat/compcamp.html.

Owens, J.K. 2002. *NASA Marshall Engineering Thermosphere Model–Version 2.0.* NASA Marshall Space Flight Center Technical Memorandum NASA/TM—2002–211786 (Alabama). 41 pages.

Press, W.H., S.A. Teukolsky, W.T. Vetterling and B.P. Flannery. 2002 (2nd Ed.). *Numerical Recipes in C++: The Art of Scientific Computing.* Cambridge University Press (USA). 1002 pages.

Rapp, R.H. 1998. "Past and future developments in geopotential modelling," in *Geodesy on the Move: Gravity, Geoids, Geodynamics, and Antarctica* (Eds. Forsberg, R., M. Feissl and R. Dietrich). Springer-Verlag (Berlin). Pp. 58-78.

Reid, H.F. 1910. *The Mechanics of the Earthquake*, Vol. II of The California Earthquake of April 18, 1906, Report of the State Earthquake Investigation Commission. Carnegie Institution of Washington (Washington D.C.), publication 87.

Reigber, C., Y. Xia, H. Kaufmann, F.H. Massmann, L. Timmen, J. Bodechtel and M. Frei. 1996. *Impact of Precise Orbits on SAR Interferometry.* http://www.geo.unizh.ch/rsl/fringe96/papers/reigber-et-al/

Restitution d'Orbites Department, CNES. 2002. "README_macromodels". ftp://spike.cst.cnes.fr/pub/ENVIS. Accessed 12/07/03.

Rosborough, G.W. and P.G. Antreasian. 1990. "Radiation Force Modelling for the Topex/Poseidon Spacecraft," in *AIAA/AAS Astrodynamics Conference*, Portland, OR. Aug. 20-22, 1990, Technical Papers (AIAA-90-2895). Pp. 168-178.

Saaf, E. and A. Kuijlaars. 1997. "Distributing Many Points on a Sphere," in *Mathematical Intelligencer* **19**(1). Pp. 5-11.

Schamberg, R. 1959. *A New Analytic Representation of Surface Interaction for Hyperthermal Free Molecule Flow with Application to Neutral-Particle Drag Estimates of Satellites*. USAF Project RAND Research Memorandum RM-2313. 88 pages.

Scharroo, R. 2002. *A Decade of ERS Satellite Orbits and Altimetry*. DUP Science (The Netherlands). 195 pages.

Scott, D. and A. Leonov. 2004. *Two Sides of the Moon*. Simon & Schuster UK Ltd (UK). 415 pages.

Seeber, G. 2003 (2nd Ed.). *Satellite Geodesy*. De Gruyter (Germany). 589 pages.

Shewchuk, J.R. 1999. *Lecture Notes on Delaunay Mesh Generation*. Department of Electrical Engineering and Computer Science, University of California at Berkeley, Berkeley, CA 94720. http://citeseer.nj.nec.com/shewchuk99lecture.html (downloaded 17/02/2004).

Shoemake, K. 1992. "ARCBALL: a user interface for specifying three-dimensional orientation using a mouse," in *Proceedings of the conference on Graphics interface '92, Vancouver, Canada*. Morgan Kaufmann Publishers Inc. (San Francisco, CA, USA). Pp. 151-156.

Stark, J. 1986. *Aerodynamic Modelling of Spacecraft for Precise Orbit Determination*. Proceedings of the 2nd International Symposium on Spacecraft Flight Dynamics, Darmstadt, Germany, 20-23 October 1986. ESA SP-255. Pp. 239-246.

Stroud, K.A. 1996 (3rd Ed.). *Further Engineering Mathematics*. Macmillan Press (London). 1068 pages.

Tanaka, S., S. Yoshida, A. Hagermann, M. Hayakawa, A. Fujimura, and M. Mizutani. 2001. *In Situ Lunar Heat Flow Experiment Using the LUNAR-A Penetrator*. 32nd Annual Lunar and Planetary Science Conference, March 12-16, 2001, Houston, Texas. 2 pages.

Tapley, B.D., B.E. Schutz and G.H. Born. 2004. *Statistical Orbit Determination.* Elsevier Inc. (USA). 547 pages.

Taylor, G. (1994). "Point in polygon test," in *Survey Review* **32**(October). Pp. 479-484.

Tobiska, W.K. 2003. "Forecast E10.7 for Improved Low Earth Orbit Satellite Operations," in *Journal of Spacecraft and Rockets* **40**(3). Pp. 405-410.

Torres, R. 2002. *Asar Instrument Stability.* Proceedings of the ENVISAT Calibration Review, Special Publication SP-520. ENVISAT Programme Division, ESA-ESTEC. http://envisat.esa.int/calval/proceedings/asar/asar_02.pdf (downloaded 03/08/2005). 7 pages.

Torres, R., C. Buck, J. Guijarro, J.L. Suchail and A. Schönenberg. 1999. *The ENVISAT ASAR Instrument Verification and Characterisation.* ENVISAT Payload Division, ESA-ESTEC (The Netherlands). http://www.estec.esa.nl/ceos99/papers/p099.pdf (downloaded 06/01/2005).

Vallado, D.A. 2001 (2nd Ed.). *Fundamentals of Astrodynamics and Applications.* Microcosm Press & Kluwer Academic Publishers (USA). 958 pages.

Vigue, Y., S.M. Lichten, R.J. Mullerschoen, G. Blewitt and M.B. Heflin. 1994a. "Improved GPS Solar Radiation Pressure Modeling for Precise Orbit Determination," in *Journal of Spacecraft and Rockets*, **31**(5). Pp. 830-833.

Vigue, Y., B.E. Schutz and P.A.M. Abusali. 1994b. "Thermal Force Modelling for Global Positioning System Satellites Using the Finite Element Method," in *Journal of Spacecraft and Rockets* **31** (5). Pp. 855-859.

Vokrouhlický, D., P. Farinella and D. Lucchesi. 1993a. "Albedo Perturbation Models: General Formalism and Applications to LAGEOS, " in *Celestial Mechanics and Dynamical Astronomy* **57**. Pp. 225-244.

Vokrouhlický, D., P. Farinella and D. Lucchesi. 1993b. "Long-Periodic Albedo Perturbations on LAGEOS," in *Astronomy and Astrophysics* **280**. Pp. 282-294.

Vokrouhlický, D., P. Farinella, and F. Mignard. 1993c. "Solar Radiation Pressure Perturbations for Earth Satellites I. A Complete Theory Including Penumbra Transitions," in *Astronomy and Astrophysics* **280**. Pp. 295-312.

Vokrouhlický, D., P. Farinella, and F. Mignard. 1996. "Solar Radiation Pressure Perturbations for Earth Satellites IV. Effects of the Earth's Polar Flattening on the Shadow Structure and the Penumbra Transitions," in *Astronomy and Astrophysics* 307. Pp. 635-644.

Wachman, H.Y. 1962. "The Thermal Accommodation Coefficient: A Critical Survey," in *American Rocket Society Journal* **32**. Pp. 2-12.

Watt, A.H. and M. Watt. 1992. *Advanced animation and rendering techniques: theory and practice.* ACM Press (NY). 455 pages.

Willis, P. and J.C. Ries. 2005. "Defining a DORIS core network for Jason-1 precise orbit determination based on ITRF2000: methods and realization," in *Journal of Geodesy* **79**. Pp. 370-378.

Willis, P., F. Deleflie, F. Barlier, Y.E. Bar-Sever, and L.J. Romans. 2004. *Effects of thermosphere total density perturbations on a LEO orbit during severe geomagnetic conditions (oct - nov 2003) using DORIS and SLR data.* 35th COSPAR Scientific Assembly, Paris, France. COSPAR04-A-01470.

Willis, P. and M.B. Heflin. 2004. "External validation of the GRACE GGM01C Gravity Field using GPS and DORIS positioning results," in *Geophysical Research Letters* **31** (13), L13616, doi:10.1029/2004GL020038.

Woodburn, J. 2000. *Effects of Eclipse Boundary Crossings on the Numerical Integration of Orbit Trajectories.* AIAA-2000-4027.

http://www.stk.com/pdf/white_papers/0800_shadow_boundary.pdf (downloaded 22 February 2003).

Wooden, W. and D. Gambis. 2003. *Explanatory Supplement to IERS Bulletins A and B*. http://hpiers.obspm.fr/iers/bul/bulb/explanatory.html (downloaded 30/07/2004).

Wright, T.J. 2002. "Remote Monitoring of the Earthquake Cycle using Satellite Radar Interferometry," in *Philosophical Transactions of the Royal Society of London, SERIES A* (**360**). Pp.2873-2888.

Wright, R.S. and M. Sweet. 2000 (2nd ed.). *OpenGL Super Bible*. Waite Group Press, USA (Indiana). 696 pages.

Young, H.D. and R.A. Freedman. 2000 (10th ed.). *University Physics*. Addison-Wesley (USA). 1274 pages.

Zebker, H.A. and J. Villasenor. 1992. "Decorrelation in Interferometric Radar Echoes", in *IEEE Transactions on Geoscience and Remote Sensing* **30**(5). Pp. 950-959.

Zebker, H.A., P.A. Rosen, R.M. Goldstein, A. Gabriel, C.L. Werner. 1994. "On the Derivation of Coseismic Displacement Fields Using Differential Radar Interferometry: The Landers Earthquake," in *Journal of Geophysical Research* **99**(B10). Pp. 19617-19634.

Zebker, H.A., P.A. Rosen and S. Hensley. 1997. "Atmospheric Effects in Interferometric Synthetic Aperture Radar Surface Deformation and Topographic Maps," in *Journal of Geophysical Research* **102**(B4). Pp. 7547-7563.

Ziebart, M. 2001a. "Analytical Solar Radiation Pressure Modelling for GLONASS Using a Pixel Array," in *Journal of Geodesy* **75**. Pp. 587-599.

Ziebart, M. 2001b. *High Precision Analytical Solar Radiation Pressure Modelling for GNSS Spacecraft*. PhD thesis, University of East London. 272 pages.

Ziebart, M. 2002. "*guidelines.doc*". ftp.ge.ucl.ac.uk/pub/JASON-models. Accessed 16/12/02.

Ziebart, M. 2004. "Generalised Analytical Solar Radiation Pressure Modelling Algorithm for Spacecraft of Complex Shape," in *Journal of Spacecraft and Rockets* **41**(5). Pp. 840-848.

Ziebart, M., S. Adhya, A. Sibthorpe and P. Cross. 2003. Residual systematic biases in spacecraft orbits. *European centre for geodynamics and seismology*, Luxembourg, April 2003.

Ziebart, M., S. Adhya, A. Sibthorpe, S. Edwards and P.A. Cross. 2004. *A High Precision Analytical Surface Force Model for GPS Block IIR Satellites*. IGS Workshop & Symposium, March 1-5, 2004. Berne, Switzerland. Poster presentation.

Ziebart, M., S. Adhya, A. Sibthorpe, S. Edwards and P.A. Cross. 2005. "Combined Radiation Pressure and Thermal Modelling of Complex Satellites: Algorithms and On-orbit tests," in *Advances in Space Research*. Accepted for publication 06/01/2005.

APPENDICES

14. Appendix A

14.1. Area Modelling Tool

Accurate projected ram areas calculated at many different viewing locations are critical when evaluating atmospheric drag models for satellites. Yet even a modern CAD package may take many minutes to evaluate the area of a very complicated satellite. It may be thought that a viable alternative is to use the pixel array tool from UCL_SRP, and simply sum the areas of those pixels whose central ray intersects a component of the satellite. However, it may take up to 30 minutes for this approach to compute the area of the ENVISAT bus only, at one pixel array location with a 5mm pixel resolution. Adding in the solar array would significantly increase the number of pixels and therefore the run time.

Experiments were therefore conducted with the viewer tool to see if it could do better. OpenGL provides routines for converting 2D screen coordinates to 3D object coordinates, and vice versa. A rendered image of a satellite can therefore have its corner points transformed into real world coordinates, and the total area of the image can be easily calculated. Looping over all of the pixels, and checking to see how many contain an object pixel, allows us to recover that fraction of the image area covered by the satellite, and hence the ram area of the satellite for that viewing location. It is also possible to render to an off-screen buffer in order to take advantage of higher than standard screen resolutions. A resolution of 2048 x 2048 pixels is very similar to a 5mm pixel array for ENVISAT, and the process is completed within less than 30 seconds; a speed up improvement factor of 60.

Results from this area tool were then compared to results generated by a CAD package (Rhino V.2.0) for ENVISAT from three distinct viewing locations (see Figure 14-1). Table 14-1 demonstrates that the area tool tends to always overestimate the projected area, but that the errors are small and decrease further when the resolution is increased to 4096 x 4096.

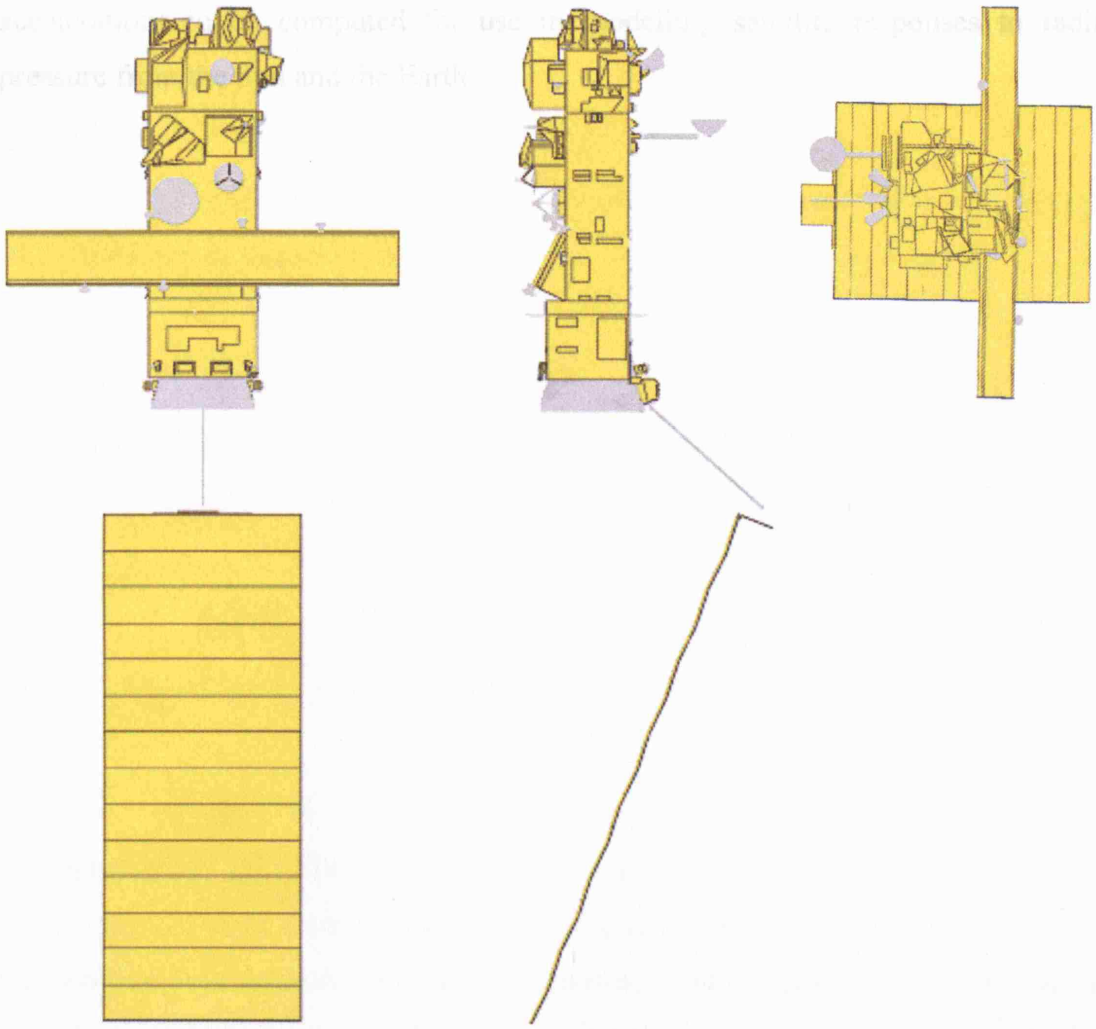

Figure 14-1: Different ENVISAT profiles with areas computed using the viewer tool.

	Areas (m^2)			% Error	
Profile	**CAD**	**2048^2 Pixels**	**4096^2 Pixels**	**2048^2 Pixels**	**4096^2 Pixels**
ENVISAT bus nadir (-Z) face + full panel	103.837	104.664	104.330	0.796	0.474
ENVISAT bus side (-Y) face + side panel	24.477	25.388	24.852	3.725	1.534
ENVISAT end on (-X) + obscured panel	31.322	31.507	31.435	0.592	0.361

Table 14-1: Viewer tool area profiling results.

To allow retrieval of satellite area profiles from any viewing direction, a new algorithm was implemented which gives the optimal separation of points (a spiral) over the surface of a sphere (Saaf & Kuijlaars, 1997). This 'spiral points' algorithm has now been put to use in the main UCL_SRP code to allow a continuous surface of

accelerations to be computed for use in modelling satellite responses to radiation pressure from the Sun and the Earth.

15. Appendix B

15.1. Viewer Tool

This appendix describes the use of a sophisticated generic software application developed during this research project.

15.1.1. Zoom and Pan Tools

A click and drag pan tool (✣) and a mouse wheel operated zoom tool allow the user to centre areas of interest, and also to check possible problems with the model.

15.1.2. Outline Tool

The outline tool is accessed by pressing the F7 key.

15.1.3. Rotate Tool

The rotate tool (⟲) allows the user, without restriction, to rotate a model to any orientation. A right mouse click inside of the sphere resets the view to that seen when the satellite was initially loaded. In addition, clicking and dragging in the viewer outside of the sphere allows a local Z axis rotation to be performed, where the local Z direction is normal to the display.

15.1.4. Component Identification

The ID component tool (🖷) allows users to trace problems seen on screen back to a specific record number in the userfile for any component type.

15.1.5. Vertex Identification

The ID vertex tool (⁺ₙ) allows users to be certain they have selected the correct point.

15.1.6. Block Modelling Display

To check the success of the block modelling algorithms the user can press the F3 key to show all of the blocks. If required, F2 can be used to remove all of the precise components from the display. Pressing F4 shows the automatically generated

überblock, in order that the user can ensure it correctly encloses all elements of the spacecraft bus.

15.1.7. Lighting and Polygon Winding

A light source is added by pressing F5 which activates a simple user interface.

15.1.8. Adding a Solar Array

A solar array description can be added to an existing bus by choosing "Add Solar Array File" from the File menu.

15.1.9. Images

The print button () prints the on-screen view to a file called "bitmap.bmp", which is saved in the directory from which the current userfile was loaded. It preserves all facets of the view, including lighting. The F1 key toggles between white and black backgrounds in the viewer.

16. Appendix C

16.1. Variational Equations

This appendix covers the estimation of small changes to the initial conditions (position and velocity) and force model parameters (only Cd is considered here) which will improve the fit between an orbit produced by orbit prediction and one produced by orbit determination. This topic is well described in modern books on orbit determination such as Montenbruck & Gill (2000), and Tapley et al. (2004). The present section therefore just consolidates and expands upon some of the details of this information with respect to the processing performed during this research.

16.1.1. The State Transition Matrix

At some epoch on orbit, a satellite's state vector and its time derivative are respectively given by:

$$\begin{aligned} \bar{X} &= \begin{pmatrix} x & y & z & u & v & w \end{pmatrix} \\ \frac{d}{dt}\bar{X} &= \dot{\bar{X}} = \begin{pmatrix} u & v & w & a_x & a_y & a_z \end{pmatrix} \end{aligned} \tag{16.1}$$

The state transition matrix:

$$\bar{\phi}_t = \frac{\partial \bar{X}(t)}{\partial \bar{X}(t_0)} \tag{16.2}$$

relates the current state $\bar{X}$ at time (t) to the initial state at time (t_0).

Under an Eulerian integration scheme:

$$\bar{\phi}_{t+1} = \bar{\phi}_t + \frac{d}{dt}\bar{\phi}_t.\delta t \tag{16.3}$$

If:

$$\frac{d}{dt}\bar{X}(t) = f(t,\bar{X}) = \begin{pmatrix} \bar{v}(t) \\ \bar{a}(t,\bar{r},\bar{v}) \end{pmatrix} \tag{16.4}$$

Then:

$$\frac{d}{dt}\bar{\phi}_t = \frac{\partial}{\partial \bar{X}(t_0)} \cdot \frac{d}{dt}\bar{X}(t) = \frac{\partial f(t,\bar{X}(t))}{\partial \bar{X}(t_0)} \tag{16.5}$$

From first principles:

$$\frac{dy}{dx} \underset{\delta x \to 0}{\overset{\lim}{=}} \left\{ \frac{f(x+\delta x) - f(x)}{\delta x} \right\} \tag{16.6}$$

which therefore means we can say that:

$$\frac{\partial f(t,\bar{X}(t))}{\partial \bar{X}(t_0)} \underset{\delta \bar{X} \to 0}{\overset{\lim}{=}} \left\{ \frac{f(t,\bar{X}+\delta \bar{X}) - f(t,\bar{X})}{\delta \bar{X}(t_0)} \right\} \tag{16.7}$$

This represents a small change in the current state with respect to the initial state.

Using Taylor's theorem:

$$\left\{ \frac{f(t,\bar{X}+\delta \bar{X}) - f(t,\bar{X})}{\delta \bar{X}(t_0)} \right\} = \left\{ \frac{f(t,\bar{X}) + f'(t,\bar{X}).\delta \bar{X} - f(t,\bar{X})}{\delta \bar{X}(t_0)} \right\} \tag{16.8}$$

where:

$$f'(t,\bar{X}) = \frac{\partial f(t,\bar{X})}{\partial \bar{X}(t)} \tag{16.9}$$

Therefore:

$$\frac{\partial f(t,\bar{X}(t))}{\partial \bar{X}(t_0)} \underset{\delta \bar{X} \to 0}{\overset{\lim}{=}} \frac{\partial f(t,\bar{X})}{\partial \bar{X}(t)} \cdot \frac{\delta \bar{X}}{\delta \bar{X}(t_0)} = \frac{\partial f(t,\bar{X})}{\partial \bar{X}(t)} \cdot \frac{\partial \bar{X}}{\partial \bar{X}(t_0)} = \frac{\partial f(t,\bar{X})}{\partial \bar{X}(t)} . \bar{\phi}_t \tag{16.10}$$

where:

$$\frac{\partial f(t,\bar{X})}{\partial \bar{X}(t)} = \frac{\partial \dot{\bar{X}}(t)}{\partial \bar{X}(t)} = \begin{bmatrix} \frac{\partial u}{\partial x} & \frac{\partial u}{\partial y} & \frac{\partial u}{\partial z} & \frac{\partial u}{\partial u} & \frac{\partial u}{\partial v} & \frac{\partial u}{\partial w} \\ \frac{\partial v}{\partial x} & \frac{\partial v}{\partial y} & \frac{\partial v}{\partial z} & \frac{\partial v}{\partial u} & \frac{\partial v}{\partial v} & \frac{\partial v}{\partial w} \\ \frac{\partial w}{\partial x} & \frac{\partial w}{\partial y} & \frac{\partial w}{\partial z} & \frac{\partial w}{\partial u} & \frac{\partial w}{\partial v} & \frac{\partial w}{\partial w} \\ \frac{\partial a_x}{\partial x} & \frac{\partial a_x}{\partial y} & \frac{\partial a_x}{\partial z} & \frac{\partial a_x}{\partial u} & \frac{\partial a_x}{\partial v} & \frac{\partial a_x}{\partial w} \\ \frac{\partial a_y}{\partial x} & \frac{\partial a_y}{\partial y} & \frac{\partial a_y}{\partial z} & \frac{\partial a_y}{\partial u} & \frac{\partial a_y}{\partial v} & \frac{\partial a_y}{\partial w} \\ \frac{\partial a_z}{\partial x} & \frac{\partial a_z}{\partial y} & \frac{\partial a_z}{\partial z} & \frac{\partial a_z}{\partial u} & \frac{\partial a_z}{\partial v} & \frac{\partial a_z}{\partial w} \end{bmatrix} \tag{16.11}$$

We now have all the elements required to propagate the state transition matrix over time including its initial value, which is given by the identity matrix. The calculation of the necessary partials due to Earth gravity, which fill the bottom left 3x3 sub-matrix of (16.11) is complicated, but fully specified for arbitrary degree and order by Cunningham (1970). Initially, the top left and bottom right 3x3 sub-matrices are set to null values, the top right 3x3 sub-matrix is set to the identity matrix, and the bottom left 3x3 sub-matrix filled with the Earth gravity partials.

16.1.2. Estimating a Drag Parameter

By analogy with the state transition calculation, the sensitivity matrix:

$$\bar{S}_t = \frac{\partial \bar{X}(t)}{\partial \bar{p}} \tag{16.12}$$

relates the current state to some parameter set.

Under an Eulerian integration scheme:

$$\bar{S}_{t+1} = \bar{S}_t + \frac{d}{dt}\bar{S}_t.\delta t \tag{16.13}$$

If:

$$\frac{d}{dt}\bar{X}(t) = f(t,\bar{X},\bar{p}) \tag{16.14}$$

Then:

$$\frac{d}{dt}\bar{S}_t = \frac{\partial}{\partial \bar{p}(t_0)} \cdot \frac{d}{dt}\bar{X}(t,\bar{p}) = \frac{\partial f(t,\bar{X}(t),\bar{p})}{\partial \bar{p}(t_0)} \tag{16.15}$$

From first principles, we can say that:

$$\begin{aligned} &\frac{\partial f(t,\bar{X}(t),\bar{p})}{\partial \bar{p}(t_0)} \underset{\delta \to 0}{\overset{\lim}{=}} \left\{ \frac{f(t,\bar{X}+\delta\bar{X},\bar{p}) - f(t,\bar{X},\bar{p})}{\delta \bar{p}(t_0)} \right\} \\ &+ \left\{ \frac{f(t,\bar{X},\bar{p}+\delta\bar{p}) - f(t,\bar{X},\bar{p})}{\delta \bar{p}(t_0)} \right\} \end{aligned} \tag{16.16}$$

This represents a small change in the current state with respect to a change in some parameter set. There are two terms on the right-hand side because, for drag at least, a change to the parameters will cause a change both to the current state (first term) and to the parameters themselves (second term).

Using Taylor's theorem:

$$\begin{aligned} &\left\{ \frac{f(t,\bar{X}+\delta\bar{X},\bar{p}) - f(t,\bar{X},\bar{p})}{\delta \bar{p}(t_0)} \right\} \underset{\delta \to 0}{\overset{\lim}{=}} \\ &\left\{ \frac{f(t,\bar{X},\bar{p}) + f'(t,\bar{X},\bar{p}).\delta\bar{X} - f(t,\bar{X},\bar{p})}{\delta \bar{p}(t_0)} \right\} \end{aligned} \tag{16.17}$$

where:

$$f'(t,\bar{X},\bar{p}) = \frac{\partial f(t,\bar{X},\bar{p})}{\partial \bar{X}(t)} \tag{16.18}$$

And:

$$\begin{aligned} &\left\{ \frac{f(t,\bar{X},\bar{p}+\delta\bar{p}) - f(t,\bar{X},\bar{p})}{\delta \bar{p}(t_0)} \right\} = \\ &\left\{ \frac{f(t,\bar{X},\bar{p}) + f'(t,\bar{X},\bar{p}).\delta\bar{p} - f(t,\bar{X},\bar{p})}{\delta \bar{p}(t_0)} \right\} \end{aligned} \tag{16.19}$$

where:

$$f'(t,\bar{X},\bar{p}) = \frac{\partial f(t,\bar{X},\bar{p})}{\partial \bar{p}(t)} \tag{16.20}$$

Assembling these and cancelling terms gives:

$$\frac{\partial f(t,\bar{X}(t),\bar{p})}{\partial \bar{p}(t_0)} \underset{\delta\to 0}{\overset{\lim}{=}} \frac{\partial f(t,\bar{X},\bar{p})}{\partial \bar{X}(t)} \cdot \frac{\delta \bar{X}(t)}{\delta \bar{p}(t_0)} + \frac{\partial f(t,\bar{X},\bar{p})}{\partial \bar{p}(t)} \cdot \frac{\delta \bar{p}(t)}{\delta \bar{p}(t_0)} \tag{16.21}$$

$$\frac{\partial f(t,\bar{X}(t),\bar{p})}{\partial \bar{p}(t_0)} = \frac{\partial f(t,\bar{X},\bar{p})}{\partial \bar{X}(t)} \cdot \frac{\partial \bar{X}(t)}{\partial \bar{p}(t_0)} + \frac{\partial f(t,\bar{X},\bar{p})}{\partial \bar{p}(t)} = \frac{\partial f(t,\bar{X},\bar{p})}{\partial \bar{X}(t)} \cdot \bar{S}_t + \frac{\partial f(t,\bar{X},\bar{p})}{\partial \bar{p}(t)} \tag{16.22}$$

The initial sensitivity matrix is given by the null matrix, as the initial state does not depend upon any force model parameter.

Remembering that:

$$f(t,\bar{X},\bar{p}) = \frac{d}{dt}\bar{X}(t) = \begin{pmatrix} u & v & w & a_x & a_y & a_z \end{pmatrix}^T \tag{16.23}$$

The following partials in the above expression due to atmospheric drag can now be calculated:

$$\frac{\partial f(t,\bar{X},\bar{p})}{\partial \bar{X}(t)} = \frac{\partial \dot{\bar{X}}(t)}{\partial \bar{X}(t)} = \begin{bmatrix} \frac{\partial u}{\partial x} & \frac{\partial u}{\partial y} & \frac{\partial u}{\partial z} & \frac{\partial u}{\partial u} & \frac{\partial u}{\partial v} & \frac{\partial u}{\partial w} \\ \frac{\partial v}{\partial x} & \frac{\partial v}{\partial y} & \frac{\partial v}{\partial z} & \frac{\partial v}{\partial u} & \frac{\partial v}{\partial v} & \frac{\partial v}{\partial w} \\ \frac{\partial w}{\partial x} & \frac{\partial w}{\partial y} & \frac{\partial w}{\partial z} & \frac{\partial w}{\partial u} & \frac{\partial w}{\partial v} & \frac{\partial w}{\partial w} \\ \frac{\partial a_x}{\partial x} & \frac{\partial a_x}{\partial y} & \frac{\partial a_x}{\partial z} & \frac{\partial a_x}{\partial u} & \frac{\partial a_x}{\partial v} & \frac{\partial a_x}{\partial w} \\ \frac{\partial a_y}{\partial x} & \frac{\partial a_y}{\partial y} & \frac{\partial a_y}{\partial z} & \frac{\partial a_y}{\partial u} & \frac{\partial a_y}{\partial v} & \frac{\partial a_y}{\partial w} \\ \frac{\partial a_z}{\partial x} & \frac{\partial a_z}{\partial y} & \frac{\partial a_z}{\partial z} & \frac{\partial a_z}{\partial u} & \frac{\partial a_z}{\partial v} & \frac{\partial a_z}{\partial w} \end{bmatrix} \tag{16.24}$$

where the accelerations are due to drag, the upper left 3x3 block is a null matrix, and the upper right 3x3 block is an identity matrix.

$$\frac{\partial f(t,\bar{X},\bar{p})}{\partial \bar{p}(t)} = \frac{\partial \dot{\bar{X}}(t)}{\partial \bar{p}(t)} = \begin{pmatrix} \frac{\partial u}{\partial C_d} & \frac{\partial v}{\partial C_d} & \frac{\partial w}{\partial C_d} & \frac{\partial a_x}{\partial C_d} & \frac{\partial a_y}{\partial C_d} & \frac{\partial a_z}{\partial C_d} \end{pmatrix}^T \tag{16.25}$$

where the upper half of this vector is a null vector.

This means that we actually only need to calculate the following partials:

$$\frac{\partial \bar{a}}{\partial \bar{r}}, \frac{\partial \bar{a}}{\partial \bar{v}} \text{ and } \frac{\partial \bar{a}}{\partial C_d}.$$

First, we will expand all components of the drag acceleration equation as this is useful in later stages:

$$\bar{a} = -\frac{1}{2}.C_d.\frac{A}{m}.\rho.v_r^2.\hat{v}_r$$

$\bar{v}_r = \bar{v} - \bar{v}_A$, *where* $\bar{v}_A$ *is the velocity of the atmosphere.*

$$\bar{v}_A = \overline{AAM} \times \bar{r}, \text{ where } \overline{AAM} = (0 \quad 0 \quad 0.7292E-4)^T = (0 \quad 0 \quad e)^T$$

$$\bar{v}_A = \begin{bmatrix} i & j & k \\ 0 & 0 & e \\ x & y & z \end{bmatrix} = (-ey \quad -ex \quad 0)^T \tag{16.26}$$

$$\bar{v}_r = \bar{v} - \bar{v}_A$$

$$v_r^2 = \left[(v_x - v_{Ax})^2 + (v_y - v_{Ay})^2 + (v_z - v_{Az})^2 \right]$$

$$v_r = \left[(v_x - v_{Ax})^2 + (v_y - v_{Ay})^2 + (v_z - v_{Az})^2 \right]^{\frac{1}{2}}$$

Or, alternatively:

$$\bar{v}_r = \left((v_x + ey) \quad (v_y + ex) \quad (v_z) \right)^T$$

$$v_r = \left[(v_x + ey)^2 + (v_y + ex)^2 + (v_z)^2 \right]^{\frac{1}{2}}$$

$$v_r.\bar{v}_r = \begin{bmatrix} (v_x + ey)\left[(v_x + ey)^2 + (v_y + ex)^2 + (v_z)^2 \right]^{\frac{1}{2}} \\ (v_y + ex)\left[(v_x + ey)^2 + (v_y + ex)^2 + (v_z)^2 \right]^{\frac{1}{2}} \\ (v_z)\left[(v_x + ey)^2 + (v_y + ex)^2 + (v_z)^2 \right]^{\frac{1}{2}} \end{bmatrix} \tag{16.27}$$

$$a_x = -\frac{1}{2}.C_d.\frac{A}{m}.\rho.\left[(v_x - v_{Ax})^2 + (v_y - v_{Ay})^2 + (v_z - v_{Az})^2\right].\frac{(v_x - v_{Ax})}{v_r}$$
$$\therefore a_x = -\frac{1}{2}.C_d.\frac{A}{m}.\rho.\left[(v_x - v_{Ax})^2 + (v_y - v_{Ay})^2 + (v_z - v_{Az})^2\right]^{\frac{1}{2}}.(v_x - v_{Ax}) \quad (16.28)$$

$$a_y = -\frac{1}{2}.C_d.\frac{A}{m}.\rho.\left[(v_x - v_{Ax})^2 + (v_y - v_{Ay})^2 + (v_z - v_{Az})^2\right].\frac{(v_y - v_{Ay})}{v_r}$$
$$\therefore a_y = -\frac{1}{2}.C_d.\frac{A}{m}.\rho.\left[(v_x - v_{Ax})^2 + (v_y - v_{Ay})^2 + (v_z - v_{Az})^2\right]^{\frac{1}{2}}.(v_y - v_{Ay}) \quad (16.29)$$

$$a_z = -\frac{1}{2}.C_d.\frac{A}{m}.\rho.\left[(v_x - v_{Ax})^2 + (v_y - v_{Ay})^2 + (v_z - v_{Az})^2\right].\frac{(v_z - v_{Az})}{v_r}$$
$$\therefore a_z = -\frac{1}{2}.C_d.\frac{A}{m}.\rho.\left[(v_x - v_{Ax})^2 + (v_y - v_{Ay})^2 + (v_z - v_{Az})^2\right]^{\frac{1}{2}}.(v_z - v_{Az}) \quad (16.30)$$

16.1.3. Changes in Accelerations Due to Atmospheric Drag

We start with the final partial $\frac{\partial \bar{a}}{\partial C_d}$, as it is the simplest:

$$\frac{\partial a_x}{\partial C_d} = -\frac{1}{2}.\frac{A}{m}.\rho.v_r.(v_x - v_{Ax}) \quad (16.31)$$

$$\frac{\partial a_y}{\partial C_d} = -\frac{1}{2}.\frac{A}{m}.\rho.v_r.(v_y - v_{Ay}) \quad (16.32)$$

$$\frac{\partial a_z}{\partial C_d} = -\frac{1}{2}.\frac{A}{m}.\rho.v_r.(v_z - v_{Az}) \quad (16.33)$$

16.1.4. Changes in Acceleration Due to Changes in the Relative Velocity with Respect to Position

Both the density, and the relative velocity are affected by a change in position, and these must be accounted for when relating changes in acceleration to changes in position:

$$\frac{\partial \bar{a}}{\partial \bar{r}} = -\frac{1}{2}.C_d.\frac{A}{m}.\frac{\partial \rho}{\partial \bar{r}}.v_r.\bar{v}_r - \frac{1}{2}.C_d.\frac{A}{m}.\rho.\frac{\partial}{\partial \bar{r}}(v_r.\bar{v}_r) \quad (16.34)$$

$$\frac{\partial a_{rx}}{\partial x} = -\frac{1}{2}.C_d.\frac{A}{m}.\rho.\left[\frac{e(v_x+ey)(v_y+ex)}{v_r}\right]$$
$$\frac{\partial a_{rx}}{\partial y} = -\frac{1}{2}.C_d.\frac{A}{m}.\rho.\left[\frac{e(v_x+ey)^2}{v_r}+ev_r\right] \qquad (16.35)$$
$$\frac{\partial a_{rx}}{\partial z} = 0$$

$$\frac{\partial a_{ry}}{\partial x} = -\frac{1}{2}.C_d.\frac{A}{m}.\rho.\left[\frac{e(v_y+ex)^2}{v_r}+ev_r\right]$$
$$\frac{\partial a_{ry}}{\partial y} = -\frac{1}{2}.C_d.\frac{A}{m}.\rho.\left[\frac{e(v_y+ex)(v_x+ey)}{v_r}\right] \qquad (16.36)$$
$$\frac{\partial a_{ry}}{\partial z} = 0$$

$$\frac{\partial a_{rz}}{\partial x} = -\frac{1}{2}.C_d.\frac{A}{m}.\rho.\left[\frac{ev_z(v_y+ex)}{v_r}\right]$$
$$\frac{\partial a_{rz}}{\partial y} = -\frac{1}{2}.C_d.\frac{A}{m}.\rho.\left[\frac{ev_z(v_x+ey)}{v_r}\right] \qquad (16.37)$$
$$\frac{\partial a_{rz}}{\partial z} = 0$$

16.1.5. Changes in Acceleration Due to Changes in Atmospheric Density (Rho) with Respect to Position

$\frac{\partial \rho}{\partial \bar{r}}$ is actually very difficult to calculate analytically as, most often, it is provided by complicated atmospheric models. Therefore this parameter is usually differentiated numerically, and here the following symmetrical form is used:

$$f'(x) \approx \frac{f(x+h)-f(x-h)}{2h} \text{ (Press et al., 2002).} \qquad (16.38)$$

$\frac{\partial \rho}{\partial x}, \frac{\partial \rho}{\partial y}$ *and* $\frac{\partial \rho}{\partial z}$ can then each be fed in turn in place of ρ into the x,y,z drag acceleration equations ((16.28), (16.29) and (16.30)) given above.

16.1.6. Changes in Acceleration Due to Changes in Velocity

$$\begin{aligned}
\frac{\partial a_x}{\partial v_x} &= -\frac{1}{2}.C_d.\frac{A}{m}.\rho.v_r\left(1+\frac{(v_x-v_{Ax})^2}{v_r^{\,2}}\right)\\
\frac{\partial a_x}{\partial v_y} &= -\frac{1}{2}.C_d.\frac{A}{m}.\rho.\left(\frac{(v_x-v_{Ax})(v_y-v_{Ay})}{v_r}\right)\\
\frac{\partial a_x}{\partial v_z} &= -\frac{1}{2}.C_d.\frac{A}{m}.\rho.\left(\frac{(v_x-v_{Ax})(v_z-v_{Az})}{v_r}\right)
\end{aligned} \tag{16.39}$$

$$\begin{aligned}
\frac{\partial a_y}{\partial v_x} &= -\frac{1}{2}.C_d.\frac{A}{m}.\rho.\left(\frac{(v_x-v_{Ax})(v_y-v_{Ay})}{v_r}\right)\\
\frac{\partial a_y}{\partial v_y} &= -\frac{1}{2}.C_d.\frac{A}{m}.\rho.v_r\left(1+\frac{(v_y-v_{Ay})^2}{v_r^{\,2}}\right)\\
\frac{\partial a_y}{\partial v_z} &= -\frac{1}{2}.C_d.\frac{A}{m}.\rho.\left(\frac{(v_y-v_{Ay})(v_z-v_{Az})}{v_r}\right)
\end{aligned} \tag{16.40}$$

$$\begin{aligned}
\frac{\partial a_z}{\partial v_x} &= -\frac{1}{2}.C_d.\frac{A}{m}.\rho.\left(\frac{(v_x-v_{Ax})(v_z-v_{Az})}{v_r}\right)\\
\frac{\partial a_z}{\partial v_y} &= -\frac{1}{2}.C_d.\frac{A}{m}.\rho.\left(\frac{(v_y-v_{Ay})(v_z-v_{Az})}{v_r}\right)\\
\frac{\partial a_z}{\partial v_z} &= -\frac{1}{2}.C_d.\frac{A}{m}.\rho.v_r\left(1+\frac{(v_z-v_{Az})^2}{v_r^{\,2}}\right)
\end{aligned} \tag{16.41}$$

16.1.7. Solving for Changes to the Initial Conditions

We can now solve for changes to the initial conditions with respect to a precise reference trajectory. Our 'observations' are simply the X, Y and Z positions of the satellite as described by the reference trajectory (supplied through an orbit determination procedure).

The least squares solution to this system of equations is given by:

$$\left(\bar{A}^T \bar{A}\right)^{-1} \bar{A}^T \bar{b} = \bar{x} \tag{16.42}$$

At each epoch, three rows of the $\bar{A}$ matrix are computed and added onto the bottom of the existing $\bar{A}$ matrix, one for each of the X, Y and Z components:

$$\bar{A} += \bar{H} * \bar{\Phi} \Big| \bar{S} \tag{16.43}$$

where $\bar{H} = \begin{bmatrix} 1 & 0 & 0 & 0 & 0 & 0 \\ 0 & 1 & 0 & 0 & 0 & 0 \\ 0 & 0 & 1 & 0 & 0 & 0 \end{bmatrix}$

The $\bar{b}$ vector contains the observed minus computed X, Y and Z differences (i.e. 3 rows at each epoch), calculated by subtracting the X, Y and Z components of the integrated trajectory from that of the precise orbit. A solution is obtained after iterating over a desired integration period, where the $\bar{x}$ vector has the form:

$$\bar{x} = \left[\Delta\bar{r} \quad \Delta\bar{v} \quad \Delta\bar{p}\right]^T \tag{16.44}$$

17. Appendix D

17.1. ENVISAT SAR Baselines Tool - ESARB

For reasons outlined in section 2.4, deformation monitoring using SAR performs best when orbits over the area of interest are separated by short perpendicular baselines. While ESA provide several pieces of software to help streamline this process (DESCW[38] and EOLI-SA[39]), several bugs have been found by members of the COMET group. This resulted in the development of the ENVISAT SAR baselines (ESARB) tool by this author as part of the current study, which complements ESA's existing ones. The processing methodology and the web interface are detailed below.

The user enters a point at the centre of the area of interest using its latitude and longitude (see Figure 17-1):

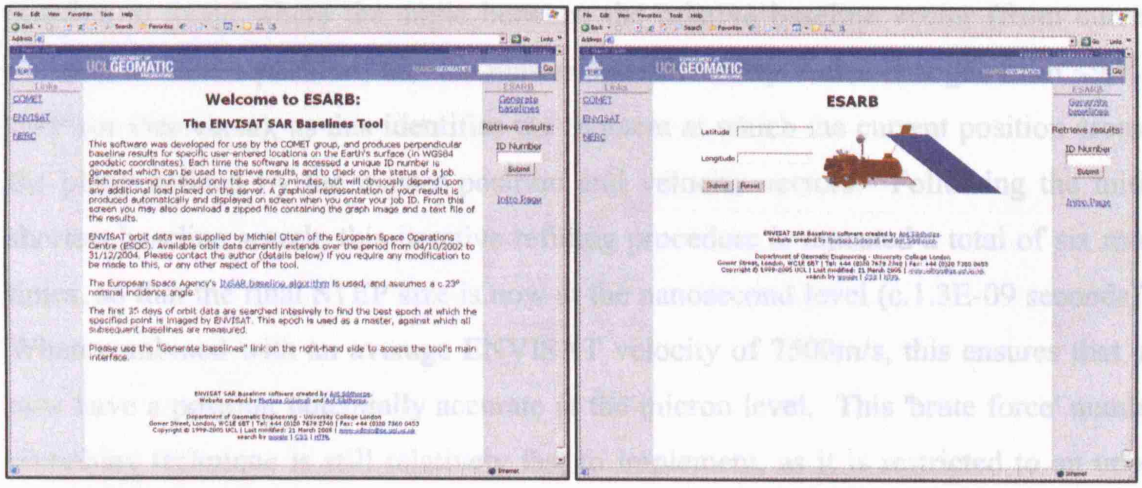

Figure 17-1: The ESARB web interface.

ECEF Cartesian positions and velocities at one minute intervals covering the on-orbit period of ENVISAT's life are obtained either directly from an ECEF orbit file, or by transformation from an ECI orbit file. ESARB constructs a +/-5° 'box' around the user entered point, and the orbit data is searched for the first point which lies inside the box. This point (epoch, position and velocity) is now stored as a master dataset and all of the following actions are referenced to it. We now search through the remaining orbit data

[38] http://earth.esa.int/descw/

[39] http://eoli.esa.int/geteolisa/index.html

for other orbit data which covers the area of interest. As ENVISAT has a repeat period of 35 days, the master epoch is first incremented by 34 days and 22 hours.

1. A continuous time series of orbit positions is provided by uniquely fitting a series of 12^{th} order polynomials to four hours of one minute interval orbit data (i.e. two hours either side of the stated repeat period), with only the middle four minutes of each polynomial being used to ensure a good fit. A quick technique is used which minimises the number of passes over this four hour period whilst looking for the shortest perpendicular baseline between the current epoch and the master epoch. An interval parameter, now referred to as STEP, is initially set to 60 seconds; the four hour orbit window is incremented by STEP until the point with the shortest baseline is found. A new search space of 2*STEP around this shortest baseline position is defined, and then STEP is divided by 60. The new space is looped over in STEP increments until a position is found where the angle between the relative baseline vector (from current position to master position) and the master epoch velocity vector changes from <90° to >90° (or vice versa), as this identifies the moment at which the current position crosses the plane defined by the master position and velocity vectors. Following the initial shortest baseline search, this iterative refining procedure is repeated a total of six more times, so that the final STEP size is now at the nanosecond level (c.1.3E-09 seconds)[40]. When combined with an average ENVISAT velocity of 7500m/s, this ensures that we now have a position potentially accurate at the micron level. This 'brute force' number crunching technique is still relatively fast to implement, as it is restricted to an upper bound of 7*240 simple calculations.

2. A local coordinate system must be constructed, and then rotated through 69.645°[41] in order to recover the nominal SAR antenna look angle. The offset from the reference position can then be decomposed into parallel and perpendicular components. As defined, this local coordinate system is left-handed, with the $\bar{Z}$ axis parallel to the satellite velocity vector ($\bar{v}$). The $\bar{X}$ axis is an across track vector, given by:

$$\bar{X} = \bar{v} \times \bar{r} \tag{17.1}$$

[40] Fewer iterations can of course be used depending upon the required accuracy.

[41] http://earth.esa.int/rootcollection/sysutil/01178.html

where $\overline{r}$ is the ECEF position vector.

To complete the mutually orthogonal system, a radial vector $\overline{Y}$ which is positive in the direction away from the Earth, is computed from:

$$\overline{Y} = \overline{X} \times \overline{Z} \tag{17.2}$$

The vectors which define the local coordinate system are then normalised ($\hat{X}, \hat{Y}, \hat{Z}$).

At this time the ECEF relative baseline between the current and master positions is computed, and projected onto the $\hat{X}$ and $\hat{Y}$ local vectors. A simple frame rotation, anti-clockwise around the velocity ($\hat{Z}$) vector, can then be applied to recover nominal parallel and perpendicular vectors, where the parallel vector points along the rotated $\hat{X}'$ axis, and the perpendicular vector points along the rotated $\hat{Y}'$ axis (see Figure 17-2 and equation (17.3)).

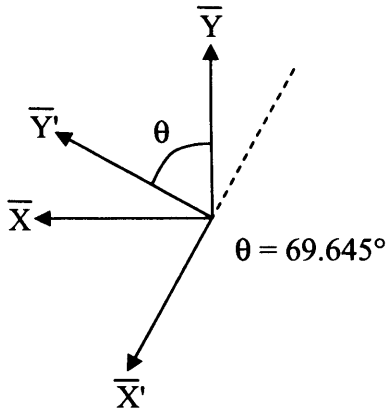

Figure 17-2: SAR frame rotation for perpendicular baseline recovery.

$$\begin{bmatrix} X' \\ Y' \end{bmatrix} = \begin{bmatrix} -\cos\theta & \sin\theta \\ \sin\theta & \cos\theta \end{bmatrix} \begin{bmatrix} X \\ Y \end{bmatrix} \tag{17.3}$$

3. A new current position is generated by incrementing the epoch of the position just used by 34 days and 22 hours, STEP is reset to 60 seconds, and then we return to (1) above and repeat until the supply of orbit data is exhausted.

The website then provides a plot of the results (see Figure 17-3) for quick analysis.

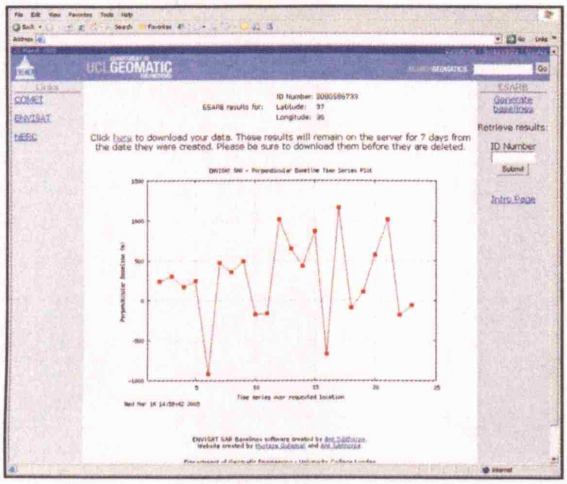

Figure 17-3: Plot of ENVISAT perpendicular baselines.

Users can then download this plot and a text file which contains all epochs and parallel and perpendicular baseline lengths relevant to the search over their area of interest. Figure 17-3 also shows that ESA is tasking ENVISAT to within its specified[42] maximum orbit track deviation of +/- 1Km across track, i.e. a maximum float of 2000m.

[42] http://envisat.esa.int/m-s/mission/operations.html#envisat%20orbit